ISSN 1451 - 9372 (Print) ISSN 2217 - 7434 (Online) JULY-SEPTEMBER 2026
Vol. 32, Number 3, 175-267

Chemical Industry & Chemical Engineering Quarterly

The AChE Journal for Chemical Engineering, Biochemical Engineering, Chemical Technology, New Materials, Renewable Energy and Chemistry

www.ache.org.rs/ciceq

The activities of the Association of Chemical Engineers of Serbia are supported by:

MINISTRY OF SCIENCE, TECHNOLOGICAL DEVELOPMENT AND INNOVATION OF REPUBLIC OF SERBIA

Faculty of Technology and Metallurgy, University of Belgrade

Faculty of Science, University of Novi Sad

Institute for Technology of Nuclear and Other Mineral Raw Materials, Bekgrade

Faculty of Technology, University of Novi Sad

Institute of Chemistry, Technology and Metallurgy, University of Belgrade

Faculty of Technical Sciences University of Novi Sad

Faculty of Technology, University of Niš, Leskovac

Faculty of Technical Sciences, University of Priština, Kosovska Mitrovica

IMS Institute, Belgrade

DCP HEMIGAL
Leskovac

Elixir Prahovo

Journal of the
Association of Chemical Engineers of
Serbia, Belgrade, Serbia

Chemical Industry & Chemical Engineering Quarterly

Journal of the
Association of Chemical Engineers of
Serbia, Belgrade, Serbia

Chemical Industry & Chemical Engineering Quarterly

Vol. 32 Belgrade, July-September 2026 No. 3

Chemical Industry & Chemical Engineering Quarterly (ISSN 1451-9372) is published quarterly by the Association of Chemical Engineers of Serbia, Kneza Miloša 9/I, 11000 Belgrade, Serbia

Editor:
Vlada B. Veljković
veljkovic@yahoo.com

Editorial Office:
Kneza Miloša 9/I, 11000 Belgrade, Serbia
Phone/Fax: +381 (0)11 3240 018
E-mail: shi@ache.org.rs
www.ache.org.rs

For publisher:
Ivana T. Drvenica

Secretary of the Editorial Office:
Ksenija Kostić

Marketing and advertising:
AChE Marketing Office
Kneza Miloša 9/I, 11000 Belgrade, Serbia
Phone/Fax: +381 (0)11 3240 018

Publication of this Journal is supported by the Ministry of Education, Science and Technological Development of the Republic of Serbia

Subscription and advertisements make payable to the account of the Association of Chemical Engineers of Serbia, Belgrade, No. 205-2172-71, Komercijalna banka a.d., Beograd

Technical Editor:
Ana V. Veličković

Journal Manager:
Aleksandar B. Dekanski

Printed by:
Faculty of Technology and Metallurgy, Research and Development Centre of Printing Technology, Karnegijeva 4, P.O. Box 3503, 11120 Belgrade, Serbia

Abstracting/Indexing:
Articles published in this Journal are indexed in *Thompson Reuters* products: *Science Citation Index - Expanded*™ - access *via Web of Science*®, part of *ISI Web of Knowledge*℠

CONTENTS

CI&CEQ
Chemical Industry & Chemical Engineering Quarterly

Available online at
Association of the Chemical Engineers of Serbia AChE
www.ache.org.rs/CICEQ

Chem. Ind. Chem. Eng. Q. 32 (3) 175–186 (2026) CI&CEQ

MARIJA MENKINOSKA[1]
TATJANA PAVLOVA[2]
ZHIVKA GORANOVA[3]
ANGELINA SREDOVSKA BOZHINOV[4]
ZLATIN ZLATEV[5]
HYRIJE KORAQI[6]
ANKA TRAJKOSKA PETKOSKA[7,8]

[1]Faculty of Technology, Goce Delcev University, Stip, North Macedonia
[2]Zan Mitrev Clinic, Skopje, North Macedonia
[3]Agricultural Academy, Department of Food Technology, Institute of Food Preservation and Quality, Plovdiv, Bulgaria
[4]International Balkan University, Faculty of Dental Medicine, Skopje, North Macedonia
[5]Trakia University, Faculty of Technics and Technologies, Yambol, Bulgaria
[6]Faculty of Food Science and Biotechnology, UBT-Higher Education Institution, Pristina, Kosovo
[7]University St Kliment Ohridski Bitola, Faculty of Technology and Technical Sciences – Veles, Veles, North Macedonia
[8]Department of Materials Science and Engineering, Korea University, Seoul, South Korea

SCIENTIFIC PAPER

UDC 664.681:66:547.56

GLUTEN AND GLUTEN-FREE BISCUITS WITH FUNCTIONAL COMPONENTS: PHYSICOCHEMICAL, NUTRITIONAL AND ANTIOXIDANT PROPERTIES

Highlights

- Functional additives for gluten and gluten-free biscuits with enhanced nutritive status
- Utilization of byproducts for the preparation of fine bakery products and better sustainability and circular economy concepts.
- Gluten-free biscuits rich in fiber

Abstract

This study aims to determine the effect of different compounds on the nutritional, antioxidant, microstructural, and color characteristics of biscuits classified as gluten and gluten-free. Namely, biscuits are enriched with dietary fibers, acacia fibers, spent coffee grounds, and anthocyanins. The addition of these functional components to biscuit matrix affected the physical properties of the biscuits; namely, the spread factor value of all biscuits ranged from 2.98 to 7.88, the content of total polyphenols increased, the highest polyphenol content was obtained in the gluten-free biscuits with added coffee grounds (77.98 mg), while in the biscuits with wheat flour has in the range of 44.62-128.63 mg. All gluten-free biscuits can be labeled as products with "rich in fiber" (6.32-7.68 g/100 g) and with a higher antioxidant content compared to biscuits without added ingredients. The total number of microorganisms in the tested cookies is below acceptable limits. The findings of this study show that the inclusion of raw nutritional components in the recipe of traditional gluten and gluten-free biscuits leads to an improvement in the nutritional value and other quality characteristics of the fortified food products.

Keywords: Antioxidant activity, polyphenol content, biscuits, gluten-free biscuits.

INTRODUCTION

Consumer demand for health-enhanced products is constantly increasing due to socio-economic trends and environmental concerns, such as longer life expectancy, rising health care costs, pursuit of a better quality of life, as well as better planetary health [1-4]. To develop value-added and functional food products, the addition of nutritive components could be a potential solution. The benefits are even greater when the added functional compounds are originally coming from biowaste or byproducts, e.g., from the food sector with functional properties. Most of them are already reported in the literature and are a valuable source of dietary fibers, vitamins, minerals, etc. [5-9].

The bakery products are an important part of the human diet. At a global level, bakery products constitute an essential part of human nutrition. The development of innovative products using value-added ingredients has become an important trend in the bakery sector to meet the demand of a new generation of consumers seeking healthier lifestyles [9]. Thanks to their ready-to-eat, long shelf life, and affordable price, biscuits are one of the most popular bakery products consumed worldwide [10-13].

Correspondence: M. Menkinoska, Faculty of Technology, Goce Delcev University, Goce Delcev 89, 2000 Stip, North Macedonia.
Email: marija_menkinoska@yahoo.co.uk
Paper received: 14 October 2024
Paper revised: 24 June 2025
Paper accepted: 9 July 2025

https://doi.org/10.2298/CICEQ241014021M

In most cases, biscuits are high in sugar and fat but low in vitamin content, minerals, fiber, and phenolic compounds [14]. Based on the literature, there are a lot of studies on the enrichment of biscuits, e.g., with a collagen peptide [10], olive stone powder [15], and green tea [16], that are mainly used as sources of dietary fiber, proteins, and phenolic compounds to fortify the biscuits.

On the other hand, gluten-free biscuits tend to be low in protein and high in starch compared to traditional gluten biscuits, according to many scientific findings, for example, by Cervini *et al.* [17]. Other authors have also reported that gluten-free biscuits have a different protein and starch content compared to traditional biscuits, etc. [18-20] On the other hand, Hopkin *et al.* [21] suggests that alternative flours, such as coconut and almond, that can improve the functionality of gluten free products; namely, they can be used in gluten-free biscuit recipes to achieve a similar texture and taste to traditional biscuits. Moreover, the use of plantain and amaranth flours could serve as a rich source of polyphenols and dietary fibers in gluten-free bread formulation [22].

The author's position is that incorporating functional additives such as acacia fiber, citrus fiber, spent coffee grounds, and anthocyanins into traditional and gluten-free biscuits can improve their nutritional value and sensory properties. Namely, *Robinia pseudoacacia* L. (acacia) belongs to the *Fabaceae* family; it is a honey tree. Acacia flowers are white and form inflorescences that are 10–15 cm long; it is edible and nutritious, rich in proteins and trace nutrients, flavonoids, robinin, polysaccharides, zinc, magnesium, iron, calcium, β-carene, linalool, anthranylated aldehyde, and (*Z*)-β-farnesene provide a pleasant aroma. Acacia flower contains bioactive components – phenols and ascorbic acid. Therefore, it is used in the food industry for the preparation of a variety of sweets as well as in functional products as a source of antioxidants [23]. In addition, acacia flower flour [24] is rich in dietary fiber, and it has a beneficial effect on blood sugar and cholesterol levels.

On the other hand, the use of biowaste and byproducts from the food industry as ingredients in the development of new products represents an important approach for a better economic and environmental qualification of these materials [25-27]. Therefore use of extracted nutritive components from them and their utilization in bakery products becomes very attractive nowadays. There are a lot of studies on this topic. For example, dietary fibers from different fruit waste, like citrus ones, anthocyanins from certain fruit peels, or spent coffee grounds, are only a few examples that are considered in this study. Namely, citrus fibers have a low glycemic index and can reduce the glycemic content of foods. Citrus fibers possess high water and fat-binding capacities due to their physicochemical properties, which are similar to those of the original citrus fruits [28]. Furthermore, coffee is a rich source of antioxidants and has been shown to have anti-inflammatory effects [29]. Coffee by-products have significant potential to be used as additives in food products. Coffee by-products have relatively high antioxidant properties, and they are rich in fiber and nutrients, making them potential functional components in many products [30]. Despite their high antioxidant activity, fiber source, and polyphenol content, the use of coffee by-products is relatively scarce [31,32].

In addition, Acacia fiber in the form of flour is often used as a thickener or emulsifier in food processing. It is also a good source of fiber and has been shown to have prebiotic properties that help maintain gut health [33]. On the other hand, anthocyanins are water-soluble pigments found in various fruits and vegetables, such as berries, red cabbage, and black rice, responsible for their red, purple, and blue colors. These compounds have been shown to have antioxidant and anti-inflammatory effects [34].

The color of the biscuits can be an indicator of their nutritional value, taste, as well as customer acceptance, like the orange color is often seen in food with high vitamin C and carotenoid content, while green foods are often rich in chlorophyll and antioxidants [34].

Coffee has a brown color due to changes during heat treatment, while anthocyanins are responsible for the red, blue, or purple color, depending on their origin, fruit/vegetable types. These pigments are powerful antioxidants that have been linked to numerous health benefits, including reduced inflammation and improved heart health [31,32]; the addition of acacia to the biscuits will provide a high fiber content, which has the function of improving the health of the intestines while the coffee grounds addition will give a rich flavor and aroma (and possibly some caffeine) to the biscuits. In other words, the newly developed biscuits will not only be tasty but also will have high nutritional potential for the consumer; they could be classified as functional products. In this context, the addition of functional components can be associated with distinctive biscuit colors that may serve as visual indicators of their health benefits. For example, biscuits with anthocyanins may appear violet/purple and could appeal to children while indicating antioxidant content. In this context, gluten and gluten-free biscuits could be color-coded based on the addition of functional components, making them easily recognizable-especially for children. This color coding could also serve as an indicator of health benefits; for instance, one color could signify improved brain function, while another could indicate benefits for eye health, helping consumers easily identify the specific advantages of each product. In other words, the newly developed biscuits will not only be tasty but also will have high nutritional potential for the consumer; they could be classified as functional products.

The aim of this study is to compare traditional gluten-containing and gluten-free biscuits enriched with citrus fibers, acacia fiber, spent coffee grounds, and anthocyanins in terms of their physicochemical, nutritional, and antioxidant properties.

MATERIALS AND METHODS

Materials

The compounds used in this study are: flour type 400 (Zito Luks, North Macedonia), rice flour-gluten free (Vitalia, North Macedonia). Functional additives to the traditional recipes of gluten and gluten-free biscuits are:

Citri-Fi®100FG (Fiberstar Inc., River Falls, Wisconsin, United States), is finely ground citrus fiber, with more than 95% (±4%) of the particles passing through a 100-mesh sieve, and spent coffee grounds (KaffeBueno, Denmark) were used in the formulation; acacia powder (Nexira, France); anthocyanins (Currantcraft® 11%, Iprona AG S.p.A., Italy); and stevia, a commercially available blend purchased from the company Vitalia (Skopje, North Macedonia), was also included due to its role as a natural, low-calorie sweetener contributing to the functional profile of the biscuits.

Biscuit preparation method

Two types of biscuits have been prepared: gluten and gluten-free. The process involves multiple stages, each specifying time duration, temperature, and designation. The designation refers to specific labels assigned to each processing stage in order to clearly identify and differentiate steps such as mixing, baking, and cooling. This system allows for precise control, consistent replication, and easy tracking of the production process.

The initial steps (Stages 1 and 2) focus on the preliminary preparation and dosage of raw materials at a temperature of 20–22 °C. Subsequently, Stage 3 includes the mixing of ingredients for 5 to 10 minutes at 18–20 °C to prepare a crumbly butter pastry base, which is then used to form the shaped pastry biscuit dough. Stage 4 includes the resting and cooling of the prepared dough for 30–40 minutes at 3–4 °C to stabilize the structure and improve the handling properties before further shaping, and Stages 5 to 7 include cooling, rolling out, and formation, all at 18–20 °C. The biscuits are then arranged in baking trays in Stage 8, with a baking time of 10–12 minutes at 200 °C (Stage 9). Afterward, the biscuits cool again (Stage 10) before proceeding to the final stage of packaging at 20–22 °C (Stage 11). Different amounts of functional components are added to gluten and gluten-free biscuits: citrus fibers, acacia powder, coffee grounds, and anthocyanins; compositions are presented in Table 1.

The developed formulations are based on the partial replacement of wheat flour with various functional additives, while the amounts of the remaining raw materials are constant. The amount of wheat flour for gluten-free biscuits is replaced with rice flour, while the amounts of the functional components are preserved. The biscuits were evaluated for their antioxidant activity, physicochemical characteristics, and sensory qualities.

Methods

Physical characteristics of biscuits.

The thickness of the biscuits was determined using an electronic digital calliper, and the diameter was measured by the method of Chopra *et al.* [35]. Three biscuits are placed next to each other, and their diameter were measured. Then, the biscuits were rotated 90°, and their diameter (cm) was measured again. An average value was taken from the measurements. The ratio between the diameter and thickness of the biscuits (biscuit expansion factor) was also determined [36].

Color characteristics of biscuits

An instrumental measurement of the color of the crust biscuits was made, with a digital colorimeter for quality control, model PCE-CSM 5 (PCE Deutschland GmbH, Meschede, Germany). The indicators were reported according to the CIE L*a*b* system. The colorimeter was calibrated with a black-and-white color standard [37]. The color parameters L^*, a^*, and b^* from Lab, as well as C^* and h* from the LCh color models, were determined.

The color difference ΔE was determined by Eq. (1):

$$\Delta E = \sqrt{(L_c - L_a)^2 + (a_c - a_a)^2 + (b_c - b_a)^2} \qquad (1)$$

where L_c, a_c, and b_c are color components of the control sample, and L_c, a_a, and b_a are color components of the enriched samples. ΔE varies in the range of 0–100, with the closer to 0, the closer the colors of the enriched biscuits were to those of the control sample, and the closer it was to 100, the more strongly they differed.

Water activity of biscuits

The water activity (a_w) of the biscuits was determined with a water activity meter with a sensor device, model HP23-AW-A (ROTRONIC AG, Bassersdorf, Switzerland).

The moisture content of biscuits

Moisture content of the biscuits was determined by the methods of AOAC (2000) [35]. Moisture was analyzed using a moisture analyzer based on the principle of infrared dry heating (via a halogen lamp).

Microbiological analysis of biscuits

The total number of microorganisms and the number of molds and yeasts in the biscuits were determined according to the AACC method [38]. Microbiological assay results were expressed as log(CFU/g).

Antioxidant activity (DPPH) of biscuits

The determination of the antioxidant activity of the biscuits using the DPPH free radical was done according to the methodology described earlier [39]. Biologically active substances were extracted with methanol solution (methanol:water 80:20 v/v). 1 g of sample extract was mixed with 10 mL of methanol solution. The mixture was placed on an electromagnetic stirrer at room temperature for 2 h, then centrifuged at 4300 rpm for 10 min. The antioxidant activity of the extracts was expressed as milligrams of Trolox equivalents (TE) per 100 grams of dry weight (mg TE/g dw).

Total polyphenols of biscuits

The content of total polyphenols was determined by the method with a modification [40]. In a test tube, 0.1 mL of sample extract was successively mixed with 0.5 mL of Folin reagent (diluted 1:4 with distilled water) and 1.5 mL of aqueous sodium carbonate solution (7.5% w/v), with the volume made up to 10 mL with distilled water.

The reaction mixture was allowed to stand for 2 h in the dark at room temperature before the absorbance at 750 nm was measured. The results obtained are presented as gallic acid equivalents (GAE) in mg per 100 g of sample.

Determination of the nutritional value of biscuits

Crude protein content was determined by the micro-Kjeldahl method by taking 1.0 g of the sample as described in the AOAC (2000) method 920.87 [35]. The crude fat content was determined by taking 1.5 g of the sample by the Soxhlet extraction method using petroleum ether as solvent (the AOAC (2000) method 920.39) [35]. Crude fiber content was determined by the AOAC (2000) method 962.09 [35] after mixing with 1.25% H_2SO_4 and 28% KOH, sieving through 75 μm, drying, and firing in a muffle furnace to remove the ash from the raw fibers. The difference determined the total carbohydrate content [41]. The amount of carbohydrate fractions was calculated by subtracting the sum of the amounts of fat, protein, and ash from 100%. Carbohydrate content was expressed as % dry matter.

Statistical analysis

Principal component analysis (PCA) [42] is a statistical technique that is used to find patterns in data. PCA is more commonly used to reduce the dimensionality of data, which can make it easier to analyze and interpret. In this study, PCA was used to investigate the relationships between the contents of acacia, citrus fibers, coffee grounds, and anthocyanins in biscuits and their main characteristics. Before the implementation of PCA, the data were normalized in the interval [0,1]. One-way ANOVA was used to evaluate differences among group means for the relevant variables. Where ANOVA indicated statistically significant differences ($p < 0.05$), a post hoc LSD (Least Significant Difference) was performed.

Additionally, for datasets that did not meet the assumption of normality, the Kruskal-Wallis test, a non-parametric alternative to ANOVA, was applied to ensure the validity of the statistical inferences.

The MATLAB software system (The Mathworks Inc., Natick, MA, USA) was used in the processing of the obtained data. All data were processed at an accepted level of statistical significance, $\alpha < 0.05$.

RESULTS AND DISCUSSION

Physical and color characteristics

Two types of biscuits, gluten and gluten-free, with four functional components, were observed. In Figure 1, the gluten and gluten-free biscuits are presented in a general, stylized form. Usually, the gluten biscuits had a brownish color, which was consistent with their production.

However, there were some notable variations between samples, to which finely ground citrus fibers, spent coffee grounds, anthocyanins, and acacia were added. They appeared noticeably darker in color than the control sample. This observation suggested that these additives might have affected the baking process in a way that resulted in a more intense coloration of the biscuits. In contrast, the acacia biscuits appeared closer in color to the control sample, suggesting that this additive had less effect on the baking process, fewer pigments, and a color close to that of wheat flour.

Also, the gluten-free biscuits were presented in a general, stylized form. Noticeable color variation was observed between the different samples, which included a control sample as well as those supplemented with citrus fibers, acacia, coffee grounds, and anthocyanins. The control sample and those with citrus fibers and acacia were fairly similar in color, suggesting that these additives had relatively little effect on the overall appearance of the biscuits. In contrast, samples with coffee grounds and anthocyanins were significantly darker in color, indicating that these additives had a more pronounced effect on the biscuit's pigmentation. The visual presentation of color differences between samples of gluten-free biscuits might reflect differences in their composition, processing methods, or interactions between these factors. These results may be of interest to food producers seeking to optimize the visual appeal of their gluten-free products.

The change in color characteristics of the gluten-free biscuits corresponds to their visible presentation above. The addition of acacia did not result in a color change compared to the control, while samples with citrus fibers, coffee grounds, and anthocyanins appeared darker.

Table 2 shows data on gluten and gluten-free biscuits with various additives. The main effect of the addition of citrus fibers, acacia, coffee, and anthocyanins in gluten biscuits appeared to be related to their effect on the coloring of the final product. Specifically, the samples with citrus fibers, coffee grounds, and anthocyanins appeared darker in color than the control biscuits, while the acacia sample was similar in color to the control. However, it was important to note that these natural additives might have other effects on the physicochemical characteristics of biscuits. For example, Citri-Fi®100FG is a natural citrus fiber that has been shown to improve moisture retention and texture in biscuits. Acacia, also known as gum arabic, is a common food additive that improves the viscosity and stability of biscuits. Coffee and anthocyanins are sources of antioxidants that have potential health benefits.

From Table 2, it is evident that the mean values for the thickness of gluten biscuits decrease in the presence of the additive. A significant difference in thickness was observed for the sample with citrus fiber, while greater thickness was reported for the gluten-free samples, except for the coffee biscuits. All functional cookies were increased in diameter compared to the control. A significant difference in spread ratio was observed for all biscuits. The increase in the spread ratio in the gluten-free cookies with coffee addition might be due to a significant decrease in cookie thickness.

The value of the spread factor of all cookies ranged from 2.98 to 7.88. Clear differences in the spread factor were observed across all biscuit samples. In terms of physico-chemical characteristics, the moisture content of gluten-free biscuits varied depending on the type of additive used. Acacia biscuits had similar levels of moisture content to the control, while those with citrus fibers, coffee grounds, and anthocyanins showed increased moisture content. In addition, adding these additives to gluten-free biscuits increased their antioxidant activity, which might provide potential health benefits.

Polyphenol content

The content of total polyphenols for the gluten-free samples was in the range of 29.74-37.95 mg GAE/100 g. The content of total polyphenols was highest in gluten-free biscuits with coffee (77.98 mg), while in biscuits with wheat flour and supplement, it was in the range of 44.62-128.63 mg. The lowest content of these compounds was found in the control biscuits. It is worth noting that all the various types of polyphenols, the most abundant in phenolic acids, flavonoids, and anthocyanins, are acacia biscuits and coffee biscuits.

Table 1. Raw materials used for gluten and gluten-free biscuits.

Gluten biscuits					
Functional Additive	Control	Citrus fibers, 2%	Acacia, 3%	Coffee grounds, 4%	Anthocyanin, 1%
Flour type 400, g	100	98	97	96	99
Sugar, g	20	20	20	20	20
Additive, g	-	2	3	4	1
Water, ml	40	40	40	40	40
Sunflower oil, ml	30	30	30	30	30
Vanilla, g	2	2	2	-	2
Gluten-free biscuits					
Functional Additive	Control	Citrus fibers, 2%	Acacia, 3%	Coffee grounds, 4%	Anthocyanin, 1%
Rice flour, g	100	98	97	96	99
Stevia, g	10	10	10	10	10
Additive, g	-	2	3	4	1
Water, ml	50	50	50	50	50
Sunflower oil, ml	30	30	30	30	30
Vanilla, g	2	2	2	-	2

Table 2. Characteristics of gluten and gluten-free flour biscuits with various additives.

Parametar	Control	Acacia	Citrus fibers	Coffee grounds	Anthocyanins
Color characteristics					
L	56.70±0.40*	43.00±4.16**	25.68±3.13*	23.55±0.61*	25.02±3.97*
a	3.41±0.28**	2.09±0.95*	0.99±0.45**	5.55±0.61*	4.74±0.93*
b	16.33±0.98*	11.78±2.25*	7.64±2.51**	9.88±1.14*	4.79±0.65*
c	16.42±0.58*	11.97±2.38*	7.70±2.54*	11.34±1.28*	6.30±1.68**
h	78.11±0.54**	80.26±2.44**	82.80±1.03*	60.66±1.09*	40.09±5.40*
Physico-chemical characteristics					
WA	0.82±0.00***	0.83±0.01**	0.84±0.00***	0.86±0.06*	0.85±0.00***
MC, %	14.51±0.08**	15.25±0.07**	12.89±0.04*	12.08±0.04*	15.36±0.12*
D, cm	4.67±0.15**	5.03±0.15**	4.93±0.12*	4.77±0.25**	5.07±0.06*
T, cm	1.57±0.06*	1.53±0.06*	1.27±0.06*	1.40±0.10*	1.48±0.03**
SR	2.98±0.04*	3.28±0.04*	3.90±0.24**	3.41±0.07*	3.42±0.03**
Antioxidant activity					
TP, GAE/100g	44.62±0.02*	66.29±0.30*	50.93±0.23*	128.63±0.11*	58.46±0.57*
DPPH, TE/100g	250.85±0.54**	174.90±0.43*	265.98±0.07*	887.11±0.82**	490.25±0.06**
Gluten-free biscuits					
Parametar	Control	Acacia	Citrus fibers	Coffee grounds	Anthocyanins
Color characteristics					
L	31.82±2.65*	29.20±1.22*	38.08±1.22*	18.21±0.84**	16.45±4.55*
a	1.13±0.06*	0.95±0.12*	0.59±0.10*	-0.21±0.18*	-0.06±1.67**
b	6.77±0.33**	6.22±0.69*	7.44±1.10*	1.36±0.26**	-1.96±0.27*
c	6.86±0.33*	6.28±0.73*	7.49±1.16**	1.39±0.26**	2.38±0.38*
h	80.54±0.45*	83.02±2.38*	83.11±2.87*	90.41±14.56*	238.36±8.88*
Physico-chemical characteristics					
WA	0.84±0.01**	0.86±0.06**	0.85±0.00***	0.89±0.00***	0.90±0.00***
MC, %	8.99±0.05*	8.94±0.11*	9.71±0.09*	9.15±0.03*	9.50±0.06*
D, cm	4.97±0.06*	5.07±0.12*	5.00±0.00***	4.97±0.06*	5.10±0.10*
T, cm	0.77±0.06*	0.81±0.01*	0.81±0.01*	0.63±0.06*	0.90±0.10**
SR	6.51±0.56*	6.28±0.20**	6.17±0.08**	7.88±0.64**	5.71±0.53*
Antioxidant activity					
TP, mg GAE/100 g	29.74±0.08*	46.91±0.02**	31.96±0.19*	77.98±0.61**	37.95±0.57*
DPPH, mg TE/100 g	104.86±0.5*	174.80±0.2*	170.84±0.53**	348.25±0.08*	422.09±1.25*

WA-Water activity; MC-Moisture content; D-Diameter; T-Thickness; SR-Spread ratio; TP-Total polyphenols; DPPH - DPPH assay. Values are represented as mean ± standard deviation of triplicate samples. Mean values bearing different columns with superscript in the same column differ significantly (p<0,05). All data have statistically significant differences at p<0,05

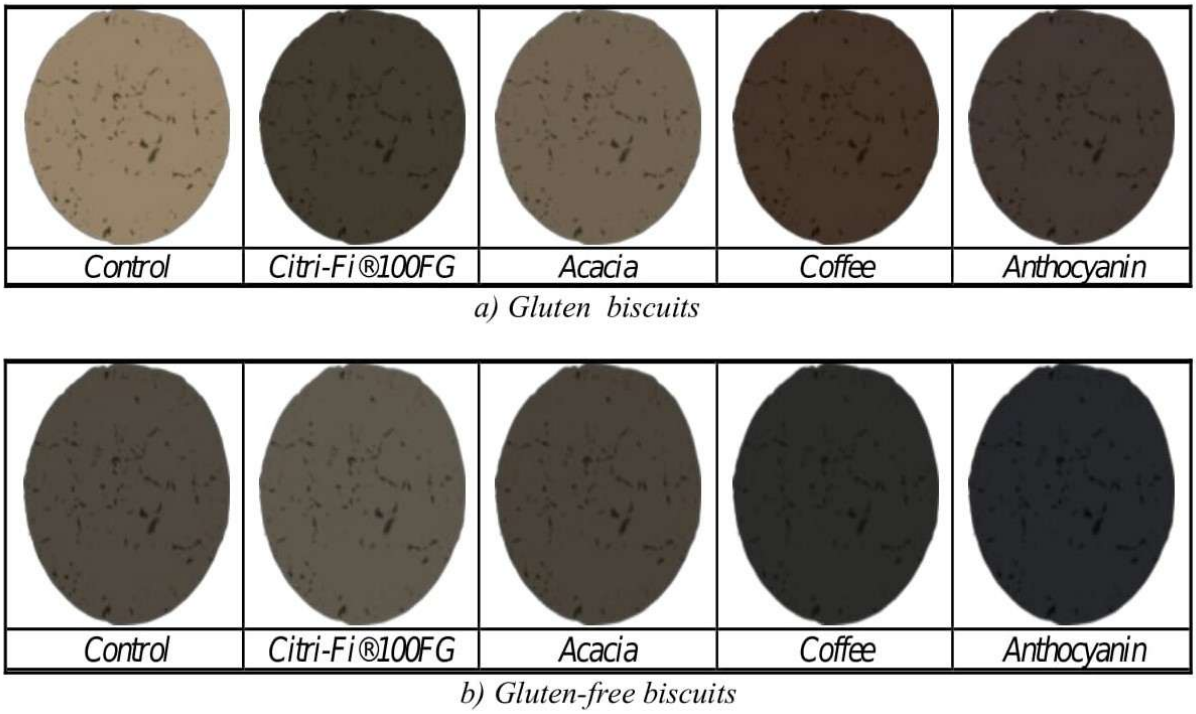

Figure 1. General view of biscuits with additives: a) gluten biscuits and b) gluten-free biscuits.

The baking process at high temperatures (>180-200 °C) can have a significant impact on polyphenolic molecules, leading to some changes in their content and structure [43]. For example, as a result of heat treatment, anthocyanins can be converted to chalcone glycosides and then hydrolyzed to chalcones, which are sequentially cleaved to form various end products such as aldehydes and acids [44]. In addition, metal ions present in food (iron, copper, and manganese) can be involved in the conversion of anthocyanins into quinones, which can react with proteins and other polyphenols to form condensation products that contribute to the browning of food [45]. In wheat grain, mostly insoluble fractions (77%) are found, followed by bound soluble acids (22%), including free and soluble fractions (0.5-1%) [46]. Baking increases the level of free phenolic acids in bread, cakes, and buns, but decreases the amount of bound phenolic acids [47], suggesting that baking may promote the release of phenolic acids from bound to free.

The antioxidant activity of biscuits

The antioxidant activity of wheat flour biscuits was between 250 and 490 mg TE/100 g, while gluten-free samples ranged from 105 to 422 mg TE/100 g (DPPH method). Nevertheless, using the measurement method, the antioxidant activity of all cookies enriched with healthy additives was greater than that of the control biscuits, except for the wheat flour and acacia samples. The observed differences in the antioxidant activity of the studied biscuits were the result not only of the differences between the plant sources of the additives but also of the antioxidant activity of the individual phenols. The structure of polyphenolic compounds also plays a significant role; the greater the number of hydroxyl groups, the better the antioxidant properties [48].

Color characteristics of gluten biscuits

Color parameters are important indicators of quality and influence consumers' willingness to buy a food product. As a result of the instrumental color analysis, it was found that the control was the lightest, with a high value for color brightness, L^*=56.27 (Table 3); higher L^* values do not necessarily mean a deterioration in product quality, rather it may be the dilution effect of the wall materials refers to the presence of light-colored components (such as dietary fibers or polysaccharides) derived from encapsulating agents, which reduce the visual intensity of natural pigments in the dough, resulting in higher L^* values (i.e., a lighter appearance).

With the darkest coloring were the samples with coffee. From Table 2 and normalized values in Table 3, it can be seen that the biscuits containing coffee have the highest values for parameter a^* (5.55). The values for the parameter a^* of the other types of biscuits are in the range from 0.99 to 4.74. This shows that all types of biscuits are in the brown-red range. From the research, we found that the lowest values for parameter b^* have the biscuits containing anthocyanins (4.79), which proves the blue-purple color characteristic of anthocyanins. The highest values for b^* were recorded for the control biscuits (16.33), which characterized them with a yellow color.

The hue angle (H^*) reflects the characteristic color of the samples. Hue angles of 0 °, 90 °, 180 °, and 270 ° represent red, yellow, green, and blue colors, respectively [50]. All samples showed values from the yellow coordinate (40.90-82.80).

Color saturation (C^*) of biscuits is a measure of color purity. The most saturated and uniform color was the control because the additives were of different particle sizes and had different color saturation in the cookies.

Figure 2 shows the color difference between a control sample and those with additives. In gluten flour biscuits, the addition of citrus fiber resulted in smaller color differences with the control sample. The samples with added coffee spent grounds and anthocyanins showed the biggest differences.

In the case of gluten-free biscuits, due to the specificity of the flour used, the control sample had a darker color. For this reason, samples with coffee spent grounds and anthocyanins had a small color difference from it. The biggest difference was seen in the acacia sample, as it was lighter in color.

Color characteristics of gluten-free biscuits

The biscuits containing citrus fibers have the highest value for the L^* parameter (38.08). The biscuits produced with the addition of anthocyanins (16.45) had the lowest values for this parameter due to the dark color of the addition. The values for the parameter a^* in biscuits made with coffee and anthocyanins were the lowest, which characterized their dark brown and blue color, as well as the absence of gluten. The highest values for the same parameter were reported for the control biscuits.

The parameter b^* indicates whether a studied object has a yellow or blue color. The lowest values for this parameter have been obtained for the biscuits produced with anthocyanins, while the highest values for the b^* parameter were reported for the biscuits with citrus fibers.

The most saturated color (C^*) is the citrus sample. The hue angle (H^*) in the gluten-free samples was quite variegated; the control and the acacia citrus biscuits were in yellow shades, the coffee sample was in brown shades, and the anthocyanin biscuits were in purple-blue shades.

Measured data for biscuits made from gluten and gluten-free flour with different additives was processed with the PCA method. Table 3 shows the quality characteristic values of gluten and gluten-free biscuits with different additives. Values were normalized in the interval [0,1]. These values were most affected by the various additives in the biscuits. The number of components required was determined under the condition that the sum of the principal components should describe more than 95% of the variance in the data. Up to 11 principal components could be calculated in rows, and up to 4 in columns.

Figure 3 shows principal component analysis (PCA) results for biscuits with gluten and gluten-free and various additives. Collectively, the three principal components describe over 95% of the variance in the experimental data. The control sample differed from the other samples with additives in the content of polyphenols and the L^* (CIE Lab) color component. Regardless of the additive, they affect the color component. A significant difference in the h (CIE Lch) color component appeared with anthocyanin and coffee supplements. Additions of citrus fibers and acacia had a significant impact on the main characteristics of the biscuits.

The specific characteristics of the composition of citrus fibers, coffee grounds, anthocyanins, and acacia, which lead to changes in the colors, physicochemical characteristics, and antioxidant activity of the biscuits, may vary for each additive. Citri-Fi®100FG is a natural citrus fiber that can function as a water-binding agent, increasing the moisture content and viscosity of biscuits. This can also potentially affect the color and texture of the biscuits. Citrus

Table 3. Normalized mean values of quality characteristics of gluten and gluten-free biscuits with various additives.

Gluten biscuits					
Parametar	Control	Acacia	Citrus fibers	Coffee grounds	Anthocyanins
L	0.22	0.24	0.09	0.03	0.05
a	0.01	0.01	0.00	0.01	0.01
b	0.06	0.06	0.03	0.01	0.01
c	0.06	0.06	0.03	0.01	0.01
h	0.31	0.45	0.31	0.07	0.08
WA	0.00	0.00	0.00	0.00	0.00
MC	0.05	0.08	0.05	0.01	0.03
D	0.02	0.02	0.02	0.00	0.01
T	0.00	0.00	0.00	0.00	0.00
SR	0.01	0.01	0.01	0.00	0.01
TP	0.17	0.37	0.19	0.14	0.12
DPPH	1.00	1.00	1.00	1.00	1.00
Gluten-free biscuits					
Parametar	Control	Acacia	Citrus fibers	Coffee grounds	Anthocyanins
L	0.30	0.16	0.22	0.05	0.04
a	0.00	0.00	0.00	0.00	0.00
b	0.06	0.03	0.04	0.00	0.00
c	0.06	0.03	0.04	0.00	0.01
h	0.76	0.47	0.48	0.26	0.57
WA	0.00	0.00	0.00	0.00	0.01
MC	0.08	0.05	0.05	0.03	0.03
D	0.04	0.02	0.03	0.01	0.02
T	0.00	0.00	0.00	0.00	0.01
SR	0.05	0.03	0.03	0.02	0.02
TP	0.28	0.26	0.18	0.22	0.09
DPPH	0.99	1.00	1.00	1.00	1.00

WA - Water activity; MC - Moisture content; D - Diameter; T - Thickness; SR - Spread ratio; TP - Total polyphenols; and DPPH - DPPH assay.

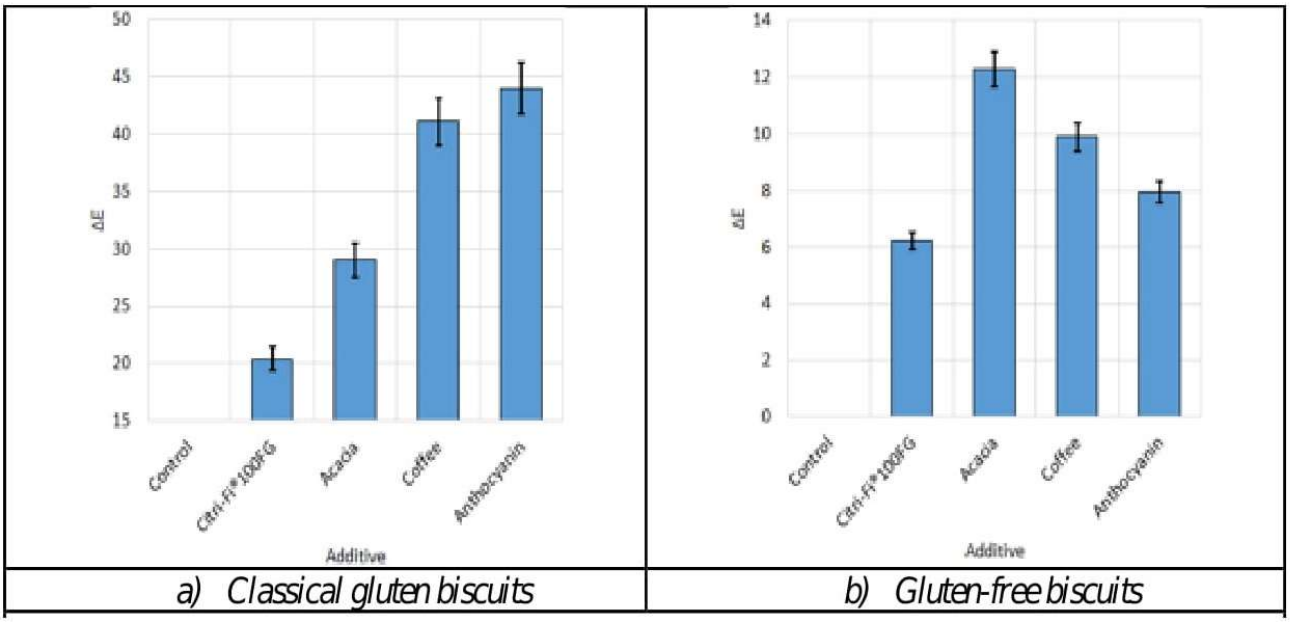

Figure 2. Color difference ΔE: a) gluten biscuits and b) gluten-free biscuits.

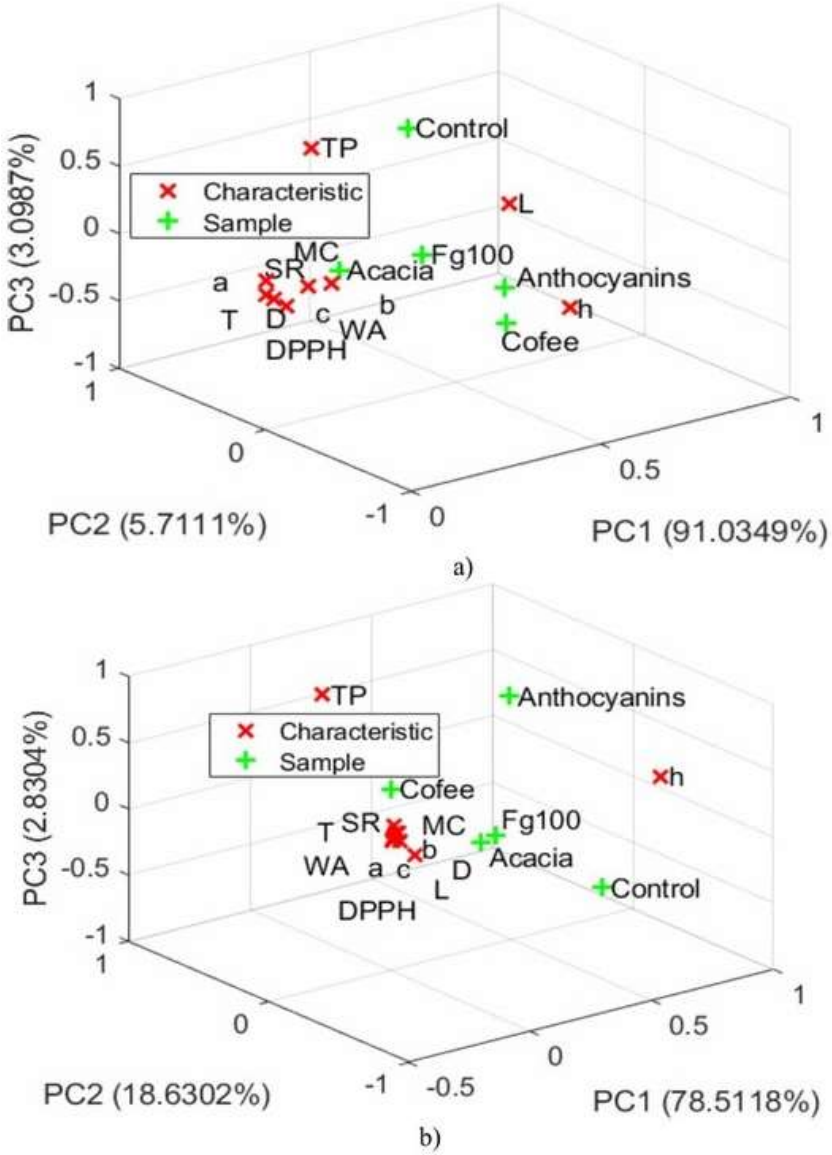

Figure 3. PCA of: a) gluten biscuits and various additives and b) gluten-free biscuits and various additives.

fibers also have antioxidant properties that may contribute to the increased antioxidant activity of the biscuits.

The results of the analysis (PCA) for gluten-free biscuits also showed a significant difference in the *h* (Lch) color component for all additives because the control sample differed from the supplemented ones precisely on this component. The sample with anthocyanins significantly changed the polyphenol content of the biscuits. The citrus fibers, coffee grounds, and acacia samples had an equally significant effect on the other biscuit characteristics.

The findings of this study complement the work of Cervini *et al.* [17], who investigated how specific formulations influence the composition and characteristics of gluten-free biscuits compared to their gluten-containing counterparts. They identified significant differences in moisture content and color attributes between the two types, highlighting the impact of gluten on sensory properties and overall product quality. These insights provide valuable guidance for biscuit manufacturers, enhancing the understanding of how formulation choices affect key product characteristics. Furthermore, this study reinforces and expands the existing body of research on gluten-free biscuit development.

Specifically, studies by Kohli *et al.* [18] and Sharoba *et al.* [19] were included in the present analysis, which found moisture content to be a crucial characteristic in the formulation of gluten-free biscuit recipes. They suggested using alternative flours rich in bioactive compounds to improve the characteristics of gluten-free biscuits.

To improve the characteristics of gluten-free biscuits, it is suggested to use alternative flours, such as coconut and almond, as recommended by Hopkin *et al.* [21]. By incorporating alternative flours, biscuit manufacturers can potentially improve the sensory characteristics and overall quality of gluten-free products.

The presence of citrus fibers and acacia indicates that the biscuits are high in fiber and may be beneficial in promoting gut health. Similarly, coffee grounds impart a rich flavor to biscuits and, together with anthocyanins, improve the antioxidant activity of the final product. In other words, the resulting biscuits are not only tasty but also useful for the consumer, thus complementing the research of Elhassaneen *et al.* [24] and Azuan *et al.* [29].

The present study provides valuable information for the characterization of gluten and gluten-free biscuits with different functional additives. Its results can serve as preliminary baseline data to be used for future evaluations and studies related to the express automated analysis of biscuits. Based on them, researchers and the food sector in general can have a better understanding of the properties of these types of biscuits and develop more efficient and effective methods for their production. Also, the results can significantly contribute to the development of high-quality biscuits with added value - improved nutritional value and sensory characteristics.

The results from the nutritional profile and energy value of biscuits with gluten and gluten-free biscuits are presented in Table 4. It can be seen that the control samples have the highest amount of carbohydrates (49.20 g/100 g), and the biscuits containing acacia have the least amount (47.98 g/100 g). There is a tendency that with the addition of a functional component in the recipe composition of biscuits, the amount of carbohydrates decreases. The protein and fat content show no statistically significant differences among the biscuit samples containing wheat flour. In addition, adding fiber-rich ingredients increases the content of dietary fiber in biscuits. Products with the additive have a reduced energy value compared to the control sample.

The nutritional composition of gluten-free biscuits is also presented in Table 4, including the content of fat, protein, dietary fiber, and carbohydrates, as well as the energy value. Biscuits mainly contain carbohydrates (45.60-47.06 g/100 g), followed by fat (~18 g/100 g). Dietary fiber contains a variety of carbohydrates that are not hydrolyzed or absorbed by the human small intestine and whose daily intake is associated with health benefits, particularly for gastrointestinal function [51]. According to European regulations [52], food can use the nutrition claim 'source of fibre' if it contains at least 3 g/100 g, and can claim rich in fiber' if it contains 6 g/100 g or more. In this sense, all samples of gluten-free biscuits could be labeled as rich in fiber" (6.32–7.68 g/100 g). The protein content was found to range from 3.39 to 3.46 g /100 g. The energy value of the gluten-free and supplemented biscuits was lower compared to the control sample. Microbiological analysis of biscuits with and without gluten

Table 5 shows the microbiological determination of biscuits with and without gluten, in which the total number of microorganisms and the presence of molds and yeasts were analyzed. Regarding the group of filamentous molds and yeasts, no presence was detected; therefore, good manufacturing practices were used during the production process of the biscuits.

The percentage of additives did not significantly affect the total number of yeasts, molds, and microorganisms. The established values of aw correspond to the obtained results of the microbiological analysis. The microbial load of the biscuit samples was compared to microbiological standards for fortified mixed products, and the total number of microorganisms was found to be less than $1 \cdot 10^5$ CFU/g. This value falls within acceptable limits.

CONCLUSION

In this study, a comparative analysis was conducted between traditional gluten and gluten-free biscuits enriched with citrus fibers and functional additives including citrus fibers, acacia, coffee grounds, and anthocyanins. The results revealed notable differences in the composition and properties of gluten and gluten-free biscuits:

Citrus fibers: Most effective in increasing dietary fiber content. At a 5% addition level, gluten-free biscuits meet the criteria for the nutritional claim 'high in fiber,' making this the simplest and fastest option for implementation in the biscuit industry.

Table 4. Nutritional profile and energy value of biscuits with gluten and gluten-free (per 100 g of product).

Gluten biscuits					
Indicators	Control	Acacia	Citrus fibers	Coffee grounds	Anthocyanins
Carbohydrates, g/100 g	47.81	45.24	46.16	46.48	47.40
Dietary fiber, g/100 g	1.39	2.74	2.22	2.05	1.38
Proteins, g/100 g	6.44	6.28	6.37	6.42	6.37
Fats,g/100 g	18.26	18.21	18.23	18.20	18.24
Energy value, kcal/100 g	378.56	364.49	369.75	371.30	376.48
Gluten-free biscuits					
Indicators	Control	Acacia	Citrus fibers	Coffee grounds	Anthocyanins
Carbohydrates, g/100 g	46.24	43.85	44.49	44.48	45.75
Dietary fiber, g/100 g	0.82	1.75	1.60	1.47	0.81
Proteins, g/100 g	3.46	3.39	3.45	3.44	3.42
Fats, g/100 g	16.86	16.82	16.83	16.85	16.84
Energy value, kcal/100 g	352.18	343.84	346.43	346.27	349.86

Table 5. Microbiological indicators of biscuits.

Microorganisms	Control	Acacia	Citrus fibers	Coffee grounds	Anthocyanins
Total number of microorganisms Total Plate Count CFU/g	< 10	< 10	< 10	< 10	< 10
Molds and yeasts CFU/g	Absence	Absence	Absence	Absence	Absence

Acacia: Contributes to increased antioxidant activity and fiber content. A 3% addition of gluten-free biscuits yielded good results without negatively affecting texture or processing.

Coffee grounds: Enhances both antioxidant activity and dietary fiber content. A 2% addition was found to be effective without complicating the production process.

Anthocyanins: Improve the visual color characteristics of the biscuits, especially in gluten-free formulations, with limited effect on antioxidant activity.

Based on the balance between nutritional benefit and ease of application, citrus fibers at 5% in gluten-free biscuits are recommended as the most effective option for industrial use. Further research is needed to investigate the effect of these additives on product shelf life.

REFERENCES

[1] M. Siol, A. Sadowska, Agriculture 13 (2023) 316. https://doi.org/10.3390/agriculture13020316.

[2] M. Ferreira, L. Santos, Food Biosci. 51 (2023) 102293. https://doi.org/10.1016/j.fbio.2022.102293.

[3] A. Babazadeh, F. Mohammadi Vahed, Q. Liu, S.A. Siddiqui, M.S. Kharazmi, S.M. Jafari, ACS Omega 8 (2023) 3667-3683. https://doi.org/10.1021/acsomega.2c06098.

[4] T. Varzakas, S. Smaoui, Foods 13 (2024) 306. https://doi.org/10.3390/foods13020306.

[5] A. Nartea, B. Fanesi, D. Pacetti, L. Lenti, D. Fiorini, P. Lucci, N.G. Frega, P.M. Falcone, Curr. Res. Food Sci. (2023) 100437. https://doi.org/10.1016/j.crfs.2023.100437.

[6] S. Nardella, A. Conte, M.A. Del Nobile Foods 11 (2022) 665. https://doi.org/10.3390/foods11050665.

[7] S.M. Ferreira, S.M. Gomes, L. Santos, Food Bioprod. Process. 15 (2024) 2721-2733. https://doi.org/10.1007/s12649-023-02366-3

[8] A. Wirkijowska, P. Zarzycki, D. Teterycz, A. Nawrocka, A. Blicharz-Kania, P. Łysakowska, Appl. Sci. 13 (2023) 9312. https://doi.org/10.3390/app13169312.

[9] V. Šimora, H. Dúranová, J. Brindza, M. Moncada, E. Ivanišová, P. Joanidis, D. Straka, L. Gabríny, M. Kačániová, Foods 12 (2023) 593. https://doi.org/10.3390/foods12030593.

[10] A. Kumar, K. Elavarasan, M.D. Hanjabam, P.K. Binsi, C.O. Mohan, A.A. Zynudheen, A.K. Less, Agric. Food Sci. 109 (2019) 450-456. https://doi.org/10.1016/J.LWT.2019.04.052.

[11] I.D. Soares, M.E.M. Cirilo, I.G. Junqueira, F.M. Vanin, C.E.d.C. Rodrigues, Foods 12 (3) (2023) 436. https://doi.org/10.3390/foods12030436

[12] D. Pinto, M.M. Moreira, E.F. Vieira, J. Švarc-Gajić, A. Vallverdú-Queralt, T. Brezo-Borjan, C. Delerue-Matos, F. Rodrigues, Foods 12 (3) (2023) 640. https://doi.org/10.3390/foods12030640.

[13] T. Ferreira, S.M. Gomes, L. Santos, Antioxidants 12 (12) (2023) 2069. https://doi.org/10.3390/antiox12122069.

[14] M. Goubgou, L.T. Songré-Ouattara, F. Bationo, H. Lingani-Sawadogo, Y. Traoré, A. Savadogo, Food Prod Process Nutr. 3 (1) (2021) 26. https://doi.org/10.1186/s43014-021-00071-z

[15] S. Bolek, Innovative Food Sci. Emerging Technol. 64 (2020) 102423. https://doi.org/10.1016/j.ifset.2020.102423.

[16] S. Mildner-Szkudlarz, R. Zawirska-Wojtasiak, W. Obuchowski, M. Gośliński, J. Food Sci. 74 (2009) S362-S370. https://doi.org/10.1111/j.1750-3841.2009.01313.x.
[17] M. Cervini, A. Frustace, G. Garrido, G. Rocchetti, G. Giuberti, Heliyon 7 (2021) e06562. https://doi.org/10.1016/j.heliyon.2021.e06562.
[18] D. Kohli, A. Jain, O. Singh, S. Kumar, J. Agric. Food Res. 14 (2023) 100683. https://doi.org/10.1016/j.jafr.2023.100683.
[19] A.M. Sharoba, A.M. Abd El-Salam, H.H. Hafez, J. Agroaliment. Process. Technol. 20 (3) (2014) 203-214. http://journal-of-agroalimentary.ro/
[20] S. Moradi Marnilo, M.S. Yarmand, M. Salami, M.A. Aliyari, Z. Emam-Djomeh, Y.S. Mostafavi, J. Food Process. Agric. Food Sci. 2023 (2023) 4923259. https://doi.org/10.1155/2023/4923259
[21] L. Hopkin, H. Broadbent, G.J. Ahlborn, Food Chem. X. 13 (2022) 100182. https://doi.org/10.1016/j.fochx.2021.100182.
[22] V. Bringas-González, L.A. Bello-Pérez, A. Contreras-Oliva, M. López-Espíndola, J.A. Herrera-Corredor, J. Food Process. Preserv. 46 (2022) e16791. https://doi.org/10.1111/jfpp.16791.
[23] M. Iancu, J. Agroaliment. Processes Technol. 27 (2021) 164-171. http://journal-of-agroalimentary.ro/
[24] Y. Elhassaneen, Y. Elhady, N. Mohamed, Life Sci. J. 11 (2014) 385-393. https://www.researchgate.net/publication/287308501.
[25] A. Pasqualone, A.M. Bianco, V.M. Paradiso, C. Summo, G. Gambacorta, F. Caponio, A. Blanco, Food Chem. 180 (2015) 64-70. https://doi.org/10.1016/j.foodchem.2015.02.025.
[26] F. Artés-Hernández, L. Martínez-Zamora, M. Cano-Lamadrid, S. Hashemi, N. Castillejo, Foods 12 (3) (2023) 561. https://doi.org/10.3390/foods12030561.
[27] A. Gupta, N. Sanwa, M.A. Baren, S. Barua, N. Sharma, O.J. Olatunji, N.P. Nirma, J.K. Sahu, Food Res. Int. 170 (2023) 113046. https://doi.org/10.1016/j.foodres.2023.113046.
[28] E.B. Giuntini, F.A. Hoffmann Sardá, E.W. de Menezes, Foods 11 (23) (2022) 3934. https://doi.org/10.3390/foods11233934.
[29] A. Azuan, Z. Mohd Zin, M. Hasmadi, N. Rusli, M. Zainol, Food Res. 4 (2020) 1181-1190. https://doi.org/10.26656/fr.2017.4(4).058.
[30] T. Klingel, J.I. Kremer, V. Gottstein, T. Rajcic de Rezende, S. Schwarz, D.W. Lachenmeier, Foods 9 (2020) 665. https://doi.org/10.3390/foods9050665.
[31] K. Socała, A. Szopa, A. Serefko, E. Poleszak, P. Wlaź, Int. J. Mol. Sci. 22 (2020) 1. https://doi.org/10.3390/ijms22010107.
[32] R.R. Ahmed, N.K. Alqahtani, K.M.A. Ramadan, H.I. Mohamed, M.A.A. Mahmoud, H.O. Elkatry, ACS Omega 8 (2023) 33593-33609. https://doi.org/10.1021/acsomega.3c03747.
[33] A.M.A. Elnour, N.H. Abdurahman, K.H. Musa, Z. Rasheed, Int J Health Sci (Qassim). 17 (2023) 4-5. https://pubmed.ncbi.nlm.nih.gov/37929233/.
[34] A. Pasqualone, A. Bianco, V. Paradiso, CyTA – J. Food 11 (2013) 301-308. https://doi.org/10.1080/19476337.2012.753113.
[35] N. Chopra, B. Dhillon, S. Puri, Int. J. Adv. Biotechnol. Res. 5 (2014) 381-387. https://www.researchgate.net/publication/264943169.
[36] A. Chauhan, D. Saxena, S. Singh, LWT – Food Sci. Technol. 63 (2015) 939-945. https://doi.org/10.1016/j.lwt.2015.03.115.
[37] D. Palatnik, M. Porcel, U. González, N. Zaritzky, M. Campderrós, LWT – Food Sci. Technol. 63 (2015) 939-945. https://doi.org/10.1016/j.lwt.2015.03.115.
[38] Approved methods of the American Association of Cereal Chemists, AACC methods (2000) 42-10, 42-11 and 42-50, 10th edn. St. Paul, Minnesota. https://www.cerealsgrains.org/resources/methods/Pages/default.aspx.
[39] Y. Wang, G. Ryu, J. Cereal Sci. 58 (2013) 110-116. https://doi.org/10.1016/j.jcs.2013.03.013.
[40] R. Alrahmany, T. Avis, A. Tsompo, Food Res. Int. 52 (2013) 568-574. https://doi.org/10.1016/j.foodres.2013.03.03.
[41] G.I. Onwuka, Food Analysis and Instrumentation: Theory and Practice, Naphthali Prints, Lagos, (2005) p. 133.
[42] M. Mladenov, J. Food Nutr. Res. 59 (2020) 108-119. https://www.researchgate.net/publication/342230957.
[43] J. Ou, M. Wang, J. Zheng, S. Ou, Food Chem. 298 (2019) 90-99. https://doi.org/10.1016/j.foodchem.2019.01.096.
[44] A. Patras, N.P. Brunton, C.O'Donnell, B.K. Tiwari, Food Sci. Technol. 21 (2010) 3-11. https://doi.org/10.1016/j.tifs.2009.07.004.
[45] A.M. Sinela, C. Mertz, N. Achir, N. Rawat, K. Vidot, H. Fulcrand, M. Dornier, Food Chem. 235 (2017) 67-75. https://doi.org/10.1016/j.foodchem.2017.05.027.
[46] P. Matilla, J.M. Pihlava, J. Hellstrom, J. Agric. Food Chem. 53 (2005) 8290-8295. https://doi.org/10.1021/jf051437z.
[47] E.S.M. Abdel-Aal, I. Rabalski, J. Cereal Sci. 57 (2013) 312-31. https://doi.org/10.1016/j.jcs.2012.12.001.
[48] M. Olszowy, Plant Physiol. Biochem. 144 (2019) 135-143. https://doi.org/10.1016/j.plaphy.2019.09.039.
[49] R. Murugesan, V. Orsat, Drying Technol. 29 (2011) 1729-1740. https://doi.org/10.1080/07373937.2011.602485.
[50] S. Santhalakshmy, S.J. Don Bosco, S. Francis, M. Sabeena, Powder Technol. 274 (2015) 37-43. https://doi.org/10.1016/j.powtec.2015.01.016.
[51] K.Y. Abboud, B.B. da Luz, J.L. Dallazen, M.F. de P. Werner, C.B.B. Cazarin, M.R. Maróstica Junior, M. Iacomini, L.M.C. Cordeiro, J. Funct. Foods 54 (2019) 552-558. https://doi.org/10.1016/j.jff.2019.02.003.
[52] European Parliament & Council of the European Union, Regulation (2006), J. Eur. Union, 304 (2006) 18-63.

MARIJA MENKINOSKA[1]
TATJANA PAVLOVA[2]
ZHIVKA GORANOVA[3] ANGELINA SREDOVSKA BOZHINOV[4]
ZLATIN ZLATEV[5]
HYRIJE KORAQI[6]
ANKA TRAJKOSKA PETKOSKA[7,8]

[1]Faculty of Technology, Goce Delcev University, Stip, North Macedonia
[2]Zan Mitrev Clinic, Skopje, North Macedonia
[3]Agricultural Academy, Department of Food Technology, Institute of Food Preservation and Quality, Plovdiv, Bulgaria
[4]International Balkan University, Faculty of Dental Medicine, Skopje, North Macedonia
[5]Trakia University, Faculty of Technics and Technologies, Yambol, Bulgaria
[6]Faculty of Food Science and Biotechnology, UBT-Higher Education Institution, Pristina, Kosovo
[7]University St Kliment Ohridski Bitola, Faculty of Technology and Technical Sciences – Veles, Veles, North Macedonia
[8]Department of Materials Science and Engineering, Korea University, Seoul, South Korea

NAUČNI RAD

BISKVITI SA GLUTENOM I BEZ GLUTENA SA FUNKCIONALNIM KOMPONENTAMA: FIZIČKOHEMIJSKA, NUTRITIVNA I ANTIOKSIDATIVNA SVOJSTVA

Cilj ovog rada je bio da se utvrdi uticaj različitih jedinjenja na nutritivne, antioksidativne, mikrostrukturne i karakteristike boje biskvita klasifikovanih kao biskviti sa glutenom i bez glutena. Naime, biskviti su obogaćeni dijetetskim vlaknima, vlaknima akacije, talogom kafe i antocijaninima. Dodavanje ovih funkcionalnih komponenti u matricu biskvita uticalo je na fizička svojstva biskvita; naime, vrednost faktora širenja svih biskvita kretala se od 2,98 do 7,88, sadržaj ukupnih polifenola se povećao, najveći sadržaj polifenola dobijen je kod biskvita bez glutena sa dodatkom taloga kafe (77,98 mg), dok je kod keksa sa pšeničnim brašnom bio u rasponu od 44,62 do 128,63 mg. Svi bezglutenski biskviti mogu se označiti kao proizvodi „bogati vlaknima" (6,32-7,68 g/100 g) i sa većim sadržajem antioksidanasa u poređenju sa biskvitima bez dodatih sastojaka. Ukupan broj mikroorganizama u testiranim biskvitima je ispod prihvatljivih granica. Rezultati ove studije pokazuju da uključivanje sirovih nutritivnih komponenti u recepturu tradicionalnih glutenskih i bezglutenskih biskvita dovodi do poboljšanja nutritivne vrednosti i drugih karakteristika kvaliteta obogaćenih prehrambenih proizvoda.

Ključne reči: Antioksidativna aktivnost, sadržaj polifenola, biskviti, biskviti bez glutena.

CI&CEQ
Chemical Industry & Chemical Engineering Quarterly

Available online at
Association of the Chemical Engineers of Serbia AChE
www.ache.org.rs/CICEQ

Chem. Ind. Chem. Eng. Q. 32 (3) 187–198 (2026) CI&CEQ

PREAM ANAND SIVA SHANKARAN
MANAMALLI DEIVASIKAMANI VASANTHI DAMODARAN
MYTHILY MANI

Department of Instrumentation Engineering, Anna University MIT Campus, Chennai, India

DESIGN OF INDUSTRY-CENTRIC CONTROLLER FOR MIMO CSTH PROCESS WITH ENHANCED DISTURBANCE REJECTION

Highlights

- A first principle and transfer function model for the CSTH process was developed and validated.
- Conventional PID, MPC, and RTD-A controllers have been designed for the developed model.
- Responses were evaluated via performance indices, focusing on disturbance rejection.

Abstract

This paper focuses on designing an advanced control scheme tailored for large-scale industrial processes, where controllers must maintain effective performance despite significant disturbances and setpoint changes. The primary focus of the proposed RTD-A controller is on robust disturbance rejection. RTD-A possesses the benefits of both conventional PID and MPC control schemes. As model-based methods face challenges in addressing increasingly complex processes, data-driven techniques have gained popularity in industrial system monitoring due to their ability to handle unknown physical models. In this work, both the first-principle and transfer function models of the CSTH system are developed using real-time data and represented as a multi-input, multi-output (MIMO) system. PID, MPC, and RTD-A controllers are then applied to regulate the temperatures of the two tanks. The performance of these controllers is carefully examined using integral performance criteria and the time domain analysis to accurately assess their dynamic behavior and control precision. The results demonstrate that the RTD-A controller exhibits superior performance in mitigating disturbances. The RTD-A control strategy exhibits outstanding performance with near-zero overshoot (0% in servo and about 0.05% in regulatory responses) and stable settling times close to 430 - 440 seconds in both tanks. Although MPC and PID controllers offer quicker responses, their greater overshoot and longer settling times establish RTD-A as the preferred method for achieving reliable, precise, and safe control in industrial processes.

Keywords: CSTH, MIMO, PID, MPC, RTD-A, Disturbance Rejection.

SCIENTIFIC PAPER

UDC 66.02:621

INTRODUCTION

Many industrial processes are inherently multi-variable and can be effectively modeled as multi-input, multi-output (MIMO) systems. The design and implementation of controllers for such MIMO systems present substantial challenges, primarily due to the complex interactions and couplings between the system's feedback loops, which result in dynamic behaviors that require sophisticated control strategies. A quintessential example of such a system is the laboratory-scale continuous stirred tank heater (CSTH) process, which consists of two interlinked tanks and a recirculation valve. This configuration creates a highly interactive system, making it an ideal experimental platform for evaluating and testing the performance and robustness of various control strategies specifically designed for MIMO systems.

The CSTH process, characterized by its non-linear dynamics, demonstrates intricate coupling between the temperature and flow rate within the two tanks. The system provides a versatile environment to examine issues like system stability, transient behavior, setpoint tracking, disturbance rejection, and optimal regulation. As such, it serves as an excellent testbed for developing and valida-

Correspondence: P.A. Siva Shankaran, Department of Instrumentation Engineering, Anna University MIT Campus, Chennai, India - 600 044.
Email: sivaanand129@tf.annauniv.edu
Paper received: 6 March 2025
Paper revised: 5 June 2025
Paper accepted: 8 August 2025

https://doi.org/10.2298/CICEQ250306022S

ting advanced control methodologies that can enhance performance, robustness, and efficiency in industrial process control.

A linearized state-space and transfer function model was developed, and a linear multivariable controller was designed. The structure and fundamental governing equations of the modified CSTH model, utilized in this work, were proposed by Thornhill *et al.* [1]. The just-in-time learning-based data-driven (JITL-DD) method was employed in the continuous stirred tank heater (CSTH) pilot system to derive the mathematical model, as outlined by Zheng *et al.* [2]. In Albagul *et al.* [3], both conventional proportional integral (PI) controllers and PI fuzzy logic controllers were proposed for regulating the concentration in the linear continuous stirred tank reactor (CSTR). It was shown that the fuzzy-based PI controller outperformed the conventional one in terms of controller performance criteria such as integral absolute error (IAE), integral square error (ISE), and settling time [4-6]. Cascade control strategies for temperature regulation in the CSTH process were explored by Mahmood and Nawaf [7]. A deadbeat controller was designed to stabilize the system and achieve optimal adaptive realization for the CSTH process, as discussed by Zhang *et al.* [8], with a focus on meeting specific performance specifications. A dual adaptive model predictive controller (DAMPC) for controlling the temperature in a cascaded CSTH process was designed and validated on a real-time setup by Kumar *et al.* [9]. Mathematical modelling, conventional control, and cascade control of the simulated CSTH process were thoroughly explained by Li and Jiang [10].

In addition, the limitations of traditional PID controllers in industrial applications were analyzed, leading to the introduction of the robustness, setpoint tracking, disturbance rejection - aggressiveness (RTD-A) controller by Ogunnaike and Mukati [11]. This controller combines the simplicity of PID with the features of model predictive controller (MPC), simplifying tuning by normalizing parameters. Simulations on a nonlinear process confirmed its effectiveness, with future research directed towards enhancing stability and optimizing parameter selection. Further advancements in the RTD-A controller were made by Mukati *et al.* [12] by developing tuning rules using M-constrained integral gain optimization to balance performance and robustness. Stability was ensured using an FOPDT model, and the controller was validated experimentally on liquid level and temperature control systems, introducing stability contour plots for optimal parameter selection. The RTDA controller was applied to nonlinear stochastic processes by Febina and Angeline [13], specifically in a conical tank system, demonstrating its advantages over traditional PID controllers and MPC in handling nonlinear dynamics. Moreover, the RTDA was shown to be highly effective in managing both minimum and non-minimum zeros in second-order plus dead time (SOPDT) processes, offering a simpler, more effective, and robust solution compared to IMC and MPC by Anbarasan and Srinivasan [14]. Applications of the RTDA include systems like CSTR and distributed control systems (DCS).

In conclusion, while much of the existing research has focused on the modelling and control of single-stage CSTH systems, advanced control strategies like fuzzy-based PI controllers, cascade control, and adaptive MPC have demonstrated considerable performance improvements. Furthermore, the RTDA controller's combination of PID simplicity and MPC features, along with its ability to handle nonlinear dynamics and optimize stability, presents significant potential for research and optimization in multi-stage CSTH systems and other industrial applications.

This paper is organized as follows: Section II describes the CSTH process setup available in the laboratory. Section III discusses the mathematical modeling of the CSTH process using both the first principle model and the transfer function model, followed by validation with the real-time CSTH process. Section IV covers the implementation of both conventional and proposed controllers. Section V presents the results, while Section VI concludes the paper and outlines future research directions.

PROCESS DESCRIPTION

The CSTH is a sophisticated multivariable system widely used in industries like chemicals and pharmaceuticals. This system serves as a module for regulating and analyzing the temperature of liquids. Temperature measurement and control in industrial settings cover a broad range of applications and requirements. To address these diverse needs, the process control industry has developed numerous sensors and cutting-edge control strategies to regulate temperature, both in industrial and domestic settings.

The process flow diagram of the CSTH process available in the Department of Instrumentation Engineering, MIT campus, is shown in Figure 1.

The CSTH process involves two separate water storage tanks. The cold water entering Tank 1 is heated by an electrical heater. The overflow from Tank 1 is transferred to Tank 2, where it is heated by a separate electrical heater. Before the heating process begins, both Tank 1 and Tank 2 are maintained at steady-state levels. A portion of the outflow from Tank 2 is recirculated back into Tank 1, which introduces the additional multivariable interaction and additional complexity to the system, while the remaining water is drained. The outflow rate is adjusted to ensure that the steady-state levels in both tanks are maintained during the recirculation process. The first-principle and transfer function models were developed based on steady-state parameter values from the real-time setup, and their responses were validated by comparing them with actual process data.

This system is a 5-input and 3-output system. The inputs include the flow rates for Tank 1 (F_1), Tank 2 (F_2), and the recirculating flow rate from Tank 2 to Tank 1 (F_R), each controlled by separate valves. Q_1 and Q_2 represent the heat inputs to the heaters in Tank 1 and Tank 2, respectively. The outputs are the temperatures (T_1 and T_2) of Tank 1 and Tank 2, and the water level (h_2) in Tank 2. The steady-state values for the real-time CSTH process are provided in Table 1.

MODELLING AND VALIDATION OF CSTH PROCESS

The first principle model is modified to suit the CSTH process in the laboratory and is validated using the process parameters of the real-time system [1].

Using Stephanopoulos [15] as the benchmark, the first principle model for the CSTH process has been further refined and modified as follows [1]:

$$V_1 \frac{dT_1}{dt} = \frac{Q_1}{\rho C_p} + F_1(T_i - T_1) + F_R(T_2 - T_1) \quad (1)$$

$$V_2 \frac{dT_2}{dt} = \frac{Q_2}{\rho C_p} + F_2(T_1 - T_2) - F_R(T_2 - T_1) - U[2\pi r_2 h_2](T_2 - T_a) \quad (2)$$

$$A_2 \frac{dh_2}{dt} = F_2 - [F_{out} + F_R] \quad (3)$$

The steady-state values are computed by performing an open-loop response analysis of the real-time CSTH process by Balakotaiah and Luss [16]. Initially, the flow rates of the tanks are regulated to maintain stable levels in both tanks. Once the steady-state level is established in Tank 2, the heater is activated to achieve the initial steady-state temperatures of Tank 1 (T_{1s}) and Tank 2 (T_{2s}). Upon reaching the initial steady state, a step change is introduced to Heater-1 to establish the first steady-state temperatures for Tank 1 (T_{1f}) and Tank 2 (T_{2f}).

Subsequently, a second step change is applied to Heater-2 to attain the second steady-state temperatures for Tank 1 (T_{1ss}) and Tank 2 (T_{2ss}). The specific heat capacity and heat transfer coefficient are derived by analyzing the steady-state thermal response curve of either Tank 1 or Tank 2, and then approximated using the following relations:

$$C_p = \frac{qQ}{m\Delta T} \quad (4)$$

$$U = \frac{Q + wC_p(T_i - T_{ss})}{A(T_{ss} - T_a)} \quad (5)$$

$$A = 2\pi rh \quad (6)$$

where are C_p is the specific heat capacity, U is the heat transfer coefficient, w is the inlet flow rate, Q is the electrical heat energy given to the tank, m is mass of liquid in the tank, ΔT is the temperature change, T_i is the initial temperature of liquid, T_{ss} is the steady state temperature of liquid, T_a is the atmospheric temperature of liquid, A is the area of the liquid in the tank, r is the radius of the tank, and h is the steady state height of the tank.

For the sake of simplicity, the proposed work considers Q_1 and Q_2 as the manipulated variables for controlling the temperatures of Tank 1 and Tank 2, respectively. Figure 2(a) illustrates the real-time steady-state response of the system.

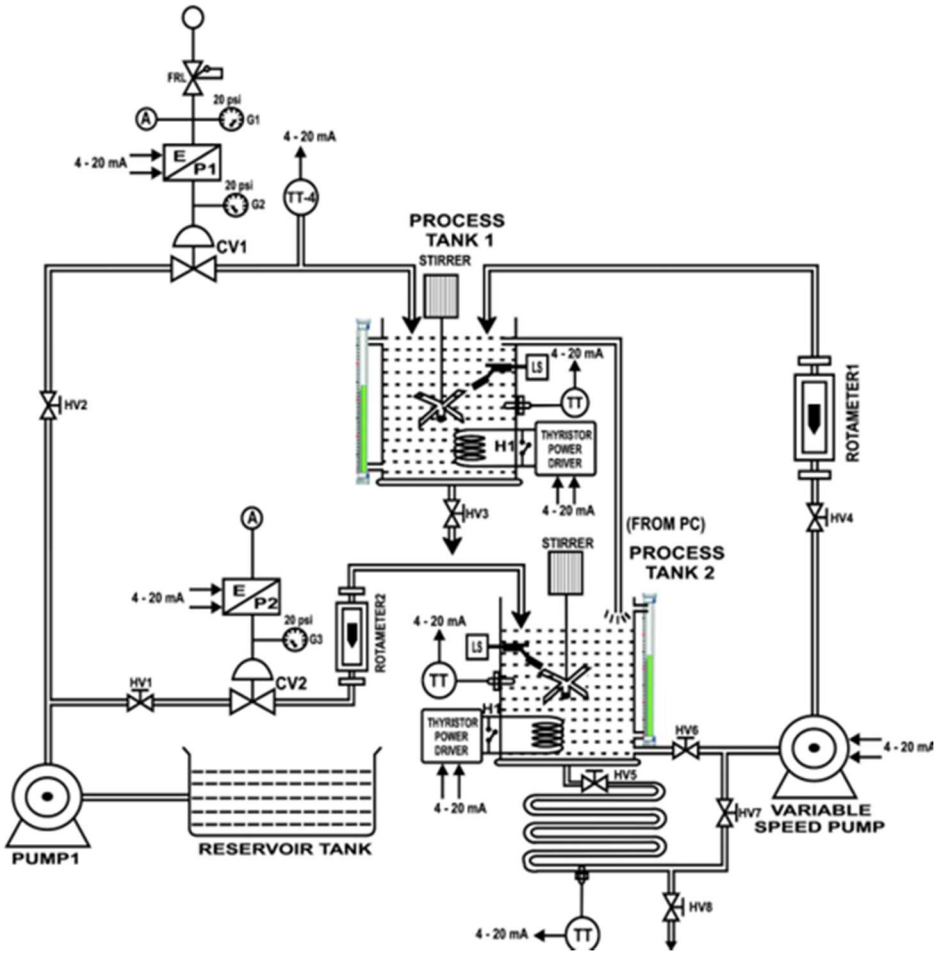

Figure 1. Schematic Diagram of CSTH Process.

Table 1. Nominal model parameters.

Parameter	Description	Value
V_1	Volume of Tank 1	0.23565 m^3
V_2	Volume of Tank 2	0.20737 m^3
A_2	Area of Tank 2	0.9426 m^2
r_2	Radius of Tank 2	0.15 m
T_1	Steady state temperature of Tank 1	40 °C
T_2	Steady state temperature of Tank 2	41.6 °C
h_2	Steady state level of Tank 2	0.22 m
T_i	Inlet water temperature of Tank 1	36 °C
T_a	Atmospheric temperature	40 °C
F_1	Input flow rate of Tank 1	2.8 10^{-5} m^3/s
F_2	Input flow rate of Tank 2	5.85 10^{-5} m^3/s
F_{out}	Output flow rate of Tank 2	2.3 10^{-5} m^3/s
F_R	Recirculating flow rate from Tank 2 to Tank 1	3.55 10^{-5} m^3/s
Q_1	Heat input to Tank 1	375 J/s
Q_2	Heat input to Tank 2	375 J/s
C_p	Specific heat capacity	4546 $JKg^{-1}K^{-1}$
U	Heat transfer coefficient	274.2 W/m^2K

The first-principle model is implemented using the nominal values obtained from the real-time data, and the corresponding responses are generated using MATLAB Simulink, as depicted in Figure 2(b). The real-time data is used to derive the transfer function model for the proposed CSTH process. As outlined by Bequette [17], the system can be modeled using three different methods: the 63.5% method, the two-point method, and the slope method. Additionally, another general approach, the system identification method with MATLAB, is also applied. All four methods are employed to determine the transfer function model, with the most suitable one selected for validation. For the proposed CSTH process, the transfer function model derived using the 63.5% method provides the most accurate steady-state responses compared to the other methods. The transfer function elements for the CSTH process, modeled as a MIMO system, are as follows:

$$G_{11} = \frac{0.2\, e^{-7.25s}}{s+0.02} \quad (7)$$

$$G_{12} = \frac{0.32\, e^{-2.5s}}{s+0.0159} \quad (8)$$

$$G_{21} = \frac{0.18\, e^{-10s}}{s+0.0088} \quad (9)$$

$$G_{22} = \frac{0.24\, e^{-8.25}}{s+0.0053} \quad (10)$$

The steady-state response of the transfer function model for the proposed CSTH process is obtained using MATLAB Simulink and is presented in Figure 2(c).

Table 2 illustrates the steady-state values of the proposed CSTH process in real time, including those for both the first-principle and transfer function models.

By comparing the responses and steady-state values of the first principle model and the transfer function model, it is determined that the transfer function model better matches the real-time steady-state values. Therefore, the transfer function model is utilized for the controller design of the proposed CSTH process.

IMPLEMENTATION OF CONTROLLERS

PID Controller

The PID controller, a traditional feedback control method, adjusts the manipulated variable (such as heater input) by responding to the difference between the desired setpoint and the actual temperature. Its simplicity and reliability make it a widely used approach.

The parameters of the PID controller are calculated using the Z-N method for the control action [18]. The PID control parameters are configured as follows: Tank 1's controller is set to P = 1.540, I = 0.019, and D = 3.68, while Tank 2's controller is set to P = 0.337, I = 0.004, and D = 0.592.

Model Predictive Controller

Model predictive control (MPC) is an advanced control technique that utilizes a model to forecast the future behavior of a dynamic system and optimize control inputs based on these predictions.

The prediction horizon (P) determines how many future time steps the MPC considers when predicting system behavior. This enables the controller to anticipate disturbances or reference changes. The optimal choice of P depends on the system's dynamics; for slower systems, a longer prediction horizon is typically more useful, as it provides a broader view of future behavior. However,

extending the horizon too much can increase computational demands and potentially delay the system's response.

The control horizon (M) refers to the number of future control actions the MPC optimizes. A smaller M reduces computational complexity but limits the controller's ability to adjust future actions. On the other hand, a larger M offers greater flexibility but requires more computational power. For example, with a prediction horizon of 10, the controller predicts the system's behavior for the next 10 intervals, while a control horizon of 2 optimizes the control actions for the next two intervals, with subsequent inputs remaining constant. Thus, the optimized values for the controller are the prediction horizon of 10 and the control horizon of 2.

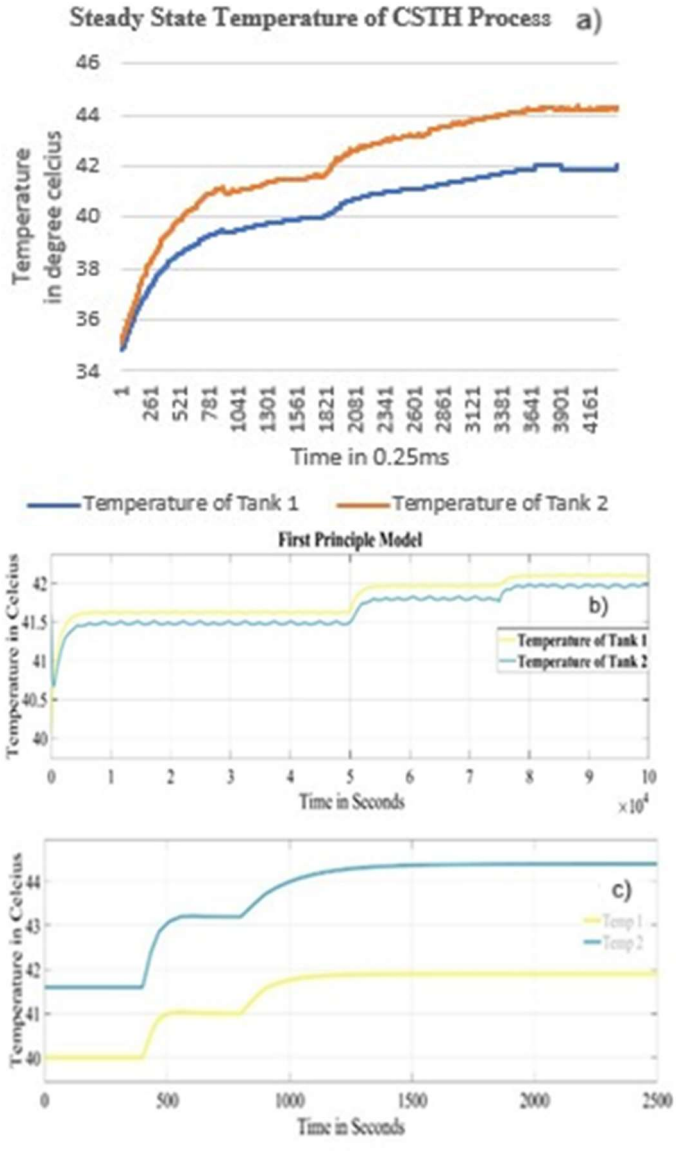

Figure 2. Steady state responses of different models: (a) response of real-time CSTH process, (b) response of first principle model, and (c) response of transfer function model.

RTD-A Controller

The RTD-A controller is an innovative solution designed to tackle the challenges of controlling nonlinear systems. A standout feature is its ability to independently adjust parameters for setpoint tracking, disturbance rejection, robustness, and aggressiveness. This flexibility simplifies control design and ensures optimal performance for each objective, without the need for the complex interdependent adjustments required by traditional controllers. By combining the simplicity of a PID controller with the advanced predictive capabilities of MPC, the RTD-A controller offers a powerful and user-friendly approach for controlling nonlinear systems. This hybrid method capitalizes on the strengths of both PID and MPC, overcoming common tuning issues and providing superior system performance.

One of the major advantages of the RTD-A controller is its robustness in handling uncertainties. It remains reliable even when there are discrepancies between the system model and the actual plant, making it particularly suitable for dynamic environments where precise models are hard to obtain. Additionally, studies have demonstrated that the RTD-A controller outperforms alternatives like PI-IMC and MPC in areas such as disturbance rejection and setpoint tracking, confirming its effectiveness in managing nonlinear system behavior.

The block diagram of the RTD-A controller is shown below in Figure 3, which illustrates the structure of a robust predictive control system designed to track a desired setpoint, handle disturbances, and ensure overall system robustness. The process begins with the reference trajectory, which generates a target path ($y_t(k)$) based on the setpoint (s_p). The control input calculation block determines the control signal $u(k)$ by minimizing the error between the reference trajectory and the predicted output ($\hat{y}(k)$), taking into account parameters like setpoint tracking (σ_T) and control aggressiveness (σ_A).

The plant represents the actual physical system, which generates the output $y(k)$ in response to the control signal. A model of the plant predicts the system's output, and this prediction is compared to the actual output to calculate the error $e(k)$. The current disturbance estimation block processes this error to identify any disturbances affecting the system, while the future disturbance prediction block forecasts their impact.

By integrating all these components, the controller adapts dynamically to disturbances, ensuring robust and accurate tracking of the desired trajectory. The control action $u(k)$ is designed to minimize the difference between the predicted output of the model and the reference trajectory over the prediction horizon P.

$$u(k) = \left(\frac{1}{b}\right)\left(\frac{\sum_{i=1}^{P} \eta_i \psi_i(k)}{\sum_{i=1}^{P} \eta_i^2}\right) \quad (11)$$

$$\psi_i = y_t(k+i) - a^i \hat{y}(k) - \hat{e}_d(k+i) \quad (12)$$

where P is the prediction horizon determined by control aggressiveness σ_A, η_i is the process parameter, $\Psi i(k)$ is the stipulated error, $y_t(k+i)$ is the desired output trajectory and $\hat{y}(k)$ is the predicted output.

The aggressiveness parameter σ_A depends on the prediction horizon P and is given by:

$$P = 1 - \left(\frac{\tau}{t_s}\right) ln(1 - \sigma_A) \quad (13)$$

In this robust predictive control system, several key

components are crucial in determining the control action:

Table 2. Steady state values of the proposed CSTH process.

	Inputs		Outputs					
	Heater-1	Heater-2	Tank 1 temperature (°C)			Tank 2 temperature (°C)		
	(J/s)	(J/s)	RT	FPM	TFM	RT	FPM	TFM
Initial Steady State	375	375	40	41.5	40	41.6	41.6	41.6
First Steady State	450	375	41.1	41.8	41.1	43.2	41.9	43.2
Second Steady State	450	450	42	41.9	41.9	44.3	42.1	44.4

RT - Real time; FPM - First principle model; TFM - Transfer function model

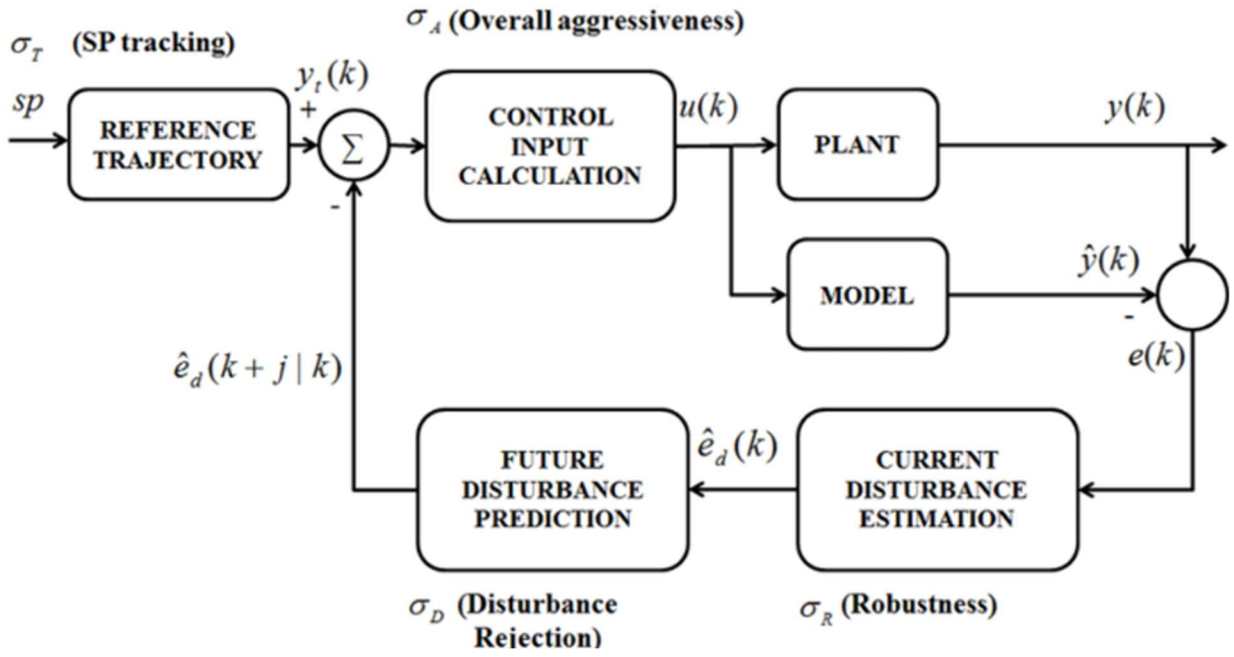

Figure 3. Block diagram of RTD-A controller.

in this robust predictive control system, several key components are crucial in determining the control action:

Projected effect of past control actions: This component evaluates the influence of previously applied control signals on the system's current and future behavior. It ensures that the control action accounts for the system's dynamics and the delayed effects of earlier inputs.

Reference trajectory *(σ_T):* The reference trajectory defines the desired output path the system should follow over time. By comparing the predicted output to this trajectory, the controller calculates the error and adjusts the control action to maintain setpoint tracking.

Projected effect of unmeasured disturbances: This component estimates disturbances that cannot be directly measured by using the error signal *e(k)* and predictive techniques. By forecasting their future impact, the controller can proactively address these disturbances and minimize their effect on system performance.

Together, these components ensure precise setpoint tracking, effective disturbance rejection, and robust control.

The tuning parameters for each performance aspect of the controller are as follows:

- *Robustness:* $0 < \sigma_R < 1$, depends on the current disturbance effect $\hat{e}_d(k)$
- *Setpoint Tracking:* $0 < \sigma_T < 1$, depends on the desired output trajectory $y_t(k+i)$
- *Disturbance Rejection:* $0 < \sigma_D < 1$, depends on the predicted future disturbance effect $\hat{e}_d(k+i)$
- *Overall Aggressiveness:* $0 < \sigma_A < 1$, depends on the prediction horizon P

The tuned values are presented in Table 3.

RESULTS AND DISCUSSION

Simulation Results

The servo and regulatory performance of the proposed controller is validated on the CSTH process. The Tank 1 and Tank 2 temperature set points are perturbed by ±20 % for validating the servo performance. For validating the regulatory response, a perturbation of about +5 °C change in temperature is given (by changing the recirculation water flow rate) at the 1800th time instant.

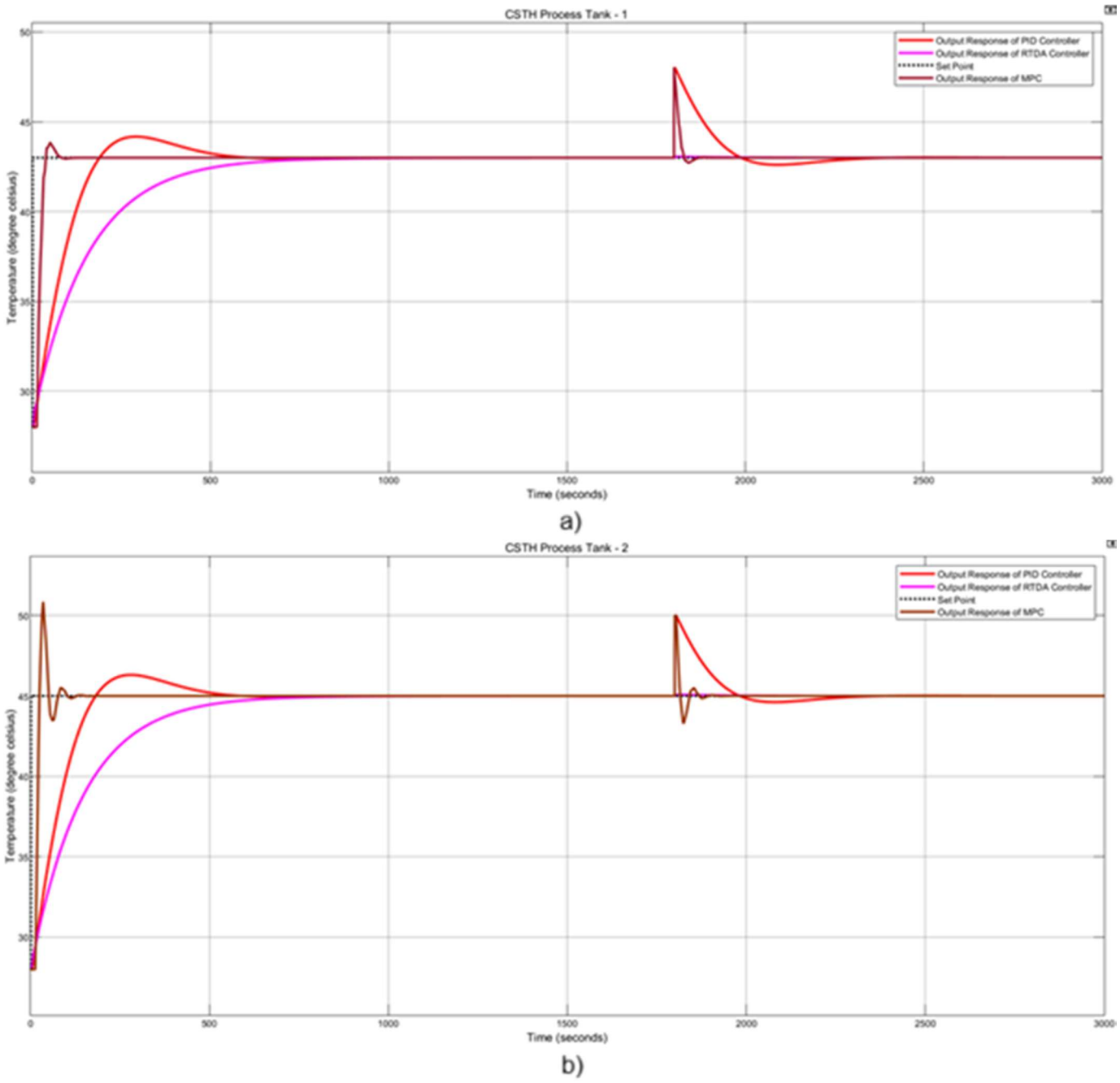

Figure 4. Analysis of the temperature responses of Tank 1 and Tank 2 with different controllers (temperature in °C vs time in seconds): (a) Comparative response of the Tank 1 temperature for different controllers and (b) comparative response of the Tank 2 temperature for different controller.

Table 3. Parameter values for RTD-A controller.

Controller parameter	Gain value for Tank 1	Gain value for Tank 2
Robustness (σ_R)	0.3	0.3
Setpoint Tracking (σ_T)	0.2	0.2
Disturbance Rejection (σ_D)	0.1	0.1
Overall Aggressiveness (σ_A)	0.3	0.3

The servo and regulatory responses of PI, MPC, and RTD-A controllers for the temperature of Tank 1 and Tank 2 are depicted in Figure 4(a) and Figure 4(b), respectively.

The performance criteria for the obtained responses of the PI, MPC, and RTD-A controllers for both Tank 1 and Tank 2 temperatures are listed in Table 4.

Inference

1. PID controller: The PID controller consistently performs poorly for both Tank 1 and Tank 2, exhibiting high error values, slow response times, and long-term instability.
2. MPC controller: The MPC controller shows a significant improvement over the PID, with better error reduction, faster stabilization, and enhanced overall system stability.

RTD-A controller: The RTD-A controller outperforms both the MPC and PID controllers in terms of peak process

variable values. However, compared to the RTD-A, the MPC reaches the setpoint more quickly.

In conclusion, the PID controller consistently underperforms for both Tank 1 and Tank 2, showing high error values, slow response times, and long-term instability, making it unsuitable for this application. The MPC controller provides a significant improvement over the PID, with better error reduction, faster stabilization, and enhanced system stability. However, it still slightly falls short of the RTD-A controller in terms of long-term error minimization. The RTD-A controller outperforms both the MPC and PID controllers in peak process variable values, offering the best balance of error reduction, stability, and response time for regulating the temperatures of Tank 1 and Tank 2. While the MPC reaches the setpoint more quickly, the RTD-A excels in long-term performance, making it the most effective choice for this application.

Additionally, the RTD-A controller excels in disturbance rejection, outperforming both the PID and MPC controllers. Figure 5(a) and Figure 5(b) offer a detailed comparison of disturbance rejection for Tank 1 and Tank 2 temperatures across the different controllers. The RTD-A controller can reject disturbances more quickly and with less overshoot than the PID and MPC controllers.

The disturbance rejection characteristics of these controllers are summarized below:

RTD-A Controller

- Response characteristics: The RTDA controller quickly rejects disturbances, rapidly bringing the system to the desired setpoint with minimal overshoot and no noticeable oscillations.
- Settling time: The settling time is longer than that of the MPC controller, due to the predictive action for disturbance handling.
- Disturbance rejection performance: This controller excels in rejecting disturbances, providing a fast, stable, and precise response.

MPC Controller

- Response characteristics: The MPC controller initially shows considerable oscillations and overshoot before stabilizing near the setpoint.
- Settling time: It demonstrates the fastest settling time compared to other controllers.
- Disturbance rejection performance: While the MPC controller eventually rejects the disturbance, its performance is moderate, owing to the overshoot and oscillations observed during the transient phase.

PID Controller

- Response characteristics: The PID controller exhibits a slow and steady approach to the setpoint without oscillations. However, it takes considerably longer to stabilize.
- Settling time: It has the longest settling time, reflecting its sluggish response to disturbances.
- Disturbance rejection performance: The PID controller has the least effective disturbance rejection, due to its delayed response and extended settling time.

In terms of performance metrics such as ISE, IAE, ITSE, and ITAE, the MPC controller outperforms both the RTD-A and PID controllers. While the RTD-A controller excels in disturbance rejection, it falls short in these performance metrics because it doesn't exactly track the setpoint before the disturbance is introduced, due to the predictive action for disturbance handling. However, it converges closely to the setpoint, with deviations typically below 0.08, as illustrated in Figure 6. The RTD-A's response includes the entire time response when calculating integral errors, which contributes to its lower performance compared to the MPC. However, this drawback can be disregarded due to the RTD-A controller's exceptional overall performance, particularly in disturbance rejection.

The RTD-A controller offers the best disturbance rejection, providing a fast and stable response with minimal overshoot. The step response characteristics for both servo and regulatory responses in Tank 1 and Tank 2 reveal that the RTD-A method delivers the most stable and controlled performance among the three control strategies. In the servo response, RTDA achieves zero overshoot (0% in both tanks), with peak values of 43 and 45, and settling times of 437 s (Tank 1) and 428 s (Tank 2), ensuring smooth and steady control despite having slower rise times (191 s and 195 s). In contrast, although MPC offers faster rise times (17.75 s and 21.30 s) and shorter settling times (33.18 s and 68.58 s), it shows higher overshoot (2.10% and 13.09%), which is not recommended for industrial applications. For regulatory response, RTDA again outperforms by maintaining minimal overshoot (0.05% and 0.06%) and significantly faster settling times (437 s and 428 s) compared to PID (1928 s and 1921 s) and MPC (1809 s and 1833 s), which exhibit large overshoot values (~11–13%) and long stabilization periods. Even though MPC and PID provide quicker initial actions, RTD-A is the most reliable and robust control strategy, particularly suited for applications demanding long-term stability, safety, and precision.

CONCLUSION

This paper presents the development of the first principle model for the CSTH process, derived from steady-state real-time data, and the transfer function model, which is obtained from real-time measurements. Both models are validated using data obtained from the real-time experimental setup. Conventional PID, MPC, and RTD-A controllers are designed for the 2x2 transfer function model, and their performance is systematically evaluated. For regulatory response, RTD-A outperforms by maintaining minimal overshoot (0.05% and 0.06%) and significantly faster settling times (437 s and 428 s) compared to PID (1928 s and 1921 s) and MPC (1809 s and 1832 s), which exhibit large overshoot values (~11–13%) and long stabilization periods. Even though MPC and PID provide quicker initial actions, RTD-A is the most reliable and robust control strategy, particularly suited for applications demanding long-term stability, safety, and precision. Based on the result analysis, the RTD-A controller is identified as the optimal choice for disturbance rejection in regulating the

temperatures of Tank 1 and Tank 2 in the CSTH process, making it highly suitable for industrial process control applications.

Table 4. Performance metrics of Tank 1 and Tank 2.

Controller	Tank 1				Tank 2			
	ISE	IAE	ITSE	ITAE	ISE	IAE	ITSE	ITAE
PID	11880	1834	-536300	1028000	14470	1939	-520900	997900
MPC	4031	399.1	93050	123600	5384	516.4	-47410	159300
RTD-A	16700	2272	330800	367400	20960	2480	337500	384100

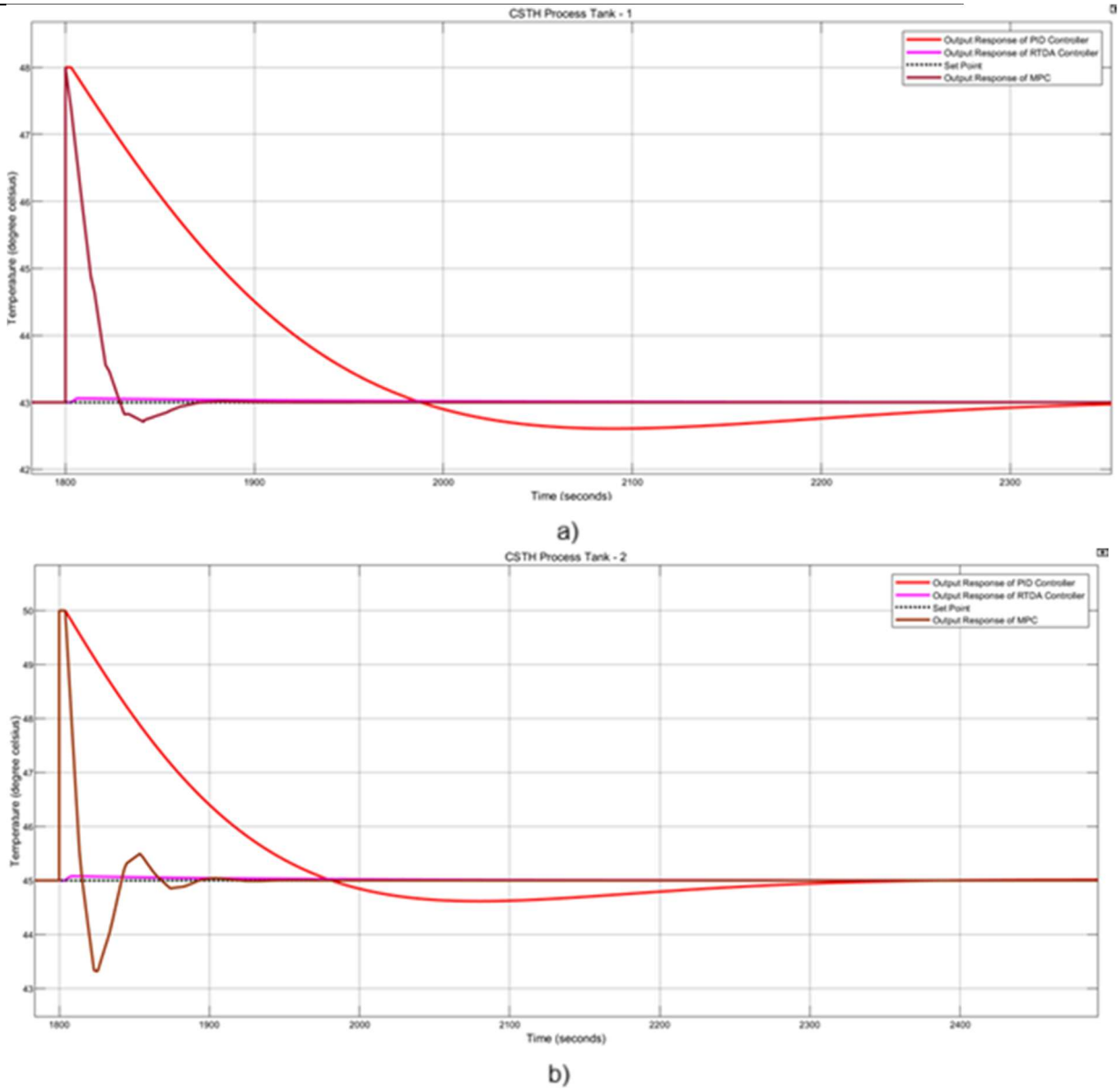

Figure 5. Emphasizing the disturbance rejection efficacy in the temperature profiles of Tank 1 and Tank 2 across different controller configurations (temperature in °C vs time in seconds): (a) highlighting the disturbance rejection of Tank 1 temperature for different controllers, and (b) highlighting the disturbance rejection of Tank 2 temperature for different controllers.

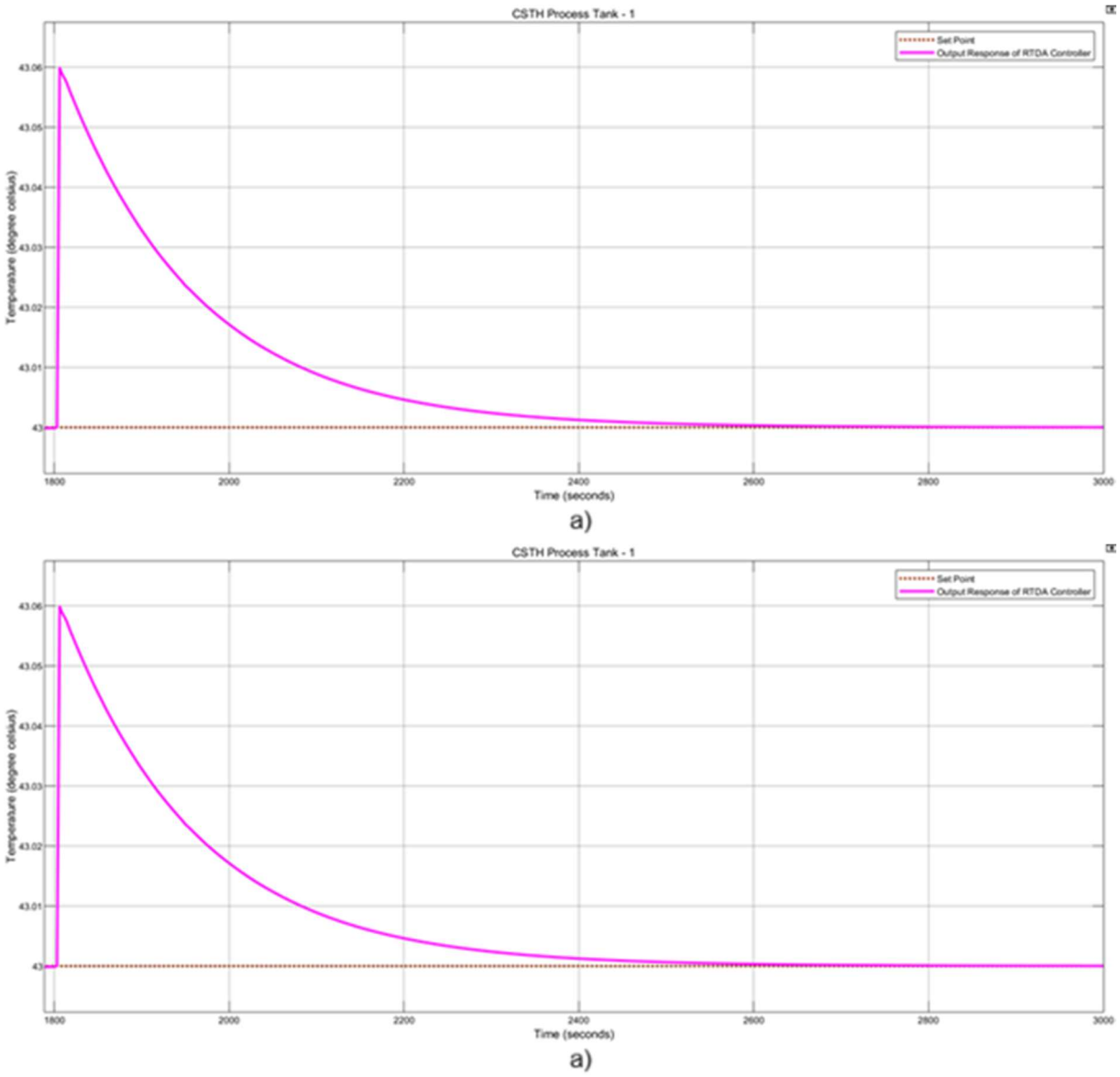

Figure 6. Emphasizing the disturbance rejection efficacy in the temperature profiles of Tank 1 and Tank 2 for RTD-A controller (Temperature *in °C* Vs Time *in seconds): (a) highlighting the disturbance rejection of the Tank 1 temperature for RTD-A controller, and (b) highlighting the disturbance rejection of the Tank 2 temperature for RTD-A controller,.*

ABBREVIATIONS

CSTH - continuous stirred tank heater
CSTR - continuous stirred tank reactor
DAMPC - dual adaptive model predictive controller
DCS - distributed control systems
IAE - integral absolute error
ISE - integral square error
ITAE - integral time absolute error
ITSE - integral time square error
JITL-DD - just-in-time learning based data-driven
MIMO - multiple input multiple output
MPC - model predictive controller
PI - proportional integral
PID - proportional integral derivative
PI-IMC - proportional integral-internal model controller
RTD-A - robustness, setpoint tracking, disturbance rejection – aggressiveness
SOPDT - second-order plus dead time

NOMENCLATURE

V_1 - volume of tank 1 (m^3)
V_2 - volume of tank 2 (m^3)
A_1 - area of tank 1 (m^2)
A_2 - area of tank 2 (m^2)
r_1 - radius of tank 1 (m)
r_2 - radius of tank 2 (m)
T_1 - steady state temperature of tank 1 (°C)
T_2 - steady state temperature of tank 2 (°C)
h_1 - steady state level of tank 1 (m)
h_2 - steady state level of tank 2 (m)
T_i - inlet water temperature of tank 1 (°C)
T_a - atmospheric temperature (°C)
F_1 - input flow rate of tank 1 (m^3/s)
F_2 - input flow rate of tank 2 (m^3/s)
F_{out} - output flow rate of tank 2 (m^3/s)
F_R - recirculating flow rate from Tank 2 to Tank 1 (m^3/s)
Q_1 - heat input to tank 1 (J/s)

Q_2 - heat input to tank 2 (J/s)
C_p - specific heat capacity ($JKg^{-1}K^{-1}$)
U - heat transfer coefficient (W/m^2K)
Q - electrical heat energy given to the tank (J/s)
m - mass of liquid in the tank (kg)
ΔT - change in temperature (°C)
T_{ss} - steady state temperature of liquid (°C)
A - area of the liquid in the tank (m^2)
r - radius of the tank (m)
h - steady state height of the tank (m)
P - proportional parameter of PID controller
I - integral parameter of PID controller
D - derivative parameter of PID controller
y_t(k) - target path of RTD-A controller
s_p - setpoint of process where the RTD-A controller is implemented
u(k) - control signal of RTD-A controller
$\hat{y}$(k) - predicted output of RTD-A controller
σ_T - setpoint tracking parameter of RTD-A controller
σ_A - control aggressiveness parameter of RTD-A controller
σ_T - disturbance rejection parameter of RTD-A controller
σ_R - robustness parameter of RTD-A controller
y(k) - generated output in response to the control signal of RTD-A controller
e(k) - error signal of predicted system's output and actual output of RTD-A controller
P - prediction horizon for both MPC and RTD-A controller
M - control horizon for MPC controller
η_i - process parameter
Ψ(k) - stipulated error of RTD-A controller
$y_t(k+i)$ - desired output trajectory of RTD-A controller

REFERENCES

[1] N.F. Thornhill, S.C. Patwardhan, S.L. Shah, J. Process Control 18 (2008) 347-360. https://doi.org/10.1016/j.jprocont.2007.07.006.
[2] J. Zheng, H. Wang, H. Zhou, T. Gao, IEEE Seventh Int. Conf. Intell. Control Inf. Process Siem Reap, Cambodia (2016) p. 98-104. https://ieeexplore.ieee.org/document/7885883.
[3] Albagul, M. Saad, Y. Abujeela, Int. J. Comput. Sci. Electron. Eng. 2 (2014) 130-134. https://www.researchgate.net/publication/324165363.
[4] Simorgh, A. Razminia, V. Shiryaev, Math. Comput. Simul. 173 (2020) 16-31. https://doi.org/10.1016/j.matcom.2020.01.010.
[5] V. Kabila, G. Devadhas, Indian J. Sci. Technol. 8 (2015) 1-7. https://indjst.org/articles/comparative-analysis-of-pid-and-fuzzy-pid-controller-performance-for-continuous-stirred-tank-heater https://doi.org/10.17485/ijst/2015/v8i23/85351.
[6] A.D. Priya, G. Tamilselvan, T. Rajesh, Int. J. Adv. Sci. Eng. Res. 10 (2018) 78-81. https://www.ciitresearch.org/dl/index.php/fs/article/view/FS032018006.
[7] Q.A. Mahmood, A.T. Nawaf, Mater. Today: Proc. 42 (2022) 2545-2552. https://doi.org/10.1016/j.matpr.2020.12.577.
[8] Y. Zhang, Y. Yang, S.X. Ding, L. Li, IEEE Trans. Ind. Electron. Control Instrum. 61-11 (2014) 6409-6417. https://ieeexplore.ieee.org/document/6718131.
[9] K. Kumar, T.A.N. Heirung, S.C. Patwardhan, B. Foss, IFAC-Papers Online 48 (2015) 545-550. https://www.sciencedirect.com/science/article/pii/S2405896315011052.
[10] X. Li, X. Jiang, Int. Conf. Adv. Control, Autom. Artif. Intell., Shenzhen, China (2018), p. 163-167. https://www.atlantis-press.com/proceedingsacaai-18/25892485.
[11] B.A. Ogunnaike, K. Mukati, J. Process Control 16 (2006) 499-509. https://doi.org/10.1016/j.jprocont.2005.08.001.
[12] K. Mukati, M. Rasch, B.A. Ogunnaike, J. Process Control 19 (2009) 272-287. https://doi.org/10.1016/j.jprocont.2008.03.004.
[13] Febina, V.D. Angeline, Int. Conf. Adv. Electr., Comput., Commun. Sustainable Technol. Bhilai, India (2021) p. 1-8. https://ieeexplore.ieee.org/document/9392600.
[14] K. Anbarasan, K. Srinivasan, ISA Trans. 57 (2015) 231-244. https://doi.org/10.1016/j.isatra.2015.02.016.
[15] G. Stephanopoulos, Chemical Process Control, Prentice Hall, New Jersey (1984), p. 43. https://www.google.co.in/books/edition/Chemical_Process_Control/rhUTrgEACAAJ?hl=en ISBN: 9788177584035
[16] V. Balakotaiah, D. Luss, Chem. Eng. Sci. 38 (1983) 1709-1721. https://doi.org/10.1016/0009-2509(83)85028-3.
[17] B.W. Bequette, Process Control: Modeling, Design, and Simulation, Prentice Hall, New Jersey (2003), p. 196. https://books.google.co.in/books/about/Process_Control.html?id=PdjHYm5e9d4C ISBN: 0-13-206889-3
[18] O'Dwyer, in Handbook of PI and PID Controller Tuning Rules. Imperial College Press, London (2009), p. 350. https://www.google.co.in/books/edition/Handbook_Of_Pi_And_Pid_Controller_Tuning/hF-7CgAAQBAJ?hl=en&gbpv=1&dq=pid+controller+tuning&pg=PR7&printsec=frontcover

PREAM ANAND SIVA SHANKARAN
MANAMALLI DEIVASIKAMANI VASANTHI DAMODARAN
MYTHILY MAN
Department of Instrumentation Engineering, Anna University MIT Campus, Chennai, India

PROJEKTOVANJE INDUSTRIJSKOG CENTRIČNOG KONTROLERA ZA PROCES SA KONTINUALNIM REAKTOROM SA MEŠANJEM SA VIŠE ULAZA I VIŠE IZLAZA SA POBOLJŠANIM ODBACIVANJEM POMREMEĆAJA

Ovaj rad se bavi projektovanjem napredne šeme upravljanja prilagođene velikim industrijskim procesima, gde kontroleri moraju da održavaju efikasne performanse uprkos značajnim poremećajima i promenama zadatih vrednosti. Primarni fokus predloženog RTD-A kontrolera je na robusnom odbacivanju poremećaja. RTD-A poseduje prednosti i konvencionalnih PID i MPC šema upravljanja. Kako se metode zasnovane na modelima suočavaju sa izazovima u rešavanju sve složenijih procesa, tehnike vođene podacima su stekle popularnost u praćenju industrijskih sistema zbog svoje sposobnosti da obrađuju nepoznate fizičke modele. U ovom radu, i modeli prvog principa i modeli prenosne funkcije sistema sa kontinualnim reaktorom sa mešanjem su razvijeni korišćenjem podataka u realnom vremenu i predstavljeni kao sistem sa više ulaza i više izlaza. PID, MPC i RTD-A kontroleri se zatim primenjuju za regulisanje temperatura dva rezervoara. Performanse ovih kontrolera su pažljivo ispitane korišćenjem integralnih kriterijuma performansi i analize vremenskog domena kako bi se precizno procenilo njihovo dinamičko ponašanje i preciznost upravljanja. Rezultati pokazuju da RTD-A kontroler pokazuje superiorne performanse u ublažavanju poremećaja. RTD-A strategija upravljanja pokazuje izvanredne performanse sa skoro nultim prekoračenjem (0% u servo i oko 0,05% u regulatornim odzivima) i stabilnim vremenima smirivanja blizu 430-440 sekundi u oba rezervoara. Iako MPC i PID kontroleri nude brže odzive, njihovo veće prekoračenje i duže vreme smirivanja čine RTD-A preferiranom metodom za postizanje pouzdane, precizne i bezbedne kontrole u industrijskim procesima.

NAUČNI RAD

Ključne reči: Kontinualni reaktor sa mešanjem, više ulaza i više izlazaO, PID, MPC, RTD-A, odbacivanje poremećaja.

Chemical Industry & Chemical Engineering Quarterly

Available online at
Association of the Chemical Engineers of Serbia AChE
www.ache.org.rs/CICEQ

Chem. Ind. Chem. Eng. Q. 32 (3) 199–212 (2026) CI&CEQ

MOHANRAJHU NATHAMUNI[1]
PREMKUMAR DURAISAMY[2]
RAJAKUMAR MUTHUSAMY PALANI[3]

PADMAVATHI KUPPUSAMY RAMAMOORTHY[4]

[1]Department of Mechanical Engineering, R.M.K. Engineering College, Chennai, TN, India.

[2]Department of Mechanical Engineering, Easwari Engineering College, Tamil Nadu, India.

[3]Department of Artificial Intelligence and Data Science, St. Joseph's College of Engineering, TN, Chennai, India.

[4]Department of Mechanical Engineering, Panimalar Engineering College, TN, Chennai, India.

SCIENTIFIC PAPER

UDC 662.756.3:662.7558.2:621.43

STUDY OF COMBUSTION AND PERFORMANCE IN A DIESEL ENGINE FUELED BY BIODIESEL-NANOPARTICLE BLENDS

Highlights

- Energy utilization from Avocado waste peel is extensively studied.
- GONPs nanoparticles were used as an ignition enhancer.
- AWPB+GONPs 50 ppm improved BTE by 5.98% and BSEC reduced by 30.12% compared to diesel.
- AWPB+GONPs blends, with their stable and reliable performance, are promising alternatives to diesel.

Abstract

This study examines the combustion and performance of avocado waste peel biodiesel (AWPB) combined with graphene oxide nanoplates (GONPs) as a substitute fuel for diesel engines. It also aims to assess the impact of engine combustion and performance while considering the feasibility of employing waste materials in fuel generation. The test fuels diesel, AWPB, AWPB+GONPs 50 ppm, and AWPB+GONPs 100 ppm were evaluated. The results showed that in-cylinder pressure in AWPB decreased by approximately 3.6% compared to diesel, while the heat release rate (HRR) increased notably in the AWPB+GONPs 100 ppm blend. Additionally, diesel exhibited higher ignition delay (ID) and combustion duration (CD) than all biodiesel blends. The addition of GONPs in AWPB led to a 5.98% increase in brake thermal efficiency (BTE) and a 30.12% reduction in brake-specific energy consumption (BSEC) compared to diesel. However, diesel still demonstrated higher engine torque, indicated mean effective pressure (IMEP), and air-fuel ratio (A/F ratio) relative to biodiesel fuels, whereas AWPB showed a higher exhaust gas temperature (EGT). These findings suggest that avocado peel biodiesel, when enhanced with GONPs, is a viable and cleaner alternative to conventional diesel, offering improved combustion efficiency and reduced energy consumption.

Keywords: waste to energy; avocado waste peel biodiesel; graphene oxide nanoplates; performance.

INTRODUCTION

The global fuel demand has increased due to the exhaustion of fossil fuel sources. Fossil fuels are paramount in facilitating the operation of the entire transportation system. Diesel engines substantially improved the country's energy efficiency because of their efficient fuel consumption and decreased engine exhaust emissions [1]. The presence of temporary urban differentiation and pollutants emitted at the road level presents a significant peril to the natural surroundings and has detrimental effects on human well-being [2]. Automobile research has brought attention to this highly significant issue. Consequently, a considerable amount of research is being conducted on alternative fuels, which have the potential to be derived not just from renewable sources but also yield substantial reductions in emissions. This fuel possesses the potential to not only mitigate the challenges associated with fossil fuels but also to facilitate further exploration of alternative energy resources, thereby decreasing our reliance on fossil fuels. Biodiesel, a fuel obtained from diverse sources such as vegetable oil, animal fat, and waste cooking oil, is the only feasible alternative in this context [3]. Environmental degradation and significant expansion in the usage appropriate to fossil fuels emphasize the potential usage of biodiesel as a diesel replacement [4].

Correspondence: M. Nathamuni, Department of Mechanical Engineering, R.M.K. Engineering College, Chennai, TN, India.
Email: nmj.mech@rmkec.ac.in
Paper received: 12 November 2024
Paper revised: 4 July 2025
Paper accepted: 1 September 2025

https://doi.org/10.2298/CICEQ241112024N

Biofuels, an environmentally friendly fuel, are increasingly recognized as a viable and promising alternative for diesel engines in current and future contexts. Biodiesel is derived from sustainable and enduring feedstocks through transesterification, characterized by the absence of aromatics or sulfur compounds [5]. In recent years, a significant study has been undertaken to employ algal oil, pine oil, lemon, and orange peel oil with enhanced diesel engine outcomes [6]. On the other hand, the oil obtained from the new peel of lemon fruits and the orange peel has received virtually little research [7]. The studied orange peel biodiesel blends in a diesel engine showed a significant 15% decrease in nitrogen oxide (NOx) emissions relative to pure diesel. This is attributed to the oxygen content in biodiesel, which improves combustion efficiency and diminishes NOx production [8]. Evaluated lemon peel biodiesel and observed a 12% decrease in carbon monoxide (CO) emissions at higher biodiesel blend ratios. The lower CO emissions indicate more complete combustion, as the oxygenated nature of biodiesel facilitates better oxidation of carbon compounds [9]. Investigated mosambi peel biodiesel blends and found a 10% reduction in NOx emissions, alongside a 20% reduction in smoke opacity. The reduced smoke levels were attributed to the biodiesel's cleaner combustion properties, which resulted in fewer soot particles [10]. Mosambi peel biodiesel increased brake-specific fuel consumption (BSFC) by 5%, reducing carbon monoxide emissions by 18% and contributing to a cleaner exhaust profile [11].

Recent advances in biodiesel research have focused on using nanoparticles to enhance performance and reduce emissions in diesel engines. Iron oxide nanoparticles in neem oil biodiesel resulted in a 25% reduction in CO emissions and improved overall engine performance by 8% [12]. Evaluated by using silicon dioxide nanoparticles with Pongamia biodiesel in a diesel engine, the results observed a 19% decrease in hydrocarbon (HC) emissions [13]. Evaluated magnesium oxide nanoparticles in rice bran biodiesel blends, which reduced NOx emissions by 12% and improved thermal efficiency by 5% [14]. Cerium oxide nanoparticles in rubber seed oil biodiesel increased thermal efficiency by 9% and reduced particulate emissions by 20% [15]. The results achieved a 10% improvement in BSFC and a 15% reduction in smoke emissions using titanium dioxide (TiO_2) nanoparticles in biodiesel derived from fish oil [16]. The diesel engine's brake thermal efficiency (BTE) was enhanced using different percentages of TiO_2 nanofluid synthesized with orange peel oil. This composition was blended with diesel fuel and found to increase BTE [17]. *Bauhinia parviflora* biodiesel (BPB), with the addition of water and di-tert-butyl peroxide (DTBP) emulsion, is utilized in diesel engines. They discovered that using a BPB and water/DTBP combination efficiently improves engine performance. Waste pork fat is effectively extracted as biofuel, mixed with GONPs, and tested by an engine. The best oxygen concentration increases engine efficiency with reduced NOx smoke. It acts as the best additive and is activated by good solubility [18].

Avocado peel is a significant agro-industrial waste byproduct generated from food processing industries, with global avocado production exceeding 8 million metric tons annually. The peel accounts for roughly 12–15% of the total fruit weight and is often discarded without valorization. Studies have shown that avocado peels contain a considerable amount of extractable oil (up to 15–18% by dry weight), making them a promising non-edible, lignocellulosic feedstock for biodiesel production. Its availability, high oil yield, and low economic value make it a sustainable candidate for second-generation biodiesel, aligning with waste-to-energy goals.

Novelty and motivation of the research

This study presents a novel and sustainable approach to biofuel production by utilizing avocado peel waste, an underutilized byproduct of the fruit processing industry, as a feedstock for biodiesel synthesis. This agro-waste valorization not only addresses waste management challenges but also contributes to circular bioeconomy practices. Additionally, the research examines the role of GONPs, a material with exceptional thermal and oxidative properties, as a performance-enhancing additive in biodiesel blends. The application of GONPs in avocado biodiesel combustion has been sparsely explored in prior literature, making this study a significant contribution to the field.

The primary objective is to evaluate the combustion and performance characteristics of AWPB and its blends with varying concentrations of GONPs in a diesel engine. Rather than aiming to surpass diesel in every metric, the study seeks to optimize thermal efficiency, reduce energy consumption, and assess the combustion behaviour of a renewable, waste-derived fuel enhanced by nanotechnology. This research ultimately aims to advance sustainable fuel alternatives that align with global efforts toward carbon neutrality, energy diversification, and the development of a circular economy.

MATERIALS AND METHODS

Avocado peel oil extraction

This work used the steam distillation method for avocado peel oil extraction, as shown in Figure 1. This plant consists of four sections. In the first section, the water is heated and converted into steam, and then the steam passes into the second section over the avocado peel. Then, steam is cooled in the third section and collected in the fourth section as a combination of water and avocado peel oil. Due to density discrepancies, the oil of avocado peel was separated from the combination. A 580 mL avocado peel oil was produced from 1 kg of avocado peel. The direct utilization of avocado peel oil in diesel operations is unsuitable due to its viscosity.

Avocado peel biodiesel production

The transesterification process, a crucial step in biodiesel production, is intricately dependent on the oil's free fatty acid (FFA) level. Since the FFA content of the extracted avocado peel oil was measured at 1.11%, which

is below the 2% limit that necessitates acid esterification, a single-step base-catalyzed transesterification process was sufficient and appropriate. This approach ensured efficient conversion while maintaining biodiesel quality as per ASTM standards. The experimental process was meticulously executed: 100 mL of avocado peel oil was added to a 500 mL flask and heated using an oil bath. A catalyst was introduced under a 1:6 methanol-to-oil molar ratio, followed by sonication for 30 minutes to enhance reaction kinetics. The transesterification reaction used potassium hydroxide (KOH) as a catalyst at a concentration of 1 wt% of oil. Methanol (purity ≥ 99%) and KOH were produced by Chennai Chemicals, Chennai. Moreover, the reaction was carried out under continuous stirring to ensure homogeneity. A reflux condenser was used to minimize methanol loss, and the reaction was maintained at 80 °C for 90 minutes. The resulting mixture, containing methyl esters, glycerol, and catalyst residues, was centrifuged at 1,500 rpm for 10 minutes to achieve phase separation. The upper methyl ester layer was collected and further purified using a rotary evaporator to remove excess methanol. Finally, the biodiesel and glycerol layers were separated using a separating funnel. To ensure fuel quality and reproducibility, key physicochemical properties, including kinematic viscosity, density, calorific value, cetane index, and flash point, were measured and are presented in Table 1. These properties not only confirm the quality of our biodiesel but also its compliance with ASTM standards, thereby bolstering the scientific validity and repeatability of our experimental process.

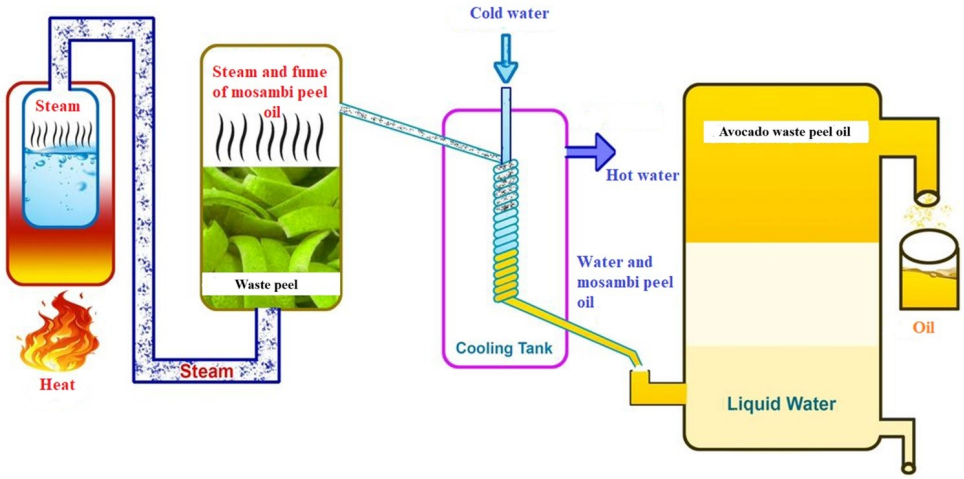

Figure 1. Schematic layout of the steam distillation method.

Nanoparticles

In this research, GONPs are selected for their role as an antioxidant that enhances the stability of Avocado peel biodiesel blends. To further improve biodiesel performance, nanoparticles are incorporated as additives. This innovative approach optimizes fuel properties such as combustion efficiency, oxidative stability, and emissions reduction. Nanoparticles are chosen based on their small size (typically 10–100 nm), which increases surface area and catalytic activity [19]. Nanoparticles offer excellent thermal stability and improve combustion by promoting more complete fuel burning, thus reducing harmful emissions [20]. Their ability to enhance oxidative stability is crucial for prolonging the storage life of biodiesel, especially in combination with GONPs, which scavenges free radicals to prevent fuel degradation. The nanoparticles are carefully dispersed using ultrasonication and mechanical stirring to ensure uniform distribution in the biodiesel blend, preventing agglomeration [21]. Nanoparticles were dispersed using an ultrasonicator operating at 40 kHz and 300 W for 30 minutes, combined with mechanical stirring at 500 rpm. The dispersion was conducted at room temperature to avoid thermal degradation of the biodiesel blend. By integrating GONPs with these nanoparticles, the research aims to significantly enhance the biodiesel's stability and overall performance, making it a sustainable and efficient alternative to conventional diesel.

GONPs are two-dimensional carbon-based nanomaterials with a high surface area and excellent thermal and oxidative properties. It appears as a white crystalline powder and is highly stable, with a melting point of 70–71 °C. GONPs work by donating hydrogen atoms to neutralize free radicals, thus halting the oxidation process in food, pharmaceuticals, and fuels. GONPs play a crucial role in preventing oxidative degradation in the context of biodiesel, a common issue due to the unsaturated fatty acids in biodiesel. GONPs improve biodiesel's shelf life and overall quality by stabilizing the fuel and reducing the formation of gums and peroxides. Typically added at concentrations between 0.01% and 0.1% by weight, GONPs ensure the biodiesel remains stable during storage and under various environmental conditions. Its effectiveness in fuel applications makes it a vital additive for improving biodiesel blends' long-term performance and stability [22].

Characterization of GONPs

GONPs used in this study were procured from Chennai Chemicals, Chennai, Tamil Nadu, India, with a reported

purity of 99.9%. To verify the structural and morphological characteristics of the GONPs, two complementary analytical techniques, X-ray diffraction (XRD) and scanning electron microscopy (SEM), were employed. The XRD analysis was performed to identify the crystalline structure and phase composition of the GONPs. The XRD pattern displayed three significant peaks at 2θ angles of 31.596°, 27.038°, and 45.399°, indicating the presence of an amorphous carbon-rich phase. The broad and low-intensity nature of these peaks confirms the semi-crystalline, layered structure typical of graphene oxide, with partial disorder and oxidation. SEM was used to evaluate the surface morphology and microstructure of the GONPs. GONPs exhibited wrinkled and layered sheet-like morphology with randomly distributed ultrathin flake structures. These features confirm the large surface area and high aspect ratio, which are advantageous for improving fuel atomization and combustion when blended with biodiesel. These characterization results support the functional role of GONPs as combustion enhancers, owing to their high surface reactivity, oxidative stability, and morphological suitability for uniform dispersion in fuel. Figure 2 shows the XRD and SEM analysis of GONPs.

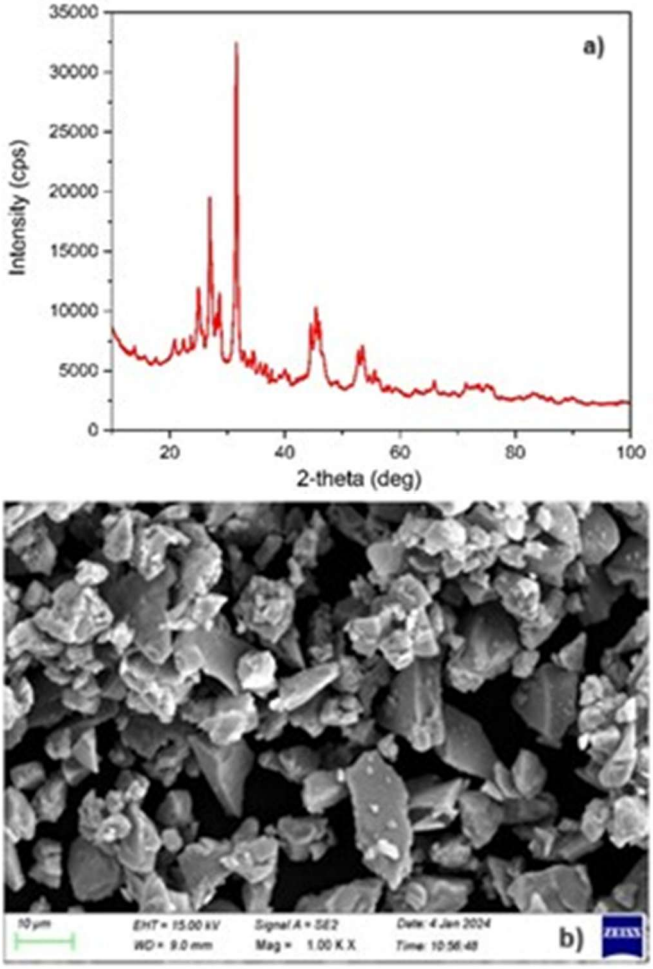

Figure 2. (a) The XRD and (b) SEM analysis of GONPs.

Preparation of test fuels

Two different biodiesel blends were prepared, incorporating GONPs nanoparticles in different ratios, such as 50 and 100 ppm. These GONPs nanoparticles play a crucial role in the blending process, as they act as stabilizers, preventing phase separation and sediment formation in the blends. The blending process is a meticulous operation initiated by a mechanical agitator to ensure thorough mixing of the components. This sets the stage for the ultrasonicator, a vital tool in the process, to further enhance the homogeneity of the mixture. The high-frequency sound waves generated by the ultrasonicator create microscopic bubbles and pressure fluctuations, which break down any immiscible components and ensure complete mixing. This method accelerates the blending process, eliminating the need to wait long periods (such as an hour) to ensure complete miscibility. The fuels are diesel, AWPB, and AWPB-GONPs blends (AWPB+GONPs 50 ppm and AWPB+GONPs 100 ppm), respectively. After blending, the fuel mixtures are left to stabilize and subjected to a 30-day long-term stability test. This comprehensive testing period ensures that all properties of the blends, such as phase separation, sediment formation, oxidative degradation, and overall compatibility, are thoroughly monitored. The results from this testing show that the biodiesel-diesel blends, including those with GONPs, exhibit no significant differences or instability, confirming that the mixtures remain stable over time and are suitable for further application and research. Table 1 shows the properties of the test fuels.

Experimental facilities and setup

In this study, the electronic fuel injection (EFI) system of a Kirloskar TV1 diesel engine was upgraded and modified with electronic sensors and transducers, all integrated via an open-type electronic control unit (ECU) using Nira i7r specifications. The system architecture was designed to optimize the control of fuel injection parameters such as pressure, timing, and delivery rate, which are crucial for improving engine performance and emission characteristics. Figure 3 (a) shows the experimental layout, and Figure 3 (b) shows the photograph of the test rig, which involved retrofitting the engine with advanced EFI components to replace the traditional mechanical system. Various tortious sensors were employed to monitor and regulate the engine's Rail pressure sensors along the fuel delivery path to measure and control the pressure in the common rail. This data was continuously fed to the ECU and processed in real-time to maintain the required fuel pressure for precise delivery. The Nira i7r ECU played a central role in managing these parameters, as it is designed to handle complex multi-variable inputs and control multiple aspects of the engine's fuel injection system with high precision. This ECU is compatible with various sensor inputs, including temperature, pressure, and flow sensors, making it ideal for high-performance diesel engine management. The fuel injection system was also modified to incorporate a high-pressure fuel pump attached to the fuel filter. This setup ensured that the injection pressure remained consistent throughout the engine's operation, which is critical for efficient fuel atomization and combustion. The common rail in this system was responsible for distributing fuel at high pressure to each injector. Under the precise control of a six-pole solenoidal

valve, the injectors played a crucial role in the system. This valve provided precise control over the fuel injection timing and duration, allowing the system to sustain higher injection pressures, leading to more efficient combustion.

The fuel line modifications and the addition of the high-pressure pump and sensors were crucial in ensuring that the fuel was delivered with the appropriate pressure and timing, which the Nira i7r ECU regulated. This sophisticated control system allowed for enhanced engine performance, including improved fuel efficiency, lower emissions, and better overall combustion characteristics. The upgrade involved integrating advanced sensors, transducers, and a highly capable ECU to control fuel injection parameters accurately. This system allowed the Kirloskar TV1 engine to operate more efficiently, with better emission control and improved performance metrics.

Table 1. Physical properties of the fuel.

Characteristics	Standard	Diesel	AWPB	AWPB + GONPs 50 ppm	AWPB + GONPs 100 ppm
Kinematic viscosity, CST at 40 °C	ASTM D 445	3.1	2.6	2.595	2.4
Density (kg/m^3)	ASTM D 1298	840	790	840.8	866.6
Lower heating value (LHV) (MJ/kg)	ASTM D 240	42.51	39.26	38.29	35.78
CCI	ASTM D 976	47	51	47.7	46.4
Flashpoint (°C)	ASTM D 93	75	165	122	124

The setup demonstrated the potential for significant enhancements in diesel engine technology by adopting electronic fuel injection systems and modern control units. Test engine specifications are mentioned in Table 2. The test engine was coupled with an eddy current dynamometer to apply a controlled load. A piezoelectric pressure transducer was mounted on the cylinder head for in-cylinder pressure measurements, while a K-type thermo-couple was used for exhaust gas temperature monitoring. Fuel consumption was measured using a burette and stopwatch method, and all signals were recorded via a high-speed NI data acquisition system.

Table 2. Specification of the engine.

Make and model	Kirloskar, TV1
Cylinder & Stroke	1 & 4
Bore X Stroke	87.5 x 110 mm
Swept volume	661cc
Speed	1500 rpm
Rated output	3.5 kW at 1500 rpm
CR	1:17.5
Cooling method	Water-cooled
IT, CA bTDC	23°
Injection Pressure	600 bar

EXPERIMENTAL PROCEDURE

The impact of biodiesel and biodiesel mixing with GONPs nanoparticles was tested in the diesel engine. To acquire early data, initially, the engine operated with diesel fuel and ensured stable conditions; the engine was run five minutes before each examination. The engine was tested under the brake power of 1.1, 2.2, 3.3, 4.4, and 5.5 kW at standard working conditions. The temperature range at which the lubricating oil is kept is typically between 85 and 90 °C. The test engine undergoes continuous operation for 15 minutes, during which its performance is systematically observed. After three test iterations, the accuracy numbers were merged.

To ensure the reliability and repeatability of the experimental data, each test was conducted three times under identical conditions, and the average values were used for all performance and combustion parameters. Standard deviations were calculated to assess variability. Furthermore, a one-way ANOVA test was performed to statistically validate the differences in BTE across the four test fuels. The results confirmed statistically significant differences (F = 1245.0, p < 0.05), indicating that the variations in BTE among Diesel, AWPB, AWPB+GONPs 50 ppm, and AWPB+GONPs 100 ppm are meaningful and not due to random error.

RESULTS AND DISCUSSIONS

The investigators observed and studied various engine attributes, encompassing combustion and performance. These specific attributes will be elaborated upon further in the following sections. By generating a graphical representation, the researchers also compare the AWPB, AWPB+GONPs 50 ppm, and AWPB+GONPs 100 ppm with the baseline diesel.

Combustion analysis

Measurement of combustion in diesel engines is significant in studying the impact of biodiesel/nanoparticle blends on standard working conditions. Combustion analysis comprises measuring the cylinder pressure and HRR concerning the crank angle (CA).

In-cylinder pressure

Fuel usage measured during the premixed ignition phase of a diesel engine is an effective indicator for evaluating combustion efficiency. The presence of CA during combustion significantly affects pressure [23]. Moreover, the assessment of the inner cylinder pressure of an engine holds significant importance as it indicates the efficiency of the air-fuel mixture during the combustion process. It significantly impacts engine brake power and exhaust emissions [24]. Figure 4(a) illustrates the cylinder pressure variances from various crank angles among test fuels. The peak in-cylinder pressure was observed to be 74.2 bar for diesel, 71.5 bar for AWPB, 72.4 bar for AWPB+GONPs 50 ppm, and 72.8 bar for AWPB+GONPs 100 ppm. The diesel fuel demonstrated a higher peak in-cylinder pressure than other test fuels. This phenomenon primarily arises due to the extended duration of the ignition delay (ID) time. This occurrence leads to enhanced air/fuel mixture homogeneity, resulting in a robust premixed combustion stage and increasing maximum cylinder pressure [25]. AWPB-GONPs blends decreased in-cylinder pressure compared to diesel fuel, which is attributable to many aspects, including combustion characteristics and fuel qualities. Biodiesel generally exhibits greater viscosity and reduced energy density than diesel, resulting in less effective atomization and air-fuel mixing. This may lead to incomplete combustion and diminished peak combustion temperatures, decreasing the total pressure produced in the combustion chamber [26].

Moreover, utilizing nanoparticle blends is frequently lower than conventional diesel fuel, attributable to nanoparticles' distinct combustion properties and behaviour [27]. Although nanoparticles are incorporated to enhance combustion efficiency and diminish emissions, they may also affect ignition characteristics and combustion dynamics in a manner that could hinder the formation of more significant pressure [28]. The nanoparticles might prolong ID, leading to a diminished combustion rate, which may decrease the peak combustion temperature and lower the in-cylinder pressure [29]. Moreover, nanoparticles may modify the fuel's viscosity and surface tension, influencing the atomization and amalgamation of the fuel-air combination. This suboptimal atomization may result in incomplete combustion, hence contributing to reduced pressure levels within the combustion chamber. Consequently, whereas nanoparticle mixes may improve specific facets of engine performance, their influence on combustion dynamics might lead to a reduction in in-cylinder pressures relative to traditional diesel [30].

Heat release rate

The HRR serves as a numerical measurement for assessing the efficacy of combustion processes. The analysis of HRR has the potential to provide a significant number of valuable insights into many aspects of cylinder head design, strategies of fuel injection, fuel properties, working conditions, and their respective influences on combustion behaviour and overall engine performance [31]. The diesel engine consists of two primary combustion stages: premixed and diffusion. The initial HRR curve segment exhibited a negative magnitude because of the evaporation of fuel commencement occurring within the ID period [32]. The HRR variations for the test fuels are shown in Figure 4(b). The maximum HRR record was 72.7 J/°CA for diesel, 74.1 J/°CA for AWPB, 76.3 J/°CA for AWPB+GONPs 50 ppm, and 80.6 J/°CA for AWPB+GONPs 100 ppm. The 20 μm GONPs blend exhibited a greater HRR than other test fuels. This can be attributed to the positive effects of the large size of the GONPs, such as facilitating a uniform mixture, enhancing fuel spray, improving atomization of fuel, promoting efficient fuel vaporization during combustion, and ultimately resulting in a superior HRR [19].

Furthermore, GONPs are a crucial factor as an additive in biodiesel combustion. It enhances the fuel's oxidation stability, promoting a more complete combustion process. This improved combustion efficiency can lead to rapid energy release, increasing the heat release rate despite the reduced cylinder pressure. The reduced pressure can be attributed to a more volatile combustion environment, where the rapid flame propagation and combustion dynamics prevent sufficient pressure accumulation time before expansion [33]. However, the use of nanoparticles is also significant. They can modify combustion properties by facilitating heterogeneous nucleation, increasing combustion rates, and accelerating heat release rates, even under conditions of reduced cylinder pressure [34]. These nanoparticles can influence the thermal characteristics of the fuel, potentially enhancing heat transmission and accelerating ignition timings, further increasing HRR. Therefore, while seemingly counterintuitive, the observed phenomenon is crucial in understanding the complex interplay among fuel content, combustion dynamics, and the thermodynamic properties of biodiesel blends in engine contexts [35].

Ignition delay

ID refers to the interval between fuel injection and the initiation of combustion within an engine. It is pivotal to engine performance, affecting the smoothness and efficiency of combustion. An extended ID in diesel engines can result in quick, uncontrolled combustion, causing knocking and increased engine stress. In contrast, a reduced delay facilitates more controlled combustion, enhancing power and efficiency. Variables such as engine temperature, pressure, and fuels influence ID, rendering its management essential for enhanced performance and reduced emissions [36]. Figure 4 (c) illustrates the variances of ID for the test fuels. The ignition delay was measured as 9.2°CA for diesel, 11.3°CA for AWPB, 10.5°CA for AWPB+GONPs 50 ppm, and 10.0°CA for AWPB+GONPs 100 ppm. The diesel has the shortest ID owing to its elevated cetane number, which enhances fuel combustion relative to biodiesel and blends with GONPs. This marginal increase in ID with the addition of GONPs is attributed to their antioxidant nature, which inhibits free radical formation during low-temperature oxidation. Additionally, the high thermal conductivity and surface activity of GONPs can alter local spray and vaporization behaviour, slightly delaying ignition initiation, especially at higher concentrations

(100 ppm), where agglomeration or uneven dispersion may occur [21]. Biodiesel has an extended ID because of its diminished cetane number, elevated viscosity, and augmented oxygen concentration, all of which impede combustion kinetics. Incorporating GONPs (an antioxidant) at 10 ppm and 20 ppm significantly prolongs the ID, as antioxidants impede oxidation reactions and diminish the fuel's reactivity. This trend corresponds with studies demonstrating that antioxidants such as GONPs inhibit ignition by averting early combustion reactions [19].

GONPs possess high thermal conductivity and excellent oxidative stability, which contribute to improved heat transfer and promote more uniform and complete combustion. Their large surface area facilitates enhanced interaction with fuel molecules, aiding in better atomization and vaporization. Upon dispersion via ultrasonication, the GONPs remain uniformly distributed within the biodiesel matrix, thereby minimizing agglomeration and ensuring consistent combustion behaviour. During combustion, GONPs act as micro-reactive sites, accelerating local oxidation reactions and reducing ignition delay through faster pre-flame reactions. This effect is particularly evident in the increased HRR observed for AWPB+GONPs 100 ppm. However, the comparatively lower BTE of the 100 ppm blend, despite the higher HRR, indicates that excessive nanoparticle content may alter combustion phasing or reduce volumetric efficiency due to slower evaporation and denser spray. This emphasizes the need for optimal GONPs concentration, aligning with prior findings that show beyond-threshold nanoparticle additions lead to reduced performance due to altered spray dynamics and inconsistent fuel-air ratios [35].

Combustion duration

The CD in an engine denotes the period required for the air-fuel mixture to fully ignite and combust within the combustion chamber, spanning from ignition to the conclusion of combustion. It directly influences engine performance, efficiency, and emissions. A reduced combustion period facilitates faster and more efficient energy conversion, enhancing power output and fuel efficiency [37]. Nonetheless, if combustion transpires too rapidly, it may result in knocking and increased engine strain. Conversely, an extended combustion period may diminish efficiency and result in more emissions. Enhancing CD is crucial for achieving power, efficiency, and engine durability equilibrium [38]. Figure 4(d) illustrates the variances of CD for the test fuels. The combustion duration increased from 23.8°CA in diesel to 25.4°CA in AWPB, 26.2°CA in AWPB+GONPs 50 ppm, and 27.0°CA in AWPB+GONPs 100 ppm. Diesel has the briefest CD owing to its elevated energy density and accelerated combustion kinetics. Biodiesel has an extended CD due to its elevated oxygen concentration and diminished calorific value, which impedes combustion [39]. The biodiesel blends containing GONPs at concentrations of 10 ppm and 20 ppm demonstrate increasingly extended CDs. GONPs, as antioxidants, suppress oxidation, decreasing the combustion rate and extending the burning duration [40]. Elevated amounts of GONPs (20 ppm) further impede the process, as antioxidants often obstruct the oxidation reactions that facilitate fuel burning. This observation is consistent with recent studies regarding the impact of antioxidants on biodiesel combustion, indicating that antioxidants can prolong CD by diminishing the fuel's reactivity [41].

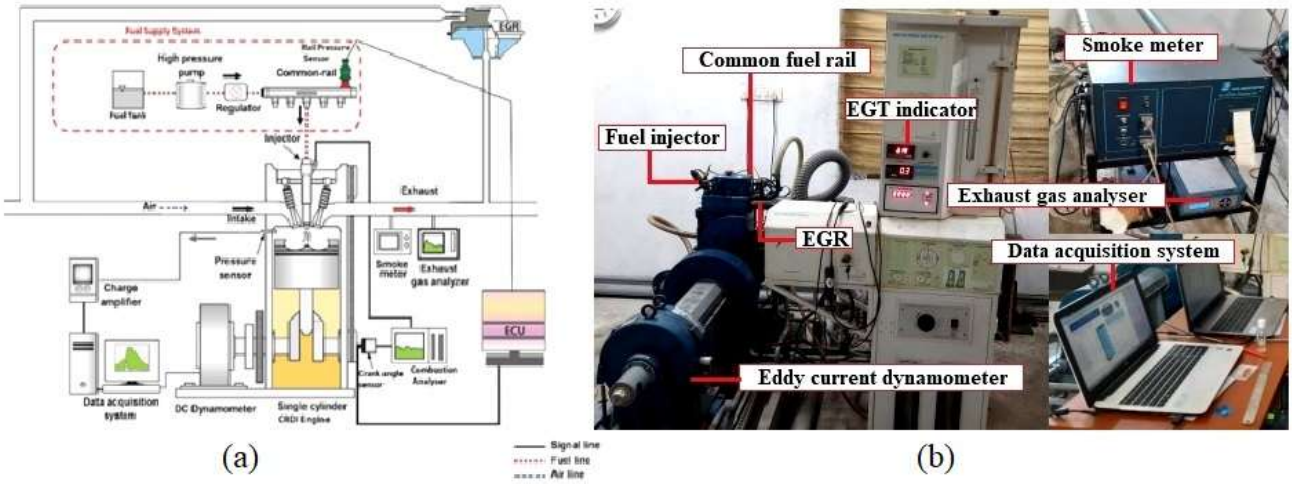

Figure 3. (a) Experimental layout and (b) photographic view of the test rig.

Performance analysis

The experimental investigation involves testing a research diesel engine powered by a blend of AWPB-GONPs under standard operating conditions. This section examines engine performance precisely regarding two key parameters: the brake-specific energy consumption (BSEC) and BTE.

Brake thermal efficiency

BTE quantifies the effectiveness of an engine in transforming the chemical energy of fuel into productive mechanical work, represented as a percentage by contrasting the brake power output with the fuel energy input. An elevated BTE signifies enhanced fuel economy, as a more significant portion of the fuel's energy is

transformed into work [42]. Diesel engines generally attain superior BTE compared to gasoline engines owing to their elevated compression ratios and more effective combustion mechanisms. Elements like fuel characteristics, combustion efficiency, engine load, and technology such as turbocharging and efficient fuel injection systems substantially affect BTE. Enhancing BTE is essential for diminishing fuel consumption, augmenting engine performance, and decreasing emissions [43]. Figure 5 (a) shows the variations of BTE.

Diesel exhibits the highest BTE across all brake power levels owing to its exceptional combustion properties and energy density, enabling a more effective fuel energy transformation into work. AWPB has inferior BTE relative to diesel, principally due to biodiesel's diminished energy content and elevated viscosity, which result in heightened fuel consumption and decreased combustion efficiency [44]. The AWPB+GONPs mixtures demonstrate enhanced brake thermal efficiency compared to AWPB, with 50 and 100 ppm GONPs outperforming pure biodiesel. The antioxidant capabilities of GONPs improve fuel stability and combustion characteristics, hence alleviating certain efficiency limitations of biodiesel. The trend indicates that when BP rises, BTE is enhanced for all fuels, aligning with the anticipation that engines function more effectively under elevated loads, whereby a larger fraction of the fuel's energy is transformed into productive work [45]. The blend AWPB+GONPs 50 ppm produced 5.98% and 2.96% higher BTE than the AWPB and AWPB+GONPs 100 ppm blend at maximum brake power due to their increased fuel consumption during the premixed ignition area, and rapid combustion led to a high oxygen concentration of the GONPs [19]. GONPs exhibit exceptional thermal conductivity and surface reactivity due to their high aspect ratio and large surface area, which promote uniform heat distribution and enhance local combustion zones. Their ability to scavenge free radicals stabilizes the oxidative environment within the combustion chamber, reducing the formation of incomplete combustion byproducts [21]. Furthermore, the nanoscale size of GONPs facilitates improved atomization of the fuel blend, promoting micro-explosions that enhance droplet breakup and increase the surface area for combustion, thereby accelerating the combustion rate [26]. These effects collectively reduce ignition delay and enhance the premixed combustion phase, resulting in more efficient energy conversion. As a result, less fuel is required to produce the same output power, resulting in improved BTE [31].

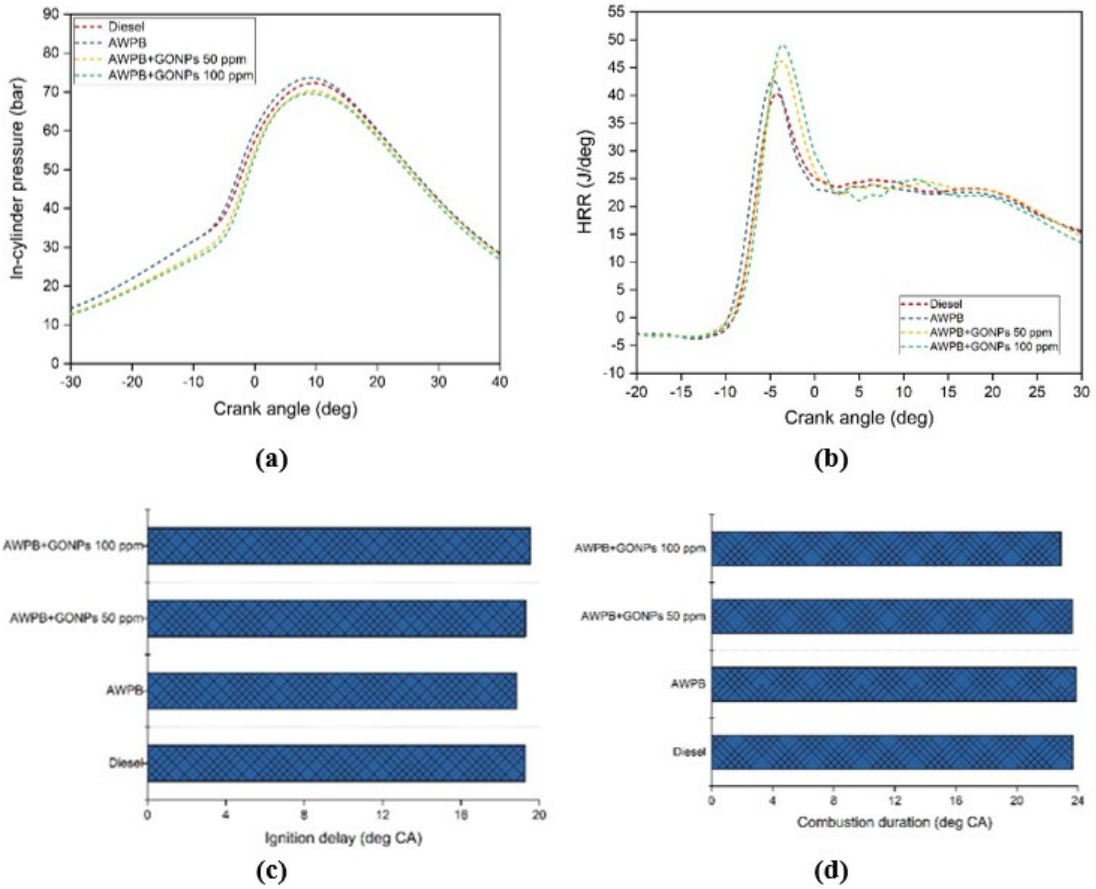

Figure 4. (a) In-cylinder pressure, (b) HRR, (c) ID, and (d) CD for the test fuels.

Brake-specific energy consumption

BSEC has combined the calorific fuel value and brake-specific fuel. There is an inverse relationship between BTE and BSFC: as one increases, the other decreases, indicating the trade-off between fuel efficiency and energy conversion efficiency in engines [46]. The outcome result and the details for the variations in BTE between biodiesel,

biodiesel-GONPs blends, and diesel also apply to BSFC [47]. Figure 5 (b) shows BSEC decreasing while increasing brake power. This is owing to the mixture's LHV compared to neat diesel fuel, which needs more fuel to achieve a given plunger movement for the injection system. BSEC increased all fuel variants relative to neat diesel. Diesel demonstrates the lowest BSEC values, indicating its superior energy density and enhanced combustion efficiency, particularly at elevated loads, where engines function nearer to ideal conditions [48]. Conversely, biodiesel exhibits consistently elevated BSEC owing to its diminished energy content and augmented oxygen content, resulting in heightened fuel consumption for equivalent power output. Biodiesel increased BSEC by 30.12% compared to diesel. The blended AWPB+GONPs 50 ppm was made with the least BSEC rather than other blends due to the addition of GONPs. GONPs' high oxygen content could hasten combustion, using less fuel to generate a similar power [19].

Engine torque

Engine torque denotes the rotational force generated by an engine's crankshaft, essential for assessing a vehicle's towing capacity and acceleration. Torque is produced when the engine's pistons move, resulting in the rotation of the crankshaft. The torque magnitude depends on engine displacement, combustion pressure, and crankshaft configuration variables. Peak torque is generally attained at reduced speed, where torque is most essential for practical driving conditions [6]. Figure 5 (c) illustrates the variances of engine torque for the test fuels. In contrast to biodiesel alone, the enhancement of engine torque noted in diesel and biodiesel-GONPs nanoparticle mixes can be ascribed to many causes elucidated in recent studies. The main reason is the improved combustion properties provided by incorporating GONPs and nanoparticles, which boost the fuel mixture's ignition quality and combustion efficiency. GONPs boost the oxidative stability of biodiesel and improve combustion characteristics by diminishing ID and increasing fuel volatility, resulting in a more complete combustion process. Integrating nanoparticles into the fuel mixture reduces the viscosity of biodiesel, enhancing atomization and spray characteristics during fuel injection. Enhanced atomization improves air-fuel mixing in the combustion chamber, leading to greater combustion efficiency and better torque output [49]. The appropriate amalgamation of biodiesel with additives such as GONPs and nanoparticles can improve performance metrics, including torque, by optimizing energy release during combustion. The synergistic effects of GONPs and nanoparticles enhance torque performance in diesel and biodiesel-GONPs nanoparticle blends relative to biodiesel alone [50].

Exhaust gas temperature

EGT denotes the temperature of the gases leaving an engine's combustion chamber via the exhaust system. It serves as a crucial metric for engine performance and combustion efficiency. Elevated EGT may indicate that the engine is under significant strain due to excessive fuel consumption or suboptimal combustion. In contrast, diminished EGT could signify incomplete combustion or reduced engine load. Monitoring EGT is essential for optimizing engine performance, as elevated temperatures can result in engine overheating and possible damage, particularly to exhaust valves, turbochargers, or catalytic converters. Conversely, sustaining appropriate EGT enhances fuel efficiency, lowers emissions, and promotes engine longevity [24]. Figure 5 (d) illustrates the variances of EGT for the test fuels. The engine EGT in diesel and biodiesel-GONPs nanoparticle blends is often lower than that of biodiesel, attributed to superior combustion efficiency and increased thermal characteristics of the fuel mixture. Incorporating GONPs in biodiesel enhances oxidation stability and combustion properties, leading to more complete fuel combustion and reduced production of unburned HC [27]. This complete combustion reduces energy loss as heat, directly contributing to decreased EGT. Integrating nanoparticles promotes superior fuel atomization, improving air-fuel mixing and combustion efficiency. Enhanced combustion dynamics facilitate a more efficient use of the fuel's energy content, resulting in reduced exhaust temperatures. The thermal features of the biodiesel-GONPs nanoparticle blend can affect EGT since the enhanced heat transfer capabilities of the blend may facilitate superior heat absorption during combustion, leading to lower EGT than biodiesel alone. The synergistic actions of GONPs and nanoparticles enhance the combustion process, reducing EGT [3]. The reduction in EGT observed with AWPB+GONPs blends is primarily due to the high thermal conductivity and oxidative stability of GONPs. These nanoparticles improve heat transfer and promote complete combustion by accelerating oxidation reactions and stabilizing the fuel against degradation. This leads to more efficient energy conversion and reduces heat loss. However, while lower EGT typically indicates better combustion, excessively low values, especially at light loads, may also suggest incomplete combustion [22].

GONPs possess high thermal conductivity, which facilitates rapid heat transfer within the combustion chamber, promoting a uniform temperature distribution and minimising localised hot spots. This enhances the combustion of fuel-air mixtures by accelerating oxidation reactions, resulting in more complete combustion [16]. Moreover, GONPs improve the oxidative stability of biodiesel blends by scavenging free radicals and reducing the likelihood of fuel degradation during storage and combustion. As a result, the fuel maintains its reactivity and ignition quality, enabling more efficient energy conversion. This improvement in combustion completeness reduces the formation of unburned hydrocarbons and decreases the amount of residual heat released into the exhaust stream, thereby lowering the EGT [31].

Indicated mean effective pressure

The IMEP is a critical metric that denotes the average pressure applied to the pistons during the combustion cycle. This metric assesses the engine's capacity to transform combustion energy into productive work derived from the pressure within the combustion chamber across a

whole engine cycle. IMEP is intrinsically linked to engine torque and power output, rendering it a crucial parameter for assessing engine efficiency and performance. Figure 6 (a) illustrates the variances of IMEP for the test fuels. The observed rise in IMEP in diesel and biodiesel-GONPs nanoparticle mixes, relative to biodiesel, can be ascribed to the improved combustion efficiency and power production stemming from the distinctive characteristics of the blend. Incorporating GONPs as an antioxidant in biodiesel enhances the fuel's oxidation stability and volatility, resulting in lessened IDs and more thorough combustion. This enhancement enables elevated combustion pressures throughout the power stroke, augmenting IMEP [39]. Integrating nanoparticles into the biodiesel-GONPs mixture improves fuel atomization and spray properties by decreasing viscosity and facilitating superior air mixing. An enhanced air-fuel mixture yields more efficient combustion, resulting in elevated peak pressures within the cylinder and increased IMEP. The combined effects of GONPs and nanoparticles in biodiesel substantially enhance engine performance, as evidenced by the elevated IMEP relative to biodiesel alone [5].

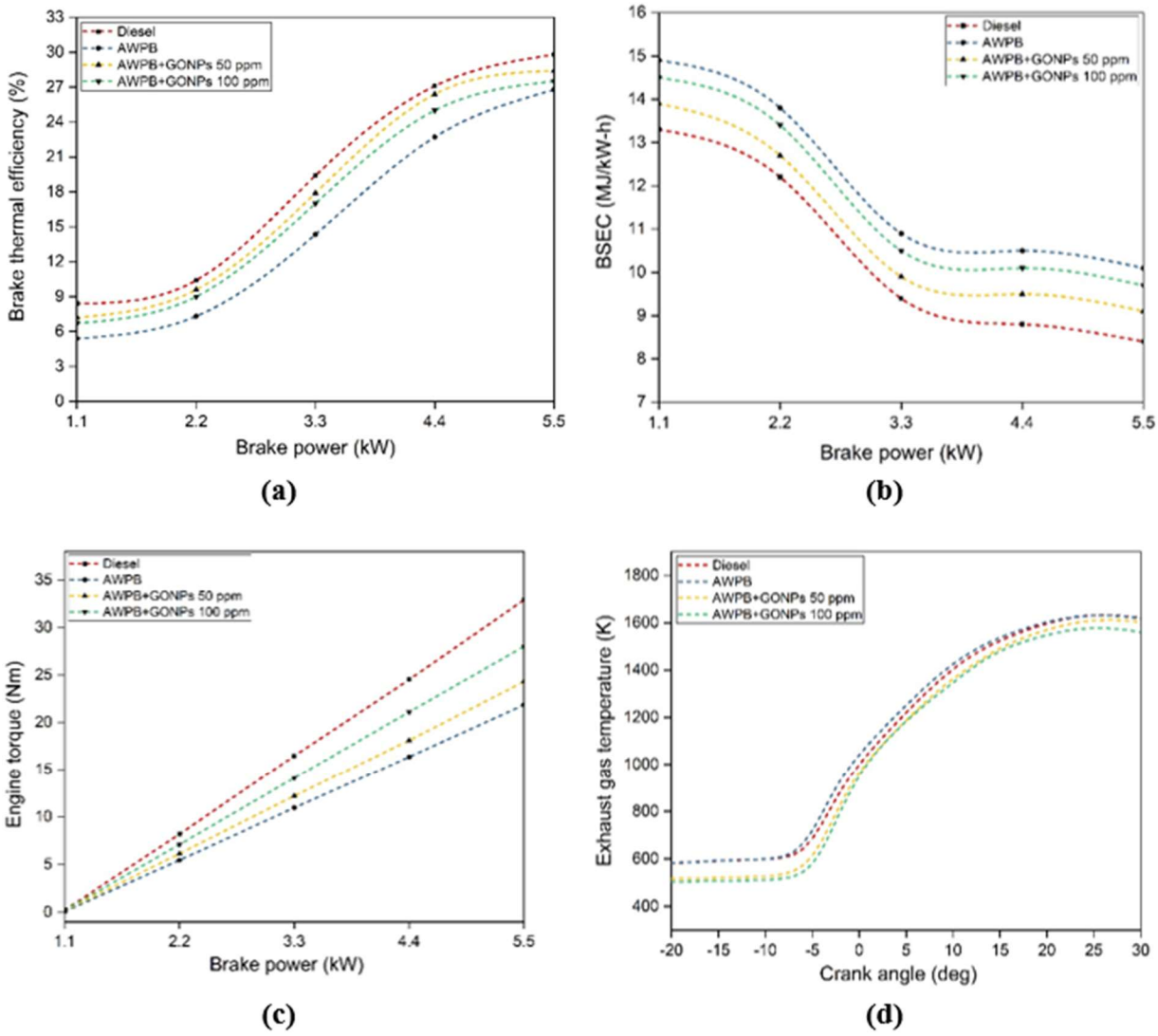

Figure 5. (a) BTE, (b) BSEC, (c) engine torque, and (d) EGT for the test fuels.

Air-fuel ratio

An engine's A/F ratio is the air-to-fuel (A/F) ratio combined and ignited in its cylinders. Assessing engine efficiency, performance, and emissions requires it. The ideal A/F ratio for gasoline engines is 14.7:1, or 14.7 parts air to 1 part fuel. The combustion process produces power, fuel economy, and low pollutants most efficiently at this ratio. A "rich" mixture has more fuel than air, increasing engine output, fuel consumption, and pollutants. A "lean" mixture has more air than gasoline, improving fuel efficiency and lowering pollutants, but it may also raise engine temperatures and cause engine knock. Proper A/F ratios improve engine durability, efficiency, and environmental compliance [23]. Figure 6 (b) illustrates the variances of the A/F ratio for the test fuels. The A/F ratio in diesel and biodiesel-GONPs nanoparticle blends is more optimal than in biodiesel alone, owing to the enhanced combustion characteristics provided by the additives. GONPs improve biodiesel's oxidative stability and volatility, facilitating superior atomization and a more consistent fuel distribution throughout the combustion chamber.

This enhanced atomization results in more efficient air mixing, improving the A/F ratio and facilitating complete combustion [51]. Furthermore, including nanoparticles in the biodiesel-GONPs blend further diminishes the fuel's viscosity, promoting finer spray patterns during injection and improving the overall quality of the air-fuel mixture. A more uniform air-fuel mixture facilitates more efficient combustion processes, yielding an optimal A/F ratio that enhances engine performance and reduces emissions. Thus, the combined actions of GONPs and nanoparticles in biodiesel yield a more advantageous A/F ratio than biodiesel alone, improving engine efficiency and performance [12].

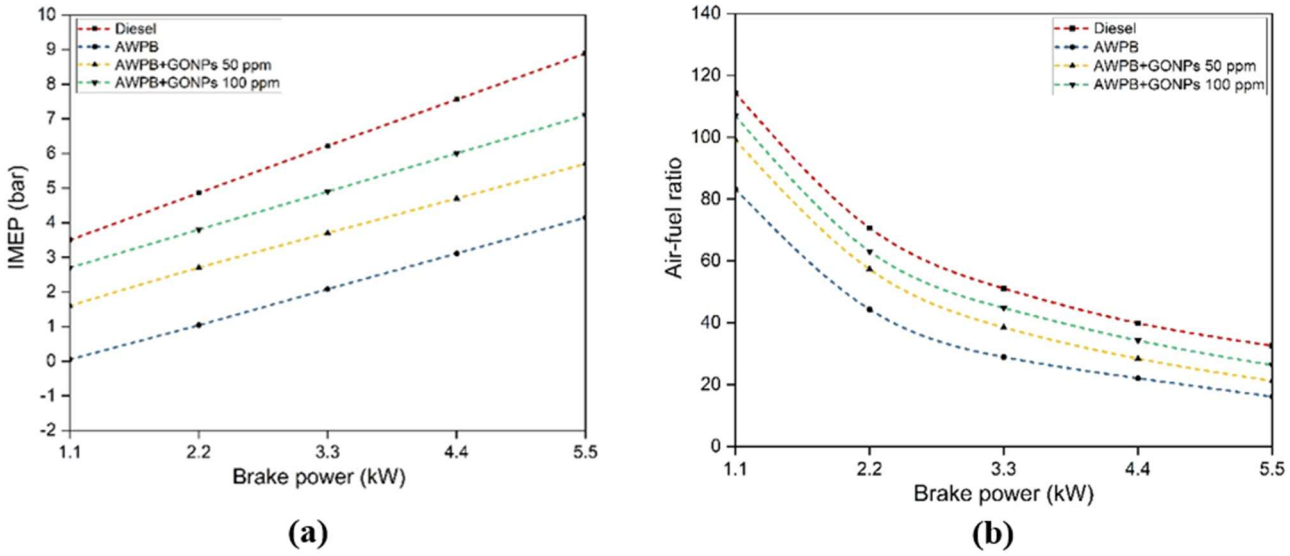

Figure 6. (a) IMEP, and (b) A/F ratio for the test fuels.

AWPB+GONPs blends exhibited an improvement in BTE and a reduction in BSEC. These enhancements were observed alongside relatively lower engine torque, indicating a mean adequate pressure and volumetric efficiency compared to diesel. This performance divergence is attributed to the inherently lower energy density and slightly higher viscosity of biodiesel, which adversely affect air-fuel mixing and combustion pressure development. Despite the oxidative and catalytic benefits provided by GONPs, these blends experience reduced torque output due to incomplete utilization of the lower heating value. Additionally, volumetric efficiency tends to decrease because biodiesel combustion increases the residual gas content and intake temperature, thereby affecting the fresh charge density.

CONCLUSION

This investigation describes the utilization of biodiesel produced from avocado fruit peel waste using the transesterification method to fuel diesel engines by adding GONPs as an ignition enhancer.

- The in-cylinder pressure increased in AWPB, and HRR increased in AWPB+GONPs 100 ppm blend compared to diesel, but the diesel fuel has a higher ID and CD than other test fuels.
- Biodiesel increased BSEC by 30.12% compared to diesel. The blended AWPB+GONPs 50 ppm was made with the least BSEC rather than other blends.
- The BTE increased in AWPB+GONPs 50 ppm blends by 5.98% and 2.96% compared to AWPB and AWPB+GONPs 100 ppm blends, but lowered by 4.92% compared to neat diesel at maximum brake power.
- Furthermore, diesel fuel has a higher engine torque, IMEP, A/F ratio, and volumetric efficiency than other test fuels, but AWPB has higher EGT than diesel.

This work concludes that adding GONPs to a biodiesel blend enhances performance, and this combination of blends is suitable for diesel engine operations.

Practical and economic considerations. Avocado waste peel offers a promising, low-cost, abundant feedstock, particularly in fruit-processing regions. Its collection, drying, and oil extraction processes must be optimized for industrial-scale implementation. Furthermore, although GONPs offer substantial benefits in improving combustion and oxidative stability, their current production cost remains a constraint for widespread commercial use. However, recent advances in green synthesis methods and waste-derived graphene oxide production pathways suggest the potential for cost reduction. We acknowledge that a detailed techno-economic assessment is necessary to validate the long-term viability of this biodiesel-nanoparticle system. Hence, we have stated this as a key direction for future work. This addition reinforces the need to balance performance advantages with economic practicality, supporting a more holistic evaluation of the fuel blend's sustainability.

Future research direction. Integrating hydrogen and bioethanol fuel injection as a dual fuel system in diesel engines can enhance performance and diminish greenhouse gas emissions, particularly with AWPB-diesel mixtures. The impact of various fuel injection techniques can be assessed to analyze a diesel engine's performance efficiency and environmental emissions, utilizing test fuels such as AWPB and diesel fuel.

NOMENCLATURE

GONPs Graphene oxide nanoplates
AWPB Avocado waste peel biodiesel
HRR Heat release rate
NOx Nitrogen oxide
CO Carbon monoxide
BSFC Brake-specific fuel consumption
BTE Brake thermal efficiency
HC Hydrocarbon
OB20L5 Orange peel oil biodiesel 20+L-ascorbic acid 5 % by volume
OB20L10 Orange peel oil biodiesel 20+L-ascorbic acid 10 % by volume
BPB Bauhinia parviflora biodiesel
DTBP Di-tert-butyl peroxide
FFA Free fatty acid
ppm part per million
LHV Lower heating value
CCI Calculated cetane index
EFI Electronic fuel injection
ECU Electronic control unit
BSEC Brake-specific energy consumption

REFERENCES

[1] R.K. Babu, R. Jayabal, Y. Devarajan, Environ. Sci. Pollut. Res. 30 (2023) 26020-26026. https://doi.org/10.1007/s11356-023-26020-6.
[2] R. Jayabal, G.M.L. Leo, M.C. Das, S. Sekar, S. Arivazhagan, Process Saf. Environ. Prot. 188 (2024) 1398-1410. https://doi.org/10.1016/j.psep.2024.06.016.
[3] G.M.L. Leo, M.C. Das, R. Jayabal, M.S. Murugapoopathi, D. Srinivasan, N. Mukilarasan, Energy 282 (2023) 128923. https://doi.org/10.1016/j.energy.2023.128923.
[4] S. Madhu, G.M.L. Leo, P. Prathap, Y. Devarajan, R. Jayabal, Process Saf. Environ. Prot. 169 (2023) 102957. https://doi.org/10.1016/j.psep.2023.02.057.
[5] N. Mohanrajhu, S. Sekar, R. Jayabal, R. Sureshkumar, Process Saf. Environ. Prot. 187 (2024) 332-342. https://doi.org/10.1016/j.psep.2024.04.115.
[6] M.A. Asokan, S.S. Prabu, S. Prathiba, D.S. Sukhadia, V. Jain, S.M. Sarwate, Mater. Today Proc. 46 (2021) 8114-8118. https://doi.org/10.1016/j.matpr.2021.03.060.
[7] P. Duraisamy, S. Subramani, R. Jayabal, Int. J. Environ. Sci. Technol. 20 (2023) 12251-12266. https://doi.org/10.1007/s13762-023-04891-z.
[8] Y. Chen, J. Zhang, Z. Zhang, W. Zhong, Z. Zhao, H. Jingyi, Heliyon 9 (2023) e19196. https://doi.org/10.1016/j.heliyon.2023.e19196
[9] O. Ogunkunle, N.A. Ahmed, Sustainability 13(10) (2021) 5465. https://doi.org/10.3390/su13105465.
[10] K. Masera, A.K. Hossain, Renewable Sustainable Energy Rev. 178 (2023) 113235. https://doi.org/10.1016/j.rser.2023.113235.
[11] S. Ahmad, A.T. Jafry, M.U. Haq, N. Abbas, H. Ajab, A. Hussain, U. Sajjad, Energies 16 (13) (2023) 5153. https://doi.org/10.3390/en16135153.
[12] F. Zheng, H.M. Cho, Energies 17(16) (2024) 4126. https://doi.org/10.3390/en17164126.
[13] R. Senthil Kumar, S. Mahalingam, J. Clean. Prod. 236 (2019) 117-128. https://doi.org/10.1016/j.jclepro.2019.117348.
[14] A. Karthikeyan, A. Elango, Renewable Energy 138 (2019) 647-654. https://doi.org/10.1016/j.renene.2019.02.032.
[15] J. Mathew, S. Varghese, J. Thomas, Fuel 299 (2021) 120-132. https://doi.org/10.1016/j.fuel.2021.120651.
[16] M.E.M. Soudagar, N.N. Nik-Ghazali, Energy Convers. Manage. 215 (2020) 120-132. https://doi.org/10.1016/j.enconman.2020.112649.
[17] A.A. Prabu, M.A. Asokan, Renewable Energy 116 (2018) 573-583. https://doi.org/10.1016/j.renene.2018.03.046.
[18] R. Jayabal, Process Saf. Environ. Prot. 186 (2024) 694-705. https://doi.org/10.1016/j.psep.2024.04.019.
[19] M.E.M. Soudagar, N.-N. Nik-Ghazali, M.A. Kalam, I.A. Badruddin, N.R. Banapurmath, M.A. Bin Ali, S. Kamangar, H.M. Cho, N. Akram, Renewable Energy 146 (2020) 2291-2307. https://doi.org/10.1016/j.renene.2019.08.025.
[20] M.E.M. Soudagar, M.A. Mujtaba, M.R. Safaei, A. Afzal, D.R. V, W. Ahmed, N.R. Banapurmath, N. Hossain, S. Bashir, I.A. Badruddin, M. Goodarzi, K. Shahapurkar, S.N. Taqui, Energy 215 (2021) 119094. https://doi.org/10.1016/j.energy.2020.119094.
[21] M.E.M. Soudagar, A. Afzal, M.R. Safaei, A.M. Manokar, A.I. EL-Seesy, M.A. Mujtaba, O.D. Samuel, I.A. Badruddin, W. Ahmed, K. Shahapurkar, M. Goodarzi, J. Therm. Anal. Calorim. 147 (2020) 525-542. https://doi.org/10.1007/s10973-020-10293-x.
[22] M.E.M. Soudagar, T.S. Kiong, S. Ramesh, N.N.N. Ghazali, M.A. Kalam, M.A. Mujtaba, H. Venu, M. Nur-E-Alam, H.M. Ali, J. Therm. Anal. Calorim. 149 (2024) 10165-10165. https://doi.org/10.1007/s10973-024-13373-4.
[23] S. Vellaiyan, M. Kandasamy, Y. Devarajan, Waste Manage. 162 (2023) 63-71. https://doi.org/10.1016/j.wasman.2023.03.012.
[24] S. Boopathi, J. Ravikumar, R. Devanathan, S.A.A. Anicia, Adv. Mater. Manuf. Eng. 279 (2020) 279-284. https://doi.org/10.1007/978-981-15-6267-9_33.
[25] A. Çakmak, H. Özcan, Fuel 315 (2022) 123200. https://doi.org/10.1016/j.fuel.2022.123200.
[26] S. Vellaiyan, Results Eng. 24 (2024) 102953. https://doi.org/10.1016/j.rineng.2024.102953.
[27] M.E.M. Soudagar, V.V. Upadhyay, N.N. Bhooshanam, R.P. Singh, D. Rabadiya, R. Venkatesh, V. Mohanavel, M.A. Alotaibi, A.H. Seikh, Biomass Bioenergy 190 (2024) 107379. https://doi.org/10.1016/j.biombioe.2024.107379.
[28] Y. Devarajan, R. Jayabal, D.B. Munuswamy, S. Ganesan, E.G. Varuvel, Process Saf. Environ. Prot. 165 (2022) 374-379. https://doi.org/10.1016/j.psep.2022.07.001.
[29] M.E.M. Soudagar, S. Shelare, D. Marghade, P. Belkhode, M. Nur-E-Alam, T.S. Kiong, S. Ramesh, A. Rajabi, H. Venu, T.M. Yunus Khan, M. Mujtaba, K.

Shahapurkar, M. Kalam, I.M.R. Fattah, Energy Convers. Manag. 307 (2024) 118337. https://doi.org/10.1016/j.enconman.2024.118337.
[30] S.M. Jiangjun, W.Y. Zhang, Q. Dai, Y. Qian, Energy 300 (2024) 131616. https://doi.org/10.1016/j.energy.2024.131616.
[31] G. Pullagura, J.R. Bikkavolu, S. Vadapalli, V.V. Siva Prasad, K.R. Rao Chebattina, D. Barik, M.S. Dennison, Heliyon 10 (2024) e026519. https://doi.org/10.1016/j.heliyon.2024.e026519.
[32] F.O. Olanrewaju, H. Li, G.E. Andrews, H.N. Phylaktou, J. Energy Inst. 93 (2020) 1901-1913. https://doi.org/10.1016/j.joei.2020.04.005.
[33] P. Sharma, J. Energy Resour. Technol. 144 (2021) 144007. http://doi.org/10.1115/1.4052237.
[34] B.J. Rao, G. Pullagura, S. Vadapalli, K.R.R. Chebattina, AIP Conf. Proc. 2943 (2023) 020017. https://doi.org/10.1063/5.0182876.
[35] R. Jayabal, Process Saf. Environ. Prot. 186 (2024) 694–705. https://doi.org/10.1016/j.psep.2024.04.019.
[36] V. Rathinavelu, A. Kulandaivel, A.K. Pandey, R. Bhatt, M.V. De Poures, I. Hossain, A.H. Seikh, A. Iqbal, P. Murugan, Heliyon 10 (2024) e23988. https://doi.org/10.1016/j.heliyon.2024.e23988.
[37] R. Jayabal, L. Thangavelu, S. Subramani, Fuel 276 (2020) 118020. http://doi.org/10.1016/j.fuel.2020.118020.
[38] S. Senthil Kumar, K. Rajan, Energy Sources, Part A 43 (2019) 1-13. http://doi.org/10.1080/15567036.2019.1654565.
[39] G. Pullagura, V.S. Prasad Vanthala, S. Vadapalli, J.R. Bikkavolu, K.R.R. Chebattina, Biofuels 15 (2023) 449-460. https://doi.org/10.1080/17597269.2023.2256105.
[40] S. Krishnakumar, T.M Yunuskhan, C.R. Rajashekhar, M. Elahi, M. Soudagar, A. Afzal, A. Elfasakhany, Energies 14(14) (2021) 4306. https://doi.org/10.3390/en14144306.
[41] G. Zamboni, Energies 11(10) (2018) 2531. https://doi.org/10.3390/en11102531.
[42] B.J. Rao, J. Mech. Eng. 20 (2023) 313-333. https://doi.org/10.24191/jmeche.v20i3.23915.
[43] T. Krishnamoorthi, G. Sudalaimuthu, D. Damodharan, R. Jayabal, J. Clean. Prod. 420 (2023) 138413. https://doi.org/10.1016/j.jclepro.2023.138413.
[44] B.J. Rao, V. Srinivas, C.K.R. Rao, P. Gandhi, Emerg. Mater. 7 (2023) 847-866. https://doi.org/10.1007/s42247-023-00609-6.
[45] R. Jayabal, Process Saf. Environ. Prot. 188 (2024) 1346-54. https://doi.org/10.1016/j.psep.2024.06.012.
[46] S.M. Veeraraghavan, M.V. De Poures, G. Kaliyaperumal, D. Dillikannan, Int. J. Hydrogen Energy 87 (2024) 227-237. https://doi.org/10.1016/j.ijhydene.2024.08.393.
[47] R. Jayabal, Process Saf. Environ. Prot. 183 (2024) 890-900. https://doi.org/10.1016/j.psep.2024.01.046.
[48] V. Modi, P.B. Rampure, A. Babbar, R. Kumar, M. Nagaral, A. Bhowmik, S. Pandey, S.M. Hasnain, M.M. Ali, M.N. Bashir, Mater. Sci. Energy Technol. 7 (2024) 257-273. https://doi.org/10.1016/j.mset.2024.02.001.
[49] B.K.M. Mahgoub, Heliyon 9 (2023) e21367. https://doi.org/10.1016/j.heliyon.2023.e21367.
[50] J. Romola, M. Meganaharshini, S.P. Rigby, I.G. Moorthy, R. Shyam Kumar, S. Karthikumar, Renewable Sustainable Energy Rev. 145 (2021) 111109. https://doi.org/10.1016/j.rser.2021.111109.
[51] M.G.B. Millerjothi, N. Kalamegam, S. Muyiwa, Adaramola, F. Yohaness, H. Ram, C. Singh. Int. J. Engine Res. 24 (2022) 4459-4469 https://doi.org/10.1177/14680874221097574.

ISTRAŽIVANJE SAGOREVANJA I PERFORMANSI DIZEL MOTORA NAPAJANOG MEŠAVINAMA BIODIZELA I NANOČESTICA

MOHANRAJHU NATHAMUNI[1]
PREMKUMAR DURAISAMY[2]
RAJAKUMAR MUTHUSAMY PALANI[3]

PADMAVATHI KUPPUSAMY RAMAMOORTHY[4]

[1]Department of Mechanical Engineering, R.M.K. Engineering College, Chennai, TN, India.

[2]Department of Mechanical Engineering, Easwari Engineering College, Tamil Nadu, India.

[3]Department of Artificial Intelligence and Data Science, St. Joseph's College of Engineering, TN, Chennai, India.

[4]Department of Mechanical Engineering, Panimalar Engineering College, TN, Chennai, India

NAUČNI RAD

Ovaj rad istražuje sagorevanje i performanse biodizela od otpadne kore avokada (AWPB) pomešanog sa nanopločama grafen-oksida (GONP) kao potencijalnog alternativnog goriva za dizel motore. Takođe, rad ima za cilj da proceni uticaj sagorevanja i performansi motora, uz razmatranje izvodljivosti korišćenja otpadnih materijala u proizvodnji goriva. Procenjena su sledeća goriva: dizel, AWPB, AWPB+GONP 50 ppm i AWPB+GONP 100 ppm. Rezultati su pokazali da je pritisak u cilindru u AWPB smanjen za približno 3,6% u poređenju sa dizelom, dok je brzina oslobađanja toplote značajno porasla u mešavini AWPB+GONP 100 ppm. Pored toga, dizel je pokazao veće kašnjenje paljenja i trajanje sagorevanja od svih mešavina biodizela. Dodavanje GONP-ova u AWPB dovelo je do povećanja termičke efikasnosti kočnice za 5,98% i smanjenja potrošnje energije specifične za kočenje za 30,12% u poređenju sa dizelom. Međutim, dizel je i dalje pokazao veći obrtni moment motora, indicirani srednji efektivni pritisak i odnos vazduh-gorivo (A/F odnos) u odnosu na biodizel goriva, dok je AWPB pokazao višu temperaturu izduvnih gasova. Ovi nalazi ukazuju na to da je biodizel od kore avokada, kada je poboljšan GONP-ovima, održiva i čistija alternativa konvencionalnom dizelu, nudeći poboljšanu efikasnost sagorevanja i smanjenu potrošnju energije.

Ključne reči: otpad u energiju, biodizel, kora avokada, nanoploče grafen-oksida; performanse.

CI&CEQ
Chemical Industry & Chemical Engineering Quarterly

Available online at
Association of the Chemical Engineers of Serbia AChE
www.ache.org.rs/CICEQ

Chem. Ind. Chem. Eng. Q. 32 (3) 213–223 (2026) CI&CEQ

AMIRAH NASUHA MOHD RAZIB[1,3]

NIK MUHAMMAD AZHAR NIK DAUD[1]

MOHD AL HAFIZ MOHD NAWI[2]

BANU RAMASAMY[1]

MOHD SHARIZAN MD SARIP[1,3]

AMIRUL RIDZUAN ABU BAKAR[1]

MOHD ASRAF MOHD ZAINUDIN[1]

AHMAD HAZIM ABDUL AZIZ[4]

[1] Faculty of Chemical Engineering & Technology, University Malaysia Perlis, Perlis, Malaysia

[2] Faculty of Mechanical Engineering Technology, University Malaysia Perlis, Perlis, Malaysia

[3] Center of Excellence for Frontier Materials Research (FrontMate), University Malaysia Perlis, Perlis, Malaysia

[4]Faculty of Food Science and Nutrition, University Malaysia Sabah, Kota Kinabalu, Malaysia.

SCIENTIFIC PAPER

UDC 678.664:66:628.477.6.043

POTENTIAL OF ULTRASONIC IRRADIATION IN POLYURETHANE DEGRADATION IN DEEP EUTECTIC SOLVENTS

Highlights

- Enhanced polyurethane degradation using DES and ultrasonication.
- Green solvent for polyurethane recycling
- Green recycling pathway for polyurethane waste
- Depolymerization of polyurethane to *o*-toluidine.

Abstract

This study explores the degradation of polyurethane (PU) using deep eutectic solvents (DES) combined with ultrasonic irradiation, aiming to develop sustainable recycling techniques for PU waste. DES, formed from choline chloride and urea, possesses environmentally friendly properties such as low toxicity and high solubility, making it suitable for chemical recycling. Degradation experiments were conducted at elevated temperatures (130-150 °C), both with and without ultrasonic assistance. The technique of GPC is applied to determine the molecular weight of raw PU and the degradation product. The structures of DES, PU, and its degradation products were analysed using FTIR and NMR. The results indicate that the application of ultrasonics significantly enhances the degradation rate at approximately 5.20% from 58.51 ± 0.04% to 63.71 ± 0.03% at a constant temperature of 150 °C. This improvement is attributed to cavitation-induced effects, which facilitate polymer chain breakdown. Molecular transformations were confirmed through the presence of NH_3 groups resulting from the break of the PU structure to form o-toluidine, as identified by NMR. Reaction pathways were established through structural analysis of both raw PU and its degradation products. These findings demonstrate the potential of ultrasonic-assisted DES in advancing chemical recycling strategies for PU, addressing environmental concerns related to persistent PU waste, and promoting sustainable waste management practices.

Keywords: Ultrasonic, Polymer recycling, o-toluidine.

INTRODUCTION

Polyurethane (PU) represents a multifaceted polymer extensively employed in diverse industrial applications, attributed to its remarkable characteristics such as durability, flexibility, and abrasion resistance [1]. PU is frequently utilized in a variety of applications, including foams, adhesives, coatings, elastomers, and membranes [2-5]. PU has also proven to be applied as a sheath for elastic electromagnetic fibers [6]. Its versatile properties have established it as a preferred material across multiple sectors, including construction, automotive, and consumer goods. The persistent nature of PU presents serious environmental problems, notwithstanding its benefits. Conventional disposal methods for non-biodegradable materials, including landfilling and incineration, are unsustainable [7]. These practices result in the accumulation of PU waste, which significantly contributes to environmental pollution.

Recent advancements have highlighted a growing focus on the formulation of sustainable recycling methodologies aimed at mitigating the environmental challenges posed by PU waste. Various techniques have been established for the degradation of PU, encompassing thermal, chemical, biological, and mechanical recycling methods. Chemical degradation is extensively researched due to its potential for recovering valuable raw materials

Correspondence: M.S. Md Sarip, Faculty of Chemical Engineering & Technology, University Malaysia Perlis, 02600, Arau, Perlis, Malaysia
Center of Excellence for Frontier Materials Research (FrontMate), University Malaysia Perlis, Perlis, Malaysia
Email: sharizan@unimap.edu.my
Paper received: 3 April 2025
Paper revised: 7 August 2025
Paper accepted: 30 August 2025

https://doi.org/10.2298/CICEQ250403023N

such as polyols and amines. Common methods of chemical degradation encompass glycolysis, hydrolysis, aminolysis, and alcoholysis [8–10]. However, these techniques sometimes involve the use of hazardous solvents, high temperatures, or lengthy reaction times, which lessens their viability from an economic and environmental standpoint [9,11]. The innovations are not only focused on the PU recycling process but also on other sustainable strategies. They include innovations in sustainable plastics, such as a new biocompatible and biodegradable polyurethane elastomer with self-healing properties [12], recyclable and degradable gelatin glycerohydrogel [13]. Despite the various technically feasible methods of polyurethane recycling and sustainable products, the current recycling rate is below 10%, with the majority ending up in landfills [14].

The emergence of deep eutectic solvents (DES) as environmentally friendly solvents offers a novel approach to addressing the issues associated with polyurethane degradation. DES are synthesized through the interaction of a hydrogen bond donor (HBD) and a hydrogen bond acceptor (HBA) at defined molar ratios, resulting in distinctive characteristics including low toxicity, elevated solubility, and diminished volatility [15–17]. The aforementioned characteristics significantly augment their applicability in chemical recycling processes.

Ultrasonic irradiation represents an advanced methodology that has garnered significant interest due to its capacity to accelerate degradation processes. Ultrasonic waves facilitate the generation of cavitation bubbles, which induce localized high temperatures and pressures, thereby markedly improving the degradation of polymer chains in the presence of DES [18]. A combination of DES and this method facilitates the recovery of valuable monomers while promoting a more environmentally sustainable approach to addressing polyurethane waste. Thermoplastic PU, which consists of o-toluidine and polycarbonate diol (PCDL), was utilized in this study.

Recent advancements in plastic waste management highlight the significance of integrating green chemistry principles into recycling technologies. Many studies have highlighted the necessity of sustainable degradation solutions that reduce environmental impact while facilitating the effective recovery of valuable monomers [19]. Current research conducted by Zhang *et al.* explores novel solvent systems, including DES and their role in enhancing the depolymerization of PU under milder reaction conditions [14]. The recent advancements highlight the importance of investigating environmentally sustainable and scalable methods, such as DES-assisted degradation, especially when integrated with physical enhancements like ultrasound to enhance degradation rates and optimize material recovery.

This study investigated the effect of ultrasonic irradiation at different temperatures on the PU degradation in the DES. Degradation of PU was investigated through the o-toluidine structure identification using 1H NMR spectra. The research aims to enhance sustainable waste management strategies for polyurethane materials, thereby advancing polymer recycling and addressing critical environmental issues.

EXPERIMENTAL

Materials

The high flow thermoplastic polyurethane (TPU) was obtained from Revlogi Materials Solutions Sdn Bhd (Malaysia). Urea and choline chloride (ChCl) were obtained from Sigma-Aldrich, Germany. Acetone was obtained from HMBG Chemical, Germany. The solvent used for NMR was deuterated dimethyl sulfoxide (DMSO-d_6) obtained from Sigma Aldrich, Germany.

Preparation of DES

ChCl and urea were mixed with a ratio of 1:2 at 70 °C for 2 h until a clear, transparent, and homogeneous mixing liquid was obtained.

Physical Properties of DES

Density

The pycnometer was used to determine the density of the DES components (ρ_L), which was calculated by Eq. (1) [20].

$$\rho_L = \frac{m_L}{m_{H2O}} \cdot \rho_{H2O} \qquad (1)$$

where m_L is the mass of liquid, m_{H2O} is the mass of water, and ρ_{H2O} is the density of water. The measurement was conducted in duplicate.

The average absolute deviation (AAD) was calculated for each set of measurements by Eq. (2):

$$AAD = \frac{1}{N}\sum_{I=1}^{N}\frac{|x_i - \bar{x}|}{x_i} \qquad (2)$$

where n is the number of runs for one experimental condition, N is the total number of runs, x_i is the data for one experimental condition and $\bar{x}$ is the average for one experimental condition.

Viscosity

The viscosity of the DES was assessed by a regular viscosity (RV) spindle viscometer (Brookfield, United Kingdom) through the rotation of a spindle that was submerged in the liquid medium. The viscosity values were computed directly through the application of conversion factors derived from the scale readings corresponding to the specific rotational speeds [21]. The measurement was conducted in duplicate.

Degradation of PU in DES with and without a sonication-aided system

In this experiment, 25 g of the DES solution and 2.5 g of the PU were mixed in a 100 ml beaker. Then, the degradation took place at 130, 140, and 150 °C for 2 hours. The sample was subjected to the post-treatment process.

An ultrasonic bath (Scientz, SB-5200DTD, Ningbo, China) was used to perform sonication at a frequency of 40 kHz and an ultrasonic input power of 250 W. The degrading process was conducted at 130, 140, and 150 °C for 2 hours. Then, the sample was prepared for the post-treatment process.

Post-treatment process after degradation of PU with and without a sonication-aided system

The degradation product was processed to separate the unreacted PU, DES, and the degradation product, namely o-toluidine. The mixture was cooled down to room temperature before being filtered with a 125 mm Whatman filter. The remaining unreacted PU made up the filter cake (1), while the DES and o-toluidine made up the majority of the filtrate (1).

Initially, an excess of distilled water was introduced into the filtrate (1) to separate o-toluidine (insoluble in water) and recover the DES (soluble in water) from the filtrate solution. This process was repeated once again to get filter cake (2) and filtrate (2). The filter cake (2) was then dried at 70 °C and measured as *W1*. The filtrate (2) was recycled using a vacuum rotary evaporator at 60 °C and 100 Pa to recover the DES.

The filter cake (1) was washed with distilled water to dissolve the remaining DES. This part of the DES was also recovered using the vacuum rotational evaporator at 60 °C. The clean filter cake (1) was completely dissolved in acetone to recover the unreacted PU. The filter cake (3) and filtrate (3) were obtained after the third filtering. The filtrate (3) mostly contained acetone and other possible degradation products, while the filter cake (3) contained the unreacted PU. A vacuum rotary evaporator was used to eliminate acetone from the filtrate (3) at 35 °C, and the unreacted PU was dried and measured as *W2*. The filter cake (3), which contained the unreacted PU, was then dried and weighed as *W3*. Figure 1 shows the overall process for the post-treatment process for the degradation of PU. Based on this posttreatment process, *W1* and *W3* were identified as o-toluidine and unreacted PU, respectively. The degradation rate was calculated by Eq. (3):

$$Degradation\,rate = \frac{W0 - W3}{W0} \cdot 100\% \qquad (3)$$

where *W0* is the initial weight of PU and *W3* is the weight of PU that was not degraded.

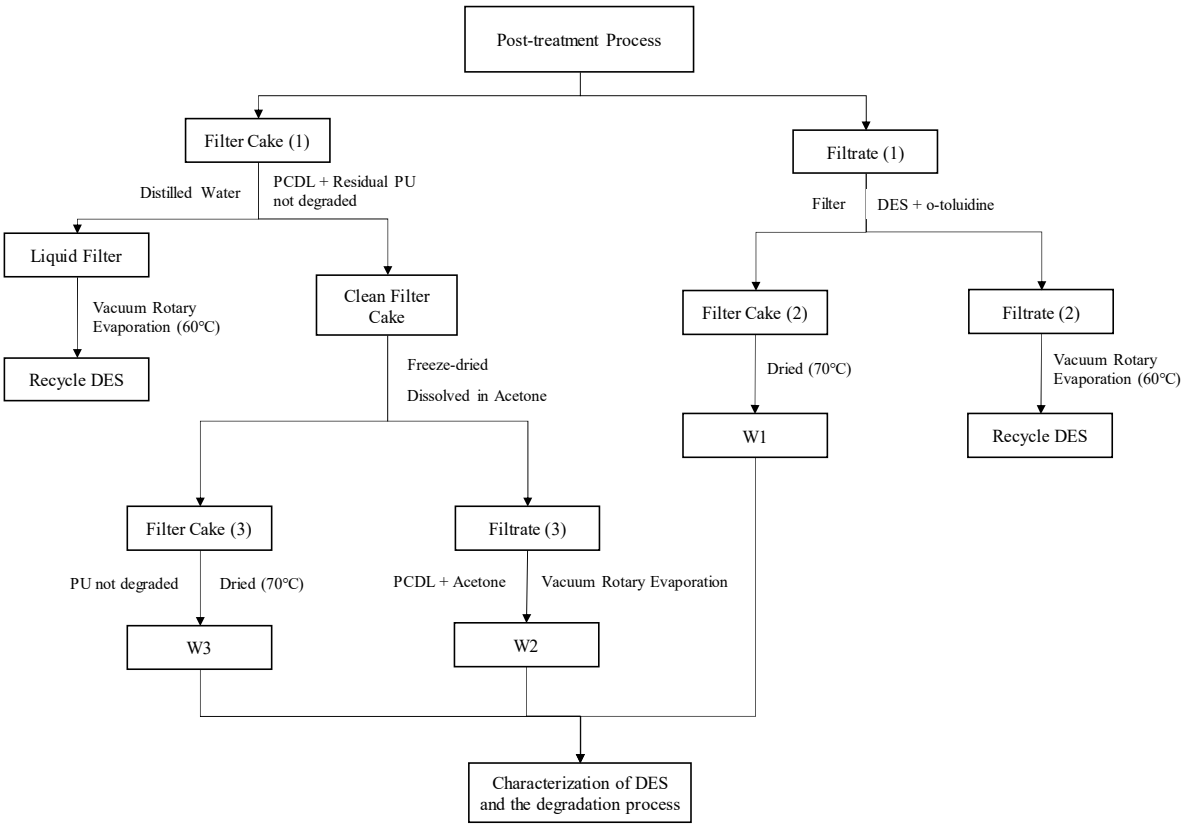

Figure 1. The overall post-treatment process for the degradation of PU.

Gel Permeation Chromatography

The molecular weight distribution of the raw polyurethane and the degradation products with and without sonication was analyzed using Gel Permeation Chromatography (GPC) (Agilent 1260 Infinity II LC, CA, USA). Tetrahydrofuran (THF) was used as the eluent at a concentration of 1.0 g/L and a constant flow rate of 0.6mL/min. The sample solution was prepared at a concentration of 1.0 g/L, and an injection volume of 50.0 µL was used for each run with a flow rate of 0.6 mL/min. Detection was carried out using a refractive index detector (RID1A, Refractive Index Signal). The delay volume was set to 0.0 mL, and data acquisition was performed at an interval of 0.21 seconds.

Characterization of DES and the degradation product

FT-IR spectra of the DES solvent and its degradation products were obtained using a Perkin-Elmer (USA) spectrometer within the wave-number range of 4000-400 cm^{-1} with a resolution of 4 cm^{-1}.

To study the structure of degradation products, 1H NMR spectra were recorded using an AVANCE 3TM spectrometer (Bruker, Switzerland) operating at a frequency of 400 MHz. The solvent employed for NMR analysis was deuterated dimethyl sulfoxide (DMSO-d_6).

RESULTS AND DISCUSSION

Physical Properties of DES

Key physical properties of the DES as an efficient solvent are viscosity and density. Table 1 shows the physical properties of ChCl and urea in comparison with the previous study.

The measured density of the synthesized DES was determined to be 1.19 ± 0.01 g/cm³, which was comparable with the literature value of 1.24 g/mL [18]. ChCl acts as a hydrogen bond acceptor, whereas urea acts as a hydrogen bond donor. The high density of this DES arises from the strong hydrogen-bonding interactions between ChCl and urea, leading to a tight molecular structure [22,23]. These interactions decrease intermolecular distances, resulting in a compact and cohesive solvent structure. The strong hydrogen-bonding environment of the ChCl-urea DES boosts its efficacy in polymer solubilization [14]. The density of the DES aligns closely with literature values for comparable DES formulations, thereby confirming the reliability of this property in promoting degradation reactions.

The synthesized DES had a viscosity of 755 ± 0.14 cP, comparable with the literature value of 750 cP [17]. Viscosity is another key physical parameter that impacts polymer degradation in solvent systems. The solvent's viscosity affects its flow and interaction rate with polyurethanes. The viscosity found is noticeably altered by a strong hydrogen-bonding network between ChCl, an ionic chemical, and urea, a polar molecule [24]. These component interactions raise viscosity by increasing internal friction [25]. ChCl ionic properties improve viscosity by slowing solvent molecules and generating a structured fluid network. ChCl and urea mixed at this ratio provide a viscosity greater than expected from their separate components, indicating strong intermolecular interactions. Lower viscosity usually allows for greater mixing and quicker solute diffusion, which may greatly speed up chemical processes in the solvent.

Table 1. Properties of the DES.

Properties	This work	Literature Review	Ref.
Density, ρ (g cm^{-3})	1.19 ± 0.01	1.24	[15]
Viscosity, μ (cP)	755 ± 0.14	750	[41]

Characterization of the DES and degradation products

The Fourier Transform Infrared (FTIR) spectra were recorded to identify significant functional groups present in the DES obtained from ChCl and urea are shown in Figure 2(a). The vibrational bands observed at 3329 cm^{-1} correspond to the symmetric stretching mode of the amide functional group (-NH) present in urea [26]. The vibrational band observed at 3203 cm^{-1} is attributed to the O-H stretching modes associated with hydroxyl groups present in ChCl. This observation suggests the presence of a robust hydrogen bonding interaction between the constituent components. The peaks rarely visible at 3000 cm^{-1} were attributed to the CH stretching vibrations of alkyl groups present in ChCl, indicating its role in the structural integrity of the solvent [27]. Additionally, the peak at 958 cm^{-1} is associated with C-N stretching vibrations linked to the quaternary ammonium group of ChCl, reflecting the ionic characteristics of the deep eutectic solvent. The observed peaks at 1670 cm^{-1} and 1618 cm^{-1} are attributed to the urea functional group [27]. The spectral bands observed at 1670 cm^{-1} are indicative of C=O stretching associated with amide functional groups, while the band at 1618 cm^{-1} corresponds to N-H scissoring vibrations. The observed peaks validate the presence of carbonyl and amine groups in urea, which engage with ChCl to enhance the stability of the deep eutectic solvent structure.

PU is a high polymer characterized by a repetitive urethane bond (-NHCOO-), which is synthesized through the polymerization process involving isocyanates and polyols. Figure 2(b) shows the FTIR spectrum of PU. A prominent peak observed at 3350 cm^{-1} corresponds to N-H stretching. The observed peak at 1732 cm^{-1} was attributed to the ester C=O. The additional peak observed at 1602 cm^{-1} corresponds to C=C vibrations within benzene rings. Soft segment polyether polyols exhibit the C-H stretching vibration at 2967 cm^{-1} [28,29].

Degradation product

The influence of temperature on the degradation rates of PU was examined under two different conditions: without sonication and with sonocatalytic assistance. Four distinct temperatures, 130, 140, 150, and 160 ℃, were utilized, and the experiments were conducted for two hours. Figure 3 shows the effect of the temperature on the degradation of PU.

Without sonication, the degradation rate of PU was measured at 27.41 ± 0.02% at 130 °C. When the temperature increased to 140 °C, the degradation rate more than doubled, reaching 52.12 ± 0.07%. Further elevation to 150°C resulted in a degradation rate of 58.51 ± 0.04%. This shows that longer reaction time and higher temperature are important to achieve complete breakdown of the polymer. These findings suggest that thermal conditions significantly influence the polymer breakdown, as higher temperatures enhance molecular kinetic energy, increasing the probability of chemical bond disruption [30]. The urethane linkages, which are the characteristic backbone of PU, become more susceptible to cleavage as the provided energy surpasses the activation threshold necessary for bond rupture [31]. Moreover, increased temperatures improve the interaction between the DES and the PU matrix, enhancing solvent solubility and diffusion. This process facilitates deeper penetration, which promotes chemical structure breakdown, primarily targeting urethane and urea bonds crucial for polymer stability [10].

Under sonication-assisted degradation, the degradation rates were significantly higher. At 130 °C, the degradation rate reached a 19.79 ± 1.75% decrease in

7.62% compared with the process without sonication assistance. When the temperature increased to 140 °C, the degradation rate rose to 54.79 ± 0.02% and at 150 °C, it further escalated to 63.71 ± 0.03%. A clear improvement in plastic degradation was also observed in the study by Attallah *et al.* [32]. In this research, the biodepolymerization of PET showed an increase of around 16% (w/w) in monomer conversion when sonication was applied together with enzymatic treatment, compared to the process without using sonication [32]. This method can be useful for improving the biodegradation process of plastics in more eco-friendly conditions.

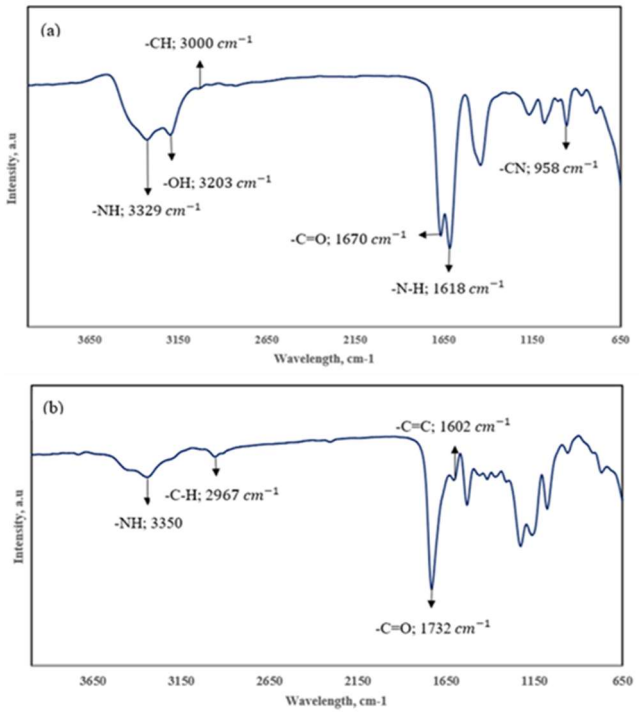

Figure 2. The FTIR spectra: a) DES and b) PU.

The higher efficiency observed in sonication-aided degradation can be attributed to the combined effects of ultrasonic irradiation and elevated thermal conditions. The key mechanism contributing to this enhancement is cavitation, where rapid formation and implosion of microbubbles generate localized hot spots with extreme temperature and pressure [18,33,34]. These localized conditions intensify the degradation process by accelerating polymer bond rupture beyond what is achievable with thermal degradation alone.

Additionally, ultrasonic waves decrease solvent viscosity, which further optimizes mass transfer characteristics [31]. A solvent with lower viscosity allows for better penetration and interaction between DES and the PU matrix, improving solvation and degradation. This enhanced mass transfer ensures a uniform distribution of reactants, leading to more efficient degradation.

Furthermore, ultrasonic waves intensify molecular motion, promoting more successful collisions between reactant molecules. These amplified interactions facilitate essential chemical reactions, accelerating the cleavage of weaker bonds and leading to the generation of smaller molecular fragments that are more prone to further degradation [35].

Overall, the results demonstrate that both thermal conditions and ultrasonic assistance play crucial roles in polyurethane degradation. The increase in kinetic energy at elevated temperatures enhances polymer bond disruption and solvent interactions, leading to higher degradation rates. In conclusion, the presence of ultrasonic irradiation significantly amplifies these effects through cavitation, enhanced mass transfer, and increased reaction rates. The synergistic combination of temperature and ultrasonic assistance presents a promising approach to optimizing PU degradation, offering insights into improved recycling methodologies for PU waste.

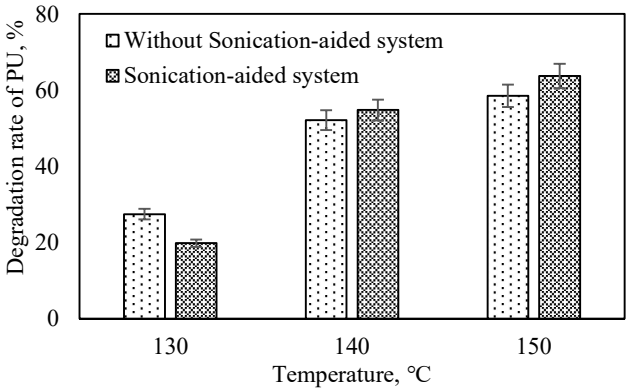

Figure 3. Effect of temperature on the degradation of PU in the DES.

Characterization of the Degradation product

Figure 4 shows the functional groups identified in the *W3*, consisting of the unreacted PU facilitated with and without a sonication effect.

The analysis reveals multiple peaks, with significant peaks identified at 3424 cm^{-1} and 3327 cm^{-1} were attributed to the amine (-NH) groups. The peaks observed at 1676 cm^{-1}, 1699 and 1732 cm^{-1} correspond to the presence of C=O functional groups, while the peaks at 1089 cm^{-1} and 1084 cm^{-1} are associated with the C-O group [36]. Furthermore, the observed peaks at 769 cm^{-1} indicate the presence of C-H functional groups. The results indicate that the functional groups present in the original PU have transformed into new groups within the residual material, thereby demonstrating the effective degradation of urethane bonds throughout the degradation process. The transformation resulted in the generation of smaller molecular entities, such as alcohols, ethers, and carboxylic acids, while retaining certain aromatic compounds [37]. The sonication-assisted degradation process effectively modifies the molecular structure of PU by the existence of a new group at 1236 cm^{-1}.

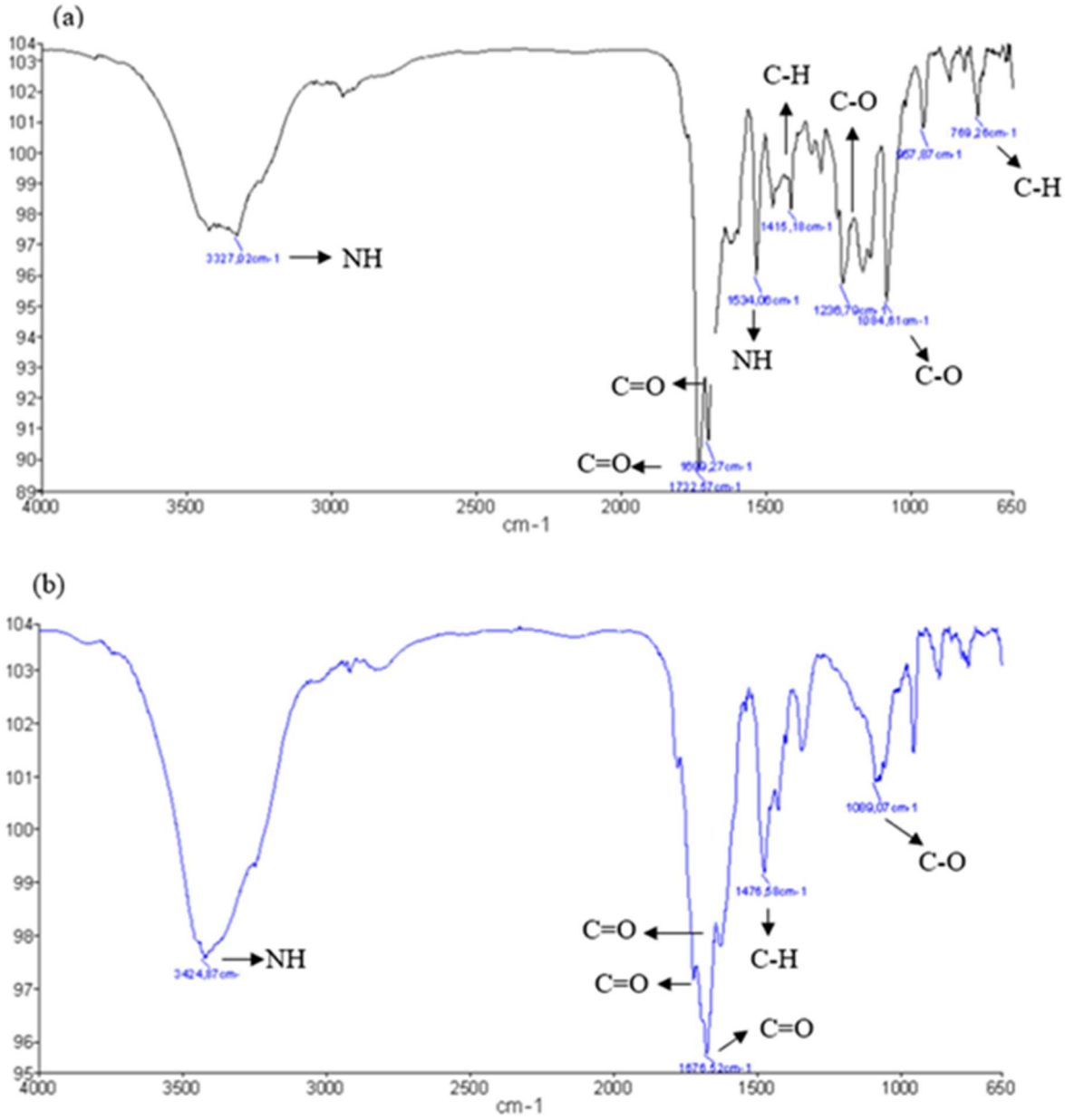

Figure 4. FTIR analysis of the unreacted PU (W3) (a) without and (b) with sonication.

Gel Permeation Chromatography

Gel Permeation Chromatography (GPC) was used to determine the molecular weight distribution of the raw PU before the degradation process. The chromatogram presented in Figure 5 displays a clear monomodal distribution, suggesting a consistent molecular weight distribution throughout the sample. The primary elution peak is observed at an elution volume ranging from 6.5 to 7.5 mL, which is indicative of high molecular weight polymer fractions. The number average molecular weight (*Mn*) was determined to be 5.985×10³ g/mol, while the weight average molecular weight (*Mw*) was found to be 9.080×10⁴ g/mol, resulting in a polydispersity index of approximately 15.17. The observed high PDI indicates a wide molecular weight distribution, which is characteristic of PU produced through step-growth polymerization processes, where the regulation of chain length is not as precise as in living polymerization methods [38]. The tailing observed at elevated elution volumes 9 to 11 mL suggests the presence of lower molecular weight species or oligomers, which may include residual monomers or partially polymerized chains [38,39].

Figure 5 displays the GPC chromatogram of the degradation product, *W1*, which was derived from the degradation of PU in DES without the aid of sonication. The chromatographic profile indicates a narrower distribution of lower molecular weight species when compared to the raw polyurethane and the sonication-assisted degradation. The main peak is observed at an elution volume ranging from 8.5 to 9.5 mL, indicating the presence of smaller polymer fragments or monomeric degradation products. The *Mn* was determined to be 2.74×10² g/mol, while the *Mw* was measured at 6.47×10² g/mol, leading to a PDI of 2.36. This suggests a moderate degree of polymer chain scission and a more uniform distribution of molecular weight in comparison to the original polyurethane, with a value of 15.17. The chromatogram displays a distinct single peak,

accompanied by minimal signals at low elution volumes, indicating a restricted degradation into very low molecular weight compounds or oligomers [40]. The transition from the original high molecular weight region validates the occurrence of degradation. The tailing observed at elevated elution volumes 9 to 11 mL suggests the presence of lower molecular weight species or oligomers, which may include residual monomers or partially polymerized chains.

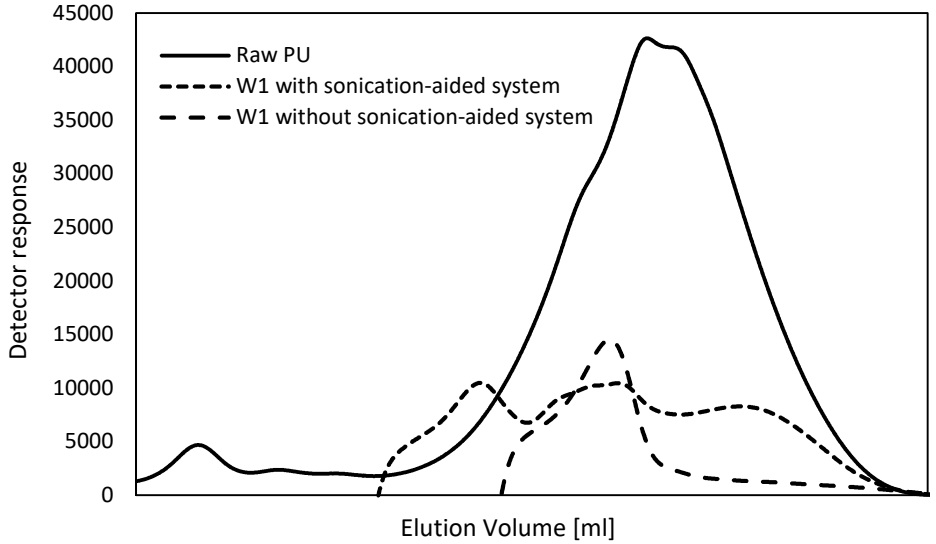

Figure 5. GPC traces recorded with the RID1A: a) raw PU, b) W1 without the sonication-aided system, and c) W1 with the sonication-aided system.

Table 2. GPC data for the molecular determination.

Sample	Raw PU	*W1* without the sonication-aided system	*W1* with the sonication-aided system
Number average molecular weight, *Mn* (g/mol)	5.99×10^3	2.74×10^2	6.29×10^2
Weight average molecular weight, *Mw* (g/mol)	9.08×10^4	6.47×10^2	3.37×10^3
Z-average molecular weight, *Mz* (g/mol)	2.13×10^5	2.83×10^3	1.03×10^4
Polydispersity index, PDI	15.17	2.36	5.36

W1 is identified as o-toluidine calcuted using posttreatment method described in Figure 1.

The chromatogram of *W1* with a sonication-aided system exhibits a notable shift toward elevated elution volumes in comparison to raw polyurethane, signifying a considerable decrease in molecular weight. The *Mn* of the *W1* product was determined to be 6.29×10^2 g/mol, while the *Mw* was found to be 3.37×10^3 g/mol, leading to a calculated PDI of 5.36. This indicates a significant reduction from the initial *Mn* and *Mw* values of 5.98×10^3 g/mol and 9.08×10^4 g/mol, respectively. The observed lower molecular weights and narrower peak profiles indicate significant depolymerization of the polyurethane backbone, thereby demonstrating the effectiveness of sonication-assisted DES treatment in the breakdown of polymer chains. The chromatographic profile displays multiple distinct peaks within the range of 7.8 to 9.5 mL, which are associated with lower molecular weight degradation products. The lack of a notable peak in the lower elution volume range 6 to 7 mL, where the high molecular weight polymer was previously identified, reinforces the successful degradation of the original polymer structure. The detection of o-toluidine, an aromatic amine that arises from the degradation of urethane linkages, aligns with earlier findings regarding the depolymerization of polyurethane. The reduction in molecular weight due to sonication demonstrates the combined effects of cavitation and localized high-energy zones in improving DES-based depolymerization [41].

Chemical structure analysis using 1H NMR

The structure of the degradation product was analyzed using NMR analysis to provide valuable insights into the chemical composition and structure during the process. Figure 6 shows the 1H NMR spectra.

The peaks at 5.5 ppm were assigned to the NH_2 group, while the peaks at 2.0-2.1 ppm were assigned to the CH_3 group. PU found that the chemical shifts of the groups are 8.3 ppm (NH), 5.9-6.7 ppm (aromatic), 2.2-2.6 ppm (CH), 1.1 ppm (CH_3) [29]. The degradation of PU using a DES formulated from ChCl and urea was examined to assess its efficacy in breaking the polymer structure. Figure 7 illustrates the breakage of urethane (-NH-COO-) connections, resulting in the generation of lower molecular weight fragments known as o-toluidine and PCDL.

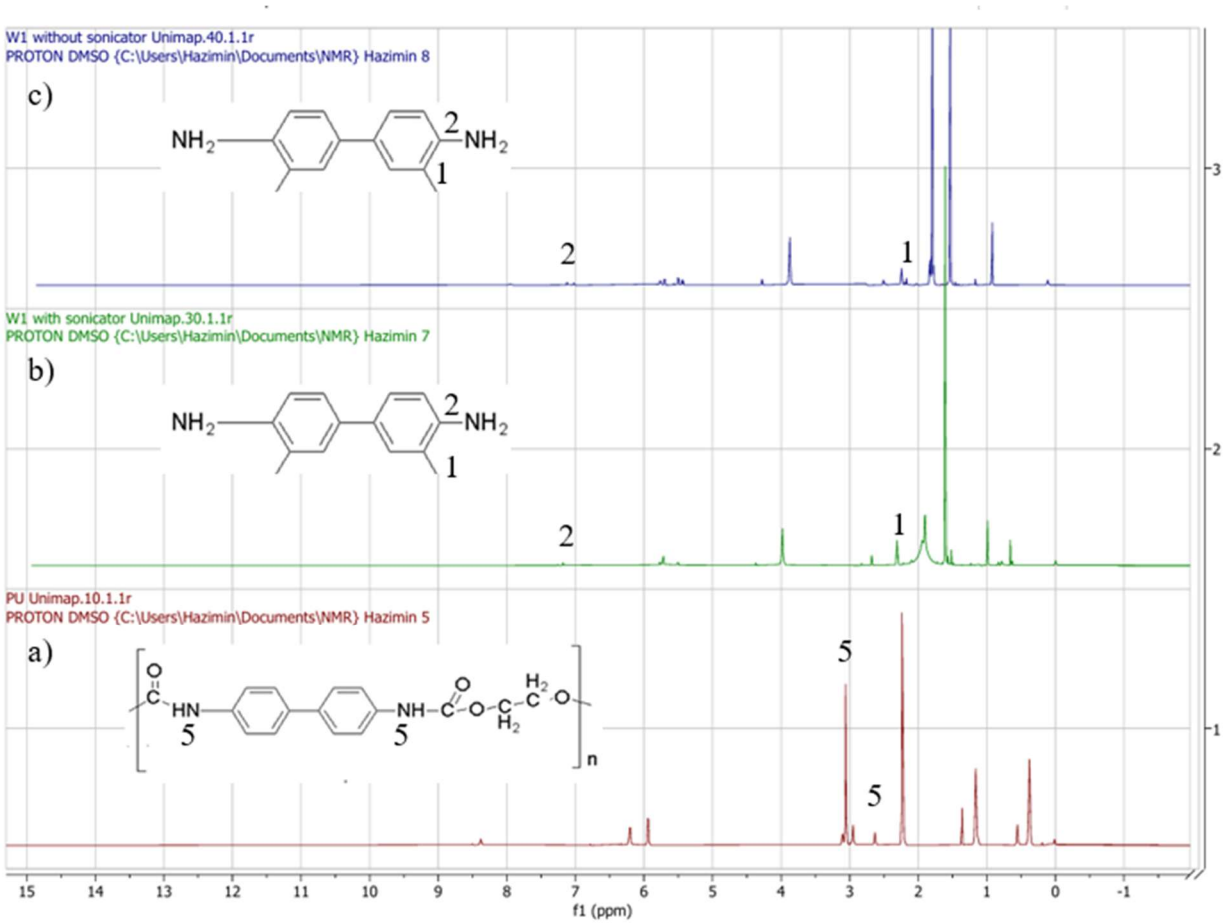

Figure 6. The 1H NMR spectrum of the W1: a) raw PU, b) W1 in the sonication-aided system, and c) W1 without the sonication-aided system. The solvent used for NMR was DMSO-d_6.

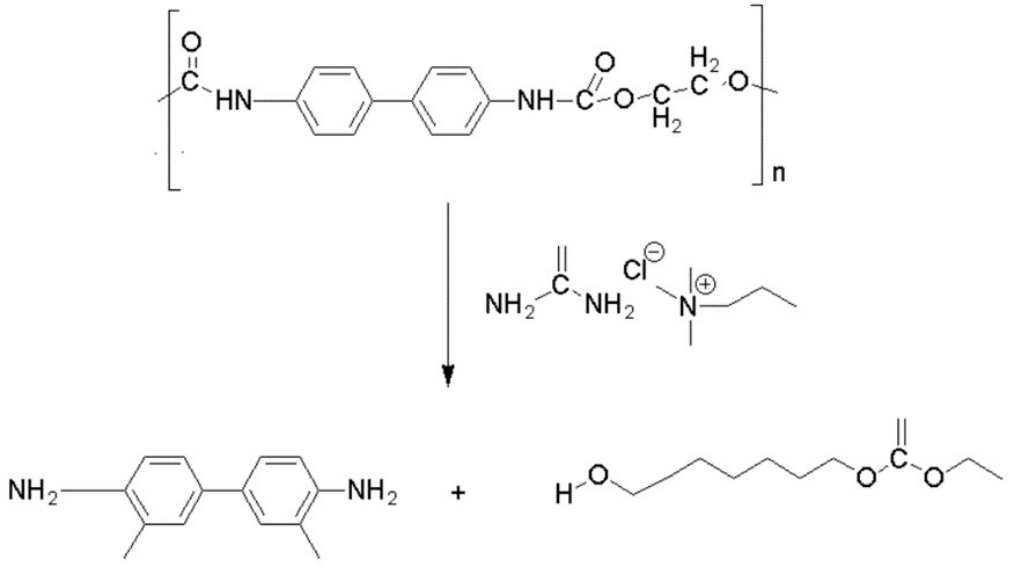

Figure 7. The degradation route of the PU elastomer.

In this study, the *W1* or o-toluidine structure was used for the structure identification after the degradation process, as shown in Figure 7. The DES medium promotes polyurethane breakdown via nucleophilic assault and hydrogen bonding interactions. The chloride anion in ChCl, in conjunction with urea, establishes strong hydrogen bonds with the carbonyl groups of urethane links, enhancing their vulnerability to nucleophilic cleavage [42]. The existence of protonated amines ($-NH_3^+$) in the degradation products indicates that the process occurs via a partial hydrolysis mechanism, whereby urea facilitates the breaking of urethane bonds. The release of an aromatic diamine fragment signifies the degradation of the hard segment of polyurethane. This indicates that the

degradation process efficiently severs the bonds linking the diisocyanate-derived segments of the polymer. The existence of polyol degradation products with hydroxyl (-OH) and carbonate (-COO-) functionalities indicates that the soft section of PU also experiences cleavage. The identified structures suggest hydrolysis or aminolysis of ester and carbonate moieties within the polymer backbone.

DESs provide an environmentally friendly option for the solubilization and depolymerization of polyurethane, owing to their capacity to dissolve and engage with polymeric structures. ChCl and urea create a eutectic combination characterized by robust hydrogen bond donor-acceptor interactions that enhance the degradation process [43]. In contrast to traditional aggressive chemical treatments, DES-based degradation provides a more eco-friendly method with less toxicity. The capacity of DES to decompose PU into its precursor constituents indicates prospective uses in polyurethane recycling and waste management. The extraction of diamines and polyols from polyurethane degradation facilitates their reutilization in polymer synthesis, hence reducing the need for fresh raw materials. Moreover, the moderate reaction conditions of DES-based degradation reduce the generation of toxic by-products, making it a sustainable choice for plastic waste processing.

CONCLUSION

This research effectively illustrates the potential benefits of deep eutectic solvents (DES) combined with ultrasonic irradiation in enhancing polyurethane (PU) degradation. The results indicate a remarkable increase in degradation efficiency, with rates rising from 19.79 ± 1.75% at 130 °C to 63.71 ± 0.03% at 150 °C under ultrasonic assistance. In contrast, degradation rates without sonication only reached a maximum of 27.41 ± 0.02% to 58.51 ± 0.04% under similar temperature conditions. The breakdown of PU polymer chains is greatly accelerated by the application of ultrasonic vibrations, which promote the formation of cavitation bubbles and localized areas of high temperature and pressure. This process marks a substantial improvement in chemical recycling techniques, especially when combined with the beneficial properties of DES, such as their high solubility for PU and low toxicity. PU degradation but also provided insight into ways to recycle polyurethane waste into valuable products. Overall, this research highlights the synergistic benefits of employing DES and ultrasonic irradiation, presenting a promising strategy for addressing the environmental issues caused by persistent PU waste while paving the way for more sustainable waste management practices. Future studies may explore the higher temperature and longer reaction time to achieve the maximum degradation rate.

ACKNOWLEDGEMENT

The financial support provided by the Ministry of Higher Education Malaysia through the Fundamental Research Grant Scheme (FRGS), reference no. FRGS/1/2023/TK05/UNIMAP/02/12, and the International Polyurethane Technology Foundation, Japan, is greatly appreciated.

REFERENCES

[1] R. Kaur, P. Singh, S. Tanwar, G. Varshney, S. Yadav, Macromol. 2 (2022) 284-314. https://doi.org/10.3390/macromol2030019.
[2] A. Das, P. Mahanwar, Adv. Ind. Eng. Polym. Res. 3 (2020) 93-101. https://doi.org/10.1016/j.aiepr.2020.07.002.
[3] A. Delavarde, G. Savin, P. Derkenne, M. Boursier, R. Morales-Cerrada, B. Nottelet, J. Pinaud, Prog. Polym. Sci. 151 (2024) 101805. https://doi.org/10.1016/j.progpolymsci.2024.101805.
[4] G. Yeligbayeva, M. Khaldun, A.A. Alfergani, Zh. Tleugaliyeva, A. Karabayeva, L. Bekbayeva, D. Zhetpisbay, N. Shadin, Z. Atabekova, Complex Use Miner. Resour. 331 (2024) 21-41. https://doi.org/10.31643/2024/6445.36.
[5] M. Ghezal, A. Moussa, I.B. Marzoug, A. El-Achari, C. Campagne, F. Sakli. Chem. Ind. Chem. Eng. Q. 31(2025) 95-104. https://doi.org/10.2298/CICEQ240202017G.
[6] X. Gao, J. Su, C. Xu, S. Cao, S. Gu, W. Sun, Z. You, ACS Nano. 18 (2024) 17913-17923. https://doi.org/10.1021/acsnano.4c04455.
[7] A. Kemona, M. Piotrowska, Polymers 12 (2020) 1752. https://doi.org/10.3390/polym12081752.
[8] M. Nees, M. Adeel, L. Pazdur, M. Porters, C.M. L. Vande Velde, P. Billen, ACS Omega. (2024) 4c04671. https://doi.org/10.1021/acsomega.4c04671.
[9] G. Rossignolo, G. Malucelli, A. Lorenzetti, Green Chem. 26 (2023) 1132-1152. https://doi.org/10.1039/d3gc02091f.
[10] J. Drzeżdżon, J. Datta, Waste Manag. 198, (2025), 21-45. https://org/10.1016/j.wasman.2025.02.043.
[11] H. Zhang, X. Cui, H. Wang, Y. Wang, Y. Zhao, H. Ma, L. Chai, Y. Wang, X. Hou, T. Deng, Polym. Degrad. Stab. 181 (2020) 109342. https://doi.org/10.1016/j.polymdegradstab.2020.109342.
[12] A. Shen , H. Xuan, Y. Jia, S. Gu, R. E. Neisiany,W.Shu, W.Sun, Z.You, Chem. Eng. J. 491(2024) 151896 https://doi.org/10.1016/j.cej.2024.151896.
[13] S. Jiang, Y. Wang, M. Tian, H. Zhang, R. Wang, H. Yan, H.Tan, R.E.Neisiany, W. Sun, Z. You, Chem. Eng. J. 504 (2025) 158881. https://doi.org/10.1016/j.cej.2024.158881.
[14] A. Karrech, H. Zhou, Circ. Econ. 4 (2025) 100129. https://doi.org/10.1016/j.cec.2025.100129.
[15] T. El Achkar, H. Greige-Gerges, S. Fourmentin, Environ. Chem. Lett. 19 (2021) 3397-3408. https://doi.org/10.1007/s10311-021-01225-8.
[16] S.A. Jen, N.M.A. Nik Daud, M.S. Md Sarip, K.A.F. Kamal Ramlee, A.R. Abu Bakar, Mohd M.A. Zainudin, K.A. Jantan, G. Siomara, J. Adv. Res. Micro Nano Eng. 35 (2025) 111-122. https://doi.org/10.37934/armne.35.1.111122.
[17] A.M. Abdul Rahman, A.R. Abu Bakar, A.Q. Yee, M.A. Mohd Zainudin, N.M.A. Nik Daud, A.A. Nagoor

Gunny, M.S. Md Sarip, R.V. Perona, N.H. Khairuddin, RSC Adv. 15 (2025) 4296-4321. https://doi.org/10.1039/D5RA00097A.
[18] S. Manickam, D.C. Boffito, E.M.M. Flores, J.M. Leveque, R. Pflieger, B.G. Pollet, M. Ashokkumar, Ultrason. Sonochem. 99 (2023) 106540. https://doi.org/10.1016/j.ultsonch.2023.106540.
[19] M.B. Johansen, B.S. Donslund, S.K. Kristensen, A.T. Lindhardt, T. Skrydstrup, ACS Sustain. Chem. Eng. 10 (2022) 11191-11202. https://doi.org/10.1021/acssuschemeng.2c02797.
[20] M. Viana, P. Jouannin, C. Pontier, D. Chulia, Talanta 57 (2002) 583-593. https://doi.org/10.1016/S0039-9140(02)00058-9.
[21] A.P. Abbott, R.C. Harris, K.S. Ryder, C. D'Agostino, L.F. Gladden, M.D. Mantle, Green Chem. 13 (2011) 82-90. https://doi.org/10.1039/C0GC00395F.
[22] K.A. Omar, R. Sadeghi, J. Mol. Liq. 360 (2022) 119524. https://doi.org/10.1016/j.molliq.2022.119524.
[23] W. Wang, Y. Xu, B. Zhu, H. Ge, S. Wang, B. Li, H. Xu, Bioresour. Technol. 385 (2023) 129401 https://doi.org/10.1016/j.biortech.2023.129401.
[24] R.J. Isaifan, A. Amhamed, Adv. Chem. 2018 (2018) 1-6. https://doi.org/10.1155/2018/2675659.
[25] H. Fang, K. Ni, J. Wu, J. Li, L. Huang, D. Reible, Int. J. Sediment Res. 34 (2019) 8-13. https://doi.org/10.1016/j.ijsrc.2018.10.008.
[26] C. Du, B. Zhao, X.B. Chen, N. Birbilis, H. Yang, Sci. Rep. 6 (2016) 1-14. https://doi.org/10.1038/srep29225.
[27] T. Jurić, D. Uka, B.B. Holló, B. Jović, B. Kordić, B.M. Popović, J. Mol. Liq. 343 (2021) 116968. https://doi.org/10.1016/j.molliq.2021.116968.
[28] D.J. Mohamed, N.J. Hadi, Z.K. Alobad, IOP Conf. Ser. Mater. Sci. Eng., 1094 (2021) 012157. https://doi.org/10.1088/1757-899x/1094/1/012157.
[29] A. Reghunadhan, S. Thomas, Elsevier Inc. (2017) https://doi.org/10.1016/B978-0-12-804039-3.00001-4.
[30] G.W. Coates,Y.D.Y.L. Getzler, Nat. Rev. Mater. 5 (2020) 501-516. https://doi.org/10.1038/s41578-020-0190-4.
[31] Y. Elhamarnah, M. AlRasheedi, W. AlMarri, A. AlBadr, A. AlMalki, N. Mohamed, I. Fatima, M. Nasser, H. Qiblawey, Materials 15 (2022) 4027. https://doi.org/10.3390/ma15114027.
[32] O. A. Attallah, M. Azeem, E. Nikolaivits, E. Topakas, M. B. Fournet, Polymers (Basel), 14 (2022) 1-15. https://doi.org/10.3390/polym14010109.
[33] Y.H. Hsieh, Y. Li, Z. Pan, Z. Chen, J. Lu, J. Yuan, Z. Zhu, Ultrason. Sonochem. 63 (2019) 104915. https://doi.org/10.1016/j.ultsonch.2019.104915.
[34] J.K. Yan, Y.Y. Wang, H.L. Ma, Z.B. Wang, Ultrason. Sonochem. 29 (2016) 251-257. https://doi.org/10.1016/j.ultsonch.2015.10.005.
[35] A. Taha, E. Ahmed, A. Ismaiel, M. Ashokkumar, X. Xu, S. Pan, H. Hu, Trends Food Sci. Technol. 105 (2020) 363-377. https://doi.org/10.1016/j.tifs.2020.09.024.
[36] S. Xu, E. Liu, R. Gao, H. Du, Z. Chen, Q. Sun, J. Anal. Appl. Pyrolysis. 177 (2024) 106301. https://doi.org/10.1016/j.jaap.2023.106301.
[37] Y. Wang, H. Song, H. Ge, J. Wang, Y. Wang, S. Jia, T. Deng, J. Cleaner Prod. 176 (2018) 873-879. https://doi.org/10.1016/j.jclepro.2017.12.046.
[38] J.U. Izunobi, C.L. Higginbotham, J. Chem. Educ. 88 (2011) 1098-1104. https://doi.org/10.1021/jacsau.5c00496.
[39] L.V. Belleghem, R. Dirix, R.D. Oliveira, J. Wery, D. Sakellariou, N.V. Velthoven, D.D. Vos, JACS Au. 5 (2025) 3444-3452. https://doi.org/10.1021/jacsau.5c00496.
[40] J. Ma, G. Sun, D. Sun, F. Yu, M. Hu, T. Lu, Constr. Build. Mater. 278 (2021) 122386. https://doi.org/10.1016/j.conbuildmat.2021.122386.
[41] T. Singh, A. Dvivedi, A. Shanu, P. Dixit, J. Mater. Process. Technol. 293 (2020) 117084. https://doi.org/10.1016/j.jmatprotec.2021.117084.
[42] S. Shafique, A.S. Belousov, R. Rashid, I. Shafiq, K.H.H. Aziz, N. Riaz, M. Saqib Khan, A. Shaheen, M. Ishaq, P. Akhter, J. Mol. Liq. 419 (2024) 126769. https://doi.org/10.1016/j.molliq.2024.126769.
[43] J.P. Wasylka, M. Guardia, V. Andruch, M. Vilková, Microchem. J. 159 (2020) 105539 https://doi.org/10.1016/j.microc.2020.105539.

AMIRAH NASUHA MOHD RAZIB[1,3]

NIK MUHAMMAD AZHAR NIK DAUD[1]

MOHD AL HAFIZ MOHD NAWI[2]
BANU RAMASAMY[1]

MOHD SHARIZAN MD SARIP[1,3]

AMIRUL RIDZUAN ABU BAKAR[1]

MOHD ASRAF MOHD ZAINUDIN[1]

AHMAD HAZIM ABDUL AZIZ[4]

[1] Faculty of Chemical Engineering & Technology, University Malaysia Perlis, Perlis, Malaysia

[2]Faculty of Mechanical Engineering Technology, University Malaysia Perlis, Perlis, Malaysia

[3] Center of Excellence for Frontier Materials Research (FrontMate), University Malaysia Perlis, Perlis, Malaysia

[4] Faculty of Food Science and Nutrition, University Malaysia Sabah, Kota Kinabalu, Malaysia

NAUČNI RAD

POTENCIJAL ULTRAZVUČNOG ZRAČENJA U RAZGRADNJI POLIURETANA U EUTEKTIČKIM RASTVARAČIMA

Ovaj rad istražuje razgradnju poliuretana (PU) korišćenjem eutektičkih rastvarača (DES) u kombinaciji sa ultrazvučnim zračenjem, sa ciljem razvoja održivih metoda reciklaže PU otpada. DES, dobijen od holin hlorida i uree, poseduje ekološki prihvatljiva svojstva, kao što su niska toksičnost i visoka rastvorljivost, što ga čini pogodnim za hemijsku reciklažu. Eksperimenti razgradnje su sprovedeni na povišenim temperaturama (130-150 °C), sa i bez efekta ultrazvuka. Molekulske mase sirovog PU i proizvoda razgradnje određene su gel permeacionom hromatagorafijom. Strukture DES, PU i proizvoda razgradnje su analizirane korišćenjem FTIR i NMR. Rezultati pokazuju da primena ultrazvuka značajno povećava stopu razgradnje za približno 5,20% (od 58,5% do 63,7%) na konstantnoj temperaturi od 150 °C. Ovo poboljšanje se pripisuje efektima izazvanim kavitacijom, koji olakšavaju raskid polimernog lanca. Molekularne transformacije su potvrđene prisustvom NH_3 grupa koje nastaju usled raskida strukture PU da bi se formirao o-toluidin, što je identifikovano NMR spektroskopijom. Reakcioni putevi su utvrđeni strukturnom analizom i sirovog PU i proizvoda njegove razgradnje. Ovi nalazi pokazuju potencijal DES uz dejstvo ultrazvuka u unapređenju strategija hemijske reciklaže PU, rešavanju ekoloških problema vezanih za postojani PU otpad i promociji održivih praksi upravljanja otpadom.

Ključne reči: Sonohemija, Reciklaža polimera, o-toluidin.

CI&CEQ
Chemical Industry & Chemical Engineering Quarterly

Available online at
Association of the Chemical Engineers of Serbia AChE
www.ache.org.rs/CICEQ

Chem. Ind. Chem. Eng. Q. 32 (3) 225–233 (2026) CI&CEQ

CHANDRA BOSE AYYAVOO NETHAJI SUBASH[1]

SARAVANAN KANDASAMY GANESAN[1]

NIRANJAN THIRUCHINAPALLI[2]

[1]Department of Mechanical Engineering, Sona College of Technology, Salem, India

[2]Department of Mechanical Engineering, Mahatma Gandhi Institute of Technology, Hyderabad, India

PERFORMANCE OPTIMIZATION OF ECM PARAMETERS FOR PALLADIUM COATED TOOL ELECTRODE USING MULTI-CRITERIA DECISION ANALYSIS METHOD

Highlights

- A palladium-coated electrode with an ascorbic acid mixed electrolyte is used for the ECM experiments.
- The optimal factors are 29 g L^{-1} electrolyte concentration, 12 V, 70% duty cycle, and 80 Hz frequency.
- Significant factors for higher MR and overcut are machining voltage and electrolyte concentration.

Abstract

Electrochemical machining is an important process for fabricating difficult-to-cut materials. It is a much more advantageous process for creating excellent surface quality on a wide range of conductive materials. In this research, the electrode (cathode) is coated with less resistive palladium material through a sputtering process, and sodium electrolyte is added with 10 gl^{1} ascorbic acid to improve Local electrolysis and reduce the sludge generation. The process parameters, specifically electrolyte concentration, machining voltage, duty cycle, and frequency, were varied on machining rate and overcut using the L_{27} orthogonal array experimental plan. ÉLimination Et Choix Traduisant la REalité (ELECTRE) is employed to find a suitable solution. Based on the ELECTRE method, the best factor combination is 29 g L^{-1} electrolyte concentration, 12 V, 70% duty cycle, and 80 Hz frequency. The analysis of variance shows that machining voltage and electrolyte concentration are the considerable factors, with contribution percentages of 43.93% and 23.34%, respectively. As per the mean effect plot, the optimal combination is 29 g L^{-1} electrolyte concentration, 12 V, 90% duty cycle, and 80 Hz frequency.

SCIENTIFIC PAPER

UDC 621.9.047:620.1

Keywords: Machining rate, overcut, orthogonal array, ANOVA, ascorbic acid, sputtering.

INTRODUCTION

Electrochemical machining (ECM) is a metal finishing process that works on Faraday's law of electrolysis, in which the tool electrode is the cathode and the workpiece is the anode, separated by a small gap and immersed in an electrolyte bath. By way of application of a potential difference between the electrodes, the dissolution of the workpiece takes place. Apart from the finishing process, the ECM is now considered for the development of holes/dimples and intricate shapes, which finds application in aerospace, biomedical, and automobile components. In ECM, the factors and optimized levels of factors play the major role in performance measures such as material removal rate (MRR)/machining speed/machining rate (MR), overcut (OC), delamination factor, surface corrosion factor, circularity, cylindricity, and surface roughness (SR). Srividya *et al.* [1] have optimized the ECM parameters on aluminum composite using the Taguchi-ANN method. For the experiment dataset, the Artificial Neural Network (ANN) predictions produce an R^2 value of 0.98003 and a mean squared error in the range of 0.02413. The regression study's findings clearly show that the ANN model is capable of accurately and consistently predicting both MRR and SR [1].

Saranya *et al.* [2] have utilized a ceramic-coated tool and optimized the ECM performance for machining aluminum composite. They used ethylene glycol mixed with sodium nitrate electrolyte, and the ideal combination, according to the Grey Relational Analysis (GRA), is 30%

Correspondence: N.S.C.B Ayyavoo, Department of Mechanical Engineering, Sona College of Technology, Salem-636007, India.
Email: nethajisubash023@gmail.com
Paper received: 16 May 2025
Paper revised: 15 July 2025
Paper accepted: 4 September 2025

https://doi.org/10.2298/CICEQ250516025B

ethylene glycol, 9 V of voltage, 70% duty cycle, and 35 g L^{-1} of electrolyte. The most encouraging factor, according to the analysis of variance (ANOVA), is electrolyte concentration, which displays 46.36%. The predicted values of the ANN model are 0.17 and 1.14, respectively, which are quite near to the GRA-optimized values of surface corrosion factors and MR, or 0.17 and 1.14, respectively [2]. Venugopal *et al.* [3] have used a polytetrafluoroethylene (PTFE)-coated electrode in ECM for machining Hastelloy C22. The ideal levels of variables for better MR, lower OC, and conicity were found by using inter-criteria correlation and basic additive weighting techniques. The investigation indicated that a PTFE-coated electrode with 20 g L^{-1} mixed electrolyte, 8 V, 85% duty cycle, and 90 Hz frequency was the ideal parameter combination. As per the results of an ANOVA, the electrode type affects MR and OC by 21.15% and 41.26%, respectively. With a 64.32% contribution, the electrolyte content is the most important element for conicity [3].

Thangamani *et al.* [4] have used a heat-treated copper electrode on aluminum 8011 alloy. The best parameters were found using the artificial bee colony (ABC) algorithm, and the error difference on the machining process was then assessed using the confirmation test. For the ECM process, the voltage (14 V), electrolyte concentration (30 g L^{-1}), frequency (60 Hz), and duty cycle (33%) for the annealed tool electrode and the voltage (14 V), electrolyte concentration (20 g L^{-1}), frequency (70 Hz), and duty cycle (33%) for the quenched tool electrode are the ideal combinations of input process parameters that were discovered using TOPSIS and the ABC algorithm. It was verified that the ideal parameter combination produced 95% of the demonstrated accurate response values [4]. Arul *et al.* [5] examined how square-shaped stainless steel (SS) and aluminum metal matrix composite tools affect the creation of square holes. The electrochemical micromachining process's performance is assessed in terms of OC and MR. At parameter combinations of 8 V, 85%, and 23 g L^{-1}, the AMC tool displays 43.22% less OC than the SS tool [5]. An ECM experiment with a persistent magnetic field effect has been planned by Palaniswamy and Rajasekaran [6]. According to the study, the MR grew quickly for voltage levels between 9 V and 10 V, although the pace of change in OC was less noticeable for voltage levels between 6 V and 10 V. A duty cycle range of 70 to 90% exhibits greater MR and a high rate of OC change in conjunction with the magnetic field effect. Higher MR is produced by an electrolyte concentration of 30 to 35 g L^{-1}, whilst an increased rate of change in OC is noted in the range of 15 to 30 g L^{-1} [6].

Palaniswamy *et al.* [7] studied the impact on the copper plate of the graphite electrode with a magnetic force. For these studies, four different tools are used: the graphite tool, the permanent magnet graphite tool (PMGT), the electromagnetic graphite tool (EMGT), and the SS tool. The primary determining parameters on MR and OC are electrolyte content in g L^{-1}, duty cycle in %, and machining voltage in volts. At a parameter level of 23 g L^{-1}, 15 V, and 85%, respectively, the results showed that EMGT, PMGT, and graphite electrodes yield MR of 106.4%, 74.6%, and 44.5% over the SS tool. Furthermore, at parameter levels of 8 V, 95%, and 28 g L^{-1}, graphite and EMGT electrodes produced, respectively, 11.9% and 3.41% lower OC than the SS tool [7]. Maniraj and Thanigaivelan [8] have used a heated electrode in ECM for improving the MRR, reducing the OC, and reducing the conicity factor. The results of the performed studies show that at 8 V, 90% duty cycle, 35 g L^{-1} electrolyte concentration, and 60 °C electrode temperature, the heated electrode increases the MR by 88.37%, lowers the radial OC by 37.03%, and lowers the conicity factor by 33.33% [8]. Cercal *et al.* [9] have experimented with ECM for the reduction of sludge during electrolysis. To accomplish this, complexing and reducing (ascorbic acid) agents were added to the electrolyte composition, resulting in parallel processes that prevented metallic ions from precipitating. They suggest that ascorbic acid is suitable to be added to the electrolyte for the ECM process [9].

It is apparent from the above literature that the research on ECM mainly focuses on the enhancement of output performances such as MRR, accuracy, and surface quality with additional energy and tool design improvement. Literature in the recent past focuses on coating the tool electrode with insulating material towards the deceleration of stray current, and it is the first attempt at coating the ECM electrode with the lowest electrical resistance material, namely palladium. The use of a high electrical conductivity tool electrode induces the enhancement of electrochemical performance. A further L27 orthogonal array (OA) experiment was conducted, and the multi-criteria decision analysis method, namely ÉLimination Et Choix Traduisant la REalité (ELECTRE), was employed to find the suitable solution.

METHODOLOGY

The ECM setup shown in Figure 1 is used for machining, and it consists of a machine structure, an electrode feeding system, an electrolyte supply system, and a power supply. The electrolyte is prepared by using sodium nitrate salt along with distilled water. The varying concentration of electrolyte was considered for the study. Along with the sodium nitrate electrolyte, a concentration of 10 g L^{-1} of ascorbic acid is used as a reducing agent to minimize the sludge formation during the electrolysis process. The stitching needle is used as a 500 μm diameter tool electrode, and a 304 SS workpiece of 0.5 mm thickness was used for the study. The needle is coated with palladium using a sputtering process. The electrode is first submerged in isopropyl alcohol, double-distilled water, and ultrasonicated acetone to remove any minute particles that may have accumulated on the electrode's surface. The ultra-high vacuum chamber was loaded with this cleaned electrode. The argon gas flow was kept at 0.12 m^3/s while the UHV DC magnetron sputtering power was fixed at 30 W, 4×10^{-5} Nm^{-2} was the base pressure, while 0.53 Nm^{-2} was the deposition pressure. The electrode was rotated at 10 rpm and pre-sputtered for 10 minutes, with a gap of 10 cm between it and the target [10,11]. An electrode was covered in palladium. The prepared coated electrode is stored in a base vacuum (high vacuum) for one day. The profile of the palladium-coated tool electrode is shown by

field emission scanning electron microscope. Figure 2 depicts the SEM picture of palladium-coated electrodes before and after machining. Table 1 presents the L_{27} OA experiments with factors, levels, and output performances. The MR is measured by noting the time taken to machine the complete hole. The thickness of the workpiece divided by the time noted provides the MR. The OC is the difference between the hole diameter and the tool diameter after coating [12].

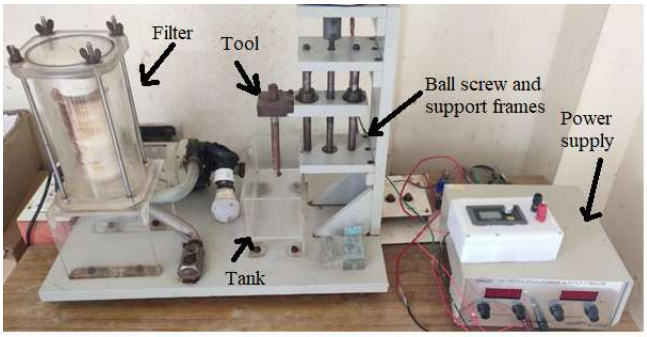

Figure 1. The ECM setup.

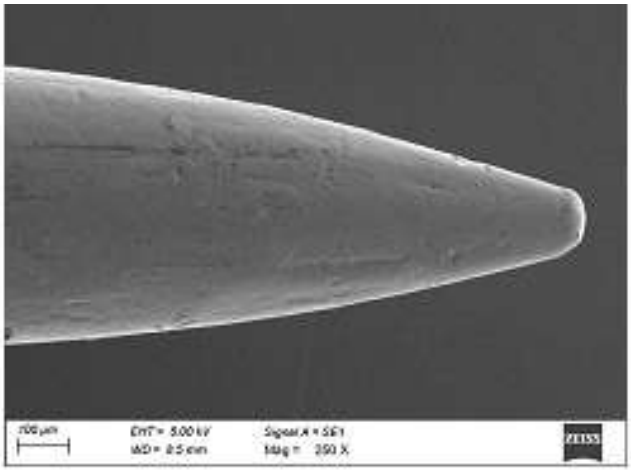

(a)

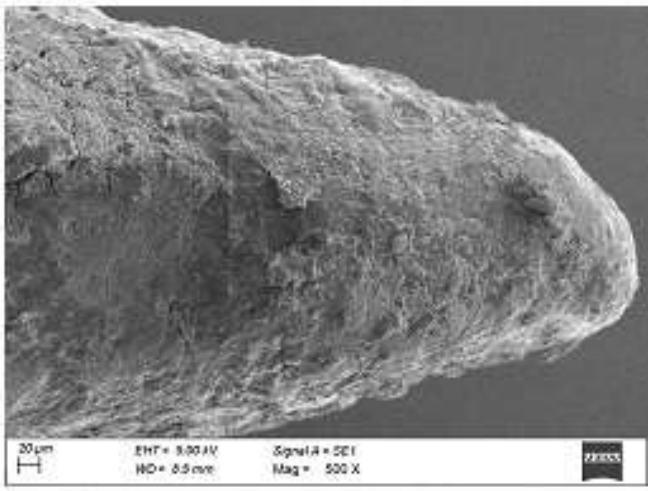

(b)

Figure 2. The SEM image of the palladium-coated tool (a) before and (b) after machining.

RESULTS AND DISCUSSION

ELECTRE Method

Decision-making techniques help in investigating multiple process attributes and optimizing the process quality [13,14]. The ELECTRE method is linked to a variety of fields to address multi-measure difficulties. In this procedure, decisions are made by comparing options pairwise depending on each appropriate criterion. The alternatives that do not meet the requirements are then discarded, allowing viable alternatives to be developed [15-18].

The goal is to rank the alternatives based on the two criteria, namely MR and OC. The steps in the multi-criteria decision analysis method are as follows:

1. Define the alternatives.
2. Construct the decision matrix for the criteria.
3. Normalize the decision matrix.
4. Assign weights to MR and OC.
5. Construct the Concordance and Discordance matrices.
6. Apply thresholds for concordance and discordance indices.
7. Determine outranking relations based on the concordance and discordance dominance.
8. Rank the alternatives.

Step 1: Define the alternatives.

Each data point is an alternative, so 27 alternatives corresponding to the pairs of MR and OC were defined.

Step 2: Construct the decision matrix.

A matrix with each row representing an alternative and each column representing a criterion (MR and OC) is formed.

$$\textbf{Decision Matrix} = \begin{bmatrix} \mathbf{0.208} & \mathbf{184} \\ \mathbf{0.278} & \mathbf{166} \\ \mathbf{0.333} & \mathbf{154} \\ \vdots & \vdots \\ \mathbf{0.490} & \mathbf{88} \\ \mathbf{0.556} & \mathbf{84} \end{bmatrix}$$

Criterion 1: MR–to be maximized.

Criterion 2: OC–to be minimized.

Step 3: Normalize the decision matrix

To normalize the decision matrix, each element is divided by the square root of the sum of squares of the corresponding criterion (for benefit criteria, such as MR) or divided by the maximum value (for cost criteria, such as overcut).

For MR (benefit criterion), vector normalization is done using the following relation:

$$x_{ij}^{'} = \frac{x_{ij}}{\sum_{i=1}^{n} (x_{ij})^2}$$

where x_{ij}' is the normalized value of the j^{th} criterion for the i^{th} alternative, x_{ij} is the actual value of the j^{th} criterion for the i^{th} alternative, i is the index for alternatives (i = 1, 2, ..., n), j is the index for criteria, and n is the total number of alternatives.

Table 1. L_{27} OA.

Expt.No	Electrolyte concentration (gl^{-1})	Machine voltage (V)	Duty cycle (%)	Frequency (Hz)	MR (μm/s)	OC (μm)
1	23	8	50	60	0.208	184
2	23	8	70	70	0.278	166
3	23	8	90	80	0.333	154
4	23	10	50	70	0.379	150
5	23	10	70	80	0.417	112
6	23	10	90	60	0.417	115
7	23	12	50	80	0.439	106
8	23	12	70	60	0.417	100
9	23	12	90	70	0.463	95
10	26	8	50	70	0.225	175
11	26	8	70	80	0.231	146
12	26	8	90	60	0.238	142
13	26	10	50	80	0.253	152
14	26	10	70	60	0.269	160
15	26	10	90	70	0.287	162
16	26	12	50	60	0.333	150
17	26	12	70	70	0.362	140
18	26	12	90	80	0.463	100
19	29	8	50	80	0.347	143
20	29	8	70	60	0.379	123
21	29	8	90	70	0.397	110
22	29	10	50	60	0.362	118
23	29	10	70	70	0.379	150
24	29	10	90	80	0.417	105
25	29	12	50	70	0.463	110
26	29	12	70	80	0.556	84
27	29	12	90	60	0.490	88

For OC (cost criterion), the normalization is divided by the maximum value:

$$x_{ij}^{'} = \frac{\mathrm{Min}\left(x_{ij}\right)}{x_{ij}}$$

Step 4: Weigh the criteria.

The weights for MR and OC were assigned as 0.5 based on the importance.

Step 5: Construct the concordance and discordance matrices.

Concordance matrix:

For each pair of alternatives, A_i and A_j, the concordance index was calculated. The concordance index is the sum of the weights of the criteria where Ai performs better than or equal to A_j.

	$A1$	$A2$	$A3$	L	$A27$
$A1$	0.0	0.5	0.5	L	0.5
$A2$	0.0	0.0	0.5	L	1.0
$A3$	0.0	0.0	0.0	L	1.0
M	M	M	M	O	M
$A27$	0.0	0.0	0.0	L	0.0

Discordance matrix:

For each pair A_i and A_j the discordance index was computed, which reflects the maximum relative difference for the criteria where A_i performs worse than A_j.

	$A1$	$A2$	$A3$	⋯	$A27$
$A1$	0.0	0.00735	0.01359	⋯	0.04202
$A2$	0.02162	0.0	0.00624	⋯	0.04298
$A3$	0.04143	0.02162	0.0	⋯	0.05763
⋮	⋮	⋮	⋮	⋱	⋮
$A27$	0.05027	0.03946	0.03321	⋯	0.0

Step 6: Apply thresholds.

The concordance threshold c^* and discordance threshold d^* were applied to filter the pairs for which A_i outranks A_j. The threshold values are set based on the average concordance and discordance values.

c^*: 0.514

d^*: 0.176

Based on these thresholds, the dominance matrix is constructed, and the dominance scores are calculated for each alternative. The alternatives were ranked according to their dominance scores (higher dominance scores indicate better performance).

Step 7: Determine outranking relations.

As per the concordance and discordance indices, dominating alternatives were determined. An alternative Ai will outrank Aj if:

$c(Ai,Aj) \geq c^*$ (sufficient concordance)

$d(Ai,Aj) \leq d^*$ (acceptable discordance)

Step 8: Rank the alternatives

Aggregate the dominance matrix by combining the concordance and discordance dominance matrices to identify the final dominance for each pair. Using the outranking relations, the ranking of the alternatives is done. The alternative that dominates the most others will be ranked highest. Hence, based on the multi-criteria decision analysis method, the best combination for obtaining optimal output performance is 29 g L^{-1} electrolyte concentration, 12 V, 70% duty cycle, and 80 Hz frequency, and the next best combination is 29 g L^{-1} electrolyte concentration, 12 V, 90% duty cycle, and 60 Hz frequency (Table 2). It can be concluded that 29 g L^{-1} of electrolyte concentration, 12 V, a 70-90% duty cycle range, and a 60-80 Hz frequency are the best parameter combinations for achieving better MR and OC.

Table 2. Ranking of attributes.

Alternative	Dominance score	Rank
A26	26	1
A27	25	2
A25	24	3
A18	24	3
A9	24	3
A8	23	6
A7	22	7
A24	22	7
A5	20	9
A6	20	9
A21	19	11
A20	15	12
A22	15	12
A23	13	14
A17	13	14
A4	13	14
A12	12	17
A19	12	17
A16	11	19
A11	10	20
A3	9	21
A13	8	22
A14	6	23
A15	5	24
A2	4	25
A10	1	26
A1	0	27

Analysis of Variables on the ECM Performance

Figure 3 depicts the mean effect plot, and an increase in electrolyte concentration first reduces the MR. A further increase in the concentration enhances the ECM performance because the ionic strength raises the electrolyte conductivity, which leads to higher current density, more heat generation, rapid gas evolution, and passive film generation, which blocks the machining performance. Further increase in electrolyte concentration improves the electrolyte's buffer capacity, leading to a slight increase in the electrolyte's viscosity. This phenomenon stabilizes the gas layer and prevents localized overheating. At a higher voltage, the sludge generation will be affected, which invariably affects the ECM dissolution process. To avoid this effect, the addition of ascorbic acid causes a parallel reduction reaction for metal ions dissolved in the electrolyte. The major goal is to lower the cation valence of metal ions by oxidizing ascorbic acid into dehydroascorbic acid [9].

The ANOVA helps in analyzing the effects of process characteristics on the performance of the process [22-24]. Based on the *F*-value, the ANOVA table (Table 3) shows that electrolyte concentration is the second-best parameter that affects the MR next to voltage. Table 4 shows the ANOVA for the OC, and it is evident that voltage is the most significant factor with an *F*-value of 12.90.

The increase in voltage levels increases the MR. As per Faraday's law of electrolysis, the rise in voltage augments the current density required for machining. The rise in voltage level accelerates the ions during the electrolysis, and the palladium-coated electrode and the addition of ascorbic acid complement the higher MR and lower OC. Moreover, based on the ANOVA table, voltage is the most significant factor that influences the machining performance, with a contributing percentage of 33.83. Figure 2(b) shows the SEM of the coated electrode after the ECM process, and the coatings are delaminated during the electrolysis process. Hence, it is evident that although the coated surface was delaminated, it was not detached from the electrode surface, leading to increased local conducti vity, which accounts for higher output performance. Figure 4 depicts the mean effect plot of OC. An increase in the electrolyte concentration decreases the OC.

Table 3. ANOVA table for MR.

Symbol	Machining parameters	Degrees of freedom	Sum of squares	Mean sum of squares	*F*-value	% contribution
A	Electrolyte concentration (gl^{-1})	2	0.072	0.036	23.73	0.000
B	Machining Voltage (V)	2	0.103	0.051	33.80	0.000
C	Duty Cycle (%)	2	0.004	0.002	1.46	0.258
D	Frequency (Hz)	2	0.007	0.004	2.84	0.084
E	Error	18	0.027	0.001		
	Total	26	0.215			

Table 4. ANOVA table for OC.

Symbol	Machining parameters	Degrees of freedom	Sum of squares	Mean sum of squares	F-value	% contribution
A	Electrolyte concentration (gl^{-1})	2	4868	2434.1	7.92	0.003
B	Machining Voltage (V)	2	7928	3964.1	12.90	0.000
C	Duty Cycle (%)	2	1308	654.1	2.13	0.15
D	Frequency (Hz)	2	1069	534.3	1.74	0.20
E	Error	18	5531	307.3		
	Total	26	20705			

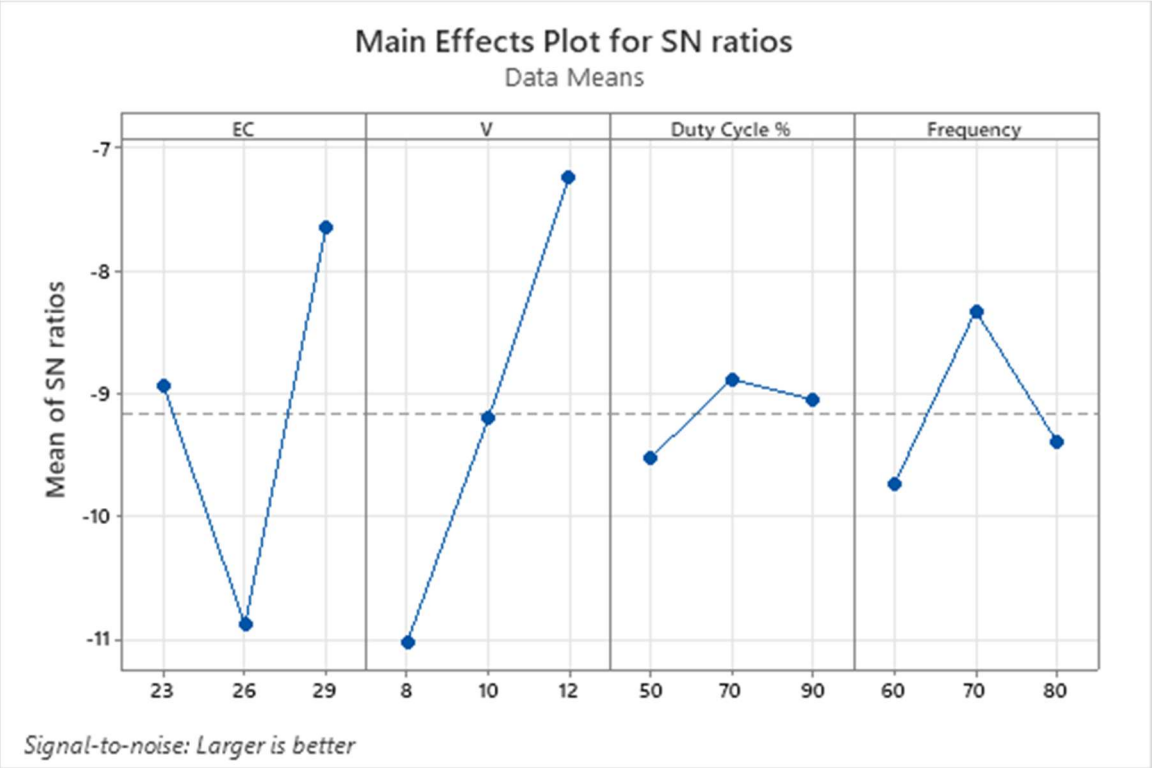

Figure3. The mean effect plot for MR.

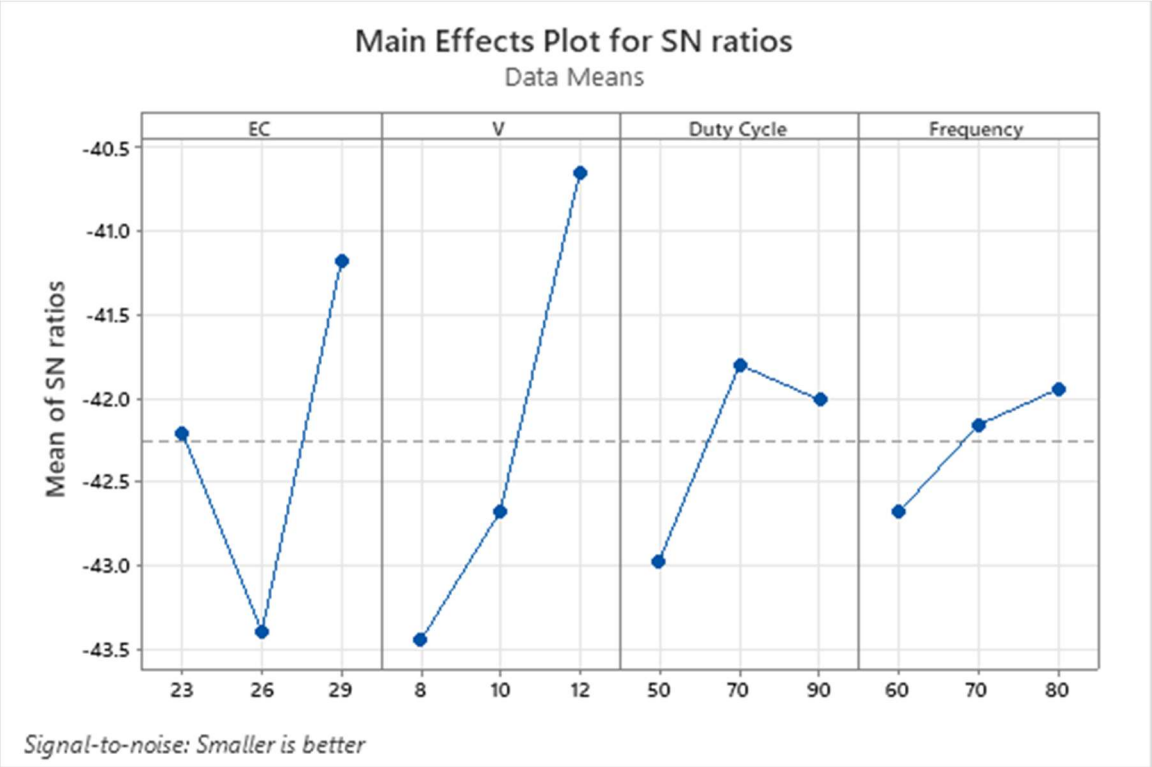

Figure 4. The mean effect plot for OC.

In ECM, to ensure stable machining, a uniform inter-electrode gap (IEG) is maintained in the range of 200µm to 300µm. Hence, during machining at a lower electrolyte concentration, the proximity of the electrodes helps to develop the required current density in the machining zone. This phenomenon contributes tostable machining without stray cuts. While an increase in electrolyte concentration beyond 26 g L^{-1}, the presence of more ions develops an intense current density between the IEG. This phenomenon develops more dissolute products in the machining zone. This debris builds up in time, resulting in micro-sparking and a stray cut effect. The OC tends to increase with

electrolyte concentration; at higher concentrations, the debris produced increases the frequency of micro-sparking. An increase in voltage level shows a significant effect on OC, which is because at a higher voltage, the current density available between IEG is more, leading to higher material removal. A huge volume of debris from the machining attributes for increased OC. The OC tends to increase with duty cycle, and the optimum range of duty cycle is 70-90%. An increase in the frequency of the pulse increases the OC. With respect to Figure 4, the points for the frequency are closer to each other, hence the optimum range of frequency is 60-80 Hz.

It is also evident from the SEM micrograph shown in Figure 5(a) that the hole generated during the ECM process at a parameter combination of 29 g L^{-1} electrolyte concentration, 12 V, 70% duty cycle, and 70 Hz. As per the mean effect plot, the former factor combination is the best combination for obtaining high MR [19]. The influence of ascorbic acid is witnessed on the whole profile and the hole surface. The perfect circular hole profile with fewer stray current-affected regions and white layers. Localized heating can still happen at the electrode-workpiece interface even though ECM mostly removes material by an electrochemical reaction. This results in a tiny area of changed microstructure close to the surface, known as the white layer. This white layer might cause residual stresses and perhaps weaken the machined component's fatigue strength; it is usually preferable to minimize its thickness. The palladium-coated electrode accounted for the reduction of stray current-affected regions on the hole due to its high electrical conductivity [20,21]. Figure 5(b) shows the hole machined at the best combination of 29 g L^{-1} electrolyte concentration, 12 V, 70% duty cycle, and 80 Hz frequency. The increase in duty cycle increases the MR, as shown in Figure 3, and a further increase in duty cycle percentage reduces the material removal performance. The proper balance of pulse-on-time and pulse-off-time attributes for higher machining performance. It is evident from the optimal parameter setting that 70% duty is the best level for achieving the best performance. Out of the total duty cycle, 1/3rd of the percentage is used for debris settlement and de-electrification of the high-conductive electrode. This phenomenon helps to improve the electrolysis in the ECM process. Although frequency is the least significant factor as per the ANOVA, the higher frequency of the pulse is good to achieve the best performance.

The developed regression equations for MR and OC are shown in Eqs.(1) and (2), respectively:

$$MR = 0.36304 + 0.0093\ EC\_23 - 0.0674\ EC\_26 + 0.0581\ EC\_29 - 0.0701V\_8 - 0.0097\ V\_10 + 0.0799V\_12 - 0.0147\ Duty\ Cycle\%\_50 + 0.0165\ Duty\ Cycle\ \%\_70 - 0.0018\ Duty\ Cycle\ \%\_90 - 0.0145\ Frequency\_60 + 0.0252\ Frequency\_70 - 0.0107\ Frequency\_80 \quad (1)$$

and

$$OC = 131.11 + 0.22\ EC\_23 + 16.33\ EC\_26 - 16.56\ EC\_29 + 18.11\ V\_8 + 4.89\ V\_10 - 23.00\ V\_12 + 9.67\ Duty\ Cycle\_50 - 6.44\ Duty\ Cycle\_70 - 3.22\ Duty\ Cycle\_90 + 8.89\ Frequecny\_70 - 4.78\ Frequency\_80 \quad (2)$$

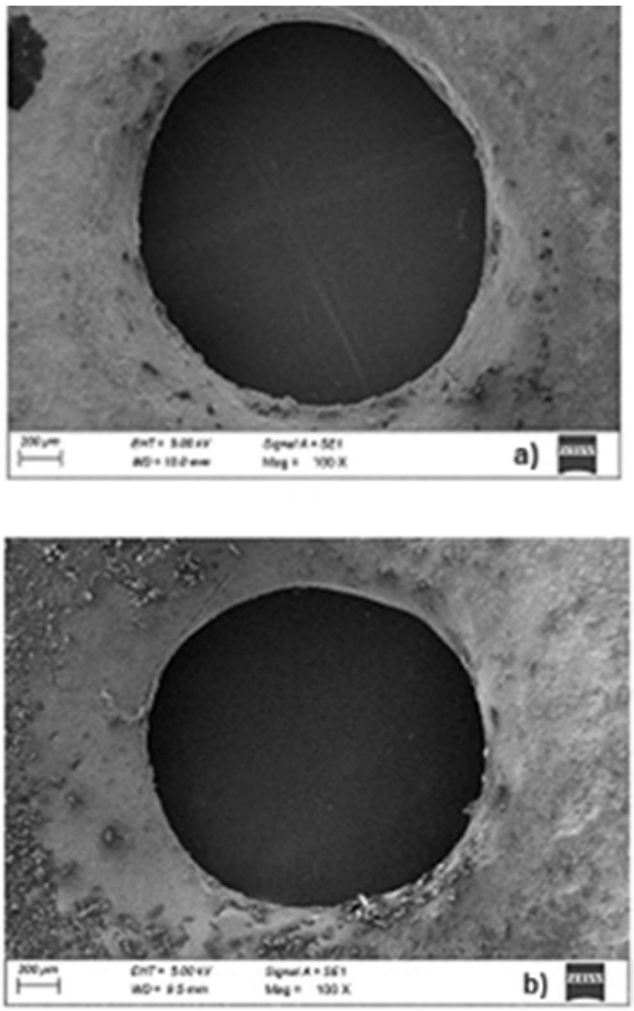

Figure 5. (a) Hole machined at the 29 g L^{-1} electrolyte concentration, 12 V, 90% duty cycle, and 80 Hz frequency, and (b) hole machined at the 29 g L^{-1} electrolyte concentration, 12 V, 70% duty cycle, and 80 Hz frequency.

CONCLUSIONS

The tool electrode is successfully coated using palladium through the DC magnetron sputtering process.

The L_{27} OA experiment was conducted successfully with sodium nitrate electrolyte mixed with 10 g L^{-1}ascorbic acid, and the multi-criteria decision analysis, namely ELECTRE, is employed to find the suitable solution.

Based on the multi-criteria decision analysis method, the best combination for obtaining the optimal output performance is 29 g L^{-1}electrolyte concentration, 12 V, 70% duty cycle, and 80 Hz frequency, whereas the next best combination is the 29 g L^{-1}electrolyte concentration, 12 V, 90% duty cycle, and 60 Hz frequency. It can be concluded that the 29 g $L^{-1}$of electrolyte concentration, 12 V, a 70-90% duty cycle range, and a 60-80 Hz frequency are the best parameter combinations for achieving better MR and OC.

As per the mean effect plot, the 29 g L^{-1} electrolyte concentration, 12 V, 70% duty cycle, and 70 Hz frequency factor combination is the best combination for obtaining a higher MR, while the 29 g L^{-1}electrolyte concentration, 12 V, 70% duty cycle, and 80 Hz frequency factor combination is the best combination for obtaining a lower OC.

The most important factor is the machining voltage, with *F*-values of 33.80 and 12.90 for MR and OC, respectively, while the next best factor is the electrolyte concentration, with *F*-values of 23.73 and 7.92, respectively.

Future work may include industry-scale validations with varying concentrations of ascorbic acid to further establish scalability.

ACKNOWLEDGEMENTS

This dataset is the outcome of the experiments carried out in the Department of Mechanical Engineering, Sona College of Technology, Salem, India, and the authors are thankful for all the support the institution provides.

REFERENCES

[1] K. Srividya, S. Ravichandran, M. Thirunavukkarasu, I. Veeranjaneyulu, P. Satishkumar, K. Bharadwaja, N. Srinivasa Rao, R. Subbiah, J.E. Manikanta, Int. J. Interact. Des. Manuf. 18 (2024) 1459–1473. https://doi.org/10.1007/s12008-024-01761-x.

[2] K. Saranya, K. Haribabu, T. Venkatesh, K.G. Saravanan, Ramya Maranan, N. Rajan, Int. J. Interact. Des. Manuf. 18 (2024) 5015–5025. https://doi.org/10.1007/s12008-024-01811-4.

[3] P. Venugopal, T.G. Arul, R. Thanigaivelan, Ionics 28 (2022) 4745–4753. https://doi.org/10.1007/s11581-022-04686-1.

[4] G. Thangamani, M. Thangaraj, K. Moiduddin, H. Alkhalefah, S. Mahalingam, P. Karmiris-Obratanski, Materials 15 (2022) 4831. https://doi.org/10.3390/ma15144831.

[5] T.G. Arul, V. Perumal, R. Thanigaivelan, Chem. Ind. Chem. Eng. Q. 28 (2022) 247–253. https://doi.org/10.1080/10426914.2019.1697445.

[6] V. Palaniswamy, T. Rajasekaran, J. Electrochem. Sci. Eng. 13 (2023) 553–561. https://doi.org/10.5599/jese.1660.

[7] V. Palaniswamy, K. Seeniappan, T. Rajasekaran, N. Lakshmaiya, Chem. Ind. Chem. Eng. Q. 29 (2023) 201–208. https://doi.org/10.2298/CICEQ240220020PS.

[8] S. Maniraj, R. Thanigaivelan, Mater. Manuf. Process. 34 (2019) 1494–1501. https://doi.org/10.1080/10426914.2019.1655153.

[9] G. Cercal, G. de Alvarenga, M. Vidotti, Processes11 (2023) 2186. https://doi.org/10.3390/pr11072186.

[10] S. Wang, W. Wei, Y. Gao, H. Pan, Y. Wang, Vacuum 188 (2021) 110200. https://doi.org/10.1016/j.vacuum.2021.110200.

[11] Y. Ni, W. Wang, C. Tang, J. Sun, W. Zhang, W. Gao, J. Zou, J. Mater. Sci. Mater. Electron. 35 (2024) 770. https://doi.org/10.1007/s10854-024-12537-0.

[12] S. Saha, A.K.Mondal, R. Čep, H. Joardar, B. Haldar, A. Kumar, S. Ataya, Machines 12 (2024) 335. https://doi.org/10.3390/machines12050335.

[13] T. Niranjan, R. Thanigaivelan, B. Singaravel, Innovations in Mechanical Engineering: Select Proceedings of ICIME, G.S.V.L. Narasimham, A.V. Babu, S.S. Reddy, R. Dhanasekaran, (Eds.), Springer, Singapore (2022), pp. 797-807. https://doi.org/10.1007/978-981-16-7282-8_60.

[14] W. Chu, M. Vicidomini, F. Calise, N. Duić, PA. Østergaard, Q. Wang, M. da GraçaCarvalho, Energies 15 (2022) 7129. https://doi.org/10.3390/en15197129.

[15] M. Carra, F. Botticini, F.C. Pavesi, G. Maternini, M. Pezzagno, B. Barabino, Transp. Res. Proced. 69 (2023) 448–455. https://doi.org/10.1016/j.trpro.2023.02.194.

[16] J. Ye, T.Y. Chen, J. Nat. Fibers 20 (2023) 2201486. https://doi.org/10.1080/15440478.2023.2201486.

[17] G. Salvador, M. Moura, P. Campos, P. Cardoso, P. Espadinha-Cruz, R. Godina, Proced. Comput. Sci. 232 (2024) 1759–1768. https://doi.org/10.1016/j.procs.2024.01.174.

[18] E.P. Özmen, B. Demir, Sigma J. Eng. Nat. Sci. 41 (2023) 232-242. https://dergipark.org.tr/en/pub/sigma/issue/83129/1403041.

[19] M.K. Dikshit, S. Singh, V.K. Pathak, K.K. Saxena, M.K. Agrawal, V. Malik, M.I. Khan, J. Mater. Res. Technol. 24 (2023) 223–235. https://doi.org/10.1016/j.jmrt.2023.03.005.

[20] U.A. Kamarulzaman, M.Y.A. Rahman, M.S. Su'ait, A.A. Umar, Chem. Pap. 77 (2023) 4625–4632. https://doi.org/10.1007/s11696-023-02812-5.

[21] A. Ngoipala, R. Lipin, R.L. Arevalo, M. Vandichel, Int. J. Hydrogen Energy 53 (2024) 829–839. https://doi.org/10.1016/j.ijhydene.2023.12.019.

[22] D. Mekebo, B.S. Chandravanshi, Bull. Chem. Soc. Ethiop. 28 (2014) 349–62. https://doi.org/10.4314/bcse.v28i3.4.

[23] N. Sivashankar, R. Thanigaivelan, K.G. Saravanan, Bull. Chem. Soc. Ethiop. 37 (2014) 1263–1273. https://doi.org/10.4314/bcse.v37i5.17.

[24] P.R. Kannan, R. Thanigaivelan, R. Thiraviam, K.P. Kumar, Mater. Sci. Pol. 41 (2023) 288–300. https://doi.org/10.2478/msp-2023-0020.

CHANDRA BOSE AYYAVOO NETHAJI SUBASH[1]

SARAVANAN KANDASAMY GANESAN[1]

NIRANJAN THIRUCHINAPALLI[2]

[1]Department of Mechanical Engineering, Sona College of Technology, Salem, India

[2]Department of Mechanical Engineering, Mahatma Gandhi Institute of Technology, Hyderabad, India

OPTIMIZACIJA PARAMETARA ELEKTROHEMIJSKE OBRADE ZA ALATNU ELEKTRODU OBLOŽENU PALADIJUMOM KORIŠĆENJEM METODE VIŠEKRITERIJUMSKE ANALIZE ODLUČIVANJA

Elektrohemijska obrada je važan proces izrade teško obradivih materijala. To je mnogo povoljniji proces za dobijanje odličnog kvaliteta površine na širokom spektru provodljivih materijala. U ovom istraživanju, elektroda (katoda) je obložena manje otpornim paladijumskim materijalom kroz proces raspršivanja, a natrijumov elektrolit je dodat sa 10 g/l askorbinske kiseline kako bi se poboljšala lokalna elektroliza i smanjilo stvaranje ulja. Parametri procesa, posebno koncentracija elektrolita, napon obrade, radni ciklus i frekvencija, varirani su u zavisnosti od brzine obrade i prerez korišćenjem eksperimentalnog plana sa ortogonalnim nizom L27. Metoda ÉLimination Et Choix Traduisant la Realité (ELECTRE) je korišćena za pronalaženje odgovarajućeg rešenja. Na osnovu ELECTRE metode, najbolja kombinacija faktora je koncentracija elektrolita od 29 g/L, napon obrade od 12 V, radni ciklus od 70% i frekvencija od 80 Hz. Analiza varijanse pokazuje da su napon obrade i koncentracija elektrolita značajni faktori, sa procentima doprinosa od 43,9% i 23,3%, redom. Prema grafikonu srednjeg efekta, optimalna kombinacija je koncentracija elektrolita od 29 g/L, napon obrade od 12 V, radni ciklus od 90% i frekvencija od 80 Hz.

Ključne reči: Brzina obrade, prerezivanje, ortogonalni niz, ANOVA, askorbinska kiselina, raspršivanje.

NAUČNI RAD

Chemical Industry & Chemical Engineering Quarterly

Available online at
Association of the Chemical Engineers of Serbia AChE
www.ache.org.rs/CICEQ

Chem. Ind. Chem. Eng. Q. 32 (3) 235–244 (2026) CI&CEQ

JASMINA VITAS
ALEKSANDAR JOKIĆ
NATAŠA LUKIĆ
SELENA DMITROVIĆ
DANICA PIPER
RADOMIR MALBAŠA

University of Novi Sad, Faculty of Technology Novi Sad, Novi Sad, Republic of Serbia

CROSS-FLOW MICROFILTRATION OF TRADITIONAL KOMBUCHA BEVERAGE USING CERAMIC TUBULAR MEMBRANE

Highlights

- The impact of microfiltration on the quality of traditional kombucha was examined.
- A ceramic tubular membrane was used for cross-flow microfiltration.
- Microfiltration effectively enhanced its visual quality.

Abstract

The traditional kombucha beverage is produced through the metabolic activity of the microorganisms present in the kombucha culture on sweetened black tea at room temperature. The aim of this study was to investigate the influence of cross-flow microfiltration on the quality of the produced beverage. The produced beverage was microfiltered to assess the effect of cross-flow microfiltration on its quality. The quality characteristics examined included pH, total acidity, total soluble solids, turbidity, organic acids, in vitro antioxidant potential, and vitamin C as an antioxidant compound. The operational parameters of the process were transmembrane pressure (0.2, 0.6, and 1 bar) and feed flow rate (30, 90, and 150 Lh^{-1}). The maximum permeate flux was achieved at the highest feed flow rates and transmembrane pressures. Microfiltration maintained (pH, total acidity, total soluble solids, lactic, formic, and oxalic acid), improved (turbidity and acetic acid), but also declined (malonic acid, vitamin C, and antioxidant potential), the quality of the traditional beverage. After the microfiltration, turbidity was reduced by 7-9 times, and the content of acetic acid amounted to around 1.20 g/L. The lowering of acetic acid content indicated the inhibition of acid buildup. Values of the coefficient of retention for all of the examined quality parameters, except turbidity, suggested that the overall influence of microfiltration was moderate.

Keywords: SCOBY, membrane filtration, physicochemical properties, biological potential.

SCIENTIFIC PAPER

UDC582.282.23:663.28:66.09

INTRODUCTION

Health drinks are one of the fastest-growing beverage categories amid growing public health concerns. These drinks include ready-to-drink teas, 100% superfruit juices such as pomegranate juice, cherry juice, and cloudy pear juice, mineral waters, herbal teas, kombucha, and other products [1]. Traditional kombucha beverage is produced as a result of the fermentation process conducted on black tea sweetened with sucrose, by the microorganisms present in kombucha. Fermentation usually lasts 7-10 days at a temperature that can be in the range 18-30 °C. Kombucha culture applied in the fermentation is mainly composed of acetic acid bacteria and several yeast species. Sucrose is usually added in the amount of 5 to 10%, and the content of black tea leaves is in the 1.5 to 12 g/L range. In the kombucha beverage production, yeasts metabolize sugars to ethanol, and acetic acid bacteria utilize the obtained ethanol and produce acetic acid. During the fermentation, two phases are formed. One is a nutritionally and pharmacologically active beverage. The other is the floating cellulosic pellicle layer. In order to conduct the production process of kombucha beverages, the liquid part of the kombucha is added to the sweetened black tea extract in the amount of 10-20% (v/v). The pellicle from previously obtained kombucha product is transferred as well [2-6].

Black tea kombucha beverage has a slightly sweet and sour taste, a characteristic odour that resembles vinegar, slight carbonation, and a blurry appearance [2,5]. It can be produced as a non-alcoholic and alcoholic beverage [2]. In our country, there is no legislation on kombucha, and kombucha is regarded as a refreshing soft drink. The alcohol content of these types of food products is defined by the Rules on the quality of refreshing non-alcoholic drinks. According to this regulation, kombucha is considered non-alcoholic when it contains no more than 0.5% (v/v)

Correspondence: D. Piper, University of Novi Sad, Faculty of Technology Novi Sad, Bulevar cara Lazara 1, 21000 Novi Sad, Republic of Serbia.
Email: danica.piper@uns.ac.rs
Paper received: 3 April 2025
Paper revised: 27 October 2025
Paper accepted: 12 November 2025

https://doi.org/10.2298/CICEQ250403026V

of ethanol [7]. The turbidity of the beverage is attributed to the presence of microorganisms, remains of cellulosic pellicle, and other suspended particles [2,8]. It is very well known that, from the consumer's point of view, blurriness is undesirable, since it can indicate poor quality or contamination. Although kombucha has been produced industrially, additional research at the laboratory scale is ongoing [9].

Techniques used in beverage production have some deficiencies and disadvantages, such as high cost and long retention time. Downstream processing (purification, dealcoholization, etc.) is the most expensive production cost in the beverage industry. The use of membranes can reduce expenses and retention time while also improving beverage quality, so membrane techniques are used at different stages of the beverage manufacturing process [10].

A membrane separation system is a process that uses a permeable membrane to separate different components of a mixture based on properties such as size, charge, and/or solubility. It functions by allowing certain molecules or particles to pass through the membrane but preventing others. A driving force could be pressure, differences in concentration, and/or electrical potential. Membrane processes are energy efficient because they do not require additional heat or chemicals for separation, resulting in less energy and costs for chemicals [10]. The selective, accurate separation results in much higher purity and fewer contaminants in the final products that would be associated with crossover during filtration [11].

In order to make the kombucha beverages clear, microfiltration (MF) can be used [8,11]. MF is a membrane separation technique with pore sizes from 0.1 to 10 μm. It retains microorganisms and particles in suspensions and colloidal solutions. The MF is widely used in the production of various beverages, for clarification, cold sterilization, as well as removing bacteria, with minimal effect on temperature during the process. In this way, the obtained kombucha products are stabilized and clarified, since microorganisms are retained [8,11]. On an industrial scale, it can be applied instead of pasteurization, as well. In this way, the increase in ethanol and acidity of kombucha beverages is prevented [2]. A study demonstrated that MF had almost the same influence as pasteurization on the microbiological quality of raw pomegranate juice [12].

MF membranes can remove particles larger than the pore size and avoid undesirable physical or chemical changes. At the same time, the retention of filtration media components reduces the permeate flow, so the efficiency of the filtration process is affected by membrane fouling. Membranes are typically classified as polymeric and ceramic depending on the material used in their manufacture. Ceramic membranes have been reported to be less susceptible to membrane fouling compared to polymeric membranes because their inorganic substance is more chemically stable, resistant to harsh environments, and has a smoother surface, which minimizes particles' adhesion [13]. With high separation accuracy and excellent resistance to acids, bases, solvents, temperature, and microbial contamination, ceramic membranes are considered an ideal choice for clarification of fermentation broths, hydrolysis, and extraction solutions [14].

The biological potential of black tea kombucha is well established. This beverage is known to possess antioxidant, antimicrobial, anti-inflammatory, antidiabetic, anticancer, and hepatoprotective activity; it improves the immune system and treats gastric ulcers [2,3,5]. However, to the authors' knowledge, there is no literature data on the effect of MF with tubular ceramic membranes on the quality of traditional kombucha beverages. Quality of the kombucha beverages is defined through pH and total acidity, as the main indicators of the fermentation. Turbidity and total soluble solids suggest the sensory receptiveness of the kombucha beverages. Determination of the organic acids profile gives a comprehensive insight into the acidity of these products, and sensory quality as well. Reducing power is a measurement of the electron transfer ability. Antioxidant activity to hydroxyl radical indicates the capacity of kombucha beverages to neutralize these highly reactive radicals that can be generated in the human organism. Reducing power and antioxidant activity to hydroxyl radical are indicators of the antioxidant potential, a type of biological potential of kombucha products. Ascorbic acid is a very well-known antioxidant compound. Biological potential suggests the quality of a food product from a health point of view. The aim of this article was to evaluate the effect of MF on the aforementioned physicochemical properties and biological potential of black tea kombucha after MF using a tubular ceramic membrane.

MATERIAL AND METHODS

Kombucha beverage

Traditional kombucha beverage with black tea was produced using local kombucha culture with the microbiological composition described in Malbaša *et al.* [6]. Fermentation medium was produced by adding 70 g of sucrose and 1.5 g of black tea leaves to 1 L of boiling tap water. Boiling of the prepared mixture was performed for 5 min, and after 20 min, black tea leaves were removed by filtration. When the prepared sweetened black tea decoction was cooled to room temperature (25 °C), 100 mL of kombucha starter liquid (kombucha beverage obtained in the previous fermentation) was added. Fermentation lasted for 7 days at 25 °C. After the production, the beverage was subjected to MF. The cellulosic pellicle layer was removed before the MF. All analyses were performed on the beverage before the MF and samples after MF.

MF experiments

Experiments were performed with black tea kombucha, and membrane cleaning was an acid-base sequence. Membrane cleaning efficiency was evaluated by testing the water flow recovery. All experiments were performed at room temperature (25 °C), repeated three times, and the results were averaged. Experiments were performed in a cross-flow MF unit shown in Figure 1. Details can be found in the literature [15]. A single-channel ceramic tubular membrane with a nominal pore size of 200 nm (Pall Membrane Co., USA) with a length of 250 mm and an inner/outer diameter of 7/10 mm was used. The effective surface area of the membrane was 4.62×10^{-3} m^2. In each

run, 500 mL of black tea kombucha was added to the feed tank. Changing the operational parameters according to the experimental design, permeate flux was calculated from the time required to collect 10 mL of permeate. Permeate was returned to the feed tank to achieve a continuous mode of operation. At the steady state, samples of permeate were collected for the determination of analytical parameters.

Response surface methodology (RSM) was used to evaluate the impact of feed flow and transmembrane pressure. The second-degree polynomial model used to fit the responses was assessed for adequacy using the coefficient of determination (R^2) and model *p*-value. A second-degree polynomial model is represented by Eq. (1):

$$Y = b_0 + \sum b_i X_i + \sum b_{ii} X_{ii}^2 + \sum b_{ij} X_i X_j \qquad (1)$$

where *Xi* represents design variables, *b0* is the intercept (constant), *bi* is the linear, *bii* is the quadratic, and *bij* is the interaction effect of the factors; *Y* represents the response

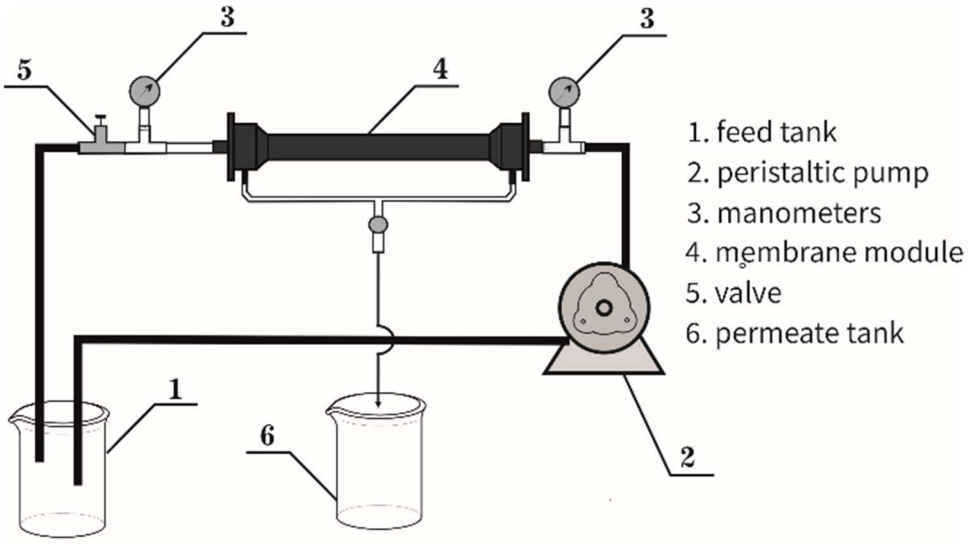

Fig. 1. Schematic diagram of MF apparatus, feed flow from tank (1) to membrane module (4), from (4) to (6) permeate flow, and from (4) to (1) retentate flow.

Physicochemical properties and biological potential

Influence of cross-flow MF on retention rate of the determined solute by the membrane during filtration was measured by the coefficient of retention (%), using Eq. (2):

$$R = 100 \times \left(1 - \frac{C_P}{C_F}\right) \qquad (2)$$

where *CP* and *CF* are the values of the solute in permeate and feed, respectively.

pH

pH values were measured using a pH-meter (ADWA AD 1000 pH/mV & Temperature Meter).

Total acidity

The total acidity was determined by a volumetric method [13]. The sample was titrated with a 0.1 mol/L standard solution of sodium hydroxide using phenolphthalein as an indicator. Results were expressed as grams of acetic acid per liter of the sample.

Total soluble solids

The total soluble solids (TSS) content was determined using a hand-held refractometer (ATC, Jiangsu Victor Instrument Meter Co., Ltd.), and the results were expressed as %Brix [17].

Turbidity

The absorbance value of the sample was measured using a spectrophotometer (LLG-uni SPEC 2 Spectrophotometer, LLG LABWARE) at 660 nm, and the turbidity was calculated by the Eqs. (3) and (4) [18]:

$$Transmittance = 100 \times 10 - absorbance \qquad (3)$$

$$Turbidity = 100 - transmittance \qquad (4)$$

Organic acids (acetic, lactic, malonic, formic, oxalic)

Reversed-phase chromatography on Agilent 1100 Series HPLC, USA, was applied for the determination of organic acids content [19]. The HPLC system consisted of a degasser, binary pump, and ZORBAX® SB-C18 column (4.6 × 150 mm, 5-µm) as the stationary phase, and a UV-DAD detector. Samples were filtered through a 0.45 µm regenerated cellulose membrane filter and, afterwards, 20 µL were directly injected into the HPLC system. Liquid chromatography in isocratic mode was performed with 6 mmol/L phosphoric acid (pH 2.1) as mobile phase and following chromatograph parameters: flow rate 1.0 mL/min, detection wavelength 220 nm, and column temperature 28 °C. External standard method calibration was done. Results were expressed in grams of organic acid per liter of the sample.

Vitamin C

Vitamin C content was analyzed by the reversed-phase HPLC method [20]. The HPLC system consisted of a degasser, binary pump, and ZORBAX® SB-C18 column (4.6 × 150 mm, 5-µm) as the stationary phase, and a UV-DAD detector. Samples were filtered through a 0.45 µm cellulosic membrane filter and, afterwards, 20 µL was injected directly into the system. The mobile phase was 0.1 mol/L ammonium-acetate (pH 5.1) in isocratic mode, with the flow rate of 0.4 mL/min, column temperature set at 40 °C, and detection wavelength of 254 nm. An external method of calibration using a vitamin C standard was performed. Vitamin C content was given in milligrams per liter of the sample.

Reducing power

Reducing power (RP) was determined by the spectrophotometric method [21] with certain modifications. To the 300 µL of the sample, 2.5 mL of 0.2 mol/L phosphate buffer (pH 6.60), and 2.5 mL of 1% potassium ferricyanide were added. The obtained solution was incubated at 50 °C for 30 min. Following, 2.5 mL of 10% trichloroacetic acid was added to the sample tubes. The 2.5 mL of the obtained solution was mixed with 2.5 mL of distilled water and 500 µL of 0.1% $FeCl_3 \times 6H_2O$. Absorbance was measured at 700 nm. The higher absorbance indicated higher reducing power.

Antioxidant activity against hydroxyl radical

Antioxidant activity to hydroxyl radical was determined by the spectrophotometric method [22] with slight modifications. To the 100 µL of the sample the 450 µL of 0.2 mol/L of sodium phosphate buffer (pH 7.00), 150 µL of 10 mmol/L of 2-deoxyribose, 150 µL of 10 mmol/L of EDTA disodium salt dihydrate, 150 µL of 10 mmol/L of $FeSO_4 \times 7H_2O$, 150 µL of 10 mmol/L of H_2O_2, and 525 µL of distilled water were added. The test tube was incubated at 37 °C for 2 h. After that, 750 µL of 2.8% trichloroacetic acid and 750 µL of 0.1% thiobarbituric acid were added, and the sample tubes were incubated at 100 °C for 10 min. Blank sample used 100 µL of distilled water instead of the sample. Absorbance was measured at 520 nm. Antioxidant activity to hydroxyl radical (AA.OH (%)) was given in percentages of inhibition and calculated using Eq. (5):

$$AA.OH(\%) = ((Ablank\ sample - Asample) \div Ablank\ sample) \times 100 \quad (5)$$

where *Ablank* sample is the absorbance of the blank sample and *Asample* is the absorbance of the sample.
All analyses were done in triplicate.

RESULTS AND DISCUSSION

Permeation flux

The permeation flux rapidly decreased with time and reached a steady state after about 1 h. The design variables and their ranges were *X1*: transmembrane pressure, TMP, (0.2, 0.6, and 1 bar) and *X2*: feed flow rate (30, 90, and 150 Lh^{-1}). The experimental plan consisted of nine variable combinations with one replication at the center point, as summarized in Table 1.

Table 1. Experimental design and steady-state permeate flux.

Exp. number	Factors		Flux
	TMP (bar)	Q (Lh^{-1})	J ($Lm^{-2}h^{-1}$)
1	0.20	150.00	52.65
2	0.60	150.00	72.38
3	1.00	150.00	88.13
4	0.20	30.00	25.17
5	0.60	30.00	21.41
6	1.00	30.00	17.44
7	0.20	90.00	30.57
8	0.60	90.00	29.41
9	1.00	90.00	40.06
10	0.60	90.00	30.00

Note: TMP, transmembrane pressure; Q, feed flow rate

The summary ANOVA results for steady state permeate flux are shown in Table 2. Quadratic polynomial equation provided more than excellent results, according to high values of the determination coefficients, suggesting that less than 1% of the variations could not be explained by the model. Lack of fit (*p*-value = 0.0923) is not significant.

Table 2. Analysis of variance (ANOVA) for steady-state permeate flux.

Source	*df*	SS	MS	*F*-value	*p*-value
Model	5	4862.22	972.44	117.53	0.0002
Residual	4	33.09	8.27		
Lack-of-fit	3	32.92	10.97	63.05	0.092
Pure error	1	0.17	0.17		
Total	9	4895.32			
	R^2		*Adj.* R^2		Adeq. Prec.
	0.993		0.985		32.0

Adequate accuracy is an indication of a signal-to-noise ratio, and its desirable value is at least 4. In this case, the flocculation efficiency ratio of 10.5085 shows that this model may be used to explore the design space and provides a suitable signal. Parity plot, Figure 2, shows reasonable agreement between the observed and the predicted permeate flux values.

Table 3 provides the coefficients of regression equations for steady state permeate flux in terms of the coded and actual variable values, together with their associated *p*-values. The significance of each coefficient was determined by *p*-values. The significance was determined at a probability level of 0.05. Linear and quadratic coefficients of feed flow rate are both statistically significant, whereas in the case of transmembrane pressure, only the linear effect is. The interaction effect is also significant.

The effects of feed flow rate and transmembrane pressure on permeate flux are given in Figure 3.

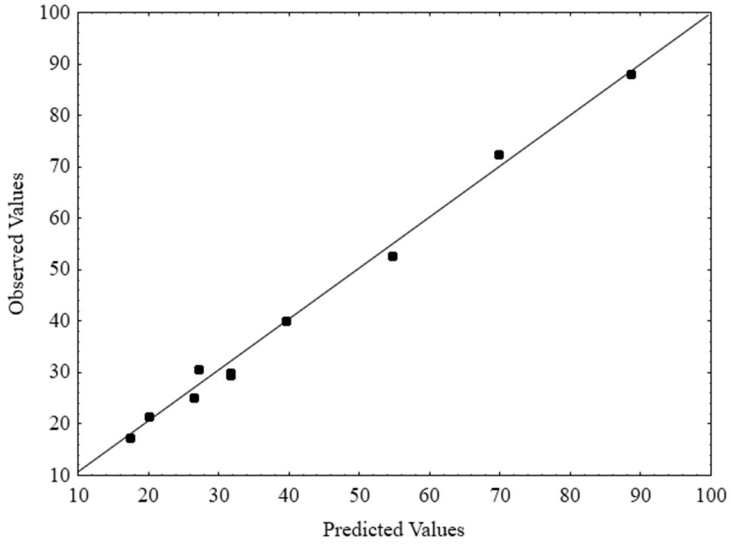

Fig. 2. Parity plot of the predicted and the observed steady state permeate flux.

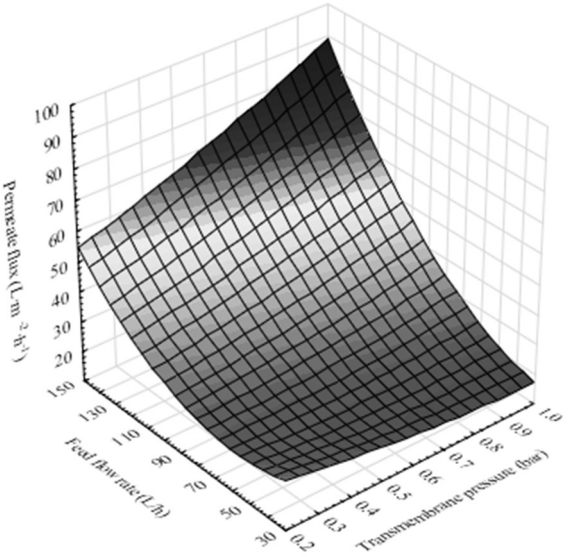

Fig. 3. The influence of transmembrane pressure and feed flow rate on the steady-state flux during kombucha MF.

Table 3. Coefficients of regression equations for steady permeate flux.

Effects	Coefficient		*p*-value
	Actual	Coded	
Intercept			
b_0	43.50	31.61	*0.0017*
Linear			
b_1	-38.54	6.21	*0.0061*
b_2	-0.53	24.86	*< 0.0001*
Quadratic			
b_{11}	11.29	1.81	0.3919
b_{22}	3.72×10^{-3}	13.39	*0.0021*
Interaction			
b_{12}	0.45	10.80	*0.0017*

As can be seen, the change in steady-state flow rate becomes more pronounced with changing feed flow rate. An increase in flow rate is observed at all transmembrane pressures. An increase in feed flow rate generates shear forces on the membrane surface, removing components deposited on the membrane surface, which reduces the formation of the polarization layer, and the generated turbulence increases the mass transfer, resulting in a higher permeate flow [23]. Higher tangential velocities tend to prevent fouling and facilitate the subsequent cleaning process of the membrane. Up to 70 Lh^{-1} increase of TMP resulted in slightly higher steady state permeate flux values. For a fixed feed flow rate in the region above 70 Lh^{-1}, the permeate flux significantly increased with the rise of TMP. Cheryan [24] explained that permeate flow is pressure dependent but at some point, becomes independent due to concentration polarization and gel formation, which are more prominent at lower feed flow rates.

pH and total acidity of black tea kombucha before and after MF

In our country, there is no legislation regarding kombucha, so all of the obtained results were discussed in regard to the published scientific literature.

Before the filtration, pH and total acidity values

amounted to 3.65 and 2.32 g/L, respectively. MF did not influence pH and total acidity values. After the filtration, pH values were in the range from 3.56 to 3.62, and total acidity amounted from 2.21 to 2.25 g/L. Coefficient of retention for pH values was around 4% and for total acidity was on stable 3%. Lower values of total acidity after MF indicated that the acidification of the beverage can be prevented by this technique [2]. The values determined for pH were in accordance with results for black tea kombucha published by Malbaša *et al.* [6]. On the other hand, total acidity was approximately two times lower in comparison to values determined by Malbaša *et al.* [6]. This difference can be attributed to the fact that kombucha fermentation was performed at different temperatures. Malbaša *et al.* [6] applied a temperature that was 3 °C higher, and it stimulated the activity of acetic acid bacteria. Daneluz *et al.* [11] also established that the MF had no influence on the pH values of kombucha feed and kombucha permeate. The kinetic diameter of the acetic acid molecule is 0.44 nm, so it passes through the applied membrane. Volatile acidity of kombucha beverages was also not influenced by the MF [11].

Total soluble solids and turbidity of black tea kombucha before and after MF

Total soluble solids are a measure of carbohydrates, proteins, fats, minerals, and organic acids. The value of TSS was not influenced by MF in a statistically significant manner. It amounted to 7.1 before and 6.9% Brix after the process. Coefficient of retention for total soluble solids was between 1 and 2%. MF reduced the TSS, regardless of the applied parameters. Daneluz *et al.* [11] established that the MF did not influence the dissolved solids (cations, anions, minerals, metals, salts) content of the filtrated kombucha beverage.

The most pronounced and statistically significant influence MF showed on the turbidity values. They were reduced by 7–9 times, and after the MF, turbidity was in the range 4.28–5.59 cm^{-1}. The coefficient of retention for turbidity was around 86% to 89%. According to the dimensions of constituents of kombucha, the membrane applied in this study retained, for example, yeasts and acetic acid bacteria, since they are about 10 times larger than the pore size. This retention resulted in visibly clearer kombucha beverages. These results are in accordance with the ones published by Daneluz *et al.* [11], who also observed a significant reduction in turbidity of kombucha products after MF. These results are presented in Figure 4a.

Organic acids and vitamin C content of black tea kombucha before and after MF

The examined organic acids (acetic, lactic, malonic, formic, oxalic) and vitamin C were detected and quantified in all samples. The content of lactic, formic, and oxalic acid was not influenced by the MF. The content range for lactic acid was 0.13–0.14 g/L, for formic acid, it was 0.07–0.09 g/L, and for oxalic acid, from 0.11–0.12 g/L. The acetic acid content was decreased after the MF and was in the range 1.19–1.22 g/L. Before the process, it amounted to 1.25 g/L. The highest malonic acid value was determined before the MF (0.21 g/L), and after the process, the determined values were in the range 0.15–0.17 g/L. The content pattern of vitamin C was the one established for acetic and malonic acid. Before the MF, it amounted to 2.55 mg/L, and after the process, it was decreased in the range of 2.17–2.33 mg/L.

The coefficient of retention was the highest for malonic acid, and it was around 20% to 30%. From the product quality point of view, higher values of feed flow rate, under all transmembrane pressure values, showed to be more suitable. For vitamin C, the coefficient of retention was around 10%. For all other organic acids, it was lower than 10% and the value was stable for oxalic acid.

This manuscript gives the first insight into the influence of MF on vitamin C and organic acids content, as well as the antioxidant potential of traditional kombucha beverages. All of the examined molecules pass through the membrane, which is in accordance with the size of their molecules. The largest one is the ascorbic acid molecule (59.8 nm), the size of malonic acid is around 0.8 nm, the kinetic diameter of formic acid is 0.4 nm, while the dimensions of others are below 0.2 nm.

Colantuono *et al.* [12] determined that the MF process mainly caused the lowering of quinic, malic, tartaric, and citric acid content in raw pomegranate juice. During the MF of mulberry wine, a small decrease in malic and succinic acid content was established, whilst contents of acetic, lactic, tartaric, and citric acid were not influenced by the filtration process [25].

Vitamin C content was not influenced by MF of acerola juice, when a membrane with 0.3 μm was applied [26]. The results of this study, regarding vitamin C content, follow the same trend as Matta *et al.* [26]. Vieira *et al.* [27] established that vitamin C content was not influenced by the MF with a 200 nm pore size membrane, when performed at 20, 30, and 40 °C. The temperature of 50 °C caused a decrease in ascorbic acid content [27]. These results are presented in Figure 4b.

Reducing power and antioxidant activity to the hydroxyl radical of black tea kombucha before and after MF

Reducing power before the MF was higher in comparison to samples after the filtration. The highest reducing power value was in sample 0 (0.510). Coefficient of retention for reducing power was between approximately 0 to around 30%, depending on the applied process parameters. Lower values of feed flow rate and the lowest and highest transmembrane pressure were found to be more suitable for better product quality characteristics.

Antioxidant activity against hydroxyl radical was the highest for sample 0 (40.31%). All other samples had lower activity in comparison to the value measured before the MF. The coefficient of retention for antioxidant activity to hydroxyl radical was lower than that determined for the reducing power. It was in the range from approximately 0 to around 20%, depending on the process parameters. On average, higher feed flow rate values under all transmembrane pressure values were more favorable for the product characteristics.

The antioxidant potential of the majority of the

examined samples was decreased after the MF, which was in accordance with the results published by Lachowicz *et al.* [28]. This trend was most pronounced for the 200 nm membrane [28]. Obtained results presented in Figure 4c indicated that compounds responsible for antioxidant potential were retained by the applied membrane. The reduction in antioxidant potential was more pronounced for reducing power than for the antioxidant activity to hydroxyl radical, on the basis of the coefficient of retention values. Since both parameters were decreased, this fact should be taken as a compromise when applying MF in kombucha beverage production.

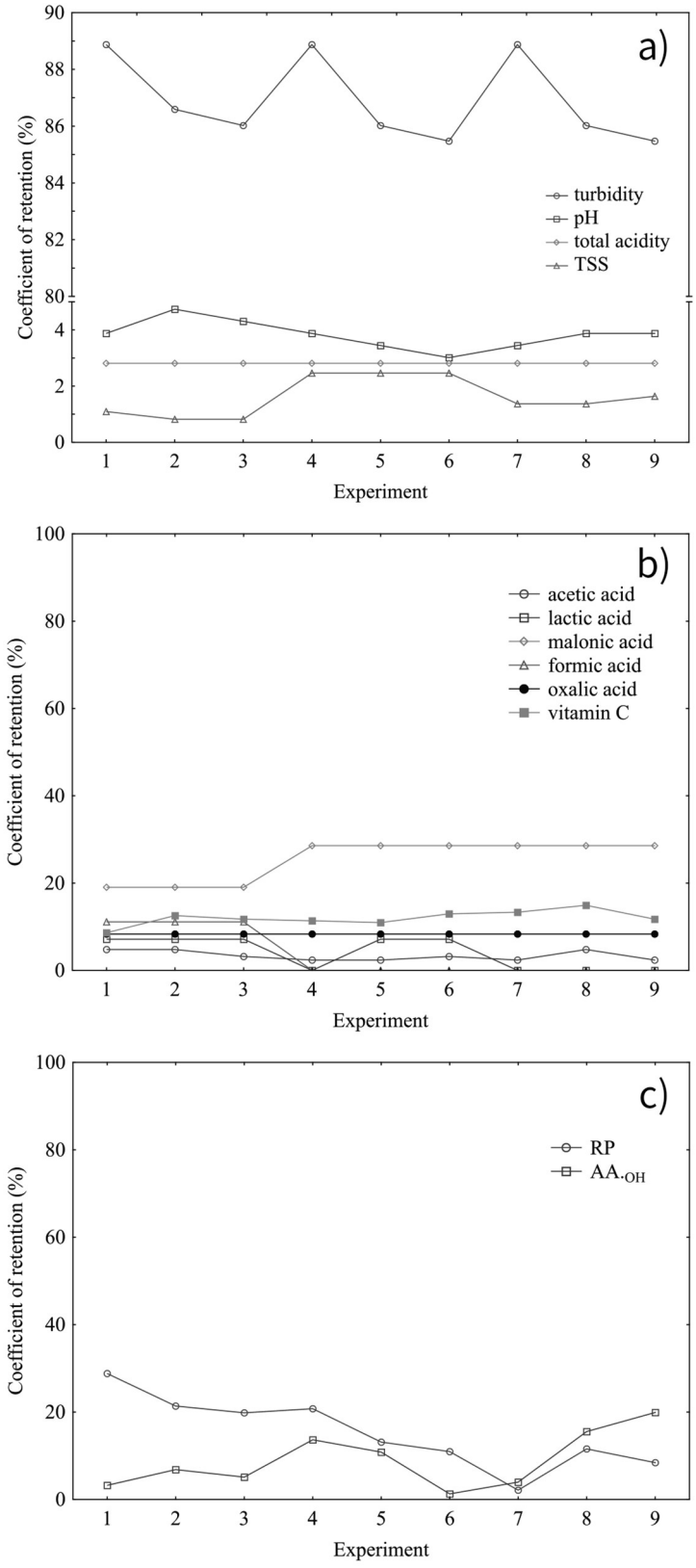

Fig. 4. Coefficient of retention for a) pH, total acidity, turbidity, and TSS; b) organic acids and vitamin C, and c) antioxidant potential.

CONCLUSION

The examined type of MF can be successfully applied in the traditional kombucha beverage production. Maximum permeate flux, around 90 $Lm^{-2}h^{-1}$, was obtained for the highest feed flow rate and transmembrane pressure of 1 bar. MF showed the main influence on the turbidity of the kombucha beverage, which was lowered, and therefore, the quality in the means of sensory acceptance of the beverage was improved. Low values of the coefficient of retention suggested that MF had a mild influence on the quality characteristics (pH, total acidity, total soluble solids, organic acids, vitamin C, and biological potential) of the examined kombucha beverage. Further investigation related to MF of kombucha beverages should provide in-depth research on the remaining microorganisms and preservation.

ACKNOWLEDGEMENT

This work was supported by the Ministry of Science, Technological Development and Innovations, Republic of Serbia, under Grant numbers 451-03-137/2025-03/ 200134 and 451-03-136/2025-03/ 200134.

REFERENCES

[1] R. Hallak, I. Onur, C. Lee, PLoS ONE 17 (2022) e0267726. https://doi.org/10.1371/journal.pone.0267726.
[2] R.M.D. Coelho, A.L. de Almeida, R.Q.G. do Amaral, R.N. da Mota, P.H.M. de Sousa, Int. J. Gastron. Food Sci. 22 (2020) 100272. https://doi.org/10.1016/j.ijgfs.2020.100272.
[3] S. Vukmanović, J. Vitas, R. Malbaša, in Kombucha Technology, Traceability, and Health-Promoting Effects, N.E. Rocha-Guzmán, R.F. González-Laredo, J.A. Gallegos-Infante, M.R. Moreno-Jiménez Eds., Academic Press, Elsevier, Amsterdam (2025), p. 69-89. https://doi.org/10.1016/B978-0-443-13297-1.00012-7.
[4] R. Malbaša, J. Vitas, S. Vukmanović, in Kombucha Technology, Traceability, and Health-Promoting Effects, N.E. Rocha-Guzmán, R.F. González-Laredo, J.A. Gallegos-Infante, M.R. Moreno-Jiménez Eds., Academic Press, Elsevier, Amsterdam (2025), p. 39-51. https://doi.org/10.1016/B978-0-443-13297-1.00003-6.
[5] R. Jayabalan, R.V. Malbaša, E.S. Lončar, J.S. Vitas, M. Sathishkumar, Compr. Rev. Food Sci. Food Saf. 13 (2014) 538-550. https://doi.org/10.1111/1541-4337.12073 .
[6] R.V. Malbaša, E.S. Lončar, J.S. Vitas, J.M. Čanadanović-Brunet, Food Chem. 127 (2011) 1727-1731. https://doi.org/10.1016/j.foodchem.2011.02.048.
[7] Rules on the quality of refreshing non-alcoholic drinks, Official Gazette of RS 88 (2017) 1-10; 124 (2020) 1-5.
[8] J. Daneluz, G.F. da Silva, J. Duarte, T.C. Turossi, V. dos Santos, C. Baldasso, A.C. Daneluz, J. Ind. Eng. Chem. 126 (2023) 264-269. https://doi.org/10.1016/j.jiec.2023.06.015.
[9] J. Bader, C.J. Brigham, U. Stahl, M.K. Popović, in Fermented Beverages, A.M. Grumezescu, A.M. Holban Eds., Woodhead Publishing, (2019), 67-101. https://doi.org/10.1016/B978-0-12-815271-3.00003-8.
[10] M. Peyravi, M. Jahanshahi, S. Banafti, in Application of Membrane Technology in Beverage Production and Safety, A.M. Grumezescu, A.M. Holban Eds., Academic Press, Cambridge, MA, United States (2020), p. 271-308. https://doi.org/10.1016/B978-0-12-816679-6.00008-5.
[11] J. Daneluz, G.F. da Silva, J. Duarte, T.C. Turossi, V. dos Santos, C. Baldasso, A.C. Daneluz, Food Chem. Adv. 3 (2023) 100451. https://doi.org/10.1016/j.focha.2023.100451.
[12] Colantuono, P. Vitaglione, N. Manzo, G. Blaiotta, I. Montefusco, A. Marrazzo, F. Pizzolongo, R. Romano, J. Sci. Food Agric. 98 (2018) 3324-3332. https://doi.org/10.1002/jsfa.8836.
[13] Li, W. Sun, Z. Lu, X. Ao, S. Li, Water Res. 175 (2020) 115674. https://doi.org/10.1016/j.watres.2020.115674.
[14] Nie, W. Luan, X. Chen, L. Li, K. Wei, M. Qiu, Y. Fan, J. Environ. Chem. Eng. 11 (2023) 109820. https://doi.org/10.1016/j.jece.2023.109820.
[15] Jokić, Z. Zavargo, Z. Šereš, M. Tekić, J. Membr. Sci. 350 (2010) 269-278. https://doi.org/10.1016/j.memsci.2009.12.037.
[16] R.V. Malbaša, E.S. Lončar, M. Djurić, I. Došenović, Food Chem. 108 (2008) 926-932. https://doi.org/10.1016/j.foodchem.2007.11.069.
[17] N. Yuliana, F. Nurainy, G.W. Sari, W. Sumardi, E.L. Widiastuti, Appl. Food Res. 3 (2023) 100297. https://doi.org/10.1016/j.afres.2023.100297.
[18] S. Wibowo, E.A. Essel, S. De Man, N. Bernaert, B. Van Droogenbroeck, T. Grauwet, A. Van Loey, M. Hendrickx, Innov. Food Sci. Emerg. Technol. 54 (2019) 64-77 https://doi.org/10.1016/j.ifset.2019.03.004.
[19] J.S. Vitas, A.D. Cvetanović, P.Z. Mašković, J.V. Švarc-Gajić, R.V. Malbaša, J. Funct. Foods 44 (2018) 95-102. https://doi.org/10.1016/j.jff.2018.02.019.
[20] S. Vukmanović, J. Vitas, R. Malbaša, J. Food Process. Preserv. 44 (2020) e14627. https://doi.org/10.1111/jfpp.14627.
[21] Yıldırım, A. Mavi, A.A. Kara, J. Agric. Food Chem. 49 (2001) 4083-4089. https://doi.org/10.1021/jf0103572.
[22] S. Deeseenthum, J. Pejovic, Biotechnol. 9 (2010) 332-337. https://doi.org/10.3923/biotech.2010.332.337.
[23] K. Rezzadori, L. Serpa, F.M. Penha, R.R. Petrus, J.C.C. Petrus, Food Sci. Technol. 34 (2014) 10030. https://doi.org/10.1590/S0101-20612014000100030.

[24] M. Cheryan, Ultrafiltration and Microfiltration Handbook, 2nd ed., CRC Press, Boca Raton (1998), p. 113-126. https://doi.org/10.1201/9781482278743.
[25] Q.M. Xiong, J. Liu, M. Liu, C.H. Shen, X.C. Yu, C.D. Wu, J. Huang, R.Q. Zhou, Y. Jin, RSC Adv. 10 (2020) 655-665. https://doi.org/10.1039/C9RA09034G.
[26] V.M. Matta, R.H. Moretti, L.M.C. Cabral, J. Food Eng. 61 (2004) 477-482. https://doi.org/10.1016/S0260-8774(03)00154-7.
[27] A.H. Vieira, C.F. Balthazar, J.T. Guimaraes, R.S. Rocha, M.M. Pagani, E.A. Esmerino, M.C. Silva, R.S.L. Raices, R.V. Tonon, L.M.C. Cabral, E.H.M. Walter, M. Q. Freitas, A.G. Cruz, Food Res. Int. 132 (2020) 109060. https://doi.org/10.1016/j.foodres.2020.109060.
[28] S. Lachowicz, J. Oszmiański, J. Kolniak-Ostek, D. Stokłosa, Eur. Food Res. Technol. 245 (2019) 1263-1275. https://doi.org/10.1007/s00217-019-03246-8.

JASMINA VITAS

ALEKSANDAR JOKIĆ

NATAŠA LUKIĆ

SELENA DMITROVIĆ

DANICA PIPER

RADOMIR MALBAŠA

Univerzitet u Novom Sadu

Tehnološki fakultet Novi Sad

Novi Sad, Srbija

UNAKRSNA MIKROFILTRACIJA TRADICIONALNOG KOMBUHA NAPITKA PRIMENOM KERAMIČKE CEVNE MEMBRANE

Tradicionalni kombuha napitak se proizvodi metaboličkom aktivnošću mikroorganizama prisutnih u kulturi kombuhe na zaslađenom crnom čaju i sobnoj temperaturi. Cilj ovog rada je bilo ispitivanje uticaja unakrsne mikrofiltracije na kvalitet proizvedenog napitka. Za ispitivanje kvaliteta kombuha napitka merene su i određivane vrednost pH, ukupna kiselost, ukupne rastvorljive materije, mutnoća, organske kiseline, in vitro antioksidativni potencijal, i vitamin C, kao antioksidativno jedinjenje. Radni parametri procesa su bili transmembranski pritisak (0,2, 0,6 i 1 bar) i protok kombuha napitka (30, 90 i 150 Lh-1). Maksimalni fluks permeata je bio postignut pri najvećim vrednostima protoka kombuha napitka i transmembranskog pritiska. Mikrofiltracija je održala pH, ukupnu kiselost, ukupne rastvorljive materije, mlečnu, mravlju i oksalnu kiselinu, poboljšala mutnoću i sadržaj sirćetne kiseline, te umanjila malonsku kiselinu, vitamin C i antioksidativni potencijal. Nakon mikrofiltracije, mutnoća je bila smanjena 7 do 9 puta, a sadržaj sirćetne kiseline je iznosio oko 1,20 g/L, što je ukazalo na inhibiciju u nagomilavanju kiseline. Vrednosti koeficijenta retencije za sve ispitane parametre kvaliteta, sem mutnoće, su ukazale da je sveukupni uticaj mikrofiltracije bio umeren.

Ključne reči: SCOBY, membranska filtracija, fizičko-hemijske osobine, biološki potencijal.

NAUČNI RAD

CI&CEQ
Chemical Industry & Chemical Engineering Quarterly

Available online at
Association of the Chemical Engineers of Serbia AChE
www.ache.org.rs/CICEQ

Chem. Ind. Chem. Eng. Q. 32 (3) 245–255 (2026) CI&CEQ

MEHMET SOYDAN
İBRAHIM DOYMAZ

Yildiz Technical University,
Department of Chemical Engineering
İstanbul, Türkiyea

INFRARED DRYING OF CARROT SLICES: EFFECT OF POWER LEVELS ON KINETICS AND ENERGY EFFICIENCY

Highlights

- The drying process of carrot slices using an infrared dryer was conducted.
- Drying time decreased with increasing infrared power level.
- The Midilli & Kucuk model better fits all the applied drying conditions.
- The highest effective moisture diffusivity was obtained in samples dried at an 88 W IR power level.

Abstract

The aim of this study is to optimize the drying conditions for yellow carrots by investigating the effects of varying infrared (IR) power levels on drying kinetics. Following drying tests at IR power levels of 38, 50, 62, 74, and 88 W, the initial moisture content of carrot slices (6.95 kg water/kg dry matter) was decreased to 0.11 kg water/kg dry matter. Drying times ranged from 300 minutes at 38 W to 110 minutes at 88 W, demonstrating an inverse relationship between IR power and drying duration. Higher IR power levels accelerated the drying rate by enhancing energy transfer, which promoted moisture removal efficiency. Effective diffusion coefficients, calculated as ranging from 7.73×10^{-10} to 2.21×10^{-9} m²/s for the power levels of 38 W to 88 W, indicate an increase in moisture migration with higher power. The process's energy requirements were reflected in the activation energy for moisture diffusion (1.967 kW/kg). The Midilli and Kucuk model offered the best fit for characterizing the drying behaviour, and statistical analysis validated the model's correctness. These findings provide valuable insights for optimizing IR drying conditions to enhance the efficiency and quality of yellow carrot drying processes.

Keywords: Infrared drying, mathematical modelling, drying kinetics, diffusion coefficient, activation energy.

SCIENTIFIC PAPER

UDC 633.43:66.047.3.085.1:519.87

INTRODUCTION

Carrots, cultivated worldwide for over two millennia, represent a versatile root vegetable characterized by variations in shape, size, and colour, with the orange type being predominant. Carrots, which have only 171.5 kJ per 100 grams, have several health benefits, such as preventing diabetes, heart disease, night blindness, cataracts, and some types of cancer [1]. Post-harvest decay remains a major obstacle to extending the shelf life of vegetables, with approximately 17% of total produce lost during post-harvest handling. Various preservation techniques are employed to mitigate this issue, including refrigeration and controlled atmosphere storage. While exposure to elevated temperatures can result in wilting and reduce the aesthetic quality of carrots, significant quantities are dried in many agricultural regions to improve durability, lower transportation weight, and maintain both flavour and nutritional integrity [2].

The primary method of heat transfer in drying operations is convection, which causes water to evaporate into the air as heat is transferred from hot air to the product. However, there are several drawbacks to convective drying of agricultural goods, mostly related to the indirect heating mechanism via air, such as long drying durations, variable product quality, low efficiency, and high energy requirements. Alternative drying methods have been developed because of these inefficiencies [3].

Infrared drying presents numerous advantages over traditional methods, including faster drying times, greater energy efficiency, uniform temperature distribution, superior product quality, improved process control, high heat transfer rates, spatial efficiency, and environmental sustainability. Recent advancements in radiator technology have enhanced its efficiency and compact design. The absorption of IR energy by water is critical to drying kinetics,

Correspondence: İ. Doymaz, Yildiz Technical University, Department of Chemical Engineering, 34220 Esenler, İstanbul, Türkiye.
Email: doymaz@yildiz.edu.tr
Paper received: 28 June 2025
Paper revised: 15 October 2025
Paper accepted: 19 November 2025

https://doi.org/10.2298/CICEQ250628028S

with moist, porous materials enabling deeper radiation penetration, which diminishes as moisture content reduces [4,5].

A precise method for describing drying kinetics, especially in agricultural products, is mathematical modelling. This approach relies on the application of correlation and regression statistical methods to formulate equations that accurately depict the dynamics of the drying process. Various experimental models have been extensively studied, particularly for the falling rate drying phase. Frequently utilized models include linear, power, exponential, Arrhenius, and logarithmic functions, with polynomial models applied when these alternatives yield low determination coefficients [6,7].

This research seeks to establish a predictive model for moisture reduction in carrot drying, aligning quality parameters with the product's thermal and moisture behaviours to enhance process control precision. Mathematical modeling provides a cost-effective alternative for manufacturers, fostering innovation in product and process development while circumventing the high costs associated with experimental trials. The study is to simulate the infrared drying process for carrot slices, evaluate the drying process's energy efficiency at different IR power levels, and ascertain the activation energy needed for efficient moisture removal. The diffusion coefficient of sample drying was calculated, and a correlation between the mathematical models and moisture ratio, indicating water loss, was established. Statistical analysis was conducted to validate and verify the models. Additionally, the study intends to assess the effectiveness of infrared drying as a drying method with the dynamics of heat and mass transfer during the process of drying samples.

This study aims to develop a predictive model for moisture reduction during the infrared drying of carrot slices, integrating key quality parameters with the fundamental thermophysical and hydric behaviour of the product to achieve superior process control. A critical synthesis of the extant literature identified a pronounced research gap: although investigations into drying kinetics, quality degradation, and empirical modeling are plentiful, there is a conspicuous absence of systematic analysis concerning energy efficiency across a spectrum of infrared power densities. This work directly addresses this omission by conducting a concurrent investigation into the drying characteristics and energy consumption metrics of carrot slices under infrared radiation. The employment of mathematical modeling presents an economically viable strategy for industry, circumventing the prohibitive costs of extensive experimental trials and thereby accelerating innovation in both product and process development. Our methodology entails the determination of the effective moisture diffusivity and the activation energy requisite for efficient desorption. Furthermore, we established a rigorous correlation between theoretical models and the experimental moisture ratio to quantitatively describe the dehydration process. The validity of these models was ascertained through robust statistical verification. Ultimately, this research provided a holistic evaluation of infrared drying by synergistically examining energy efficiency, kinetic parameters, and the underlying heat and mass transfer phenomena. This integrated approach yields novel insights for the optimization of energy utilization without compromising drying efficacy, thereby contributing advanced and actionable knowledge to the field of food engineering and drying technology.

MATERIAL AND METHODS

Materials

Freshly harvested carrots (*Daucus carota* L. subsp. sativus) were obtained from the local market in Beypazarı (Türkiye). The samples were cut into uniform discs (6 ± 0.1 mm thickness, 40 ± 0.1 mm diameter). The initial moisture content, determined by the AOAC method [8], was 87.42% (wet basis).

Experimental procedure

A laboratory-scale infrared dryer (Snijders Moisture Balance, Snijders b.v., Tilburg, Holland) with a power range of 38 W to 88 W was used for the drying tests. Carrot slices were placed evenly and homogeneously across an aluminium tray, ensuring a uniform thin-layer distribution. A sample mass of 38±0.1 g, consisting of eight cylindrical carrot slices, was loaded in a single layer for each drying run. The drying process was carried out at varying infrared power levels, set through the equipment's control unit. Moisture loss was measured at 10-minute intervals with a digital balance (Mettler-Toledo AG, Greifensee, Switzerland, model BB3000), with an accuracy of 0.1 g. The drying was continued until the samples reached a final moisture content of 10% (wb). The carrot slices were dehydrated to a final moisture content of approximately 13–14% (wet basis), which is generally regarded as the optimal level for safe storage [9]. In the present study, however, a target moisture level of around 10% was selected to ensure the stability of the dried samples for subsequent analyses. Drying beyond this point was intentionally avoided for two primary reasons: energy efficiency and product quality preservation. Excessive drying below 10% would not only lead to unnecessary energy consumption but also increase the risk of quality degradation, as prolonged exposure to hot air can adversely affect both the texture and the nutritional properties of carrots. Moreover, as the moisture content decreases, the driving force for mass transfer between the carrot slices and the drying air diminishes, thereby extending drying time. This prolonged process can further exacerbate quality losses. In addition, the phenomenon of case hardening [10] - a condition where a hardened surface layer forms during drying – impedes effective moisture removal, making it more difficult to reduce the moisture content below 10%. For these reasons, maintaining the final moisture level at approximately 10% was considered both a practical and scientifically sound approach. After drying, the samples were cooled and sealed in low-density polyethylene (LDPE) bags for storage. To form the drying curves, the average moisture content was determined after each experiment was run in triplicate.

Mathematical modeling

Moisture content was computed with the equation:

$$M = \frac{M_w}{M_d} \quad (1)$$

where M_w is the sample's wet weight (kg), M_d is its dry weight (kg), and M is the moisture content (kg water/kg dry matter). The eleven thin-layer drying models displayed in Table 1 were fitted to the data gathered from the drying of carrot slices. Eq. (2) was used to determine the moisture ratio (MR) values from the designated models.

$$MR = \frac{M_t - M_e}{M_0 - M_e} \quad (2)$$

where M_t, M_0, and M_e are the moisture content at any time, the initial moisture content, and the equilibrium moisture content (kg water/kg dry matter), respectively, and t is the drying time (min). The values of M_e are minute relative to M_t and M_0 for a long drying period, so a simplified form of the moisture ratio can be used as expressed in Eq. (3):

$$MR = \frac{M_t}{M_0} \quad (3)$$

The drying rate *(DR)* of carrot slices was calculated using Eq. (4):

$$DR = \frac{M_t - M_{t+\Delta t}}{\Delta t} \quad (4)$$

where M_t and $M_{t+\Delta t}$ is moisture contents at t and $t+\Delta t$ (kg water/kg dry matter), respectively, and t is time (min).

Statistical analysis

To analyze the data, Statistica 10.0 (StatSoft Inc., Tulsa, OK, USA) was utilized. The model parameters were estimated using a non-linear regression technique, and the fit was maximized using the Levenberg-Marquardt technique. Three statistical criteria–the coefficient of determination (R^2), reduced chi-square (χ^2), and root mean square error (RMSE)–were used to evaluate how well the model fit the experimental data. These metrics were calculated using specific equations, providing a comprehensive evaluation of the models' predictive performance by measuring the goodness-of-fit and deviation of the predicted values from the observed data. The aforementioned parameters were computed using the mathematical expressions in Eqs. (5), (6), and (7). These formulas are designed to quantify the accuracy and reliability of the model predictions. As a measure of the model's explanatory capacity, the R^2 shows the percentage of variance in the observed data that can be explained by the model. The χ^2 assesses the goodness-of-fit by accounting for the degree of freedom, while the RMSE quantifies the average deviation between predicted and observed values, offering insight into the model's predictive precision [22].

$$R^2 = 1 - \frac{\sum_{i=1}^{N}(MR_{\exp,i} - MR_{pre,i})^2}{\sum_{i=1}^{N}(MR_{pre} - MR_{\exp,i})^2} \quad (5)$$

$$x^2 = \frac{\sum_{i=1}^{N}(MR_{exp,i} - MR_{pre,i})^2}{N-n} \quad (6)$$

$$RMSE = \left[\frac{1}{N}\sum_{i=1}^{N}\left(MR_{pre,i} - MR_{\exp,i}\right)^2\right]^{\frac{1}{2}} \quad (7)$$

The experimentally observed and model-predicted moisture ratio values are denoted by MR_{exp} and MR_{pre}, respectively, in these equations. N refers to the number of parameters, whereas n indicates the total number of experimental data points. The model with the lowest values of RMSE and χ^2; the highest R^2-value indicated the best fit for explaining the drying behaviour of the samples [23].

Assessment of effective moisture diffusivity

Internal diffusion processes primarily regulate the moisture transfer during the lowering rate stage, which is when the drying process usually takes place. Fick's second rule of unsteady-state diffusion is widely used to characterize the drying kinetics in this phase for a range of materials. This equation provides a mathematical framework that links the concentration gradient of moisture within the material to the rate of diffusion, allowing a comprehensive understanding of how moisture transfers from the interior to the surface during drying. By utilizing Fick's second law, researchers can effectively model and predict the dynamics of moisture removal, facilitating the optimization of drying processes and improving the quality of the final product [24]:

$$\frac{\partial M}{\partial t} = \nabla\left(D_{\text{eff}}\nabla M\right) \quad (8)$$

When Crank [25] solved the diffusion equation (Eq. 8) for the slab geometry, it was assumed that the initial moisture distribution was uniform, with low external resistance, constant diffusion, and minimal shrinkage:

$$MR = \frac{8}{\pi^2}\sum_{n=0}^{\infty}\frac{1}{(2n+1)^2}\exp\left(-\frac{(2n+1)^2\pi^2 D_{\text{eff}}t}{4L^2}\right) \quad (9)$$

where n is a positive integer, L is the slab's half-thickness in samples (m), and D_{eff} is the effective moisture diffusivity (m^2/s).

Eq. (9) can be simplified to get an approximate but reasonable prediction of drying kinetics during the early phases of the decreasing rate period when carrot drying is viewed as an infinite slab geometry. Only the series' dominating term is considered in this simplification, which is predicated on lengthy drying times. When characterizing the behaviour of moisture diffusion during prolonged drying periods, this reduction offers a compromise between computing efficiency and allowable inaccuracy [26]. The approximate analytical solution of Eq. (9) for slab shape is provided in Eq. (10) below, assuming a uniform starting moisture distribution, negligible external mass transfer resistance, and minimum shrinkage.

$$MR = \frac{8}{\pi^2}\exp\left(-\frac{\pi^2 D_{\text{eff}}t}{4L^2}\right) \quad (10)$$

Slope from Eq. (11) is used to determine effective moisture diffusivity. A linear relationship with a slope represented by K is obtained when the natural logarithm of the moisture ratio (MR) is plotted versus time. From this, Eq. (11) is derived, allowing for a precise estimation of effective moisture diffusivity. This approach provides a robust method for analysing the drying kinetics, as the linearity in the plot reflects the diffusion-controlled nature of

the moisture removal process, further enabling the accurate quantification of diffusivity [27]:

$$K = \frac{\pi^2 D_{\text{eff}}}{4L^2} \quad (11)$$

Calculation of the activation energy

A modified form of the Arrhenius equation was applied to describe the relationship between effective diffusivity and the ratio of infrared power to sample weight. This approach allows for the calculation of activation energy, which was determined using Eq. (12). The adapted model provides valuable insight into how varying infrared power levels influence the moisture removal process, enabling more precise control and optimization of drying conditions to improve efficiency and product quality [28].

$$D_{\text{eff}} = D_0 \exp\left(-\frac{E_a m}{P}\right) \quad (12)$$

In this equation, D_0 denotes the pre-exponential factor (m²/s), E_a is the activation energy (W/kg), P is the infrared power (W), and m is the sample weight (kg), collectively governing the dependence of effective moisture diffusivity on power input.

Efficiency of drying process

Drying efficiency measures the effectiveness of energy utilization in the moisture removal process during drying. It serves as a key indicator of the performance of drying systems, reflecting the equilibrium between energy consumption and the rate of moisture evaporation. High drying efficiency suggests that a substantial portion of the input energy is efficiently used for moisture extraction, minimizing energy wastage. Several factors, including drying temperature, infrared power levels, air velocity, and the intrinsic properties of the material, significantly impact drying efficiency. Optimizing these variables is essential for enhancing process sustainability, reducing energy consumption, and lowering operational costs [29,30].

Infrared drying efficiency was calculated as the ratio of the total heat energy provided by the drying system to the thermal energy needed to remove the moisture from the carrot slices. This metric provides insight into how effectively the energy delivered by the dryer is harnessed for the intended purpose of moisture removal, offering a quantitative measure of energy utilization. A higher ratio indicates greater efficiency, signifying that a larger portion of the supplied heat is being effectively converted into latent heat for water evaporation, rather than being lost through other processes, such as heat dissipation to the surroundings [31].

$$\eta = \left(\frac{m_w \lambda_w}{P t}\right) \times 100 \quad (13)$$

In Eq. (13), η represents the infrared drying efficiency (%), where P is the applied infrared power (W), m_w is the mass of evaporated water (g), and t is the drying duration (min). The latent heat of vaporization of water (λ_w), taken as 2257 J/g, specifies the energy required for phase transition under isothermal conditions. This formulation provides a concise yet rigorous means of quantifying the proportion of infrared energy effectively utilized for moisture removal, offering a robust basis for evaluating energy efficiency, optimizing process parameters, and advancing sustainable drying technologies [28].

RESULTS AND DISCUSSION

Drying curves

Drying behavior of carrot slices under the infrared method at varying power levels, as depicted in Fig. 1, demonstrates that moisture removal rates increase with rising infrared power. This is due to a greater moisture concentration gradient within the carrot slices, accelerating moisture diffusion. The higher power densities of the halogen lamp of the infrared dryer, such as 88 W, significantly reduce the drying time.

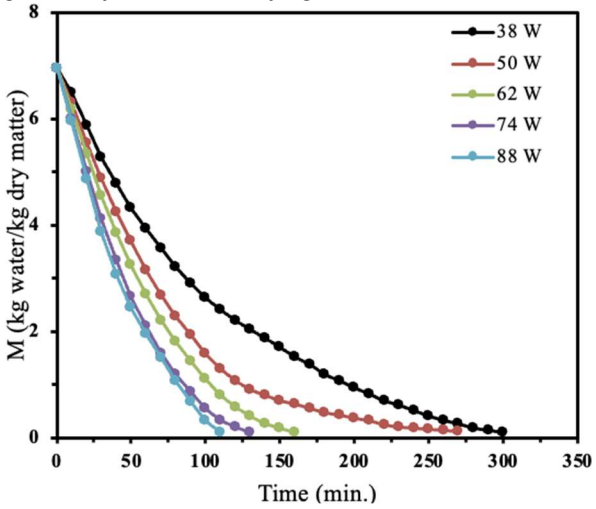

Figure 1. Carrot slice drying curves at different levels of infrared power.

Since larger energy rates are applied to the material, which results in the enlargement of both intracellular and intercellular pores in the carrot tissue, increased infrared power levels enable a quick decrease in the moisture content of the carrot. This structural change enhances water vapour diffusion from the carrot slices to the surrounding environment, thus lowering drying time. Such observations align with prior studies, including carrot [32], apple [33], and lemon slices [34]. In these studies, high drying intensities promoted structural cracking and shortened the overall processing time by improving water diffusion.

Fig. 2 shows the drying rate curves for carrot slices, where no drying period at a constant rate was observed for all experimental conditions, indicating that the drying process occurred after a short preheating period with a completely falling-rate period. This behaviour highlights diffusion as the main mechanism controlling moisture transport in carrot slices by showing a consistent drop in moisture content over the course of the drying period. This is in agreement with previously published studies on root vegetables, which emphasize that moisture removal during IR drying is predominantly governed by internal moisture diffusion rather than surface evaporation [2]. Furthermore, an increase in infrared power led to an elevated drying rate, signifying that higher infrared power enhances both heat and mass transfer, thereby accelerating water loss from the samples.

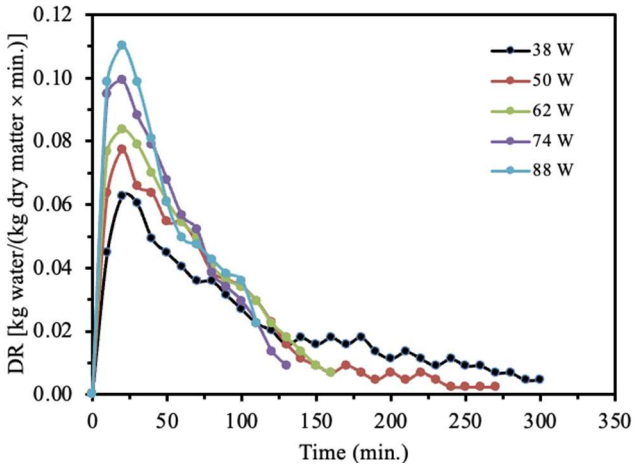

Figure 2. Carrot slice drying rate curves with respect to drying time for different IR power levels.

Initial drying rates were higher during the drying process, but they gradually decreased as the moisture content declined. This reduction in drying rate is likely due to the decreased porosity of the samples, resulting from shrinkage over time, which heightens resistance to water migration and further slows the drying rate. This shrinkage effect has been well documented in convective and infrared drying studies, where tissue densification narrows capillary pathways and lowers effective moisture diffusivity. These findings align well with prior research on drying kinetics in agricultural materials [35-37]. These studies similarly identified a falling-rate period in the drying process, attributed to structural transformations within the material that reduce moisture diffusivity. Such structural changes can hinder moisture migration pathways, thus decelerating the drying rate. This phase underscores the importance of internal structural shifts, which profoundly impact moisture retention, drying efficiency, and overall product quality throughout the drying cycle.

Modelling of thin-layer drying processes for carrot slices

The drying experiments' moisture content data were transformed into moisture ratio (MR) values, as indicated in Table 1, and these values were then applied to fit various thin-layer drying models. Eleven distinct models were evaluated to determine which one would be best for forecasting sample drying times. To assess model accuracy, statistical indices, including the R^2, the χ^2, and *RMSE*, were calculated to measure the goodness of fit, as presented in Eqs. (4), (5), and (6). The selection criterion for the optimal model was based on the highest R^2 value combined with the lowest χ^2 and *RMSE* values. For the range of experiments, the models yielded R^2 values between 0.988 and 1.000, *RMSE* values from 0.0033 to 0.0507, and χ^2 values ranging from 0.0014 to 0.3114. These statistical outputs provided insight into the precision and predictive accuracy of each model.

Table 2 presents the parameter estimates for eleven mathematical models applied to carrot slices, reflecting variations attributable to different infrared power levels. Each parameter estimate achieved statistical significance, meeting or exceeding a 1% significance level, thereby demonstrating the models' robustness and precision in characterizing drying kinetics under diverse experimental conditions. Notably, the Midilli & Kucuk model exhibited superior performance relative to the other models, as evidenced by its highest R^2 and lowest values for χ^2 and RMSE, indicating its exceptional fit and reliability in accurately modelling the drying behaviour.

Table 1. Semi-empirical models utilized in the analysis of carrot slice drying.

Name of Model	Model	Reference
Lewis	$MR = \exp(-kt)$	[11]
Henderson and Pabis	$MR = a\exp(-kt)$	[12]
Logarithmic	$MR = a\exp(-kt) + c$	[13]
Midilli and Kucuk	$MR = a\exp(-kt^n) + b$	[14]
Wang and Singh	$MR = 1 + at + bt^2$	[15]
Aghbashlo *et al.*	$MR = \exp\left(-\frac{at}{1+bt}\right)$	[16]
Page	$MR = \exp(-kt^n)$	[17]
Logistic	$MR = \frac{b}{1+a\exp(-kt)}$	[18]
Jena and Das	$MR = a\exp\left(-kt + b\sqrt{t}\right) + c$	[19]
Vega-Galvez I	$MR = \exp(n + kt)$	[20]
Vega and Lemus	$MR = (a + kt)^2$	[21]

The validity of the selected model for carrot slices dried at various infrared power levels is confirmed by comparing experimental moisture ratios (*MR*) with those predicted by the Midilli & Kucuk model in Fig. 3. Because the data points are precisely aligned along a 45° line, the findings show a significant agreement between the experimental and projected *MR* values, confirming the model's appli-cability for drying behavior of samples.

Effective moisture diffusivity

Plotting the logarithm of the moisture ratio (MR) regarding drying time at various infrared power levels was done using the experimental data. The effective moisture diffusivity (D_{eff}) values for each infrared power level, computed by Eq. (11), are shown in Fig. 4. A power level of 38 W produced the lowest D_{eff} and a power level of 88 W produced the highest D_{eff}. These findings indicate that higher power levels promote more effective drying of carrot slices within the studied parameters. This is attributed to the relatively high D_{eff} values obtained, which suggest enhanced moisture mobility within the samples. When the power level rose, the impact on the D_{eff} became significantly more apparent compared to lower power levels, as illustrated distinctly in Fig. 4. This effect can be attributed to the rapid temperature increase in carrot slices under high infrared power, which raises the vapour pressure and, in turn, accelerates the drying rate.

Table 2 Assessment of infrared-dried carrot slices at varying power levels using statistical metrics for thin-layer drying models.

IR power	Model	Model Constants					R^2	χ^2	RMSE
		a	*b*	*c*	*k*	*n*			
38	Lewis				0.0119		0.9928	0.2123	0.0363
	Henderson & Pabis	1.0803			0.0128		0.9959	0.1156	0.0231
	Logarithmic	1.1049		-0.0451	0.0113		0.9975	0.3114	0.0181
	Midilli & Kucuk	0.9978	0.0002		0.0032	1.2819	0.9997	0.0095	0.0062
	Wang & Singh	-0.0084	0.0001				0.9968	0.0957	0.0240
	Aghbashlo *et al.*	0.0092	-0.0019				0.9988	0.0110	0.0146
	Page				0.0036	1.2590	0.9996	0.0379	0.0069
	Logistic	1.7968	0.7754		0.0183		0.9995	0.0328	0.0067
	Jena & Das	-0.0905	0.3226	1.1341	0.0103		0.9982	0.1377	0.0162
	Vega-Galvez I				-0.0128	0.0773	0.9959	0.1156	0.0231
	Vega & Lemus	0.9941	-0.0041				0.9969	0.0844	0.0226
50	Lewis				0.0142		0.9957	0.1071	0.0274
	Henderson & Pabis	1.0572			0.0150		0.9973	0.0601	0.0187
	Logarithmic	1.0714		-0.0272	0.0139		0.9980	0.1681	0.0163
	Midilli & Kucuk	0.9921	0.0004		0.0050	1.2353	0.9998	0.0059	0.0050
	Wang & Singh	-0.0098	0.0002				0.9933	0.4931	0.0326
	Aghbashlo *et al.*	0.0118	-0.0017				0.9990	0.0889	0.0118
	Page				0.0060	1.1934	0.9997	0.0514	0.0070
	Logistic	2.0568	1.0470		0.0202		0.9997	0.0527	0.0064
	Jena & Das	-0.1197	0.3082	1.1565	0.0105		0.9979	0.1624	0.0176
	Vega-Galvez I				-0.0150	0.0556	0.9973	0.0601	0.0187
	Vega & Lemus	0.9775	-0.0046				0.9948	0.0734	0.0283
62	Lewis				0.0187		0.9904	0.1842	0.0434
	Henderson & Pabis	1.0724			0.0200		0.9934	0.1271	0.0360
	Logarithmic	1.1481		-0.1068	0.0156		0.9978	0.1292	0.0207
	Midilli & Kucuk	0.9949	-0.0006		0.0053	1.2996	0.9999	0.0014	0.0031
	Wang & Singh	-0.0137	0.0004				0.9993	0.0303	0.0113
	Aghbashlo *et al.*	0.0137	-0.0037				0.9994	0.0590	0.0103
	Page				0.0051	1.3114	0.9998	0.0034	0.0053
	Logistic	1.5462	0.5451		0.0316		0.9998	0.0036	0.0039
	Jena & Das	-0.0512	0.5049	1.0684	0.0211		0.9992	0.0253	0.0119
	Vega-Galvez I				-0.0200	0.0699	0.9934	0.1271	0.0360
	Vega & Lemus	1.0025	-0.0068				0.9987	0.0907	0.0137
74	Lewis				0.0204		0.9915	0.1447	0.0405
	Henderson & Pabis	1.0567			0.0216		0.9937	0.1117	0.0350
	Logarithmic	1.1788		-0.1578	0.0155		0.9993	0.0085	0.0111
	Midilli & Kucuk	0.9976	-0.0003		0.0089	1.1837	0.9999	0.0029	0.0033
	Wang & Singh	-0.0151	0.0005				0.9997	0.0084	0.0064
	Aghbashlo *et al.*	0.0153	-0.0038				0.9998	0.0010	0.0037
	Page				0.0069	1.2692	0.9993	0.0221	0.0114
	Logistic	1.6152	0.6245		0.0331		0.9995	0.0169	0.0089
	Jena & Das	-0.0555	0.5099	1.0655	0.0222		0.9996	0.0075	0.0086
	Vega-Galvez I				-0.0216	0.0551	0.9937	0.1117	0.0350
	Vega & Lemus	0.9957	-0.0073				0.9992	0.1405	0.0118
88	Lewis				0.0234		0.9876	0.1690	0.0507
	Henderson & Pabis	1.0668			0.0249		0.9905	0.1302	0.0442
	Logarithmic	1.2354		-0.2073	0.0166		0.9984	0.0146	0.0174
	Midilli & Kucuk	0.9961	-0.0003		0.0072	1.2816	0.9998	0.0037	0.0051
	Wang & Singh	-0.0172	0.0007				0.9995	0.0044	0.0093
	Aghbashlo *et al.*	0.0163	-0.0054				0.9997	0.0052	0.0067
	Page				0.0058	1.3560	0.9993	0.0167	0.0113
	Logistic	1.4242	0.4316		0.0422		0.9996	0.0124	0.0082
	Jena & Das	-0.0375	0.6307	1.0448	0.0301		0.9997	0.0079	0.0076
	Vega-Galvez I				-0.0249	0.0647	0.9905	0.1302	0.0442
	Vega & Lemus	1.0049	-0.0086				0.9995	0.0574	0.0095

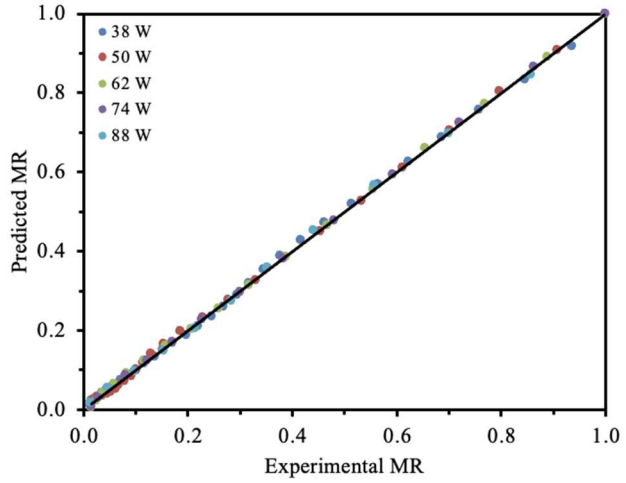

Figure 3. Carrot slice moisture ratios, both experimental and anticipated, at different IR power levels using the Midilli & Kucuk model

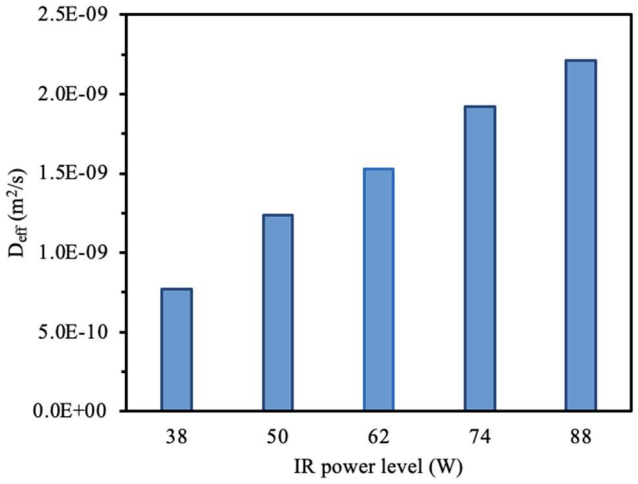

Figure 4. Effect of infrared power levels on effective diffusion coefficient.

The D_{eff} values in this study ranged from 7.73×10^{-10} to 2.21×10^{-9} m²/s, which aligns with those reported for other drying methods and agricultural products. For instance, in laboratory-scale convective drying of peach slices, D_{eff} values were reported to range from 9.57×10^{-10} to 4.33×10^{-9} m²/s across a temperature spectrum of 40-80°C [38]. In a similar context, the drying of okra yielded D_{eff} values between 2.89×10^{-9} and 12.23×10^{-9} m²/s at radiation intensities of 0.167, 0.235, and 0.520 W/cm² [39]. These comparable values reinforce the reliability of our experimental data and confirm that the observed diffusivities are within the expected range for plant-based tissues under IR drying.

To provide a prediction model for comprehending D_{eff} dynamics under various drying conditions, a multiple regression analysis was also performed to explain the relationship between moisture diffusivity and power level. The correlation between the infrared power range utilized in our experimental studies and effective moisture diffusivity is articulated through the following equation:

$$D_{eff} = 2.86\times10^{-11}P - 2.43\times10^{-10}$$
$$R^2 = 0.988 \qquad (14)$$

where P represents the power level, measured in watts (W). This equation can serve as a practical predictive tool for estimating moisture transport rates in similar food matrices under IR drying conditions, thereby assisting in the design of energy-efficient drying protocols.

Activation energy

According to Eq. (12), the activation energy (E_a) was determined by plotting ln (D_{eff}) against m/P (sample weight/infrared power in kg/W), which is the slope of the Arrhenius equation. Fig. 5 illustrates the relationship between ln (D_{eff}) and m/P. The slope of the line in Fig. 5 represents ($-E_a$), while the intercept corresponds to ln (D_0). According to these findings, the Arrhenius dependence is supported by a linear connection. The impact of the sample weight-to-power ratio on D_{eff} is captured by Eq. (15), with coefficients defining this relationship:

$$D_{eff} = 4.86\times10^{-9}\exp\left(-\frac{1967.5\ m}{P}\right)$$
$$R^2 = 0.999 \qquad (15)$$

The maximal diffusion coefficients (D_0) at infinite temperature and the activation energy (E_a) for carrot samples were derived using a modified Arrhenius-type exponential model, as indicated by Eq. (15). These parameters provide insights into the diffusion behaviours and thermal activation characteristics across the different samples. Specifically, the highest diffusivity that any sample may have under idealized thermal conditions is indicated by the theoretical diffusion coefficient at infinite temperature, or D_0. In contrast, E_a quantifies the minimum energy barrier required for diffusion to occur, reflecting the sensitivity of each sample to temperature changes. By comparing D_0 and E_a values, the model highlights the unique diffusion potential and thermal resistance for each sample, offering a detailed understanding of how each material may respond to varying thermal environments based on its molecular structure or composition [40].

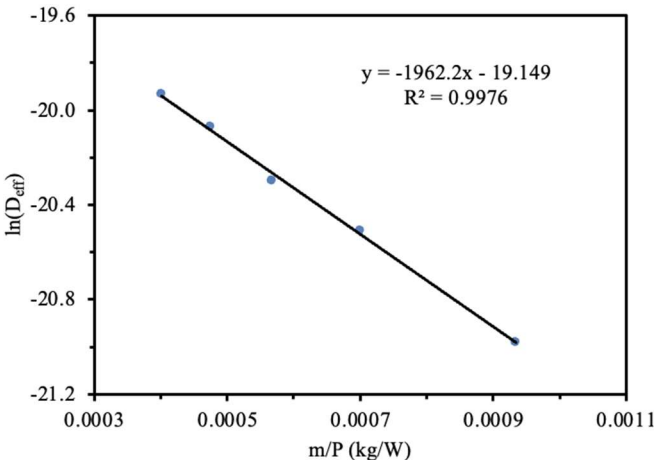

Figure 5. A relationship of the Arrhenius type between infrared power and effective moisture diffusivity.

When Eq. (15) is analysed, D_0 value is determined as 4.86×10^{-9} m²/s, and the E_a value is determined as 1.967 kW/kg. These results, with minor variations, align with earlier studies on the drying processes of black carrots

[28] and orange carrots [41]. These findings underscore the significant role of infrared power level and drying conditions in determining the activation energy necessary for moisture removal. The variability observed in activation energy during food drying processes is likely influenced by several factors, including the type of food, its moisture content, and the specific drying methods employed.

The E_a obtained in the present study (1.967 kW/kg) aligns with previously reported power-based values for carrots and carrot by-products. Doymaz [42] reported E_a = 4.247 kW/kg for carrot slices dried at 62-125 W using a modified Arrhenius approach, while E_a = 5.73 kW/kg was observed for carrot pomace (83-209 W) [43], and E_a = 3.65 kW/kg for black carrot pomace (104-230 W) [28]. The comparatively lower E_a reported here is justified by the use of lower IR power levels (38-88 W) and slightly thicker slices, which reduce power absorption per unit mass and shift drying toward a milder thermal regime.

Experimental factors such as slice thickness, sample mass, emitter-sample distance, initial moisture content, and the moisture range used for fitting D_{eff} substantially affect E_a determination. Toğrul [2] and Botelho *et al.* [32] emphasize that E_a should be interpreted within the context of these parameters, as lower IR powers generally result in slower drying rates and a smaller driving force, leading to reduced apparent E_a in power-based models.

This study contributes to the literature by providing new data on E_a behaviour under low-to-moderate IR power conditions—a regime that remains underexplored. The findings are particularly relevant for industrial applications aiming to optimize energy efficiency and minimize thermal damage while maintaining product quality.

Energy efficiency during the process of carrot drying

Energy efficiency values were calculated using Eq. (13), and Fig. 6 illustrates how energy efficiency varied over the drying period for infrared drying of yellow carrot slices. Energy efficiency was initially very high, reflecting greater infrared power absorption. As moisture content and energy absorption in the samples decreased, infrared power reflection increased instead. The highest energy efficiency was observed at an infrared power level of 88 W.

The energy efficiency of yellow carrot slices exhibited a considerable range, varying from 0.02% to 33.1%, corresponding to power levels between 38 W and 88 W, indicating a significant dependence of efficiency on applied power. These findings align with prior research conducted on okra [44], which reported analogous trends in energy efficiency under comparable power conditions, further substantiating the influence of power intensity on the energy conversion efficacy in vegetable processing. The observed variability underscores the need for optimizing power parameters to enhance efficiency in such applications.

CONCLUSION

This study systematically examined the drying behavior of carrot slices using an infrared dryer operated at power levels ranging from 38 to 88 W. The findings demonstrated that infrared radiation intensity exerted a significant influence on drying kinetics, particularly on drying time and effective moisture diffusivity. An increase in infrared power substantially reduced the overall drying duration by enhancing the moisture diffusion coefficient, which varied between 7.73×10^{-10} and 2.21×10^{-9} m²/s across the tested power range. All drying operations occurred within the falling-rate period, confirming that the moisture removal process was predominantly governed by internal diffusion mechanisms rather than surface evaporation. Among the mathematical models evaluated, the Midilli & Kucuk model exhibited the highest predictive accuracy, effectively characterizing the drying kinetics under various infrared power conditions.

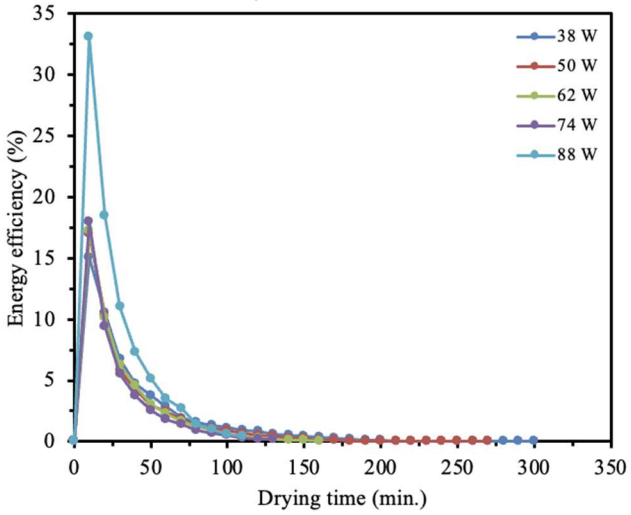

Figure 6. The change of energy efficiency (%) with respect to the infrared power level.

The activation energy, calculated using an Arrhenius-type relationship, was determined to be 1.967 kW/kg, representing the energy barrier for moisture diffusion. Although higher infrared power promoted accelerated moisture removal during the initial drying stages, prolonged exposure resulted in diminished energy efficiency due to the gradual reduction of the moisture gradient between the sample and the surrounding air, thereby lowering the driving force for mass transfer. These results emphasize the significance of defining infrared drying parameters through comprehensive kinetic modeling and energy performance evaluation rather than relying solely on process rate enhancement. The strong correlation between experimental data and the Midilli & Kucuk model underscores its applicability as a reliable predictive framework for process design and scale-up in infrared drying systems. Future investigations should integrate kinetic modeling with detailed energy analysis to further elucidate the relationship between power input, mass transfer behavior, and energy utilization efficiency, ultimately advancing the development of optimized, sustainable infrared drying technologies. Overall, the findings provide a valuable contribution to the understanding of infrared drying mechanisms, supporting the design of faster and more energy-efficient dehydration processes while maintaining desirable product characteristics.

LIST OF SYMBOLS

D_0: Pre-exponential factor in Arrhenius equation (m^2/s)
D_{eff}: Effective diffusivity (m^2/s)
E_a: Activation energy (W/kg)
K: Slope
L: Half the slice thickness of the sample
M: Moisture content (kg water/kg dry matter)
M_0: Initial moisture content (kg water/kg dry matter)
M_d: Dry weight (kg)
M_e: Equilibrium moisture content (kg water/kg dry)
MR_{exp}: Experimental moisture ratio
MR_{pre}: Predicted moisture ratio
M_t: Moisture content at any time (kg water/kg dry matter)
$M_{t+\Delta t}$: Moisture content at t+Δt
m_w: Mass of evaporated water (g)
M_W: Sample weight (kg)
n: Number of experimental data points
N: Number of parameters
P: Infrared power (W)
R^2: Coefficient of determination
Δt: Drying time (min.)
η: Drying efficiency
λ_w: Latent heat of vaporization
χ^2: Chi-square

ABBREVIATIONS

AOAC: Association of Official Agricultural Chemists
LDPE: Low-density polyethylene
MR: Moisture ratio
DR: Drying rate (kg water/kg dry matter * time)
RMSE: Estimated standard error
US: Ultrasound
HD: Hot air drying
MWD: Microwave drying
INFD: Infrared drying

REFERENCES

[1] A. Ignaczak, A. Salamon, J. Kowalska, A. Marzec, H. Kowalska, Molecules 28 (2023) 6407. https://doi.org/10.3390/molecules28176407.
[2] H. Toğrul, J. Food Eng. 77 (2006) 610-619. https://doi.org/10.1016/j.jfoodeng.2005.07.020.
[3] P. Sakare, N. Prasad, N. Thombare, R. Singh, S.C. Sharma, Food Eng. Rev. 12 (2020) 381-398. https://doi.org/10.1007/s12393-020-09237-w.
[4] N.K. Rastogi, Crit. Rev. Food Sci. Nutr. 52 (2012) 737-760. https://doi.org/10.1080/10408398.2010.508138.
[5] J.K. Yan, L.X. Wu, Z.R. Qiao, W.D. Cai, H. Ma, Food Chem. 271 (2019) 588-596. https://doi.org/10.1016/j.foodchem.2018.08.012.
[6] M. Younis, D. Abdelkarim, A. Zein El-Abdein, Saudi J. Biol. Sci. 25 (2018) 332-338. https://doi.org/10.1016/j.sjbs.2017.06.011.
[7] O.Y. Turan, F.E. Firatligil, Czech J. Food Sci. 37 (2019) 128-134. https://doi.org/10.17221/243/2017-CJFS.
[8] A. Solyom, J. Betz, P. Brown, A. Bzhelyansky, N. Chrisafis, M. Embuscado, H. Figore, H. Johnson, G. Joseph, D. Kennedy, A. Kuszak, E. Mudge, M. Phillips, T. Phillips, L. Richards, C. Rimmer, B. Sauza, B. Schaneberg, J. Skamarack, S. Coates, J. AOAC Int. 99 (2016) 1102-1104. https://doi.org/10.5740/jaoacint.SMPR2016.003.
[9] J. Akter, J. Hassan, M. M. Rahman, M. S. Biswas, H I. Khan, M.M.R. Rajib, M.R. Ahmed, M. N.-E.-A. Khan, M. F.A. Hasan, Heliyon 10 (2024) e24165. https://doi.org/10.1016/j.heliyon.2024.e24165.
[10] T. Gulati, A.K. Datta, J. Food Eng. 166 (2015) 119-138. https://doi.org/10.1016/j.jfoodeng.2015.05.031.
[11] P.C. Panchariya, Đ. Popović, A. Sharma, J. Food Eng. 52 (2002) 340-358. https://doi.org/10.1016/S0260-8774(01)00126-1.
[12] A. Manzoor, M.A. Khan, M.A. Mujeebu, R.A. Shiekh, J. Agric. Food Res. 5 (2021) 100176. https://doi.org/10.1016/j.jafr.2021.100176.
[13] D.C. Lopes, A.J. Steidle Neto, J.K. Santiago, Biosyst. Eng. 118 (2014) 105-114. https://doi.org/10.1016/j.biosystemseng.2013.11.011.
[14] A. Midilli, H. Kucuk, Energy Convers. Manage. 44 (2003) 1111-1122. https://doi.org/10.1016/S0196-8904(02)00099-7.
[15] A. Omolola, A. Jideani, P. Kapila, Interciencia 40 (2015) 374-380. https://www.researchgate.net/publication/282237695_Drying_kinetics_of_banana_Musa_spp.
[16] M. Aghbashlo, M. Kianmehr, S. Khani, M. Ghasemi, Int. Agrophys. 23 (2009) 313-317. http://www.international-agrophysics.org/Mathematical-modelling-of-thin-layer-drying-of-carrot,106450,0,2.html#ungrouped.
[17] M.M.M. Najla, R. Bawatharani, Iconic Res. Eng. J. 2 (2019) 6-10. https://www.irejournals.com/paper-details/1701096.
[18] S. Shah, M. Joshi, Int. J. Electron. Eng. 2 (2010) 159-163. https://www.semanticscholar.org/paper/Modeling-Microwave-Drying-Kinetics-of-Sugarcane-Shah-Joshi/e0b913d263f9f955b27e4eac3aa323be2e676089.
[19] S. Jena, H. Das, J. Food Eng. 79 (2007) 92-99. https://doi.org/10.1016/j.jfoodeng.2006.01.032.
[20] R. Lemus-Mondaca, N. Betoret, A. Vega-Gálvez, E. Lara-Aravena, J. Food Process Eng. 32 (2009) 645-663. https://doi.org/10.1111/j.1745-4530.2007.00236.x.
[21] R. Guiné, Electron. J. Environ. Agric. Food Chem. 9 (2010) 1772-1783. https://www.researchgate.net/publication/256444660_Analysis_of_the_drying_kinetics_of_S_Bartolomeu_pears_for_different_drying_systems.
[22] B. Alaei, R. Chayjan, J. Food Process. Preserv. 39 (2014) 1-12. https://doi.org/10.1111/jfpp.12252.
[23] T.J. Afolabi, T.Y. Tunde-Akintunde, J.A. Adeyanju, J. Food Sci. Technol. 52 (2015) 2731-2740. https://doi.org/10.1007/s13197-014-1365-z.
[24] L. Hassini, S. Azzouz, R. Peczalski, A. Belghith, J. Food Eng. 79 (2007) 47-56. https://doi.org/10.1016/j.jfoodeng.2006.01.025.

[25] J. Crank, The Mathematics of Diffusion, 2nd ed., Oxford University Press, London (1975), p. 69-88. https://dokumen.pub/the-mathematics-of-diffusion-second-edition-0198533446-9780198533443.html.
[26] N.P. Zogzas, Z.B. Maroulis, Dry. Technol. 14 (1996) 1543-1573. https://doi.org/10.1080/07373939608917163.
[27] L. Ceclu, E. Botez, O. Nistor, F. Gögüs, D. Andronoiu, G. Mocanu, Ann. Univ. Dunarea Jos Galati 39 (2015) 20-29. https://www.researchgate.net/publication/298842746_Influence_of_drying_conditions_on_the_effective_diffusivity_and_activation_energy_during_convective_air_and_vacuum_drying_of_pumpkin.
[28] İ. Doymaz, Sigma J. Eng. Nat. Sci. 37 (2019) 71-84. https://dergipark.org.tr/en/pub/sigma/issue/65450/1011078#article_cite.
[29] J. Yi, X. Li, J. He, X. Duan, Dry. Technol. 38 (2019) 1-16. https://doi.org/10.1080/07373937.2019.1628772.
[30] D. Huang, P. Yang, X. Tang, L. Luo, B. Sunden, Trends Food Sci. Technol. 110 (2021) 765-777. https://doi.org/10.1016/j.tifs.2021.02.039.
[31] M. Zarein, S.H. Samadi, B. Ghobadian, J. Saudi Soc. Agric. Sci. 14 (2015) 41-47. https://doi.org/10.1016/j.jssas.2013.06.002.
[32] F. Botelho, P. Correa, A. Goneli, M. Martins, F. Magalhães, S. Campos Botelho, Rev. Bras. Eng. Agric. Ambient. 15 (2011) 845-852. https://doi.org/10.1590/S1415-43662011000800012.
[33] H. Elmesiry, K. Ashiagbor, Z. Hu, W.G. Alshaer, Case Stud. Therm. Eng. 52 (2023) 103676. https://doi.org/10.1016/j.csite.2023.103676.
[34] A.M. Matouk, M.M. El-Kholy, A. Tharwat, W.M. Abdelrahman, J. Soil Sci. Agric. Eng. 5 (2014) 569-581. https://doi.org/10.21608/jssae.2014.49310.
[35] B. Turkan, A.B. Etemoglu, Sigma J. Eng. Nat. Sci. 38 (2020) 527-544. https://dergipark.org.tr/en/pub/sigma/issue/65153/1002263.
[36] S. Álvarez, C. Álvarez, R. Hamill, A.M. Mullen, E. O'Neill, Compr. Rev. Food Sci. Food Saf. 20 (2021) 5370-5392. https://doi.org/10.1111/1541-4337.12845.
[37] R. Shrestha, A. Dhungel, S. Dhakal, Tribhuvan Univ. J. Food Sci. Technol. 2 (2023) 17-25. https://doi.org/10.3126/tujfst.v2i2.66508.
[38] M.Y. Barforoosh, A.M. Borghaee, S. Rafiee, S. Minaei, B. Beheshti, Int. J. Low-Carbon Technol. 19 (2024) 192-206. https://doi.org/10.1093/ijlct/ctad121
[39] H.S. El-Mesery, M. Qenawy, Z. Hu, W.G. Alshaer, Case Stud. Therm. Eng. 50 (2023) 103451. https://doi.org/10.1016/j.csite.2023.103451.
[40] F. Yang, H. Schmidt, E. Hüger, ACS Omega 8 (2023) 27776-27783. https://doi.org/10.1021/acsomega.3c04029.
[41] İ. Doymaz, J. Food Process. Preserv. 39 (2015) 2738-2745. https://doi.org/10.1111/jfpp.12524.
[42] İ. Doymaz, J. Agric. Sci. 19 (2013) 1-11. https://doi.org/10.1501/Tarimbil 0000001227.
İ. Doymaz, Sigma J. Eng. Nat. Sci. 37 (2019) 161-171.https://dergipark.org.tr/en/pub/sigma/issue/65450/1011078.
[43] S. Tanta, İ. Doymaz, Sigma J. Eng. Nat. Sci. 37 (2019) 93-104. https://dergipark.org.tr/en/pub/sigma/issue/65450/1011084.

MEHMET SOYDAN

İBRAHIM DOYMAZ

Yildiz Technical University, Department of Chemical Engineering, 34220 Esenler, İstanbul, Türkiye

INFRACRVENO SUŠENJE KRIŠKI ŠARGAREPE: UTICAJ NIVOA SNAGE NA KINETIKU I ENERGETSKU EFIKASNOST

Cilj ove studije je optimizacija uslova sušenja žute šargarepe istraživanjem efekata različitih nivoa snage infracrvenog (IC) zračenja na kinetiku sušenja. Nakon testova sušenja na nivoima snage IC zračenja od 38, 50, 62, 74 i 88 W, početni sadržaj vlage u kriškama šargarepe (6,95 kg vode/kg suve materije) smanjen je na 0,11 kg vode/kg suve materije. Vremena sušenja kretala su se od 300 minuta pri 38 W do 110 minuta pri 88 W, što pokazuje obrnutu vezu između snage IC zračenja i trajanja sušenja. Viši nivoi snage IC zračenja ubrzali su sušenje poboljšanjem prenosa energije, što je podstaklo efikasnost uklanjanja vlage. Efektivni koeficijenti difuzije, izračunati u rasponu od $7,73\times10^{-10}$ do $2,21\times10^{-9}$ m²/s za nivoe snage od 38 W do 88 W, ukazuju na povećanje migracije vlage sa većom snagom. Energetske potrebe procesa odražene su u energiji aktivacije za difuziju vlage (1,967 kW/kg). Model Midilija i Kučuka ponudio je najbolje rešenje za karakterizaciju ponašanja sušenja, a statistička analiza je potvrdila ispravnost modela. Ovi nalazi pružaju vredne uvide za optimizaciju uslova infracrvenog sušenja kako bi se poboljšala efikasnost i kvalitet procesa sušenja žute šargarepe..

Ključne reči: Infracrveno sušenje, matematičko modelovanje, kinetika sušenja, koeficijent difuzije, energija aktivacije

NAUČNI RAD

Chemical Industry & Chemical Engineering Quarterly

Available online at
Association of the Chemical Engineers of Serbia AChE
www.ache.org.rs/CICEQ

Chem. Ind. Chem. Eng. Q. 32 (3) 257–267 (2026) CI&CEQ

KREŠIMIR OSMAN[1]
MATO PERIĆ[2]
DRAGI STAMENKOVIĆ[3]
MIHAILO LAZAREVIĆ[4]

[1]Department of Electrical Engineering, University of Applied Sciences, Zagreb, Croatia

[2]Department of Mechatronics, University North, Koprivnica, Croatia

[3]The College of Applied Studies "Aviation Academy", Belgrade, Serbia

[4]Chair of Mechanics, Faculty of Mechanical Engineering, University of Belgrade, Belgrade, Serbia

SCIENTIFIC PAPER

UDC 004.4:65.01

ADVISORY-BASED PRODUCT CONFIGURATOR USED IN CHILLER CONFIGURATION AND EVALUATION

Highlights

- The product configurator is designed on a combination of inference rules and similar scenarios.
- The product configurator is designed to be a user-oriented system.
- Knowledge about the chillers is captured in a matrix form.
- The selection and evaluation of chillers is carried out using the so-called CCM methodology.

Abstract

This article presents the architecture and functional principle of an advisory-based product configurator. The program is used to create new and modify similar product configurations and is intended for users without in-depth expertise in technical fields. Due to its architecture, the configurator is designed to utilise the knowledge stored in the knowledge database. The selection is based on a combination of fuzzy inference rules and mapping techniques. Knowledge regarding the product is captured by using component-based matrices. The possibility of adding new knowledge and new rules is also provided. All this enables the configurator to link customer requirements and offers the possibility of selecting one or more products. In addition, it evaluates possible product variants based on the parameters specified by the user. The graphical representation of the results obtained includes the product technical documentation as well as a matrix representation of all the selected components and modules. The functional principle and evaluation of the product selection are demonstrated using a case study of a chiller for installation in an industrial plant. During the selection and evaluation of the chiller, better system performance is achieved with a chiller that has a water-based condenser.

Keywords: product configurator architecture, fuzzy inference rule, matrix representation, CCM methodology, product selection.

INTRODUCTION

Considering the development of products in a certain area, such as the development of chillers, there are many competing companies on the market nowadays that offer similar products in regarding of cooling power, electricity consumption, energy efficiency class, and device dimensions and mass [1]. The conditions for obtaining cooling energy are becoming increasingly complex. In addition, deviations in selecting the desired device should be minimised. For this reason, many variants of similar devices have been developed. In addition to quality, which is undeniable, special attention is paid to the impact on the environment [2]. Therefore, the construction of these devices must be carried out flexibly. As new materials are developed every day, the aim is also to reduce the mass of the device [3], both for transport and its subsequent placement. Devices are ordered per piece and are therefore of great importance to configure them according to the wishes of individual users. Given the large fluctuations in product families, caused by frequent changes in standards related to the use of working fluids, many products are withdrawn from production after just a few years. The user expects the manufacturer to be able to supply spare parts throughout the entire life cycle of these products [4].

In this regard, companies try to offer their users the possibility of choosing the desired device and configuring it in a way that someone who does not possess a high level of technical knowledge can do. Computer programs of individual manufacturers have been developed, which offer

Correspondence: M. Perić, Department of Mechatronics, University North, Trg dr. Žarka Dolinara 1, 48000 Koprivnica, Croatia.
Email: mperic@unin.hr
Paper received: 9 April 2025
Paper revised: 15 October 2025
Paper accepted: 24 November 2025
https://doi.org/10.2298/CICEQ250409030O

users with non-technical knowledge the possibility of offering and choosing several device variants, according to some input parameters, with a description of the individual product, as well as a display of parameters and their price [5]. Additionally, its appearance is offered graphically and interactively with a picture, as well as a diagram of the device with a display of possible installations. It is also possible to graphically represent potential changes in the configuration, after harmonizing customer requirements with possible engineering characteristics. These programs are called product configurators and integrate the principle of an expert system with a knowledge base and a built-in set of rules for product selection. Furthermore, there is also the possibility of checking consistency, supplementing the knowledge base with new data, and maintaining knowledge, etc. Another option offered is the knowledge to recognize the problem based on similar previous cases and offer the most favourable one when choosing. For this reason, two co-approaches to expert systems, rule-based and case-based, are combined [6]. According to studies conducted, many engineering-oriented companies have benefited greatly from this type of expert system in recent years. This is primarily reflected in improved product offer quality, faster offer preparation, and fewer errors in product technical specifications [7].

This work aims to present a product configurator. The configurator is designed as an advisory system, which is adapted to users without much technical knowledge of water coolers. In addition to the knowledge base, and by selecting products using a base of built-in rules based on fuzzy logic, a base of possible similar scenarios is presented. All the knowledge bases in the program can be updated with new data and rules. The significant advantage of its program is the ability to display graphics in matrix form, where you can see the connections of all components, subsystems, and modules. Additionally, it is possible to change customer requirements and evaluate several possible product variants according to the selected requirements. All this is shown in the case study of choosing a chiller.

LITERATURE REVIEW

The available literature includes numerous works that address the topics discussed in this article. Based on the author's selection, only the most important ones are listed below.

Blecker and coworkers [8,9] provide an overview of the area by analysing product configurators. In addition, suggestions are made for possible extensions that focus on product configuration through counselling. A framework is developed with the most important requirements for such a system and the technical infrastructure required for its implementation. Antonelli *et al.* [10] demonstrate the application of concepts taken from object programming paradigms in the creation of product configurators. Class attribute inheritance is used, and a hierarchical approach to product customization is implemented. Haug *et al.* [11] present a study on the use of product configurators and how their use reduces the time required to create quotations with technical product data. For this purpose, the study was conducted in 14 engineering-oriented companies. Haug *et al.* [12] define and compare seven different strategies in the context of product configurator development. Each of the strategies was defined through a search of existing literature, examples already presented in the industry, and based on the author's experience. Haug *et al.* [13] analyse cost estimation and the benefits of using product configurators in different scenarios. A framework has been developed with which this can be assessed. The framework includes models for the relationship between the costs and benefits of configurators. It is analysed by using case studies from five projects. Shafiee *et al.* [14] analyze product configurators in terms of understanding the difference between the problem space and the solution achieved with the Design Thinking method. As an example, 4 projects were analysed, 2 of which were developed using the Design Thinking method and 2 of which were not. The study was conducted in the form of workshops and interviews. The environment was created with integrated Design Thinking techniques, involving a structured manner to support industrial companies. Poot [15] showed the development of a framework with a design automation model for mass customisation of lightweight structures. This model uses high-level templates from CAD programmes in combination with auxiliary techniques for design optimisation and tools for production preparation. Workalemahu *et al.* [16] presented an investigation on the application of product configurators in generating customer technical specifications for complex body geometries intended for production via additive manufacturing.

Nummela [17] presents configuration matrices, the idea of which is to establish the connection between the components in the modular structure of the product in matrix notation. In this way, new knowledge sets can be added during the subsequent development of new product platforms or the analysis of existing ones. Johansson and Krus [18] present an approach based on matrix representation that utilizes configurable matrices in system engineering. The approach is suitable for use in large and complex systems. It is demonstrated using the example of a model construction for a small business aeroplane. Helo [19] explores the structure of the system for the configuration of academic and non-academic works. For this purpose, the DSM method was used for configuration modelling. The DSM method enables the representation of the structure of components and subsystems in the observed system using graph theory. It provides a matrix representation in which components with the fewest interactions are positioned along the main diagonal of the matrix. This arrangement allows the distribution of individual subsystems, or modules, to be visually identified. The idea is to obtain an easily configurable product model that is flexible in terms of further customisation and changes. Germani *et al.* [20] implemented a multi-level DSM method for formalising the product structure in the product configurator. Their idea was to develop a method that is simple and robust enough to represent the product structure. The validity of the approach was tested using the example of domestic boilers. Gopsil *et al.* [21] propose a model for the automatic generation and updating of

DSM matrices. The generation and updating are linked to the development process by monitoring changes in the available digital product models. In this way, the reduction of time required for knowledge collection was aimed at, and its updating in matrix DSM structures.

Osman *et al.* [22] present the beginning of their research in the field of product configurators. The paper introduces the principle of configuration matrices for storing product data and proposes a product configurator architecture based on this principle with a description of its components. Osman et a*l.* [23] showed an iterative approach for the configuration and evaluation of chillers, which is referred to as Configuration and Change Management (CCM). The above approach is methodological, enabling product configuration through steps. This allows the selection of individual product modules depending on their purpose. In addition, it allows changes in the product configuration. The idea of the approach is to obtain the so-called optimal chiller system architecture according to predefined criteria. Osman *et al.* [24] represent a behaviour framework and mapping data between the structural and behavioural domains in studying the behaviour of the system of air handling unit variants during different modes of operation. In doing so, some of the fuzzy rules for the behaviour of the system were created by combining the automatic control method and stability check with the direct Lyapunov method. Finally, Osman *et al.* [25] show the continuation of research in the field of product configurators. The performance of a customer-oriented product configurator is presented. The dataset is based on configuration matrices to represent the modules of a single product. A case study on the configuration, evaluation, and selection of chillers is presented.

The contributions of this work are as follows:

- The system is designed so that it can be used by users without in-depth knowledge of a particular technical field.
- Through simplified dialogue boxes, it guides the user to the desired product configuration.
- The collection and modification of product data is enab-led by the so-called matrix data set using the component-based DSM method, i.e., configuration matrices.
- The knowledge data set contains similar cooler configuration scenarios for a specific application, which can be supplemented and modified.
- The matrix set enables a graphical representation of the connection of all components and subsystems in the chillers.
- The system has a base of inference rules based on fuzzy logic that can be added to.
- The inference rules can also be changed or new ones added in the case of new chiller variants.
- The system can assist in generating technical documentation using a database of CAD models, schemas, and technical specifications for each product.
- The selection can be saved for possible later changes and for future use when selecting products with similar technical characteristics.

DESCRIPTION OF ADVISORY-BASED PRODUCT CONFIGURATOR ARCHITECTURE AND REASONING PROCESS

The configurator (Fig. 1) works in such a way that it is customised to the user, i.e., it is a customer-oriented or advice-based system. This means that product selection can also be made by a person who does not have in-depth technical knowledge in this area. The user is addressed through questions in the so-called dialogue windows, through the consultation process. Simple, easy-to-understand questions are asked to guide the user to the type of product and some basic parameters that are important for product selection. It was created in an interactive way that guides the user in a simplified way to the selection of the desired and optimal product type. The so-called modelling of customer interests to improve the customer's wishes. Customer preferences are processed using the so-called mapping technique, i.e., filtering processes that are translated into technical requirements. An adequate transformation is ensured to later validate the product. The customer requirements must be recognised. The reverse is also possible. In addition to searching for existing data in the knowledge base, there is also the possibility of web mining to discover existing and new structures, patterns, and knowledge about similar products. This technique is based on the principle of a web application that helps the user search for data on the web. The mapping technique is an automatic process that selects product attributes based on implemented inference rules or according to the principle of data grouping. It also ensures that no inadvertent error has been made in the interpretation of customer queries during the validation process. It is possible to update the product by adding new components or subsystems to enhance technical specifications. During the entire interaction time, a web metric runs in the background to measure the performance of the web services used.

An in-built module automatically generates the web graphical user interface (GUI) for system communication with the user. A data repository (Fig. 1) is a knowledge base that contains implemented data on the following topics: product knowledge (including its characteristics and properties), user data, and derivation rules for retrieving product knowledge. Throughout the entire consultation process and communication between the configurator and user, the integrated CRM system (Fig. 1) is utilized to support and manage the user's wishes and any technical requirements.

It is also used to store the data obtained through the web mining process. As already mentioned, the advisory system communicates with the user via the so-called non-technical language to translate their requirements into technical features.

The system also includes a so-called decoupling interface (Fig. 2), which can be interpreted as an abstract layer that serves to separate the advisory system from the actual computer configurator. It also allows direct access to the configurator and offers the possibility of changing the proposed variants by adding new components or sub-systems to the configuration.

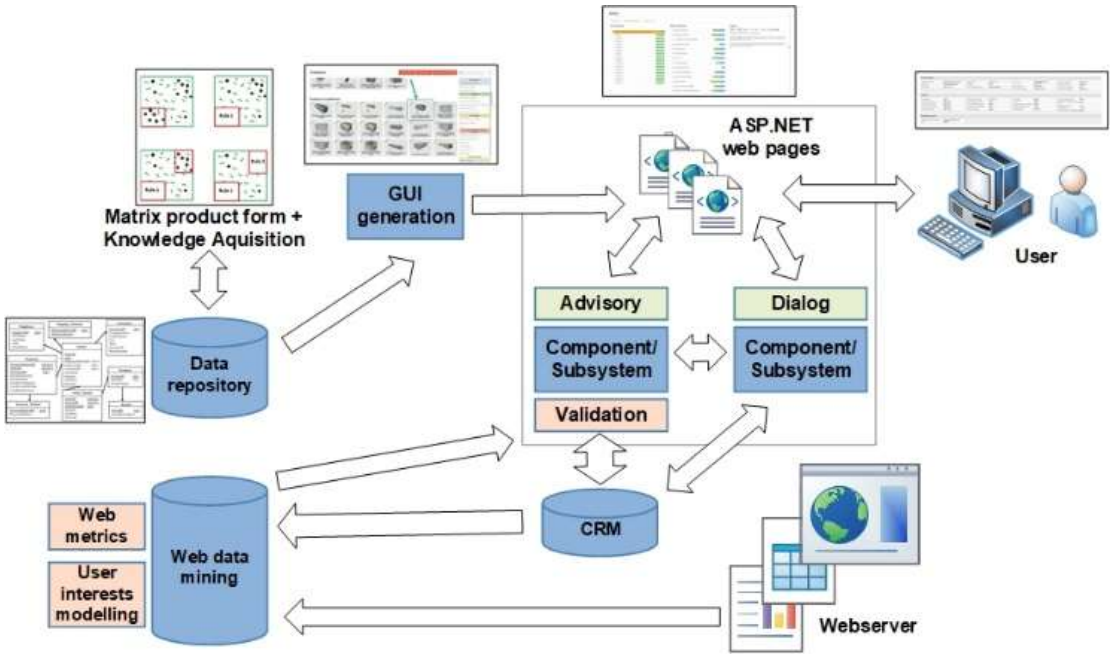

Figure 1. Simplified architecture schema of advisory-based product configurator.

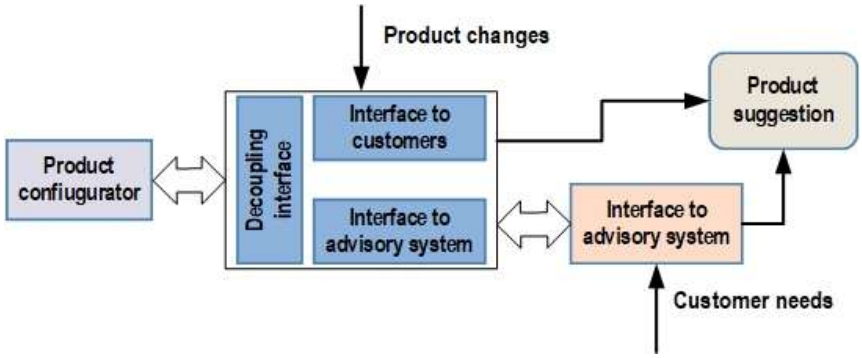

Figure 2. Block diagram for the connection between the customer advisory system and product model [9].

The user communicates with the advisory system via the following steps (Fig. 2) [26]:

1. The attributes contained in the product model are imported into the system's data repository.

2. The data collected during the consultation process is used as input data for the initial selection of the product configuration and the proposal of its possible variants, the so-called product suggestion phase.

3. The results obtained during the product configuration in the previous step are re-imported into the consulting system to provide the user with a proposal for the product variants created. Improvements can also be made to the proposed variants, known as the product change phase.

The component matrix or configuration matrix [17,18] based on the DSM method makes it possible to record components, processes, and other activities related to product development in the form of a diagram. The graph is visualised in the form of a matrix, with clusters around the main diagonal representing the components with the least interaction in the observed system. The graph illustrates very clearly: for some of the observed products, i.e., their variant, it is possible to observe several variants of the same product, which allows for new data sets or changes to data sets. It is also possible to display an advert only for a specific customer or group of customers, and it is possible to display the status of the desired product in stock and the number of pieces available. It can be seen from the illustration that changes in the matrix record are influenced by changes in sales and marketing as well as changes in the design and production process. Changes of this kind are irreversible, i.e., a reverse effect is possible, and is graphically visible in the matrix record. All changes during the sales and marketing processes are visible in the configuration matrix. In addition, changes in product design and production are also visible. Changes in the product structure, i.e., between its modules and individual components, are particularly clear.

A reasoning system based on created inference rules that contain fuzzy logic according to the Mamdani principle was shown in Fig. 4. The knowledge base contains inference rules that can be added to or changed at any time, depending on the changes the manufacturer makes to a particular product type. The reasoning steps are as follows [27,28]:

1. Softening or Fuzzyfication,
2. Inference or fuzzy decision process,
3. Sharpening or defuzzification,
4. Local and global reasoning – possible step.

All of the above processes interact and can exchange information with each other. These parts of the reasoning system are dynamically linked so that a change in one of them is automatically registered in the others.

1. *Softening or Fuzzyfication* - the input variables and the output variables are selected based on the defined influencing variables. For each variable, the number of linguistic values and the definition range of the above-mentioned variables are determined. The definition range is determined for each variable. In addition, the number and form of the membership functions that cover the definition range of the individual linguistic variables are determined. A membership function (MF) is a curve that defines the degree of membership of each point in the input space (universe of discourse). It assigns an associated value between 0 and 1 to a point in the input space. This is essentially the only condition that a membership function must fulfil in reality. The membership functions of fuzzy sets μ_A are always normalised, which means that the maximum value of the membership function is equal to 1. The form choice of the membership functions in individual fuzzy sets is subjective and depends on the problem under consideration. There are several softening functions in the Mamdani logic, of which the centre of area or centre of gravity method is the most commonly used. A linguistic variable is a variable that takes words or sentences as values.

2. *Inference or fuzzy decision process* - fuzzy inference rules are created depending on certain input and output variables. By creating behavioural rules, a rule base is created in the form of fuzzy IF-THEN rules. For each fuzzy rule, a logical operator and a weight of the fuzzy rule are selected. Known logical operators are AND, OR, and NOT. The output membership function μ_{agg} is obtained as an aggregation (combination) of the above rules.

3. *Sharpening or defuzzification* - the fuzzy output sets are converted into unique output values. There is no single method of defuzzification, but there are many methods, the most commonly used of which is the centre of area method. The results of sharpening could be presented in tabular form as rules or by graphically using the surfaces.

4. *Local and global reasoning* - possible step - the possible graphical representation of all the defined fuzzy rules, with the visualisation of their membership functions, was local reasoning. The graphical three-dimensional (3D) representation of two influential input variables and an output variable is called global reasoning.

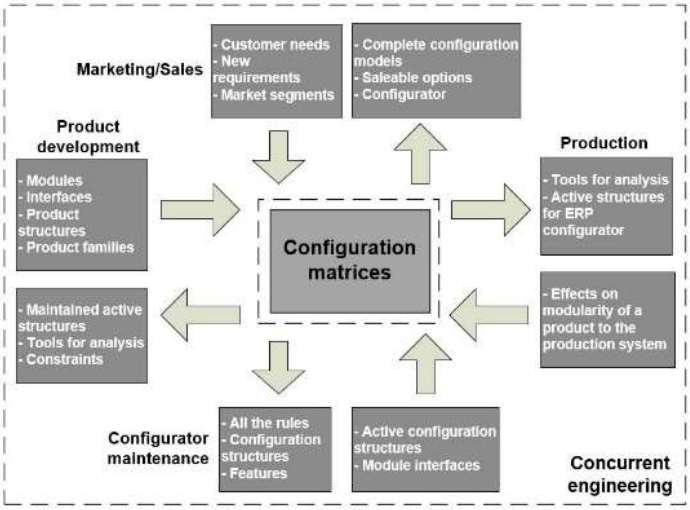

Figure 3. Influence on configuration matrix [17,22].

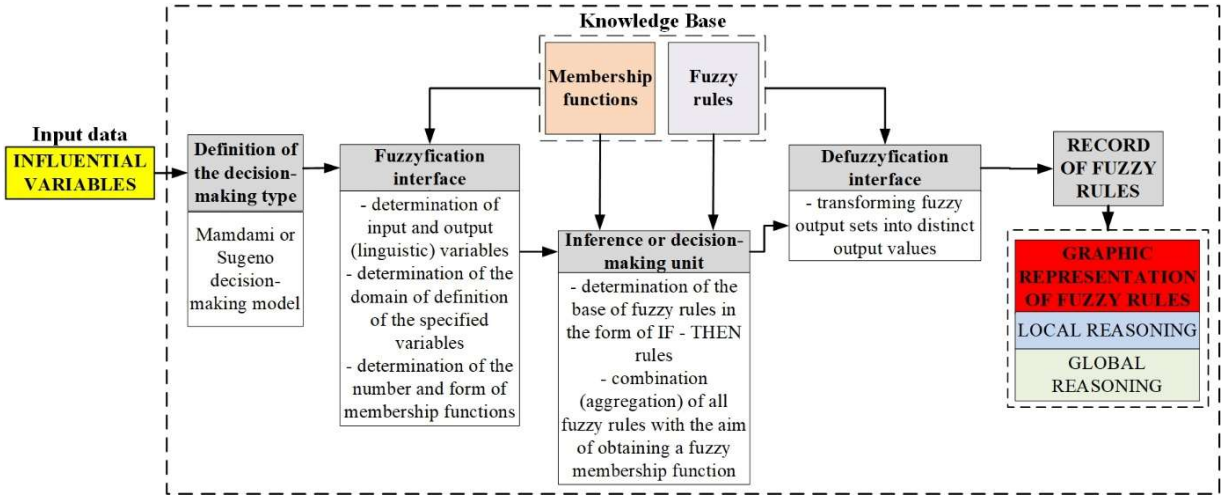

Figure 4. Reasoning system with inference fuzzy rules [24].

The Configuration and Change Management (CCM) approach (Fig. 5), which is implemented in the product configurator and used here for the selection and evaluation of cooler product variants, is described in more detail in [23]. Only the most important phases of the approach are briefly described below. The main phases are:

1. *Configuration* – an attempt is made to select and propose the most acceptable variant according to customer requirements. It is possible to propose several product variants in the first step, which differ in some characteristics.

2. *Changes* – by changing some parameters and adding or removing elements or subsystems, changes can be made. The result is systems with better values for some parameters, e.g., *EER*, operating mass, or *SPL*. To improve the desired parameters, it is sometimes necessary to change the customer requirements.

3. *Evaluation* – comparisons and evaluations are made based on the selected parameters. The chiller solution with the highest sum of all ratings for a given observed parameter is selected as the acceptable and optimal solution.

CASE STUDY – CHILLER SELECTION

The validation of the previously described approach is demonstrated on the case study of a chiller selection for an industrial plant.

The following customer requirements were drawn up with the help of the investor:

- The water cooler should operate at full thermal capaci-ty for 16 hours a day without interruption; the rest of the day, it should operate at reduced capacity (about 60% of capacity). It must function independently of changing exter-nal conditions in all operating modes (winter, transitional, and summer operation).
- There is the option of external installation (on the roof of the building) or internal installation of the chiller (in the cooling station). In the case of external installation, it must be protected from external influences.
- The noise level must be taken into account to ensure quiet operation of the device.
- Try to select the highest possible energy class for the device.
- The technical requirements were drawn up based on customer requirements:
  - Guaranteeing the operation of the device at low winter temperatures (down to -21 °C) and at high summer temperatures (up to 50 °C);
  - An uninterrupted power supply must be ensured during operation of the device (3x400 V, 50 Hz).
  - When selecting the appliance, aim for the highest possible energy class according to Eurovent.
  - The appliance should not have a hydraulic modular subsystem.
  - The appliance must be insensitive to vibrations during operation.
  - During the selection of a chiller, make sure that you choose the device with the lowest possible power consumption.
  - Also, during selection, make sure that the dimensions (and thus the mass) of the device are as small as possible.
  - Assume a value of 870 kW as the input requirement for the heat output, with the option of increasing it by up to 15%.
  - Assume a value of 70 dB(A) as the input requirement for the upper value of the permissible noise level.

The input parameters used during the first selection of variants are: cooling capacity Q, permissible noise level *SPL,* and permissible dimensions of the space ($L \times W \times H$), where the chiller would be installed.

During the first step of chiller selection, both installation options were considered. Chillers for outdoor installation (with an air-cooled condenser) and one for indoor installation (with a water-cooled condenser) were selected. Table 1 shows the parameters for both chiller variants that were determined during the selection in the first step.

Table 1. Initial step during chiller selection.

Parameters	Type of chiller	
	Air-cooled	*Water-cooled*
Q [kW]	862.2	867.6
EER [kW/ kW]	3.3	5.07
ESEER	4.4	6.22
N_{el} [kW]	284.8	176
SPL [dB(A)]	66	66
Dimensions [$L \times W \times H$] [m]	8.3×2.2×2.5	3.6×1.6×1.9
m [kg]	7040	5650
Energy class	B	B

A three-dimensional view of a chiller with an air-cooled condenser is shown in Fig. 6 (on the left side), while Fig. 6 on the right side shows a three-dimensional view of a chiller with a water-based condenser.

Already during the first selection step, it became clear that the water-based chiller has much smaller dimensions, as well as the weight of the device, and lower electricity consumption. As the customer wanted the chiller to be in energy class A, some changes were made to the product configuration, and a further validation step was carried out.

Two further validation steps were then carried out, in which a slightly larger cooling capacity was required. Variants were also obtained whose dimensions correspond to the original installation requirements, and are all designed in energy class A. Also, during the next steps of device selection, the aim was to select the one with a higher *EER* coefficient, as well as smaller device dimensions and lower weight. However, selecting a device that would be in energy class A entails an increase in the thermal capacity of the device and its dimensions. All the chiller variants selected in these 3 validation steps are listed in Table 2. As can be seen in the table, the increase in dimensions of a water-based chiller is insignificant compared to a chiller with an air-cooled condenser.

Based on the many values of the observed parameters obtained through several selection steps, it is not possible to simply make a selection, but it is necessary to carry out

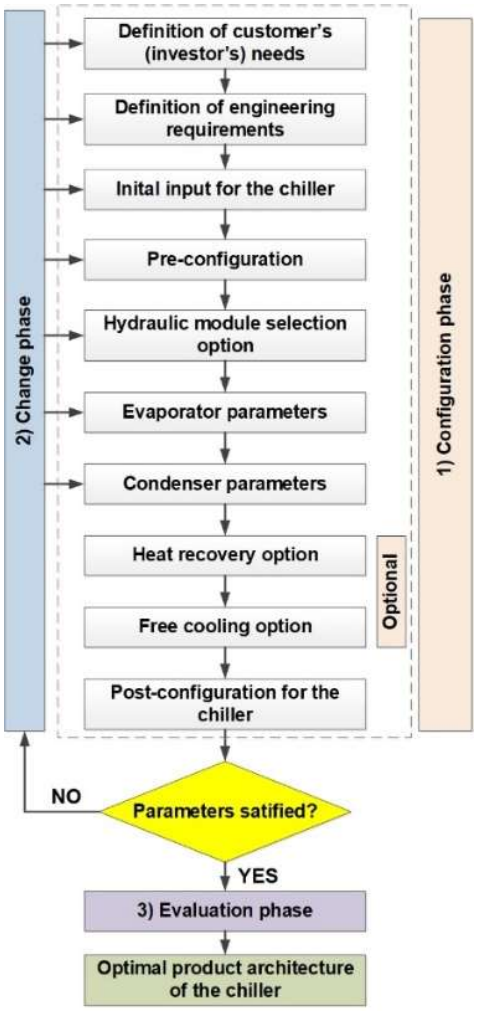

Figure 5. CCM approach [23].

Figure 6. 3D view of chillers: air-cooled chiller (left), water-cooled chiller (right).

Table 2. Several steps during the changes phase in the chiller selection process.

Parameters	Type of chiller					
	Air-cooled	*Air-cooled*	*Air-cooled*	*Water-cooled*	*Water-cooled*	*Water-cooled*
Number of iteration steps	2	3	4	2	3	4
Q [kW]	862.2	965.3	946.9	877.9	925.5	925.5
EER [kW/ kW]	3.03	3.1	3.14	5.36	6.02	5.85
ESEER	4.4	4.54	4.62	6.4	6.85	8.55
N_{el} [kW]	284.8	311.1	307.5	176	160	165
SPL [dB(A)]	63	64	61	66	66	66
Dimensions [$L \times W \times H$] [m]	8.3 × 2.2 × 2.6	10.1 × 2.2 × 2.8	10.1 × 2.2 × 2.8	3.6 × 1.6 × 1.9	4.1 × 1.6 × 1.9	4.1 × 1.8 × 2.0
m [kg]	7200	7298	5650	5790	6550	6750
Energy class	B	A	A	A	A	A

an evaluation step. The selection of the optimum type of chiller is shown in the evaluation step (Table 3). This was done by comparing the two most acceptable cooler variants for both installation methods. Depending on the values for the comparison parameters, scores of 1-10 were given. A score of 10 is the best possible score for the observed parameter. The scores in the columns were then totalled and displayed in the SUM (Σ) row.

Table 3. Evaluation step during the chiller selection process.

Parameters	Type of chiller			
	Air-cooled		*Water-cooled*	
Q [kW]	10	9	9	9
EER [kW/ kW]	9	10	10	9
ESEER	9	10	9	10
N_{el} [kW]	8	10	10	9
SPL [dB(A)]	8	10	7	7
Dimensions [$L \times W \times H$] [m]	5	5	9	9
m [kg]	6	6	10	8
Energy class	10	10	10	10
SUM (Σ)	65	70	74	71

In the evaluation process, 2 variants of air-based chillers and 2 variants of water-based chillers were considered. Two chiller variants with a water-based condenser were proposed as the final solution. Regardless of the price of the device, a water-based chiller was chosen due to its smaller dimensions, lower weight, and better *EER* coefficient. In addition, maintenance of the device should be taken into account, which is cheaper due to its internal installation.

The product configurator can also be adapted and extended for configuring other products (e.g., air conditioning units). This would require minor adjustments to dialog boxes, due to different input data and descriptions. In addition, it would be necessary to expand the knowledge base and include information about new products, such as CAD models and device schematics.

VALIDATION OF USER TESTING

To validate the configurator's performance, a survey was conducted by non-technical users. Fifteen users participated, each completing a questionnaire with ten questions about the use of the product configurator. The survey used a Likert scale with ratings from 1 to 5: 1 – Not Satisfied, 2 – Satisfied, 3 – Good, 4 – Very Good, and 5 – Excellent. The results of the survey are presented in Table 4, showing, by question, the percentage of users who selected each rating.

As shown in the attached Table 4, most non-technical users answered Excellent or Very Good. There are no unsatisfied responses in the survey. This confirms that the configurator is suitable for users without technical knowledge of the product. Additionally, only a relatively short time is needed to complete the desired selection, including any additions or corrections in configuration.

Table 4. The percentage of user responses in the survey conducted.

Questions in the survey	Percentage and number of user responses in survey [%]				
	Excellent	*Very good*	*Good*	*Satisfied*	*Not satisfied*
Q1: How do you rate the dialogue windows in the programme that guide you to the final solution?	40 (6)	33.3 (5)	13.3 (2)	13.3 (2)	0
Q2: How do you rate the accompanying graphics that assist you during product selection?	46.7 (7)	33.3 (5)	20 (3)	0	0
Q3: How do you rate the clarity and description of each step, enabling you to proceed to the next step?	46.7 (7)	40 (6)	13.3 (2)	0	0
Q4: How do you assess whether a sufficient number of steps have been provided to allow you to easily reach the final solution?	53.3 (8)	33.3 (5)	13.3 (2)	0	0
Q5: How do you rate the ability to select accessories during product selection?	60 (9)	33.3 (5)	6.7 (1)	0	0
Q6: How do you rate the quality of the files generated after product selection?	60 (9)	26.7 (4)	6.7 (1)	6.7 (1)	0
Q7: How do you rate the ability to make configuration changes during and after product selection?	53.3 (8)	33.3 (5)	13.3 (2)	0	0
Q8: How do you assess the duration of the selection process to reach the desired solution?	46.7 (7)	33.3 (5)	13.3 (2)	6.7 (1)	0
Q9: How do you rate the ability to save the selections made and the files created?	46.7 (7)	40 (6)	6.7 (1)	6.7 (1)	0
Q10: How do you rate the performance of the entire computer programme for configuring chillers?	60 (9)	33.3 (5)	6.7 (1)	0	0

CONCLUSION AND FUTURE RESEARCH

The article presents the architecture of the product configurator, which is structured as an advisory system. The functionality, data recording, and selection and evaluation of the chiller using the integrated CCM methodology were demonstrated. The research presented in the paper brings the following:

- Data retrieval is performed by a combination of mapping techniques and fuzzy rules.
- The product configurator enables the addition of the knowledge base.
- It also has the option of selecting based on a similar scenario.
- The configurator is designed in such a way that it can also be used by users who do not have in-depth specialised knowledge.
- Dialogue windows guide the user step by step to the final solution.
- The knowledge about chillers is recorded in a matrix record using the component-based DSM method.
- The CCM methodology enables the configuration and evaluation of the chiller and possible changes at the same time.
- The preparation of technical documentation.
- Matrix display of all connected components, subsystems, and modules.
- Better system performance is achieved with a chiller with a water-based condenser instead of a chiller with an air-cooled condenser.
- The option to save the completed selection as a file, to accommodate potential changes or additions to the configuration, and for possible future selections of similar products.
- Possible directions for future research are:
- A more detailed development of the knowledge base.
- Expansion of the configurator for use when selecting other products in the field of equipment for HVAC systems (e.g., air conditioning units).

NOMENCLATURE

Acronyms

CCM - Configuration and Change Management
CRM - Customer Relationship Management
DSM - Design Structure Matrix
GUI - Graphical User Interface
MF - Membership Function

VARIABLES

EER - Energy Efficiency Ratio [kW/kW]
$ESEER$ - European seasonal energy efficiency ratio
$L \times W \times H$ - chiller dimensions (length×width×height) [mm]
m - operating chiller mass [kg]
N_{el} - total electrical power input [kW]
SPL - sound pressure level at 10 m [dB(A)]
Q - cooling capacity of chiller [kW]
μ_A - membership function of fuzzy sets
μ_{agg} - output membership function

REFERENCES

[1] R. Saidur, Renewable Sustainable Energy Rev. 14 (2010) 877-898. https://doi.org/10.1016/j.rser.2009.10.018.
[2] L. Zhang, H. Fukuda, Z. Liu, J. Cleaner Prod. 228 (2019) 770-777. https://doi.org/10.1016/j.jclepro.2019.04.338.
[3] M.Y. Shabalov, Y.L. Zhukovskiy, A.D. Buldysko, B. Gil, V.V. Starshaia, Energy Rep. 7 (2021) 2664-2680. https://doi.org/10.1016/j.egyr.2021.05.001.
[4] C.C. Hampo, A.A. Mokhtar, M. Muhammed, K.A. Hewage, D. Rasangika, Y. Shanshan, Int. J. Sustainable Energy 41(8) (2021) 1-16. https://doi.org/10.1080/14786451.2021.2021907.
[5] H. Jalo, H. Pirkkalainen, Int. J. Info. Manage. 75 (2024) 102731. https://doi.org/10.1016/j.ijinfomgt.2023.102731.
[6] J. Prentzas, I. Hatzilygeroudis, Expert Syst. 24(2) (2007) 97-122. https://doi.org/10.1111/j.1468-0394.2007.00423.x.
[7] Haug, S. Shafiee, L. Hvam, Comput. Ind. 105 (2019) 133-142. https://doi.org/10.1016/j.compind.2018.11.005.
[8] T. Blecker, N. Abdelkafi, G. Kreuter, G. Friedrich, in Eight Maghrebian Conference on Software Engineering and Artificial Intelligence (MCSEAI 2004), Sousse, Tunisia (2004), pp. 25-36.
[9] T. Blecker, Encyclopedia of E-Commerce, E-Government, and Mobile Commerce, IGI Global, Hershey, PA, USA (2007) 191-196. https://doi.org/10.4018/978-1-59140-799-7.ch151.
[10] D. Antonelli, N. Pasquino, A. Villa, in Proceedings of AMST'05 Advanced Manufacturing Systems and Technology, Udine, Italy CISM 486 (2005), pp. 317-326. https://doi.org/10.1007/3-211-38053-1_30.
[11] Haug, L. Hvam, N.H. Mortensen, Artif. Intell. Eng. Des. Anal. Manuf. 25 (Special Issue 02) (2011) 197-206. http://doi.org/10.1017/S0890060410000636.
[12] Haug, L. Hvam, N.H. Mortensen, Comput. Ind. 63(5) (2012) 471-481. http://doi.org/10.1016/j.compind.2012.02.001.
[13] Haug, S. Shafiee, L. Hvam, Comput. Ind. 105 (2019) 133-142. https://doi.org/10.1016/j.compind.2018.11.005.
[14] S. Shafiee, A. Haug, S. Shafiee Kristensen, L. Hvam, J. Manuf. Technol. Manage. 32(1) (2021) 219-241. https://doi.org/10.1108/JMTM-04-2020-0137.
[15] L. P. Poot, PhD thesis, Faculty of Science and Engineering, Linköping University, Linköping, Sweden (2021). https://liu.diva-portal.org/smash/record.jsf?pid=diva2%3A1620210&dswid=6033.
[16] R.N. Workalemahu, C. Forza, N. Suzic, in Proceedings of the 26th ACM International Systems and Software Product Line Conference

(SPLC '22) - Volume B, Graz, Austria (2022), pp. 201-208. https://doi.org/10.1145/3503229.3547038.
[17] J. Nummela, in Proceedings of Nord Design 2004, Tampere, Finland (2004), 299-308. URL: https://www.designsociety.org/publication/29221/matrix_based_method_for_maintaining_configuration_knowledge.
[18] O. Johansson, P. Krus, in Proceedings of IDETC/CIE2006 ASME 2006 International Design Engineering Technical Conferences & Computers and Information in Engineering Conference, Philadelphia, USA (2006), pp. 691-700. https://doi.org/10.1115/DETC2006-99481.
[19] P.T. Helo, Ind. Manag. Data Syst. 106(7) (2006) 997-1011. http://doi.org/10.1108/02635570610688896.
[20] M. Germani, M. Mengoni, R. Raffaeli, in Proceedings of International Design Conference - DESIGN 2006, Cavtat, Croatia (2006), pp. 253-262.
[21] J.A. Gopsill, C. Snider, C. McMahon, B. Hicks, Artif. Intell. Eng. Des. Anal. Manuf. 30 (2016) 424-445. http://doi.org/10.1017/S0890060416000391.
[22] K. Osman, M. Perić, D. Stamenković, Sci.Tech. Rev. 61(3-4) (2011) 95-101.
[23] K. Osman, Ž. Tomaš, D. Pervan, Procedia CIRP. 60 (2017) 464-469. https://doi.org/10.1016/j.procir.2017.02.032.
[24] K. Osman, M. Perić, J. Cleaner Prod. 416. (2023), 137803. https://doi.org/10.1016/j.jclepro.2023.137803.
[25] K. Osman, M. Perić, T. Alajbeg, in Proceedings of SpliTech 2024 - 9th International Conference on Smart and Sustainable Technologies. Bol, Croatia (2024), pp. 1-6. https://doi.org/10.23919/SpliTech61897.2024.10612499.
[26] Zhou, Z. Lin, C. Liu, Int. J. Adv. Manuf. Technol. 38(1) (2008) 185-194. https://doi.org/10.1007/s00170-007-1089-6.
[27] H. Wu, Z. Xu, Int. J. Comput. Commun. Control. 16(1) (2021) 1-28. https://doi.org/10.15837/ijccc.2021.1.4044.
[28] T.D. Toan, Y.D. Wong, S.H. Lam, M. Meng, Phys. A (Amsterdam, Neth.) 604 (2022) 1-19. https://doi.org/10.1016/j.physa.2022.127899.

KREŠIMIR OSMAN[1]

MATO PERIĆ[2]

DRAGI STAMENKOVIĆ[3]

MIHAILO LAZAREVIĆ[4]

[1]Department of Electrical Engineering, University of Applied Sciences, Zagreb, Croatia

[2]Department of Mechatronics, University North, Koprivnica, Croatia

[3]The College of Applied Studies "Aviation Academy", Belgrade, Serbia

[4]Chair of Mechanics, Faculty of Mechanical Engineering, University of Belgrade, Belgrade, Serbia

NAUČNI RAD

KONFIGURATOR PROIZVODA ZASNOVAN NA SAVETOVANJU, KORIŠĆEN U KONFIGURISANJU I EVALUACIJI RASHLADNIH SISTEM

Ovaj članak predstavlja arhitekturu i funkcionalni princip konfiguratora proizvoda zasnovanog na na savetovanju. Program se koristi za kreiranje novih i modifikovanje sličnih konfiguracija proizvoda i namenjen je korisnicima bez većeg stručnog znanja u tehničkim oblastima. Zbog svoje arhitekture, konfigurator je dizajniran da koristi znanje uskladišteno u bazi znanja. Izbor se zasniva na kombinaciji fazizih pravila zaključivanja i tehnika mapiranja. Znanje o proizvodu se sakuplja korišćenjem matrica zasnovanih na komponentama. Takođe je obezbeđena mogućnost dodavanja novog znanja i novih pravila. Sve ovo omogućava konfiguratoru da poveže zahteve kupaca i nudi mogućnost izbora jednog ili više proizvoda. Pored toga, procenjuje moguće varijante proizvoda na osnovu parametara koje je korisnik naveo. Grafički prikaz dobijenih rezultata uključuje tehničku dokumentaciju proizvoda, kao i matrični prikaz svih izabranih komponenti i modula. Funkcionalni princip i evaluacija izbora proizvoda demonstrirani su korišćenjem studije slučaja rashladnih sistema za industrijska postrojenja. Tokom izbora i evaluacije rashladnog sistem, bolje performanse postrojenja se postižu rashladnim sistemom koji ima kondenzator na bazi vode..

Ključne reči: arhitektura konfiguratora proizvoda, pravilo fazi inferencije, matrična reprezentacija, CCM metodologija, izbor proizvoda.